Turbulent wake influence on sailplane performance

NM Mthembu

orcid.org/0000-0001-8314-6336

Dissertation submitted in fulfilment of the requirements for the degree *Master of Science in Mechanical Engineering* at the North-West University

Supervisor: Dr JJ Bosman

Co-supervisor: Dr JH Kruger

Graduation ceremony: May 2019

Student number: 25803786

Abstract

A Computational Fluid Dynamics (CFD) study was conducted to investigate the influence of a turbulent wake flow on the aerodynamic performance of the JS-1 sailplane. The Menter (1992c) SST $k-\omega$ turbulence model was coupled with the $\gamma - Re_\theta$ transition model to model a transitional and turbulent wake flow on the JS-1. As a necessary step, the SST $k-\omega$ turbulence and $\gamma - Re_\theta$ transition model was validated. The validation process comprised of four stages which ascertained the ability of the physical model to predict a transitional and turbulent wake flow on sailplane geometries. The validated CFD tool was used and it was observed that the source of the turbulent wake is a separated turbulent boundary layer from the wing-fuselage junction. A boundary layer analysis was conducted on the JS-1 fin and it was seen that approximately 23.6% of the total fin height is immersed in the turbulent wake. A quantitative drag force analysis showed that the turbulent wake has a significant contribution towards the total drag force on the JS-1 sailplane during thermal flight. The implementation of a combined low wing and high tail configuration with high aspect ratio fin was suggested as the optimal design option to enhance the performance of the JS-1 sailplane during thermal flight.

Keywords: JS-1 sailplane performance; Low Reynolds number and low turbulence intensity; Sailplane boundary layer transition and turbulent wake; Fin skin friction drag; SST $k-\omega$ turbulence modeling; $\gamma - Re_\theta$ transition modeling;

Dedication

My humble efforts are dedicated to my family, the **Mthembu family** and particularly to my loving and supportive mother, Bongiwe Mthembu whose patience, remarkable support, words of encouragement and fervent prayers have brought me thus far in my studies.

Acknowledgements

I praise the Lord God of heaven for an opportunity to pursue and to complete my MSc. Mech. Eng studies. My heavenly Father's unfailing hand of guidance and constant supply of wisdom and understanding, strength and perseverance have solely and undoubtedly brought me to the completion of this work. Indeed, every good and perfect gift is from above, coming down from the Father of lights, with whom there is no variableness, neither shadow of turning (**James 1:17**).

Every great work requires self-exertion and guidance from the grey heads of experience. My regards to my main supervisor Dr. J.J. Bosman, a senior lecturer in the school of Mechanical and Nuclear engineering at the North-West University and a chief aerodynamic design engineer for the Jonker Sailplane company and to my co-supervisor Dr. J. Kruger, a senior lecturer in the school of Mechanical and Nuclear engineering at the North-West University. Their academic and technical experience, joint supervision and efforts towards the completion of this study have been invaluable.

I would like to thank Mr. L. le-Grange, a Computational Fluid Dynamics (CFD) researcher in the Faculty of Engineering at the North-West University and Dr. J.H. Grobler a CFD researcher at the CSIR's aeronautics systems division and Mr. C. de Wet, a CFD consultant at Aerotherm computational dynamics for the North-West University. Their vast experience in practical CFD has made an immense contribution in this study.

A thank you to Dr. K. Naidoo, the competency area manager at the CSIR's aeronautics systems division, for allowing me a brief job shadow opportunity in the period 15

January - 2 February 2018. The exposure to the CSIR's aeronautics systems division has had positive and far-reaching effects in the study.

A special thanks to my best friend Baipidi Morakile for her prayers and support throughout the study period.

Finally, my deepest gratitude to my uncle Mr. B. Mwelase for playing a pivotal role in my academic pursuit.

Contents

List of Figures

List of Tables

Nomenclature

Roman symbols

C_d	Total airfoil drag coefficient
C_D	Total drag coefficient
C_{Df}	Total skin friction drag coefficient
C_f	Skin friction coefficient
C_l	Airfoil lift coefficient
C_L	Lift coefficient
C_p	Pressure coefficient
D	Total drag force
k	Turbulent kinetic energy
L	Lift force
N_{crit}	Amplication factor for eN transition model
p	Pressure
p_∞	Freestream pressure
Re	Reynolds number
Re_{crit}	Critical Reynolds number
Re_θ	Momentum thickness Reynolds number
I	Turbulence intensity
u_τ	Friction velocity
u^+	Non-dimensional velocity
$\mathbf{u}, \mathbf{v}, \mathbf{w}$	Fluctuating velocity components in x, y and z directions

U_∞	Freestream velocity
x, y, z	Cartesian coordinates
y	Wall distance
y^+	Non-dimensional normal distance from the wall
$-\overline{u_i' u_j'}$	Reynolds stress tensor
$u_i' u_j'$	Normal turbulence intensity

Greek symbols

α	Angle of attack
δ_{ij}	Kronecker delta
γ	Intermittency
δ	Boundary layer thickness
ϵ	Turbulent kinetic energy dissipation rate
η	Length scale
θ	Momentum thickness
κ	von Kàrmàn constant
μ	Molecular dynamic viscosity
μ_τ	Turbulent dynamic viscosity
ν_τ	Kinematic eddy-viscosity
ρ	Density
ρ_∞	Freestream density
τ	Viscous shear stress
$\underline{\tau}$	Time scale
τ_{ij}	Viscous stress component
$\overline{\tau_{ij}}$	Time averaged viscous stress component
υ	Velocity scale
ϕ	Variable parameter
$\overline{\phi}$	Time-averaged value of a variable
$\phi^{'}$	Fluctuating part of variable ϕ

ω	Specific dissipation rate

Acronyms

AIAA	American Institute of Aeronautics
CFD	Computational Fluid Dynamics
GCI	Grid Convergence Index
DES	Detached Eddy Simulation
DNS	Direct Numerical Simulation
EARSM	Explicit Algebraic Reynolds Stress Model
JS-1	Jonker Sailplanes 18m class sailplane model number 1
LES	Large Eddy Simulation
Mu-31	15m class sailplane model number 31 designed by Akaflieg Munchen
NACA	National Advisory Committee on Aeronautics (USA)
NPL	National Physical Laboratory (USA)
RANS	Reynolds Averaged Navier-Stokes models
RSM	Reynolds Stress Models
SNL	Sandia National Laboratries (USA)

Glossary

CAD - Computer-aided design involves the use of computer systems to aid in the modeling and analysis of a design.

CFD - Computational Fluid Dynamics is a branch of fluid mechanics that uses numerical methods and algorithms to solve fluid flow problems.

DES - Dettached Eddy simulation is a solution approach in Computational Fluid Dynamics that involves the space filtering of the Navier-Stokes equations to separate the resolvable scales of the largest eddies from the subgrid scales of the small eddies.

DNS - Direct Numerical Simulation is a solution approach in Computational Fluid Dynamics in which the exact Navier–Stokes equations are solved numerically.

LES - Large Eddy Simulation is a solution approach in Computational Fluid Dynamics which involves the space filtering of the Navier-Stokes equations to separate the resolvable scales of the large eddies from the subgrid scales of the smallest eddies.

RANS - Reynolds-Averaged Navier-Stokes equations are a mathematical model that is used in Computational Fluid Dynamics to solve the Navier-Stokes equations by averaging all the unsteadiness that is associated with turbulence.

Chapter 1

Introduction

1.1 Background

Gliders, also known as sailplanes, are a special kind of aircraft that do not make use of an engine whilst in flight. Therefore, compared to powered aircraft, gliders fly in the absence of thrust thus making lift, weight and drag, the only forces that act on this type of craft whilst in flight (U.S. Department of Transportation, 2013). The influence of a turbulent wake on the performance of a sailplane can be contextualised by considering the principles of gliding and the analysis techniques required for aircraft design.

1.1.1 Principles of sailplane flight

A comparison of the forces that act on powered and un-powered aircraft in their respective equilibrium positions is given in figure 1.1.

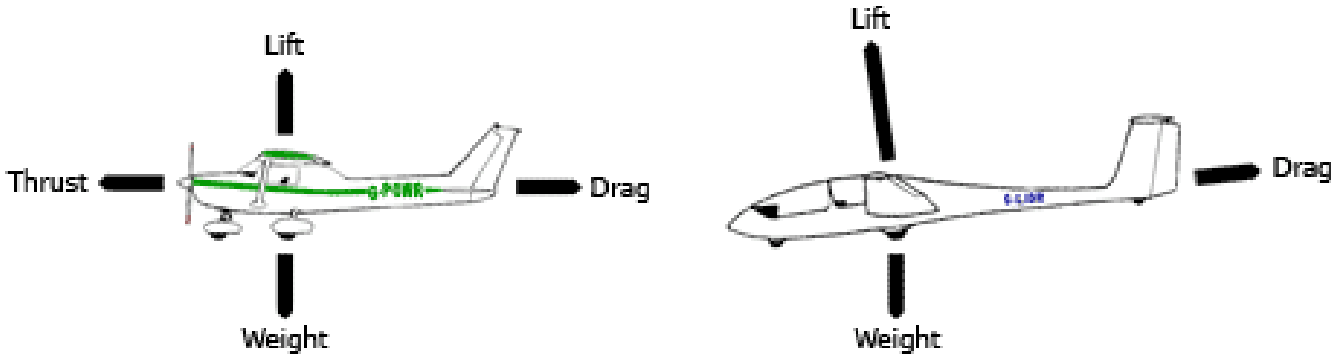

Figure 1.1: Comparison of forces that act on powered (left) and un-powered (right) aircraft (Club, 2018).

Gliders do not have thrust which is generated by an engine, but acquire thrust and hence lift by an application of the Energy conservation law, Newton's third law of motion and the Bernoulli principle (United States Department of Transport, 2016). When ascending from lower to higher altitudes, the glider accumulates potential and kinetic energy and when descending from higher to lower altitudes, it trades that potential energy for kinetic energy and thus produces forward propulsion and lift (U.S. Department of Transportation, 2013). In addition, the lift force is generated as the result of the pressure difference between the top and bottom surface of the wing. The conversion between the potential and the kinetic energy takes place until the glider finally comes to rest on the surface of the earth.

Figure 1.2 shows a basic diagram of the vector forces acting in equilibrium on a descending glider.

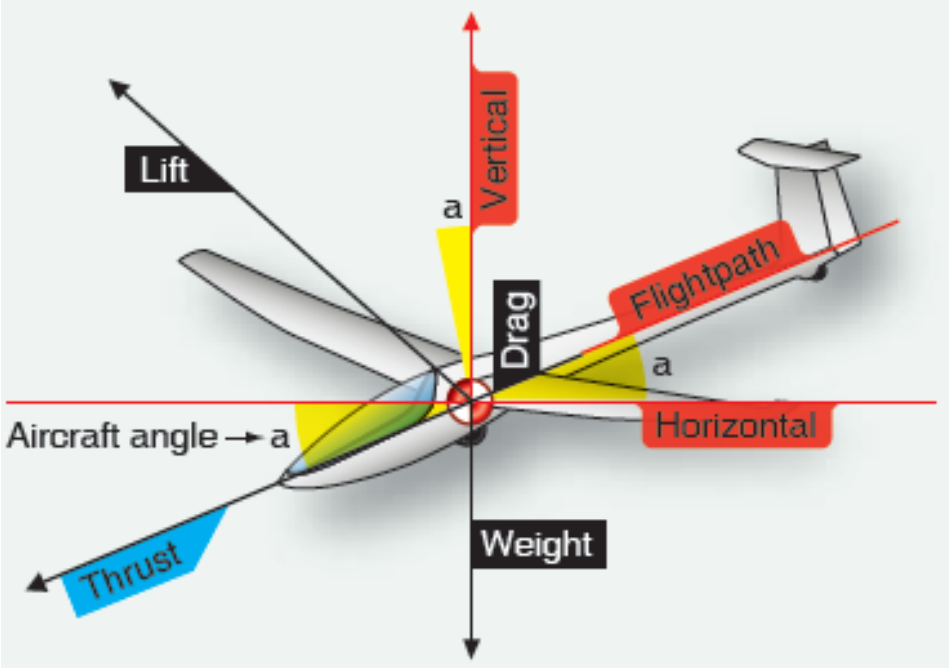

Figure 1.2: Vector balance forces for a glider (U.S. Department of Transportation, 2013).

The weight vector always acts from the glider's center of gravity towards the center of the earth and its magnitude depends on the mass of aircraft and its payload. The lift vector always acts perpendicular to the flight path and its magnitude is dependent on the design of the geometry and lifting surfaces and the velocity of the aircraft U.S. Department of Transportation (2013); United States Department of Transport (2016). The drag vector always acts parallel to the flight path and opposite to the flight direction and its magnitude depends on the design of geometry and lifting surfaces and velocity of the aircraft U.S. Department of Transportation (2013); United States Department of Transport (2016). For small glide angles, the ratio of the glider's lift to its drag is equal to the inverse of its angle of descent as shown in equation (1.1).

$$\frac{\mathbf{L}}{\mathbf{D}} = \frac{1}{\alpha}. \tag{1.1}$$

The lift to the drag ratio of an aircraft is known as the glide ratio and is an efficiency factor for aircraft, with high glide ratio being the goal in aerodynamic design. Two

deductions can be thus made: for aerodynamic efficiency, it is necessary to reduce drag and for a high glide ratio the angle of descent must be minimal.

Current optimization strategies in sailplane development rely on validated numerical simulation models as the design tool to achieve these goals.

1.1.2 Boundary layer analysis on the JS-1 sailplane fin

Sailplanes operate in a flow regime ($Re \approx O(10^6)$) where both laminar and turbulent boundary layers exist on the surfaces. High performance sailplane design focuses a lot of attention on controlling the behavior of the boundary layer to minimize drag over the surfaces of the aircraft. For minimal overall drag, laminar flow is preferred which gives roughly five to ten times less drag than turbulent flow (U.S. Department of Transportation, 2013). Therefore, the boundary layer must be controlled such that the transition from laminar to turbulent flow is delayed as much as possible over all the surfaces.

The high-performance JS-1 sailplane is designed and manufactured by the Jonker Sailplane company in Potchefstroom, South Africa. Oil flow visualization experiments are regularly used to determine the effect of geometric features on boundary layer behavior during flight. Figure 1.3 shows the boundary layer flow on the JS-1 fin surface as a consequence of upstream flow from the fuselage and wing-fuselage junction.

(a) Straight and level flight.

(b) Ascent.

(c) Descent.

Figure 1.3: Oil flow free-flight experiment on the JS-1 fin.

Figures 1.3a, 1.3b and 1.3c show the results of the oil flow experiment at straight and level flight, at ascent and at descent, respectively. It was observed that while there were some differences in the flow pattern at the three different flight stages, the general boundary layer flow behavior was similar, with a transitional separation bubble observed in all three cases. This bubble is a visualization of stagnant air beneath a separated layer of air from the aircraft surface, which later reattaches downstream of the separation point and indicates a transition from a laminar to a turbulent boundary layer (Hermann and Gersten, 2017.; Houghton, 2012).

The analysis of the oil flow experiment results revealed an influence of the upstream flow from the fuselage and wing-fuselage junction, on the boundary layer behavior on the fin surface. As shown in figure 1.4, this influence, reduces the amount of possible laminar flow on the fin surface and thus causes, unwanted, additional drag.

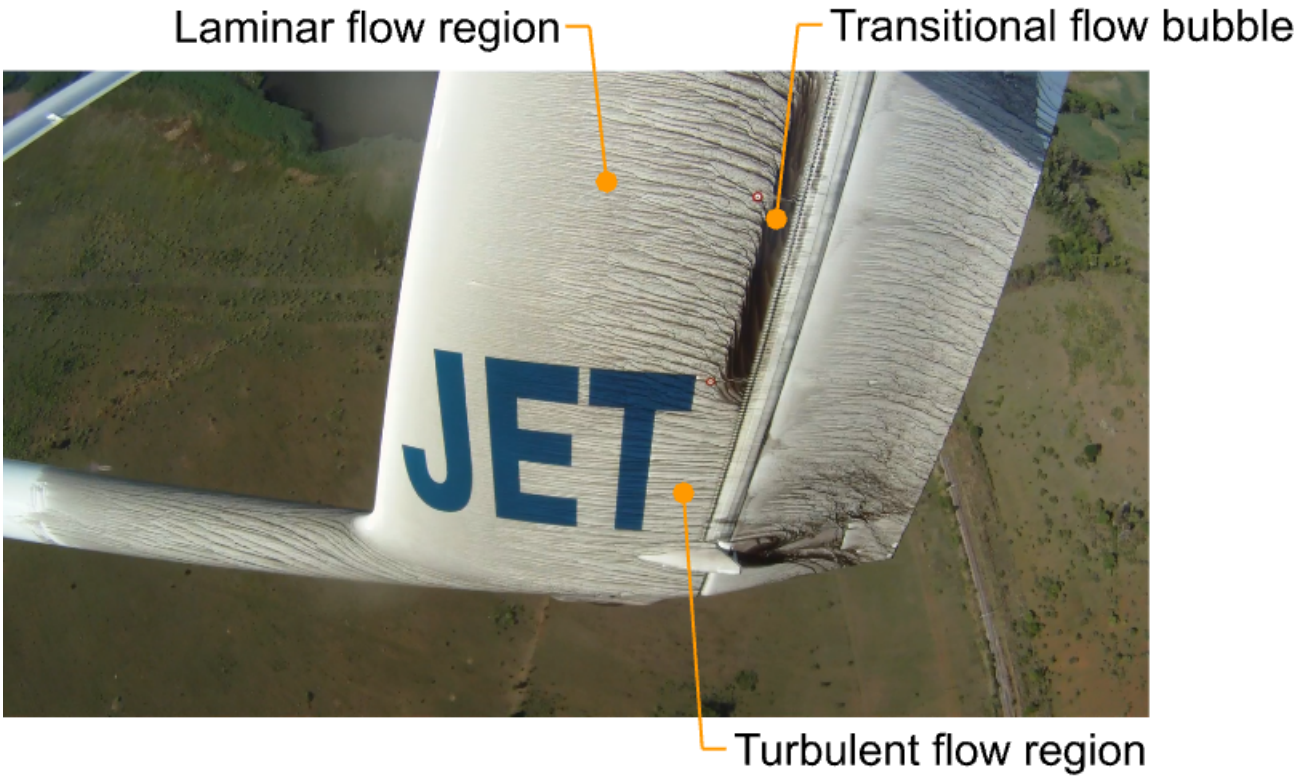

Figure 1.4: Laminar and turbulent flow regime over fin surfaces of the JS-1 sailplane in flight.

The boundary layer transitions from a laminar to a turbulent state on the top part of the fin where a transitional flow separation bubble is seen. In the transition region, the disturbances in the laminar boundary layer flow are at their peak and the flow begins to break down into small vortices which grow in size and energy until the flow becomes fully turbulent (Anderson, 2010; Hermann and Gersten, 2017.; Versteeg and Malalasekera, 2007). The transition from a laminar to a turbulent boundary layer flow on the top part of the fin is expected since the air upstream is not obstructed and consequently, not disturbed, i.e., the top part of the fin only comes into contact with the free stream flow.

On the other hand, it is noteworthy that the separation bubble does not exist on the bottom part of the fin. This suggests that the boundary layer flow on the bottom part of the fin is already fully turbulent. The turbulent flow on the bottom part of the fin indicates the possible existence of a turbulent wake as a consequence of already turbulent flow across the fuselage and the wing-fuselage junction.

1.2 Problem statement

A sizeable body of low-speed aerodynamics research has been undertaken to optimize sailplane flight performance by reducing the aerodynamic drag acting on its surfaces. The research has been successfully undertaken on individual sailplane geometries to optimize their efficiency. Airfoil design has been the chief area of study (see Abbott and von Doenhoff, 1959; Lyon et al., 1997; Selig and Bryan, 2004; Williamson et al., 2012; Selig, 1989; Selig et al., 1995; 1996; Williamson, 2012). The fuselage and the wing-fuselage combination has also received considerable attention (see Boermans and Terleth, 1984; Bosman, 2012; Popelka et al., 2012).

The past research has, however, neglected the effects that the upstream flow from the geometric features such as the fuselage, wing and wing-fuselage junction have on the fin which is far downstream in the flow. An in-depth scientific study was thus necessary to investigate the influence of the turbulent wake from the fuselage and the wing-fuselage junction on the JS-1 fin and consequently, its influence on the aerodynamic performance of the JS-1 sailplane.

1.3 Research aims and objectives

The main goal of the current study was to investigate the turbulent wake influence on the JS-1 sailplane aerodynamic performance. In order to achieve this goal, the following objectives had to be met.

- The validation of a Computational Fluid Dynamics design analysis tool for a

transitional and turbulent wake flow on sailplane geometries.

- A CFD investigation of the characteristics of the turbulent wake from the JS-1 sailplane fuselage and fuselage junction with the validated CFD tool.

- A CFD investigation of the boundary layer behavior on the JS-1 fin, as a consequence of the turbulent wake from the fuselage and wing-fuselage junction.

1.4 Research methodology

A Computational Fluid Dynamics (CFD) study was conducted to investigate the influence of a turbulent wake flow on the JS-1 sailplane performance. The literature review that was conducted motivated the implementation of the Menter (1992c) SST $k-\omega$ turbulence model with the $\gamma - Re_\theta$ transition model to model a transitional and turbulent wake flow on the JS-1 sailplane. A necessary step was to validate the SST $k-\omega$ turbulence model with the $\gamma - Re_\theta$ transition model to justify its use and to provide confidence in its ability to accurately represent the flow physics. A validation process that is endorsed by the CFD best practice guidelines by AIAA (1998) and Oberkampf and Trucano (2002), was used. The process comprised of four levels, namely, unit cases, benchmark cases, a subsystem case and a complete system case.

Unit cases

The first level of the validation process considered three unit cases.

- The first case was concerned with a steady-state, two-dimensional and transitional flow of an incompressible fluid on the NACA 0012 airfoil at low-Reynolds number and low-turbulence level. The engineering quantities of interest were pressure coefficient, skin friction coefficient and onset boundary layer transition points for a range of incidence angles.

- The second case considered a steady-state, two-dimensional and transitional flow of an incompressible fluid on the NACA 0012 airfoil at low-Reynolds number and low-turbulence level. The engineering quantities of interest were lift coefficient and drag coefficient for a range of incidence angles.

- The third case focused on a steady-state, two-dimensional, transitional and turbulent wake flow of an incompressible fluid on the NACA 0012 airfoil at low-Reynolds number and low-turbulence level. The engineering quantities of interest were the mean velocity and turbulence stresses (**uu**, **vv**, **ww** and **uv**) in the wake.

Benchmark cases

The second level of the validation process considered three benchmark cases. The benchmark cases were in effect a consideration of the unit cases in a three-dimensional flow level.

Subsystem case

The third level of the validation process was concerned with a steady-state, three-dimensional and transitional flow of an incompressible fluid on the Mu-31 sailplane fuselage at low-Reynolds number and low-turbulence level. The engineering quantity of interest was the fuselage and wing drag coefficient (interference drag). Flow streamlines on the fuselage, wing and wing-fuselage junction were also considered.

Complete system case

The final stage of the validation process considered a steady-state, three-dimensional, transitional and turbulent wake flow of an incompressible fluid on the JS-1 sailplane at low-Reynolds number and low-turbulence level. The validation focused on flow streamlines on the JS-1 fin.

The verification method that was proposed by Roache (1997) formed an integral part

of the validation process. The validated CFD tool was finally used to investigate the influence of the turbulent wake flow on the JS-1 sailplane performance.

1.5 Dissertation layout

The dissertation comprises of 8 chapters.

Chapter 1 presents a background to the present work, problem statement, aims and objectives of the study and a brief methodology that was employed in the study.

Chapter 2 is a first of two literature review chapters. The low-Reynolds number ($Re \approx O(10^6)$) boundary layer flow phenomena which is encountered in sailplane flight and their relation to the drag force are discussed. Flow phenomena such as transition, separation, reattachment and turbulent wake are considered.

Chapter 3 is the second literature review chapter and considers the mathematical modeling of the low-Reynolds number ($Re \approx O(10^6)$) flow phenomena which is encountered in sailplane flight. The aim of this chapter was to determine a physical model that can adequately model a sailplane flight.

Chapter 4 presents the methodology that was employed in the current study. The verification and validation processes are discussed.

Chapter 5 is a 2D and 3D flow validation study of the SST $k-\omega$ turbulence model with the $\gamma - Re_\theta$ transition model on the NACA 0012 airfoil and wing. The capability of the SST $k-\omega$ turbulence and $\gamma - Re_\theta$ transition model to accurately predict lift coefficient, drag coefficient, pressure coefficient, skin friction coefficient, onset transition points, mean velocity and turbulent stresses in a turbulent wake is validated against experimental data and XFOIL results.

Chapter 6 is a 3D flow validation study of the SST $k-\omega$ turbulence and $\gamma - Re_\theta$ transition model on the Mu-31 sailplane fuselage. The ability of the SST $k-\omega$ turbulence model with the $\gamma - Re_\theta$ transition model to accurately predict drag coefficient and fuselage flow streamlines is tested against experimental data.

Chapter 7 presents a brief validation case for a transitional and turbulent wake flow on the JS-1 sailplane. The ability of the SST $k-\omega$ turbulence and $\gamma - Re_\theta$ transition model to model a transitional and turbulent wake on the JS-1 is investigated. An analysis of the JS-1 turbulent wake and fin boundary layer is presented and the implications of the turbulent wake on the JS-1 sailplane performance are discussed.

The conclusions and recommendations for further work are presented in **Chapter** 8.

Chapter 2

Sailplane boundary layer and wake phenomena

Introduction

This chapter presents the first part of the literature review. The low-Reynolds number ($Re \approx O(10^6)$) flow phenomena that are encountered in sailplane flight and their relation to the drag force are discussed. Section 2.1 introduces the boundary layer concept and the relevance of shear stress. Section 2.2 discusses the shear stresses in the laminar and turbulent boundary layer flows and their influence on skin friction and interference drag. Section 2.3 covers the three boundary layer transition mechanisms. Section 2.4 deals with boundary layer separation and its influence on form drag. Section 2.5 focuses on boundary layer reattachment and the relevance of a boundary layer separation bubble. Section 2.6 covers the structure and dynamics of a turbulent wake flow. Section 2.7 discusses the calculation of aerodynamic forces and the relevance of shear stress and pressure distribution on the aerodynamic forces.

2.1 Boundary layer flow

The boundary layer concept, introduced by Prandtl in 1904, forms the basis for the analysis of viscosity affected flows or so-called boundary layer flows (Anderson, 2010; Hermann and Gersten, 2017.; Houghton, 2012; Wilcox, 2006). The boundary layer is the thin region of flow adjacent to an aerodynamic surface. Basic assumptions of the boundary layer theory, as shown in figure 2.1a, are that, the boundary layer is very thin in comparison to the scale of the body and it occupies a very small region of the entire flow domain (Anderson, 2010; Houghton, 2012).

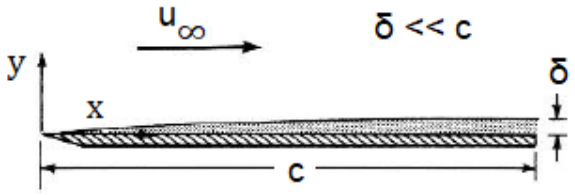

(a) Basic assumptions of boundary layer theory.

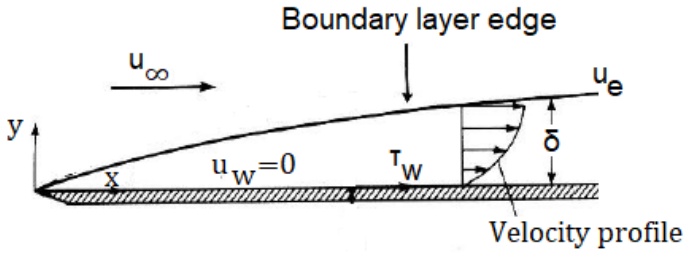

(b) Boundary layer properties and velocity profile.

Figure 2.1: The boundary layer concept (Anderson, 2010).

In the boundary layer, the free stream flow is retarded by the influence of friction between the solid surface and the fluid. Immediately at the surface, the no-slip condition is in effect and the flow velocity is zero relative to the surface while above the surface, the flow velocity increases in the normal direction until it reaches the free stream velocity (u_∞) at the edge of the boundary layer. The boundary layer is a height, δ, above the aerodynamic surface. The velocity at the edge of the boundary layer (u_e) is approximately equal to the free stream velocity, i.e., $u_e \approx u_\infty$, and thus viscosity effects are only contained within the boundary layer (Anderson, 2010; Houghton, 2012). The fluid elements closest to the solid wall experience the most flow resistance compared to those that are further away. This is illustrated by the velocity profile within the boundary layer, shown in figure 2.1b. The slope of the velocity profile within the boundary layer governs the wall shear stress (Anderson, 2010). The shear stress at the wall is given by equation 2.1.

$$\tau_w = \mu(\frac{du}{dy})_{y=0} \tag{2.1}$$

Equation 2.1 shows that the shear stress at the wall is directly proportional to the velocity gradients at the wall, i.e., $\tau_w \propto (\frac{du}{dy})_{y=0}$ and therefore, a larger wall shear stress is expected for a steep velocity profile.

The boundary layer grows with distance from the leading edge to the trailing edge of an aerodynamic surface as shown in figure 2.1 (Anderson, 2010). Alternatively, it can also be said that the boundary layer grows with Reynolds number, $Re_x = \frac{\rho_\infty u_\infty x}{\mu_\infty}$, from the leading edge to the trailing edge of an aerodynamic surface (Anderson, 2010; Houghton, 2012).

Using the concept of a boundary layer, the equations that govern viscous flow, i.e., the Navier-Stokes equations, can be reduced to a more manageable form [1], the so-called boundary layer equations, which can be solved to obtain the distribution of shear stress and aerodynamic heat transfer to the surface (Anderson, 2010; Wilcox,

[1] Before Prandtl's concept (established in 1904) of a boundary layer, the Navier-Stokes equations were well known, yet attempts to solve these equations for practical engineering problems was an impossibility for fluid dynamicists (Anderson, 2010; Wilcox, 2006).

2006). Boundary layer equations are model equations that describe the physics of a viscous flow inside the boundary layer; specifically they are simplified partial differential equations (Navier-Stokes equations) that apply inside the boundary layer (Anderson, 2010; Wilcox, 2006).

Although the boundary layer occupies geometrically only a small portion of the flow field, it is solely responsible for the skin friction drag on an aerodynamic body.

2.2 Laminar and turbulent boundary layer flow

Two types of boundary layer flows exist, viz., laminar and turbulent boundary layer flow. The laminar and turbulent boundary layers differ vastly in properties and the dramatic differences have a major impact on the aerodynamics of a flow.

In the laminar flow regime the fluid is considered to flow in smooth adjacent layers without lateral mixing of fluid elements (Anderson, 2010; Ferziger and Perić, 2002; Hermann and Gersten, 2017.; Houghton, 2012; Tennekes and Lumley, 1972; Versteeg and Malalasekera, 2007; Wilcox, 2006). The interaction between fluid elements is limited only to neighboring fluid elements and thus, there is no effective mixing of the fluid elements within the boundary layer. The viscous stresses due to momentum transport are manageable (Anderson, 2010; Ferziger and Perić, 2002; Hermann and Gersten, 2017.; Houghton, 2012; Tennekes and Lumley, 1972; Versteeg and Malalasekera, 2007; Wilcox, 2006).

In contrast to laminar flow, turbulent flow exhibits an irregular and chaotic motion of fluid elements (Anderson, 2010; Ferziger and Perić, 2002; Hermann and Gersten, 2017.; Houghton, 2012; Tennekes and Lumley, 1972; Versteeg and Malalasekera, 2007; Wilcox, 2006). The chaotic flow of fluid elements is characterized by eddying or swirling motions which extends the fluid element's interactions from neighboring fluid elements to distant fluid elements. This vigorous mixing causes a drastic increase in momentum exchange and consequently, the random, velocity and pressure fluctuations (Anderson, 2010; Ferziger and Perić, 2002; Hermann and Gersten,

2017.; Houghton, 2012; Tennekes and Lumley, 1972; Versteeg and Malalasekera, 2007; Wilcox, 2006).

Figure 2.2 shows the velocity profiles through a laminar and turbulent boundary layer respectively.

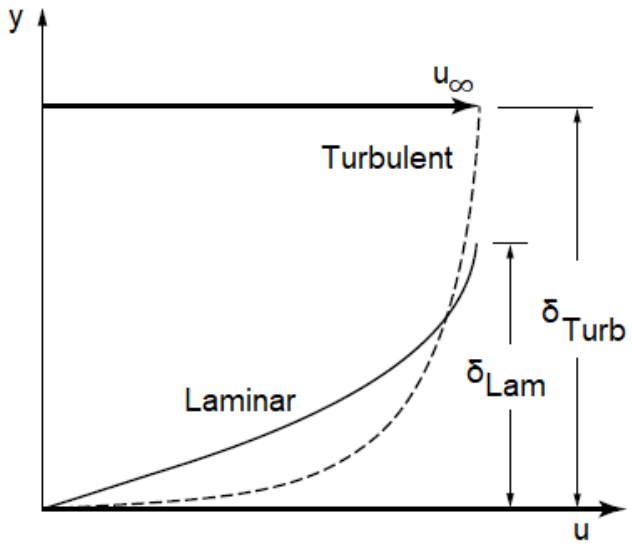

Figure 2.2: Velocity profile for laminar and turbulent boundary layers (Anderson, 2010).

The turbulent boundary layer velocity profile is thicker than the laminar boundary layer velocity profile for the same Reynolds number due to the increased momentum and energy transfer in a turbulent flow (Anderson, 2010; Houghton, 2012). According to Anderson (2010), the turbulent boundary layer thickness, δ_{Turb}, grows more rapidly with distance, x , along the surface compared to the laminar boundary layer, δ_{Lam}, i.e., $\delta_{Turb} \propto x^{4/5}$ in contrast to $\delta_{Lam} \propto x^{1/2}$.

The turbulent velocity profile is "full" compared to the laminar velocity profile. Therefore, for a turbulent boundary layer, the velocity remains reasonably close to the free stream velocity, from the edge of the turbulent boundary layer, δ_{Turb}, to a point near the surface and then rapidly decreases to zero at the surface while there is a gradual decrease in velocity from the laminar boundary layer edge, δ_{Lam}, to the surface for a laminar boundary layer. The velocity gradients at the wall are

therefore, larger in a turbulent boundary layer compared to a laminar boundary layer, i.e., $(\frac{du}{dy})_{y=0}$ laminar flow $<$ $(\frac{du}{dy})_{y=0}$ turbulent flow. This results in significantly larger shear stress at the wall for a turbulent boundary layer compared to a laminar boundary layer, i.e., τ_w laminar flow $< \tau_w$ turbulent flow (Anderson, 2010; Ferziger and Perić, 2002; Hermann and Gersten, 2017.; Houghton, 2012; Tennekes and Lumley, 1972; Versteeg and Malalasekera, 2007; Wilcox, 2006). It is the drastic increase in momentum transport that produces turbulent stresses in the turbulent boundary layer flow which are significantly larger than the viscous stresses in the laminar boundary layer flow. The turbulent stresses are several orders of magnitude larger than viscous stresses (Versteeg and Malalasekera, 2007; Wilcox, 2006). In most cases, laminar boundary layer flow is preferred on all sailplane surfaces for its modest contribution to shear stress and consequently, skin friction drag.

2.2.1 Skin friction drag

Skin friction drag is a contribution to the parasitic drag that is due to viscous effects in the boundary layer (Anderson, 2010; Hoerner, 1965; U.S. Department of Transportation, 2013; United States Department of Transport, 2016). According to U.S. Department of Transportation (2013), the boundary layer grows from a laminar to a turbulent state and that growth causes an increase in skin friction drag. Turbulent boundary layers generate five to ten times more skin friction drag than the equivalent laminar boundary layer. This type of drag can be reduced by slowing down the growth of the laminar boundary layer, therefore, glider designers try to maintain laminar boundary layer flow across as much of the aircraft as possible. However, the laminar boundary layer is susceptible to early separation and a separated boundary layer can be the source of form drag which is significantly larger than skin friction drag (Houghton, 2012; Versteeg and Malalasekera, 2007). In sailplane design, the boundary layer behavior is controlled to optimize sailplane performance.

2.2.2 Interference drag

Interference drag is another contribution to the parasitic drag that is due to viscous effects in the boundary layer. This form of drag is generated by the intersection and mixing of boundary layers between airframe components (Anderson, 2010; Hoerner, 1965; U.S. Department of Transportation, 2013; United States Department of Transport, 2016). The boundary layer across one component of an aircraft is forced to mix with the boundary layer of an adjacent or proximal component as seen in the wing-fuselage junction, i.e., the fuselage boundary layer collides with the wing boundary layer. According to Gur and Schetz (2010), other geometry intersections wherein a typical aircraft can generate interference drag is the wing-wing, wing-strut and fuselage-strut junctions and of all these, the most pronounced is the wing-fuselage junction. The mixing of two or more boundary layers of different characteristics[2], at an intersection point, causes a shearing of the boundary layers and results in a turbulent mixing of the air boundary layers to form a unique turbulent boundary layer (United States Department of Transport, 2016; Wilcox, 2006). The resulting turbulent boundary layer often separates from the aircraft surfaces and causes an increase in form drag.

2.3 Boundary layer transition

Boundary layer transition is a complex phenomenon, defined as the process of change from laminar to turbulent boundary layer flow as a consequence of instabilities in the laminar boundary layer (Anderson, 2010; Bradshaw, 1976.; Ferziger and Perić, 2002; Hermann and Gersten, 2017.; Houghton, 2012; Tennekes and Lumley, 1972; Versteeg and Malalasekera, 2007). When laminar flow develops along an aerodynamic surface,

[2]It is important to note the likelihood of the air streams across each surface differing in velocity and even direction. At the intersection point the air streams across the surfaces involved, interact and form a new air stream that can be unique in velocity, direction and flow regime (United States Department of Transport, 2016).

it is affected by various types of disturbances, which are the source of complex mechanisms which ultimately lead to turbulence. According to Anderson (2010); Aupoix et al. (2011) and Versteeg and Malalasekera (2007) boundary layer flow transition is strongly influenced by factors such as surface roughness, pressure gradients, heat transfer, wall vibrations and free stream turbulence levels. Transition from the laminar to the turbulent flow regime is of fundamental importance in the dynamics of near-wall flows. It strongly influences the evolution of aerodynamic quantities such as wall shear stress, skin friction, drag forces etc., and also determines the extent of this change (Di Pasquale et al., 2009). This is especially the case in low-speed aerodynamics which comprises of a range of Reynolds numbers wherein boundary layer transition is a key boundary layer phenomenon. There are three main mechanisms that lead to turbulence, viz., natural transition, bypass transition and separation induced transition.

Natural transition is observed when the laminar boundary layer is subjected to low free stream turbulence levels, typically, turbulence levels of less than one percent ($T_u < 1\%$) over a smooth wall (small surface roughness elements) with negligibly small surface vibrations (Aupoix et al., 2011; Eggenspieler, 2012). Natural transition results from the amplification of flow instabilities in the laminar boundary layer above a Reynolds critical number ($Re_{x,crit}$). Unstable two-dimensional disturbances, so-called Tollmien Schlichting (T-S) waves, exists at a critical point (x_{crit}) downstream of laminar boundary flow. These disturbances are amplified [3] in the flow direction over a range of low-Reynolds numbers and ultimately form vortical structures, so-called eddies, which characterize a turbulent boundary layer flow (Bradshaw, 1976.; Hermann and Gersten, 2017.; Versteeg and Malalasekera, 2007).

Bypass transition is observed when the laminar boundary layer is subjected to high free stream turbulence levels, typically, turbulence levels of more than one percent

[3] Amplification is, here, used as a generic term to encapsulate the different phases in the flow transition process. Aupoix et al. (2011); Hermann and Gersten (2017.) and Versteeg and Malalasekera (2007) give descriptions of the different phases in the natural transition process for a flat plate boundary layer.

($T_u > 1\%$) and/or over a rough surface (large surface roughness elements) and/or with significant surface vibrations. As a consequence of the significant disturbances in the laminar boundary layer an early laminar to turbulent flow transition, so-called bypass transition, occurs at unexpectedly lower Reynolds numbers than those observed for natural transition. According to Aupoix et al. (2011) and Eggenspieler (2012), high free stream turbulence, large wall surface roughness elements and significant structural vibrations are able to force the laminar boundary layer into transition far upstream of the natural transition location.

A transition from a laminar to a turbulent boundary layer flow as a consequence of laminar boundary layer separation, is known as separation induced transition. This transition takes place after the laminar boundary layer separates from an aerodynamic surface. According to Bradshaw (1976.); Houghton (2012) and Vlahostergios et al. (2009), the separation leads to a very rapid growth of disturbances in the laminar boundary layer and then to transition. In most cases the separated boundary layer reattaches to the flow surface as a turbulent boundary layer (Eggenspieler, 2012; Haggmark et al., 2001; Houghton, 2012; Vlahostergios et al., 2009). According to Anderson (2010) and Houghton (2012), the boundary layer reattaches as a result of the enhanced mixing of fluid elements caused by turbulence.

Sailplanes fly in low-turbulence intensity environments and at low-Reynolds number ranges in the order of approximately 10^6 and therefore, the natural and separation induced transition mechanisms are commonly observed.

2.4 Boundary layer separation

Boundary layer separation occurs as a consequence of a sufficiently strong adverse pressure gradient (increasing pressure gradient) in the streamwise direction on an aerodynamic surface (Anderson, 2010; Houghton, 2012; Wilcox, 2006). For a conceptual understanding of boundary layer separation, it is illustrative to consider the behavior of a boundary layer flow in an adverse pressure gradient. Figure 2.3 shows a

boundary layer flow along a surface with a gradual and steady convex curvature, i.e., a boundary layer flow along the surface of an airfoil beyond the point of maximum thickness.

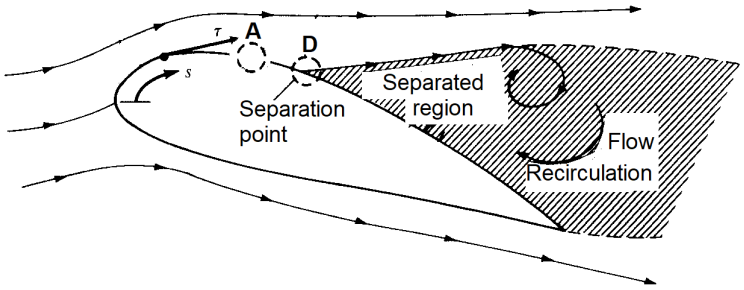

(a) Boundary layer separation nomenclature (Anderson, 2010).

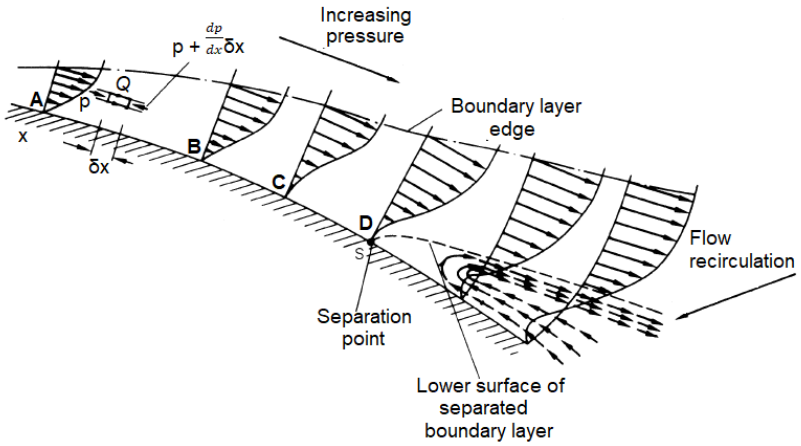

(b) Adverse pressure gradient and boundary layer separation (Houghton, 2012).

Figure 2.3: Effects of viscosity and increasing pressure gradient on boundary layer flow.

The free stream flow is decelerated in the boundary layer due to the presence of the airfoil surface and the fluid elements closest to the surface experience the most flow deceleration compared to those that are further away as illustrated by the velocity

profile at point A of figure 2.3b. A fluid element, Q, is close to the surface and is representative of the flow near the aerodynamic surface. An increasing pressure gradient exists along the flow stream, which further retards and decelerates the fluid element as it progresses downstream as shown by the progressive decrease in velocity gradients at the wall, $(\frac{du}{dy})_{y=0}$, at points B and C of figure 2.3b. The fluid element, Q, eventually comes to a halt at point D, and begins to reverse [4] from henceforth. Point D is the boundary layer separation point. Downstream of the separation point, the flow adjacent to the surface will be in the upstream direction (reversed flow) while the flow upstream of the separation point is in the streamwise direction so that the boundary layer separates at point D and flow circulation is observed near the surface, beneath the separated boundary layer. The dashed line in figure 2.3b represents the lower surface of the separated boundary layer and therefore, the mass flow above this line corresponds to the mass flow ahead of point D.

The consequence of the reversed flow phenomena is to cause the boundary layer to separate from the surface and the consequence of boundary separation is a turbulent wake downstream of flow as shown in figure 2.3a (Anderson, 2010; Houghton, 2012). On the other hand, form drag is the result of boundary layer separation.

2.4.1 Form drag

Form drag is a contribution to parasitic drag that is caused by the boundary layer separation (Anderson, 2008; Hoerner, 1965; U.S. Department of Transportation, 2013; United States Department of Transport, 2016). The resulting wake region is a low-pressure region which constitutes recirculation of flow. Boundary layer separation has a major influence on the pressure distribution, lift and drag forces of an aerodynamic body (Anderson, 2010; Houghton, 2012). Figure 2.4 gives a qualitative comparison of pressure distribution, lift and drag forces for attached and separated

[4] The velocity gradient at the wall, $(\frac{du}{dy})_{y=0}$, progressively decreases, downstream, from points A-D due to the increasing pressure gradient, such that the velocity gradient is reduced to zero at point D ($(\frac{du}{dy})_{y=0} = 0$). A negative velocity gradient, $(-\frac{du}{dy})_{y=0}$, exists after point D which is of reversed flow (Houghton, 2012).

flows. The length of the arrows denote the magnitude of the local pressure minus the free stream pressure, i.e., $p - p_\infty$ and the lift and drag forces respectively.

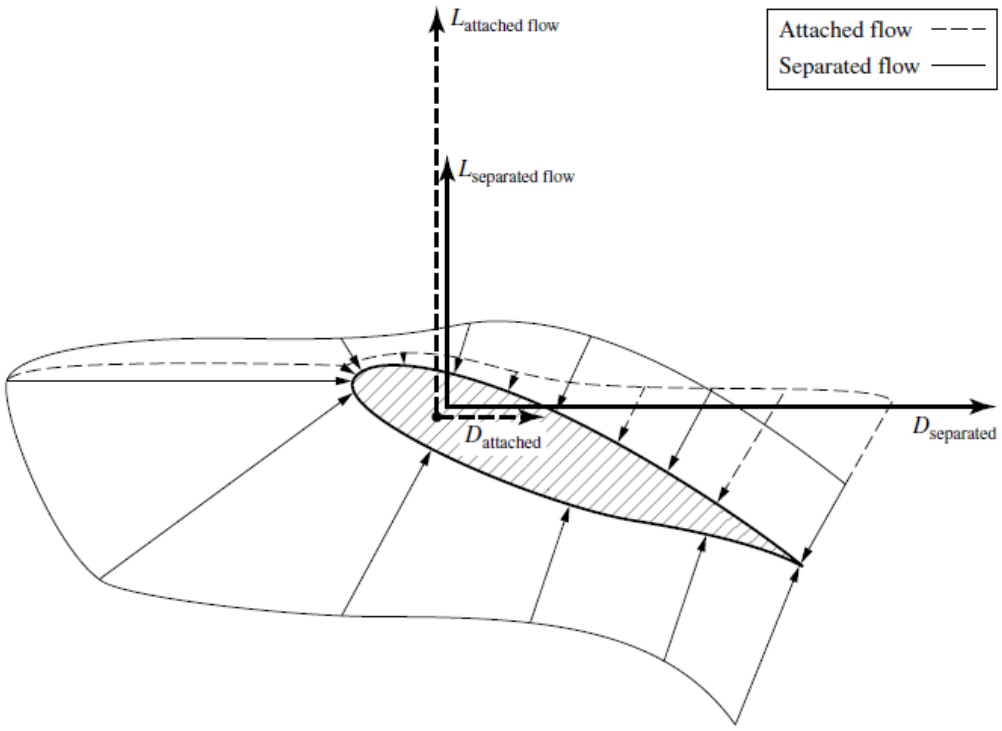

Figure 2.4: Qualitative comparison of pressure distribution, lift and drag for attached and separated flows (Anderson, 2010).

The separated boundary layer compromises the increase in pressure that occurs on the rear half of the airfoil for an attached boundary layer. For an attached boundary layer, the pressure on the rear half of the airfoil has a horizontal and forward acting component which counters the horizontal and rearward acting component of pressure on the leading edge to create zero form drag (Anderson, 2010; Houghton, 2012). According to Anderson (2010), failure to develop a pressure rise on the rear half of the airfoil, for a separated boundary layer, amounts to a net pressure force that acts in the streamwise direction. This pressure force (form drag) is exaggerated for cases with a massive separated region. According to Anderson (2010), the wake is the strength of the form drag force and the extent of this force depends on the size of the wake. Sailplanes have thin and well streamlined wings and fuselages that are designed

to delay flow separation and to offer the least amount of form drag (Anderson, 2010; U.S. Department of Transportation, 2013; United States Department of Transport, 2016).

2.5 Boundary layer reattachment

In many cases, airfoils with relatively large upper surface curvatures, experience a separation of the laminar boundary layer at moderate angles of attack as shown in figure 2.5.

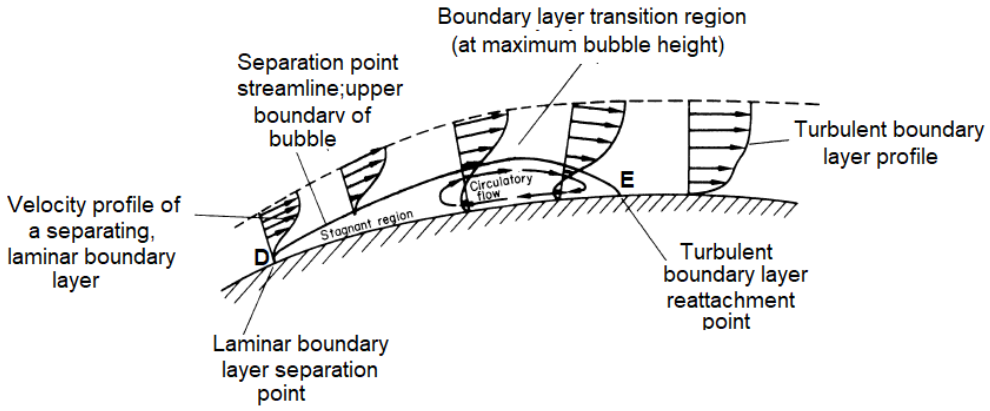

Figure 2.5: Boundary layer separation and reattachment (Houghton, 2012).

Small disturbances are more readily amplified in a separated laminar boundary layer flow compared to an attached laminar boundary layer flow. Consequently, the separated boundary layer undergoes transition to turbulence which is characterized by a rapid increase in kinetic energy and thickness of the boundary layer (Anderson, 2010; Houghton, 2012).

The turbulent boundary layer often re-attaches to the surface and in this way, a bubble of fluid is trapped under the separated shear layer, between the separation point and the reattachment point (Anderson, 2010; Houghton, 2012). Two regimes

exist within the separation bubble, viz., a region of stagnant fluid at constant pressure immediately after the laminar separation point, D, and a region of circulatory flow which is characterized by pressure that rapidly increases towards the reattachment point, E, as shown in figure 2.5 (Houghton, 2012).

Two distinct types of separation bubbles may occur, viz., a short bubble, which is of the order of 1% of the chord length and a long bubble, whose length may range from a few percents of the chord length to almost as long as the entire chord. Short separation bubbles are expected when the boundary layer reattaches soon after separation. This boundary layer behavior is typical for thin wing sections, which are typically found in sailplanes. These bubbles exert very little influence on the pressure distribution over the airfoil surface and remain small, with increasing angle of attack, right up to stall (Houghton, 2012). Short bubbles generally move slowly forward along the upper surface of the airfoil as the angle of attack is increased and will eventually lead to a leading-edge stall for relatively thin airfoils with a maximum thickness of 10-16% of chord length (Anderson, 2010; Houghton, 2012). According to Anderson (2010), for leading edge stall, flow separation takes place rather abruptly over the entire top surface of the airfoil with the origin of this separation occurring at the leading edge and the lift curve is sharp peaked at the vicinity of $c_{l,max}$ with a rapid decrease in c_l above stall. According to AlMutairi et al. (2017), the NACA 0012 airfoil which will be considered in the validation process falls under this category.

Separation bubbles can be divided into three main types, viz., laminar, transitional and turbulent, depending on the state of the boundary layer at separation and reattachment (Haggmark et al., 2001). The laminar separation bubble has a laminar boundary layer both at separation and reattachment (Haggmark et al., 2001). For a transitional separation bubble, the boundary layer separates as laminar and reattaches as turbulent whereas the turbulent separated bubble is observed for turbulent boundary layers (Haggmark et al., 2001). According to Hosseinverdi and Fasel (2015), of the three boundary layers that were mentioned, the transitional separation bubble is observed for low-Reynolds number flows at low free stream turbulence as considered in this research.

2.6 Turbulent wake flow

Amongst the simplest and practical turbulent flows of engineering interest are free shear turbulent flows (Pope, 2000; Tennekes and Lumley, 1972; Versteeg and Malalasekera, 2007; Wilcox, 2006). Free shear turbulent flows are turbulent flows that are not bounded by any solid surfaces (Pope, 2000; Tennekes and Lumley, 1972; Versteeg and Malalasekera, 2007; Wilcox, 2006). Five different types of free shear turbulent flows exist, viz., the wake, mixing layer, plane jet, round jet and radial jet. Of the five different types of free shear turbulent flows, the wake is of most interest in aerodynamics. The consequence of boundary layer separation from an aerodynamics surface is the production of a turbulent wake downstream of body (Anderson, 2010; Houghton, 2012; U.S. Department of Transportation, 2013; United States Department of Transport, 2016).

2.6.1 Turbulent wake structure

The importance of wake flows behind streamlined bodies, such as an airfoil or a flat plate, has led to a sizeable body of research on wakes. The earliest and most extensive single study on turbulent wake flows over slender bodies was conducted by Chevray and Kovasznay (1969). His pioneering work in this direction has led to a sizeable body of research that has been conducted on the turbulent wake generated by a flat plate and an airfoil and the consequent development of the nomenclature that is widely used today (see Alber, 1980; Andreopoulos, 1978; Bradshaw, 1970; Hah and Lakshminarayana, 1982; Ramaprian et al., 1982; Ramjee et al., 1988; Ramjee and Neelakandan, 1990).

The structure of wake flows is classified as either symmetric or asymmetric (Andreopoulos, 1978; Hah and Lakshminarayana, 1982). The wake of a symmetric airfoil at zero incidence angle is symmetric while it is asymmetric at non-zero incidence angle (Hah and Lakshminarayana, 1982). The asymmetric nature of the wake is due to loading on the airfoil and the differing nature of boundary layers on the pressure

and suction sides of the airfoil[5]. According to Hah and Lakshminarayana (1982), the asymmetric nature of the wake disappears after about 1.5 chords downstream from the trailing edge of the airfoil. Hah and Lakshminarayana (1982) further mentions that the asymmetric wake of an airfoil has a different decay rate of mean velocity defect and turbulence quantities from those of a symmetric wake.

The earliest studies on wake flows, by Andreopoulos (1978); Alber (1980); Bradshaw (1970); Hah and Lakshminarayana (1982); Ramaprian et al. (1982); Ramjee et al. (1988) and Ramjee and Neelakandan (1990), that have laid a foundation for wake studies were conducted for symmetrical wakes generated by a flat plate or an airfoil at zero and small incidence angles.

The wake can be classified into different regions according to the distance from the wake source and the characteristics of the wake. Alber (1980) divided the wake region into three regions, viz., near wake, intermediate wake and far wake. To determine whether the wake region is near, intermediate or far, Ramaprian et al. (1982) non-dimensionalised the downstream distance, x, by the initial momentum thickness, θ. According to Ramaprian et al. (1982) the near wake is defined by $x/\theta \leq 25$, the intermediate wake region by $25 \leq x/\theta \leq 350$ and the far wake region by $x/\theta \geq 350$. According to Alber (1980); Ramaprian et al. (1982) and Hah and Lakshminarayana (1982), laminar diffusion dominates in the near wake region while turbulent diffusion dominates the intermediate wake region. According to Hah and Lakshminarayana (1982); Ramaprian et al. (1982) and Versteeg and Malalasekera (2007)the wake reaches a self similar state in the far wake region where the historical effects such as the geometric shape of the developing turbulent flow are negligible. Ramaprian et al. (1982) further categorized the near and intermediate wake regions as the developing wake region because of the, observed, significant growth in mean velocity and turbulence profiles which is not present in the far wake.

[5]The wake of an asymmetric airfoil will be naturally asymmetric, regardless of the angle of attack.

2.6.2 Turbulent wake dynamics

A turbulent wake is formed behind an object that is immersed in a moving stream of fluid due to boundary layer separation. Beneath a separated boundary layer, immediately after the separation point, is a region of stagnant fluid which precedes a turbulent flow region which is characterized by a recirculatory or eddying motion of fluid elements (Houghton, 2012). The turbulence in the wake region is a consequence of an interaction between the fast-moving fluid in the free stream and the stagnant fluid under the separated boundary layer (Versteeg and Malalasekera, 2007). The turbulence causes a vigorous mixing of adjacent fluid layers and a rapid expansion/growth of the wake region due to a process of entrainment[6] (Versteeg and Malalasekera, 2007)

Figure 2.6a gives a sketch of the development of the mean velocity distribution in the streamwise direction for a turbulent wake flow and figure 2.6b gives a sketch of a typical mean velocity distribution for a turbulent wake flow. U_∞ is the free stream velocity, boundary layer separation takes place at points x on the airfoil, δ_{wake} is the total wake width, $\mathbf{b}$ is the wake half width $(1/2\delta_{wake})$ and $U = U(y)$ is the cross stream mean velocity.

[6]The fluid from the surrounding, free stream region, is drawn into the turbulent zone (Versteeg and Malalasekera, 2007).

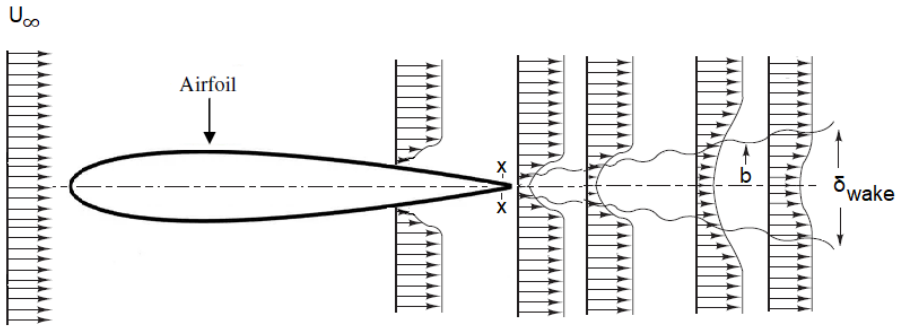

(a) Characteristics of a turbulent wake (Versteeg and Malalasekera, 2007; Farsimadan, 2008).

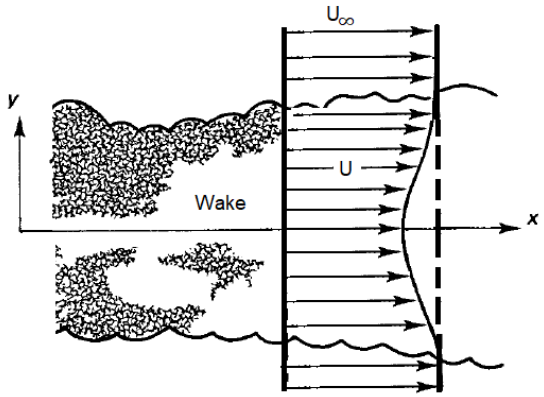

(b) Characteristics of the mean velocity profile (Tennekes and Lumley, 1972).

Figure 2.6: Turbulent wake characteristics.

The mean velocity, $U = U(y)$, changes across the initially thin turbulent shear layer with the smallest velocity at the center of the wake. The mean velocity profile improves with streamwise distance from the wake source [7]. A slow-moving and turbulent flow exists in the turbulent wake region and is surrounded by fast-moving and laminar flow in the free stream (Versteeg and Malalasekera, 2007). The turbulence

[7] The fast-moving, free stream flow, increases the velocity of the slow-moving and turbulent flow in the wake region until they are equal in magnitude (Versteeg and Malalasekera, 2007)

feeds off the flow velocity gradients between the wake region and the free stream region and thus, necessarily, the free stream maintains the turbulence for as long as the flow velocity gradients exist. The turbulence in the wake decays with distance downstream of wake source and dissipates when the flow velocity gradients between the wake region and the free stream region no longer exist (Pope, 2000; Versteeg and Malalasekera, 2007).

Figure 2.7 gives the experimentally observed values for the mean velocity and turbulence quantities for a turbulent wake flow by Wygananski et al(cited by Versteeg and Malalasekera, 2007).

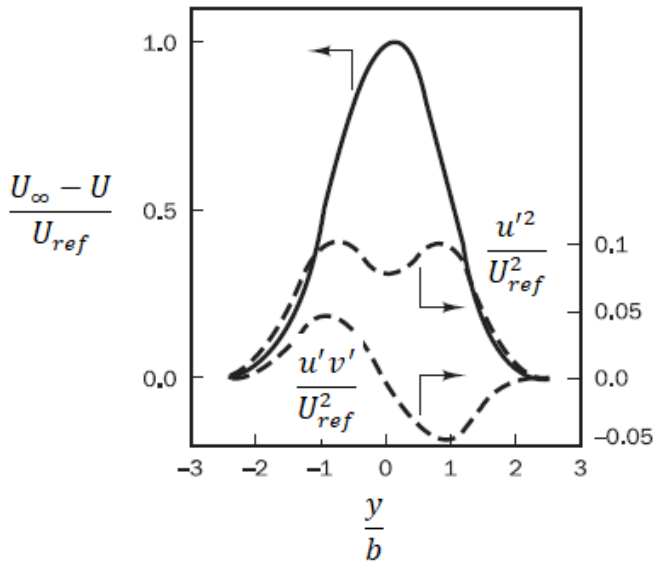

Figure 2.7: Characteristics of the mean velocity and turbulence quantities of a turbulent wake flow (Versteeg and Malalasekera, 2007).

A relationship exists between the mean velocity and the turbulence quantities. The turbulent stresses (u'^2 and $u'v'$) are directly proportional to the mean velocity gradient ($\frac{dU}{dy}$). The values of u'^2 and $u'v'$ are observed to be largest in the region where $\frac{dU}{dy}$ is largest and smaller at the centerline of the turbulent wake where the mean velocity gradient is zero ($\frac{dU}{dy} = 0$). Necessarily, no turbulence is produced at the centerline of the turbulent wake because of the absence of shear, however the value of u'^2 decreases only slightly. This is a result of a turbulent flux across the center-

line due the high turbulence production from the surrounding regions (Versteeg and Malalasekera, 2007). Furthermore the mean velocity gradients and turbulent stresses tend to zero at a distance, y, sufficiently far away from the wake centerline, towards the free stream.

The work of Piradeepan and Mokhtarzadeh-Dehghan (2005); Ramjee and Neelakandan (1990); Tulapurkara et al. (1993) and Weygandt and Mehta (1995) who have investigated straight and curved wakes in the presence of zero and non-zero pressure gradients has shown that wake dynamics, i.e the development of mean velocity and turbulence quantities, is significantly affected by streamwise curvature and pressure gradient. Sailplanes fly in free stream environments and therefore, a straight wake is expected as a consequence of boundary layer separation from the glider's surfaces. Sailplanes also fly in a constant pressure environment. Therefore, the relevant wake validation test cases are those that consider a straight wake in a constant pressure environment.

2.7 Aerodynamic forces and coefficient calculation

The aerodynamic forces and moments on a body are only due to two basic sources, viz., pressure and shear stress distribution over the body surface. According to Anderson (2010) and Houghton (2012), the only mechanisms that communicate the forces acting on a body moving through a fluid are the pressure and shear stress distribution on the body surface. Therefore, no matter the complexity of the body shape, the aerodynamic forces and moments on the body are due entirely to the pressure and shear stress distribution over the surface of the body. The pressure, p, acts normal to an aerodynamic surface while the shear stress, τ, acts tangentially to an aerodynamic surface as shown in figure 2.8a. The net effect of the pressure and shear stress distribution integrated over the surface of the entire body is a resultant aerodynamic force, R, and moment, M, on the body as shown in figure 2.8b.

The resultant force R can be split into two sets of components as shown in figure

2.8c. The one set of components are perpendicular and parallel to the chord (c), viz., a normal force, N, which is perpendicular to c and an axial force, A, which is parallel to c. The other set of components are perpendicular and parallel to the free stream velocity (V_∞), viz., a lifting force, L, perpendicular to V_∞ and a drag force, D, parallel to V_∞. The angle of attack, α, is the angle between c and V_∞.

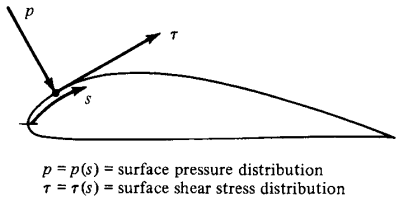

(a) Illustration of pressure and shear acting on the surface of an airfoil.

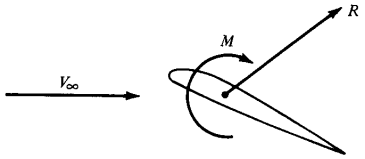

(b) Resultant aerodynamic force and moment acting on an airfoil.

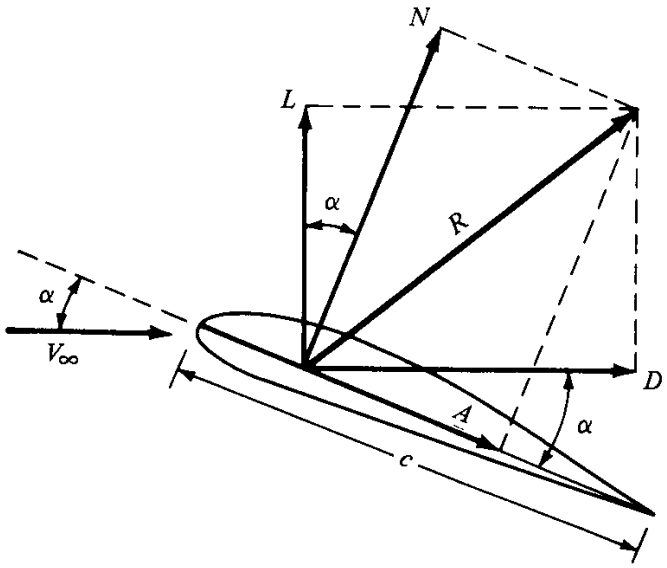

(c) Components of the resultant aerodynamic force acting on an airfoil.

Figure 2.8: Aerodynamic forces acting on a two-dimensional body (airfoil) (Anderson, 2010).

Expressions for the lifting and drag forces, given by equations 2.2 and 2.3, are ob-

tained through a geometrical relation between the two sets of components in 2.8c.

$$L = Ncos\alpha - Asin\alpha \tag{2.2}$$

$$D = Nsin\alpha + Acos\alpha \tag{2.3}$$

The pressure and shear stress distribution are integrated over the surface of an aerodynamic body to obtain the aerodynamic forces, N, A, L and D as illustrated for a wing, shown in figure 2.9.

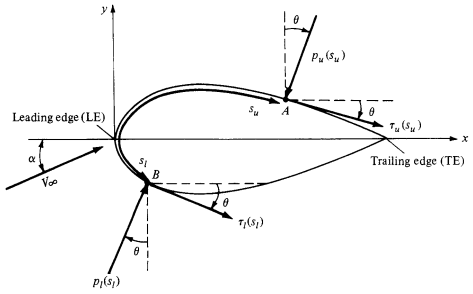

(a) Nomenclature for the integration of pressure and shear stress distribution over a wing cross-section.

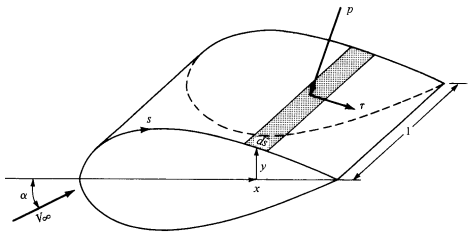

(b) Aerodynamic force on an element of the body surface for the integration of pressure and shear stress distribution over a wing.

Figure 2.9: The integration of pressure and shear stress distribution over a wing to obtain aerodynamic forces (Anderson, 2010).

The pressure and shear stress acting on the upper and lower surface of an airfoil are denoted by P_u and τ_u and P_l and τ_l respectively and are shown in figure 2.9a. P_u and τ_u and P_l and τ_l are functions of the distance, S, from the leading edge with distance S_u on the upper surface and distance S_l on the lower surface. A unit span of the wing with the elemental surface area dS[8] is shown in figure 2.9b. The normal and axial forces on the elemental area dS due to the pressure and shear stresses that are acting on it, are given by equations 2.4 and 2.5 for the upper surface and equations 2.6 and 2.7 for the lower surface.

$$dN_u^{'} = -p_u ds_u cos\theta - \tau_u ds_u sin\theta \tag{2.4}$$

[8] $dS = (ds)(1)$ for a wing of unit span.

$$dA_u^{'} = -p_u ds_u sin\theta + \tau_u ds_u cos\theta \tag{2.5}$$

$$dN_l^{'} = p_l ds_l cos\theta - \tau_l ds_l sin\theta \tag{2.6}$$

$$dA_l^{'} = p_l ds_l sin\theta + \tau_l ds_l cos\theta \tag{2.7}$$

The total normal and axial forces per unit span of the wing are obtained by integrating equations 2.4, 2.5 ,2.6 and 2.7 from the leading edge to the trailing edge to give equations 2.8 and 2.9.

$$N^{'} = -\int_{LE}^{TE} (p_u cos\theta - \tau_u sin\theta) ds_u + \int_{LE}^{TE} (p_l sin\theta - \tau_l cos\theta) ds_l \tag{2.8}$$

$$A^{'} = -\int_{LE}^{TE} (p_u sin\theta - \tau_u cos\theta) ds_u + \int_{LE}^{TE} (p_l cos\theta - \tau_l sin\theta) ds_l \tag{2.9}$$

Provided that the values of p_u, τ_u, p_l and τ_l as function of S are known [9] the integrals in equations 2.8 and 2.9 can be evaluated for the normal and axial forces and consequently, the lift and drag forces can be calculated from equations 2.2 and 2.3.

Substituting equations 2.8 and 2.9 into equation 2.3 and a slight rearrangement of terms, reveals an important fact that for any aerodynamic body, there are two drag force mechanisms that contribute to forming the total drag force, viz., pressure and shear stress (Anderson, 2010; Houghton, 2012). Pressure based drag which is due to the pressure distribution on the aerodynamic surface and shear stress (skin friction) based drag which is due to shear stress acting on the aerodynamic surface exist to form the total drag force acting on a body, i.e.,

$$\underbrace{D}_{\text{Total drag}} = \underbrace{[\int_{LE}^{TE} (-p_u cos\theta ds_u + p_l sin\theta ds_l)] sin\alpha \quad + \quad [\int_{LE}^{TE} (p_u sin\theta ds_u - p_l cos\theta ds_l)] cos\alpha}_{\text{pressure based drag}}$$

$$+ \quad \underbrace{[\int_{LE}^{TE} (-\tau_u sin\theta ds_u + \tau_l cos\theta ds_l)] sin\alpha \quad + \quad [\int_{LE}^{TE} (\tau_u cos\theta ds_u - \tau_l sin\theta ds_l)] cos\alpha}_{\text{shear stress (skin friction) based drag}}$$

(Anderson, 2010; Houghton, 2012).

[9] The values of p_u, τ_u, p_l and τ_l as a function of s can either be obtained theoretically (with a panel or cfd method) or experimentally.

Low-Reynolds number flows fall into a catergory of subsonic flows. Two distinct contributions to pressure and shear stress based drag exists to form the total drag for subsonic flow over an aircraft. Lift-induced and form drag contribute to make pressure drag while skin friction and interference drag make up shear stress(viscous) drag. Aircraft with transonic, sonic, supersonic and hypersonic flows experience shock waves which become an additional source of drag, so-called wave drag, and a significant contribution to the total drag force (Anderson, 2010; Gur and Schetz, 2010; Hoerner, 1965; Houghton, 2012; Jobe, 1984).

Integrating the pressure distribution in the perpendicular direction to the free stream, V_∞ yields a lift-induced drag as a result of the flow around the wing tips. Integrating the pressure distribution in the direction parallel to the free stream, V_∞ yields a form (pressure) drag for separated flow (Anderson, 2010; Houghton, 2012). Integrating the shear stress distribution in the direction parallel to the free stream, V_∞ yields a skin friction drag due to viscosity effects in the boundary layer (wall friction) and an interference drag due to boundary layer intersections (Anderson, 2010; Houghton, 2012). The focus of the study is on a transitional and turbulent wake flow of the JS-1 sailplane and therefore, lift-induced drag is irrelevant and will not be considered.

A major goal in the current study was to accurately calculate the pressure distribution, $p(s)$, and shear stress distribution, $\tau(s)$, for a given body shape and free stream conditions to yield the aerodynamic forces. Freestream conditions are free stream velocity (V_∞), dynamic viscosity (μ_∞), density (ρ_∞) and pressure (p_∞). Dimensional analysis is performed to reduce the dependence of the resultant force $R = f(V_\infty, \mu_\infty, \rho_\infty, p_\infty, S)$ and consequently, L and D to two non-dimensional parameters viz., free stream Reynolds number (Re_∞) and Mach number (M_∞) (Anderson, 2010). An important free stream parameter for a turbulent flow is the turbulence intensity, I (Wilcox, 2006).

Most of the aerodynamic calculations that were made in this research project, were based on the dimensionless lift coefficient and drag coefficient, rather than the dimensional lift and drag forces. The dimensionless lift coefficient and drag coefficient

are related to the dimensional lift and drag forces as shown in equations 2.10 and 2.11.

$$c_l = \frac{L}{q_\infty S} \tag{2.10}$$

$$c_d = \frac{D}{q_\infty S} \tag{2.11}$$

where, $q_\infty = \frac{1}{2}\rho_\infty V_\infty^2$ is the free stream dynamic pressure, ρ_∞ and V_∞ is the free stream density and velocity respectively.

In the same way, the dimensionless pressure coefficient and skin friction coefficient were used rather than the dimensional pressure and skin friction forces. The dimensionless pressure coefficient and skin friction coefficient are related to the dimensional pressure and shear stress as shown in equations 2.12 and 2.13.

$$c_p = \frac{p - p_\infty}{q_\infty} \tag{2.12}$$

$$c_f = \frac{\tau}{q_\infty} \tag{2.13}$$

where p_∞ is the free stream pressure.

Summary

This chapter has dealt with the low-Reynolds number ($\approx O(10^6)$) boundary layer flow phenomena that are encountered in sailplane flight and their influence on the drag force. Phenomena such as boundary layer flow, laminar and turbulent boundary layers, boundary layer transition, boundary layer separation, boundary layer reattachment and turbulent wake have been discussed in the context of sailplane flight. Finally, the importance of the distribution of shear stress and pressure in the calculation of aerodynamic forces and force coefficient was discussed.

Chapter 3

Mathematical modeling

Introduction

This chapter presents the second the literature review. The literature covers the mathematical modeling of the low-Reynolds number ($Re \approx O(10^6)$) flow phenomena that are encountered in sailplane flight as discussed in chapter 2. Section 3.1 introduces the Navier-Stokes equations as the basis for the analysis of viscosity affected flows in CFD. The incompressible flow assumption and shear stress is highlighted. Section 3.2 presents the mathematical modeling of the physical processes and turbulence scales in turbulent flows. The most common CFD turbulence approaches are discussed. Section 3.3 presents the RANS turbulence modeling approach as the most economical approach for a description of turbulent flows. Reynolds averaging and the closure problem in RANS turbulence modeling are discussed. Section 3.4 discusses all the potential RANS turbulence models for sailplane turbulent boundary layer modeling. The Eddy viscosity turbulence models were considered as the most economical approach to turbulence modeling. Subsections 3.4.1,3.4.2 and 3.4.3 review the pros and cons of the relevant zero equation, one equation and two-equation turbulence models respectively. Section 3.5 covers the importance of transition modeling and subsection 3.5.1 discusses the pros and cons of potential transition models for sailplane boundary layer flow. Section 3.6 covers the near-wall modeling of tur-

bulent flow and subsections 3.6.1 and 3.6.2 discuss the implications of the wall y^+ value and near-wall treatment on near-wall modeling of turbulent flow. Section 3.7 is based on turbulent wake modeling. Subsection 3.7.1 deals with the near, intermediate and far wake modeling while subsection 3.7.2 discusses the pros and cons of the potential zero equation, one equation and two equation turbulent wake models for modeling the wake of a sailplane. Section 3.8 presents a consolidation of the turbulence, transition and wake modeling review and selection of the most appropriate physical model description of a transitional and turbulent wake flow combination.

3.1 Computational Fluid Dynamics

Computational Fluid Dynamics (CFD) involves the analysis of systems involving fluid flow, heat transfer and associated phenomena such as turbulence by means of computer-based simulation (Versteeg and Malalasekera, 2007). The fundamental basis of most problems encountered in CFD is the renowned Navier-Stokes equations by French engineer and physicist Claude-Louis Navier and physicist and mathematician George Gabriel Stokes.

The Navier-Stokes equations (NS) describe the viscous flow of a Newtonian fluid and find their application for many single phase flows encountered in engineering. These equations are a mathematical statements regarding the momentum conservation (Newton's second law of motion) of a fluid element in motion. The behavior of the fluid particle is described in terms of the macroscopic properties of the fluid and the flow such as molecular viscosity, density, velocity and pressure, and their spatial and time derivatives (Versteeg and Malalasekera, 2007). The analysis of fluid flows at macroscopic length scales (e.g $\geq 1\mu m$) regards the fluid to be a continuum. The fluid is assumed to consist of continuous matter while the molecular structure and motion of the individual molecules are ignored. The flow properties at a given point can be considered as averages over a suitably large number of molecules (Currie, 2013; Versteeg and Malalasekera, 2007).

The NS equations are always considered with the continuity equation to ensure the mass conservation of the fluid particles in motion. The continuity and NS equations for a three-dimensional and unsteady flow of a compressible and Newtonian fluid are compactly given in conservation form by equations 3.1 and 3.2 in Einstein notation (Currie, 2013; Ferziger and Perić, 2002; Wilcox, 2006).

$$\frac{\partial \rho}{\partial t} + \frac{\partial (\rho u_i)}{\partial x_i} = 0 \tag{3.1}$$

$$\frac{\partial (\rho u_i)}{\partial t} + \frac{\partial (\rho u_j u_i)}{\partial x_j} = -\frac{\partial p}{\partial x_i} + \frac{\partial \tau_{ij}}{\partial x_j} \tag{3.2}$$

The vectors u_i and x_i are instantaneous velocity (three-dimensional and time dependent) and position vectors while t is time, p is the instantaneous pressure, ρ is density and μ is the molecular viscosity. The last term on the right hand side of equation 3.2 contains the viscous stress tensor (τ_{ij}) which accounts for the viscous stresses induced due to momentum transport (Currie, 2013; Versteeg and Malalasekera, 2007; Wilcox, 2006), viz.,

$$\tau_{ij} = \mu(\frac{\partial u_i}{\partial x_j} + \frac{\partial u_j}{\partial x_i}) - \lambda \delta_{ij} \frac{\partial u_i}{\partial x_i}. \tag{3.3}$$

The viscous stresses (τ_{ij}) in a Newtonian fluid are proportional to the rates of deformation of the fluid particles in motion (Currie, 2013; Versteeg and Malalasekera, 2007). The dynamic viscosity (μ) and the second viscosity (λ) are proportionality constants.

Engineering applications(also in this project) which consider flow involving liquids or gases at low Mach numbers ($M < 0.3$), assume fluid flow to be incompressible (Anderson, 2010). Specifically density is considered to be invariable in the flow domain for an incompressible flow. Mathematically, $\frac{\partial \rho}{\partial t} = 0$ and $\frac{\partial \rho}{\partial x_i} = 0$ such that the density (ρ) is invariable in the flow domain and thus constant. Equations 3.1 and 3.2 then simplify to equations 3.4 and 3.5.

$$\frac{\partial u_i}{\partial x_i} = 0 \tag{3.4}$$

$$\rho \frac{\partial u_i}{\partial t} + \rho \frac{\partial (u_j u_i)}{\partial x_j} = -\frac{\partial p}{\partial x_i} + \frac{\partial \tau_{ij}}{\partial x_j} \tag{3.5}$$

Necessarily, the viscous stress equation (3.3) simplifies to $\tau_{ij} = \mu(\frac{\partial u_i}{\partial x_j} + \frac{\partial u_j}{\partial x_i})$ for an incompressible flow. For a well-posed problem, with appropriate boundary conditions depending on the flow problem under consideration, the continuity and Navier-Stokes equations are solved for the instantaneous velocity and pressure to obtain the shear stress.

3.2 Turbulence modeling

In both the laminar and turbulent flow regime, the NS equations give a complete and exact description of viscous fluid flow. In the laminar flow regime the flow streamlines are smooth and regular and the fluid particles move smoothly along a streamline while the flow streamlines break up and the fluid elements move in a random, irregular and tortuous fashion in the turbulent flow regime (Anderson, 2010; Ferziger and Perić, 2002; Hermann and Gersten, 2017.; Houghton, 2012; Tennekes and Lumley, 1972; Versteeg and Malalasekera, 2007; Wilcox, 2006). There is no effective mixing of the fluid particles in the laminar flow regime and thus viscous stresses due to momentum transport are manageable. On the other hand there is a vigorous mixing of fluid particles in the turbulent flow regime which is accompanied by a drastic increase in momentum exchange and consequent random fluctuations of velocity and pressure (Wilcox, 2006). The resulting stresses, due to turbulence, are significantly larger than the viscous stresses which dominate the laminar flow. According to Versteeg and Malalasekera (2007) and Wilcox (2006) , the turbulent stresses are several orders of magnitude larger than the viscous stresses.

Turbulence consists of a wide and continuous spectrum of scales ranging from the largest to the smallest eddies (see Tennekes and Lumley, 1972; Versteeg and Malalasekera, 2007; Wilcox, 2006;section 1.5, section 3.1, chapter 1&2). Turbulent flows are typically characterized by the length, velocity and time scales of the vortical structures which make them up. Eddies overlap in space, large ones carrying smaller ones. The largest eddies dominate the flow, they interact with and extract kinetic energy from a turbulence source (typically the free stream) and transfer it to progres-

sively smaller eddies in an energy cascade process (Versteeg and Malalasekera, 2007; Wilcox, 2006). The smallest eddies have the least amount of energy and they dissipate into heat through the action of molecular viscosity. Thus turbulent flows have production and dissipation (Tennekes and Lumley, 1972; Versteeg and Malalasekera, 2007; Wilcox, 2006).

The scales of the smallest eddies at which dissipation occurs, known as Kolmogorov scales, are characteristic of the length (η), time (τ) and velocity (υ) of the dissipating eddies. Kolmogorov scales are expressed in terms of the rate of energy dissipation (ϵ) and molecular viscosity (ν) as shown in equation 3.6 (Versteeg and Malalasekera, 2007; Wilcox, 2006).

$$\eta \equiv (\nu^3/\epsilon)^{1/4} \qquad \tau \equiv (\nu/\epsilon)^{1/2} \qquad \upsilon \equiv (\nu\epsilon)^{1/4} \tag{3.6}$$

The scales of the largest eddies at which kinetic energy is extracted from a turbulence source are known as integral length and time scales, they are characteristic of the length and time of the energy-bearing eddies. These scales are expressed in terms of the turbulent kinetic energy and two-point correlations with respect to space ($R_{ii}(\mathbf{x}, t; r)$) and time ($R_{ii}(\mathbf{x}, t; t')$) respectively, as shown in equation 3.7 (Wilcox, 2006).

$$\ell(\mathbf{x}, t) = \frac{3}{16} \int_0^\infty \frac{R_{ii}(\mathbf{x}, t; r)}{k(\mathbf{x}, t)} dr \quad T(\mathbf{x}, t) = \int_0^\infty \frac{R_{ii}(\mathbf{x}, t; t')}{2k(\mathbf{x}, t)} dt' \tag{3.7}$$

where $R_{ii}(\mathbf{x}, t; r)$ is the two-point velocity correlation tensor [1], $R_{ii}(\mathbf{x}, t; t')$ is the autocorrelation tensor [2] and $k(\mathbf{x}, t)$ is the turbulent kinetic energy.

Equation 3.8 gives the ratios (relations) of the length ($\frac{\eta}{\ell}$), time ($\frac{\tau}{T}$) and velocity ($\frac{\upsilon}{v}$) scales of turbulence of the energy-bearing and the dissipating eddies to quantify the vast differences in their magnitude (Ferziger and Perić, 2002; Tennekes and Lumley,

[1] A two-point velocity correlation is a correlation of velocities at two different points at the same time in an effort to include, in turbulence modeling, information regarding the flow history of a turbulent flow with respect to space (Wilcox, 2006).

[2] Autocorrelation is a correlation of velocities at one point and two different times in an effort to include, in turbulence modeling, information regarding the flow history of a turbulent flow with respect to time (Wilcox, 2006).

1972; Versteeg and Malalasekera, 2007; Wilcox, 2006).

$$\frac{\eta}{\ell} \approx R_{e_l}^{-3/4} \qquad \frac{\tau}{T} \approx R_{e_l}^{-1/2} \qquad \frac{\upsilon}{v} \approx R_{e_l}^{-1/4} \tag{3.8}$$

These relations indicate that the length, time and velocity scales for the smallest eddies are much smaller than those of the largest eddies. The separation in scales widens as the Reynolds number increases (Tennekes and Lumley, 1972).

The turbulence scales of the energy-bearing eddies are related to those of the dissipating eddies and quantify the energy cascade by the exact relation for energy dissipation (ϵ) in equation 3.9 (Ferziger and Perić, 2002; Tennekes and Lumley, 1972; Wilcox, 2006).

$$\epsilon \backsim \frac{k^{3/2}}{\ell}. \tag{3.9}$$

Virtually all flows of practical engineering interest, such as is considered in the current research, are turbulent. In theory, the NS equation can be solved for a given flow problem by using methods from calculus. But in practice, these equations are too difficult to solve analytically. Analytical solutions only exist for the simple laminar flow problems for which the NS can be greatly simplified with no significant loss in flow physics e.g Coutte, Poisoulle, Stoke's, Convergent and Divergent flows etc (Currie, 2013).

The recent development of high-speed computers has allowed an opportunity for the use of numerical methods to obtain approximate solutions to the exact or other simplified forms of NS equations for complex flows. Commonly used numerical methods are finite difference, finite volume, finite element, and spectral methods. Complex flows include internal flows (pipe/channel flow) above the critical Reynolds number and external flows (turbulent flows over automobiles and aircraft). There are various numerical approaches that are employed to numerically solve the NS or simplification, amongst which the most popular are Direct Numerical Simulation (DNS), Large Eddy Simulation (LES), Detached Eddy Simulation (DES) and Reynolds Averaging of the Navier-Stokes equations (RANS).

DNS involves a computation of the exact unsteady NS equations. That is, for spatial grids that sufficiently fine to resolve the Kolmogorov length scales and for time steps

that are sufficiently small to resolve the Kolmogorov time scales, numerical solutions for the instantaneous (three-dimensional and time dependent) velocity and pressure are obtained (Ferziger and Perić, 2002; Versteeg and Malalasekera, 2007; Wilcox, 2006). DNS computations are invaluable in turbulence research because they are the only approach that gives proper solutions to turbulent flows.

LES is a solution approach in which the large eddies (energy-bearing) are computed and the smallest eddies (dissipating) are modeled. This approach involves the space filtering of the exact NS equations to separate the resolvable scales of large eddies from the subgrid scales of the smallest eddies. That is, the behavior of the energy-bearing eddies is filtered while excluding that of the dissipating eddies. The filtered NS equations contain an exact description of the turbulent flow of the large eddies while subgrid-scale (SGS) modeling is introduced to predict the behavior of the smallest eddies (Ferziger and Perić, 2002; Versteeg and Malalasekera, 2007; Wilcox, 2006).

DES, similar to LES in principle, is a solution approach in which only the largest eddies are computed and the smaller eddies are modeled using a Reynolds averaging approach (RANS) (Wilcox, 2006).

RANS is a full turbulence modeling approach to solving turbulent flow problems. It involves a Reynolds averaging of the unsteady NS equations and a modeling of the Reynolds stresses. That is, all of the fluctuations associated with turbulence are averaged and then modeled to give the behavior of the turbulent flow (see figure 3.1) (Ferziger and Perić, 2002; Versteeg and Malalasekera, 2007; Wilcox, 2006).

For most complex engineering applications, using DNS, LES or DES is not an option, due to their high demand in computational resources. RANS offers a modest demand in computational resources and is, hence, the most commonly used approach for solving turbulent flows.

3.3 Reynolds Averaged Navier-Stokes turbulence modeling

The Reynolds Averaged Navier-Stokes (RANS) turbulence modeling approach to solving turbulent flow problems involves either time or ensemble averaging of the NS equations, depending on the time-related behavior of the flow. A process called Reynolds decomposition is performed to decompose the flow properties of a turbulent flow into mean (time or ensemble averaged) and fluctuating components as shown in equation 3.10 (Ferziger and Perić, 2002; Versteeg and Malalasekera, 2007; Wilcox, 2006).

$$\phi(x_i, t) = \bar{\phi}(x_i, t) + \phi^{'}(x_i, t) \tag{3.10}$$

Time averaging is applied to a steady flow whilst ensemble averaging is applied to an unsteady flow. Mathematically, $\frac{\partial(\rho u_i)}{\partial t} = 0$ for a steady flow and $\frac{\partial(\rho u_i)}{\partial t} \neq 0$ for an unsteady flow. Expressions for $\bar{\phi}$ is given by equations 3.11 and 3.12 for time and ensemble averaging respectively (Ferziger and Perić, 2002; Versteeg and Malalasekera, 2007; Wilcox, 2006).

$$\bar{\phi}(x_i) = \lim_{T\to\infty} \frac{1}{T} \int_0^{\infty} \phi(x_i, t) dt \tag{3.11}$$

$$\bar{\phi}(x_i, t) = \lim_{N\to\infty} \frac{1}{N} \sum_{n=1}^{\infty} \phi(x_i, t) \tag{3.12}$$

To illustrate and underscore the nature of turbulent statistics, Cebeci and Smith(cited by Wilcox, 2006) measured velocity profiles, $u(y)$, for a flat plate at the same distance from the leading edge at different time instants using the hydrogen bubble technique. Figure 3.1a shows the boundary layer velocity profiles plotted with a series of staggered origins and figure 3.1b displays the boundary layer velocity profiles plotted with a common origin while figure 3.1c shows the average boundary layer profile (Wilcox, 2006).

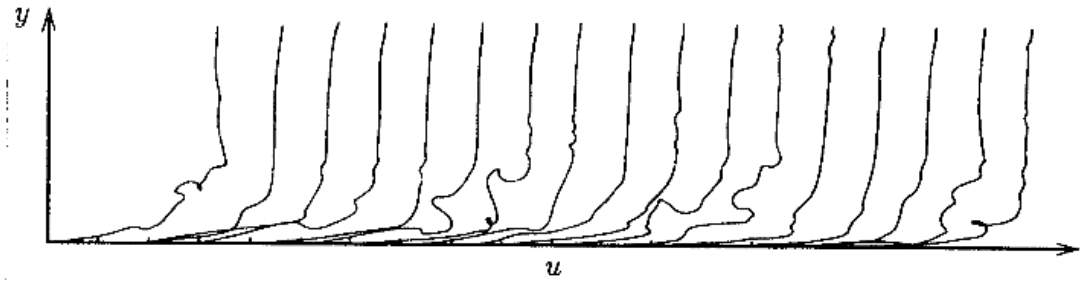

(a) Instantaneous boundary layer velocity profiles plotted with a series of staggered origins.

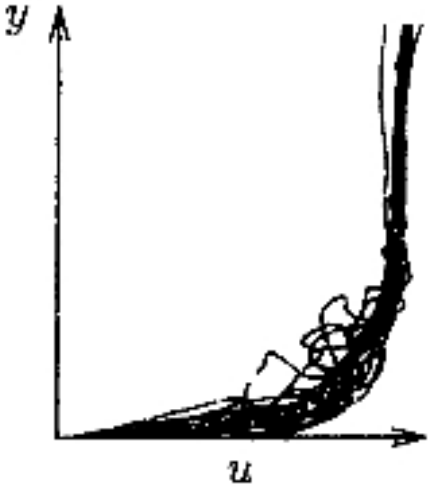

(b) Instantaneous boundary layer velocity profiles with a common origin.

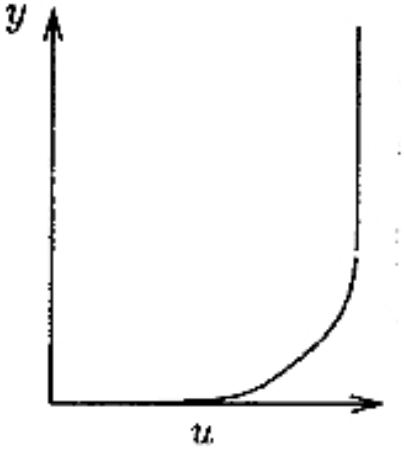

(c) Average boundary layer velocity profile.

Figure 3.1: Instantaneous and average boundary layer velocity profiles at the same distance from the leading edge of a flat plate at 17 different instants Cebeci and Smith(cited by Wilcox, 2006).

Figures 3.2a and 3.2b further depicts the concept of time averaging for a statistically steady flow and ensemble averaging for an unsteady flow respectively (Ferziger and Perić, 2002).

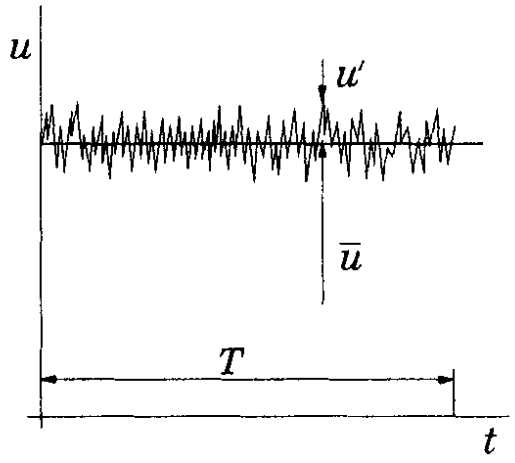

(a) Time averaging for a statistically steady flow.

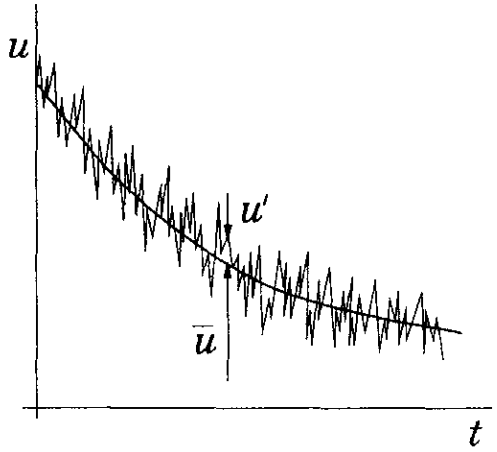

(b) Ensemble averaging for a statistically unsteady flow.

Figure 3.2: Time averaging for a statistically steady flow and ensemble averaging for an unsteady flow Ferziger and Perić (2002).

The current study in interested in a three-dimensional and steady flow of an incompressible and Newtonian fluid. Therefore, using Reynolds decomposition and time averaging (equations 3.10 and 3.11) on the steady, incompressible and Newtonian fluid (equations 3.4 and 3.5 with $\frac{\partial \bar{u_i}}{\partial t} = 0$) and using time averaging rules given in (Versteeg and Malalasekera, 2007:62) gives the RANS equations (equations 3.13 and 3.14) employed in the current study.

$$\frac{\partial \bar{u_i}}{\partial x_i} = 0 \tag{3.13}$$

$$\rho \bar{u_j} \frac{\partial \bar{u_i}}{\partial x_j} = -\frac{\partial \bar{p}}{\partial x_i} + \frac{\partial}{\partial x_j}(\bar{\tau_{ij}} - \rho \overline{u_j' u_i'}) \tag{3.14}$$

where,

$$\bar{\tau_{ij}} = \mu(\frac{\partial \bar{u_i}}{\partial x_j} + \frac{\partial \bar{u_j}}{\partial x_i}). \tag{3.15}$$

The quantity $-\rho \overline{u_j' u_i'}$ is the Reynolds stress tensor and $-\overline{u_j' u_i'}$ is the specific Reynolds stress tensor denoted by $\tau_{\mathbf{ij}}$ so that

$$\tau_{\mathbf{ij}} = \overline{u_j' u_i'} \tag{3.16}$$

The Reynolds stress tensor accounts for the Reynolds stresses in a turbulent flow. The Reynolds stress tensor is a symmetric tensor and thus has six independent components (Ferziger and Perić, 2002; Versteeg and Malalasekera, 2007; Wilcox, 2006). Hence we have produced six unknown quantities as a result of Reynolds averaging. On the other hand we have four unknown mean flow properties, viz., pressure and the three velocity components along with the six Reynolds stress components and thus we have ten unknowns but only four equations. To close the system we must find enough equations to solve for the unknowns. This is known as the closure problem of turbulence (Ferziger and Perić, 2002; Hermann and Gersten, 2017.; Versteeg and Malalasekera, 2007; Wilcox, 2006). In order to close the system of equations (3.13 and 3.14) and compute all the mean flow properties of the turbulent flow under consideration, we need a methodology to compute $-\overline{u_j' u_i'}$. Herein is the essence of turbulence modeling.

3.4 RANS turbulence models

The function of turbulence modeling is to devise approximations for the unknown correlations, introduced through averaging, in terms of flow properties that are known so that a sufficient number of equations exist and thereby closing the system of equations (Wilcox, 2006). The most complete prescription for the transport of turbulent stresses are the Reynolds Stress Models (RSM) (Versteeg and Malalasekera, 2007). The (RSM) couples six Reynolds transport equations to the RANS equation to give a prescription for turbulent stresses and to close the system of RANS equations. Each of the six partial differential equations offer a satisfactory description of the transport of the six turbulence stresses in a turbulent flow and therefore, the RSM are able to completely account for the anisotropy of turbulent flows (Versteeg and Malalasekera, 2007). The Reynolds Stress Models are the most computationally intensive of the RANS turbulence models and will, therefore, not be considered as a potential physical description of a transitional and turbulent wake flow on the JS-1 sailplane.

Besides the RSM, the fundamental basis of all other conventional RANS turbulence models is the **Boussinesq Approximation** for computing the Reynolds stresses ($\tau_{\mathbf{ij}} = \overline{u_j' u_i'}$) Ferziger and Perić (2002); Hermann and Gersten (2017.); Versteeg and Malalasekera (2007); Wilcox (2006).

$$-\overline{u_i' u_j'} = \nu_t \left(\frac{\partial \bar{u}_i}{\partial x_j} + \frac{\partial \bar{u}_j}{\partial x_i} \right) - \frac{2}{3} k \delta_{ij}, \tag{3.17}$$

[3] where ν_t is the turbulence eddy viscosity, $k = \frac{1}{2}\overline{u_i' u_i'}$ is the turbulence kinetic energy and δ_{ij} is the Kronecker delta. In 1877 Boussinesq proposed that, akin to the viscous stresses in a Newtonian fluid, the Reynolds stresses might be linearly proportional to the mean rates of deformation. Boussinesq's proposal was based on the fact that turbulent stresses tend to increase with the increase in the mean rates of deformation (Versteeg and Malalasekera, 2007). The kinematic turbulent viscosity (ν_t) is the proportionality constant. The assumption that the turbulence stresses are linearly related to the mean rates of deformation is limiting for highly turbulent flows and therefore, turbulence models that are based on the Boussinesq approximation strongly underpredict the anisotropy in highly turbulent flows (Hellsten, 2005; Siemens, 2017; Versteeg and Malalasekera, 2007; Wallin and Johansson, 2000). According to Hellsten (2005); Siemens (2017); Versteeg and Malalasekera (2007) and (Wallin and Johansson, 2000), turbulence models that are based on the Boussinesq assumption perform well for low to moderate turbulent intensity flows.

3.4.1 Zero-equation models

The simplest class of turbulence models are zero equation/algebraic turbulence models. Algebraic turbulence models compute for the Reynolds stresses, based on the Boussinesq approximation, by giving a prescription for computing the eddy viscosity (ν_t). The most common algebraic turbulence models, the mixing length models, based on Prandtl's mixing length hypothesis (1925), compute the eddy viscosity (ν_t)

[3] The Boussinesq Approximation for a compressible flow is given by $-\overline{u_i' u_j'} = \nu_t \left(\frac{\partial \bar{u}_i}{\partial x_j} + \frac{\partial \bar{u}_j}{\partial x_i} - \lambda \delta_{ij} \frac{\partial \bar{u}_i}{\partial x_i} \right) - \frac{2}{3} k \delta_{ij}$.

in terms of the mixing length (ℓ) which is a characteristic of the energy-bearing eddies as shown in equation 3.18(Ferziger and Perić, 2002; Versteeg and Malalasekera, 2007; Wilcox, 2006).

$$\nu_t = \ell_{mix}^2 \mid \frac{\partial \bar{u}}{\partial y} \mid . \tag{3.18}$$

Consequently the prescription for Reynolds stresses in equation 3.17 with boundary layer assumptions, becomes

$$\tau_{xy} = \ell_{mix}^2 \mid \frac{\partial \bar{u}}{\partial y} \mid\mid \frac{\partial \bar{u}}{\partial y} \mid . \tag{3.19}$$

The various mixing length turbulence models give a prescription for the mixing length (ℓ_{mix}).

The algebraic models that have been calibrated for boundary layer flows are the Baldwin and Lomax (1978); Cebeci and Smith (1974) and Johnson and King (1985) models. The Baldwin and Lomax (1978) and Cebeci and Smith (1974) models are two-layer models with (ν_t) given by separate expressions in each layer. From the Stanford Olympics I (1980) skin friction coefficient results and Driver's separated flow (1991) skin friction and pressure coefficient results documented in Wilcox (2006), the Baldwin and Lomax (1978) and Cebeci and Smith (1974) models prove to be accurate for attached boundary layer flows provided the pressure gradient is not too strong while they fare poorly for separated flows. The Baldwin and Lomax (1978) model predicts a separation bubble twice as long as the experimentally observed bubble (Wilcox, 2006).

Another important algebraic turbulence model that has been calibrated for boundary layer flow is the equilibrium algebraic model by Johnson and King (1985) in which the eddy viscosity is given by equation 3.20.

$$\mu_t = \mu_{T_o} tanh(\frac{\mu_{T_i}}{\mu_{T_o}}) \tag{3.20}$$

μ_{T_i} and μ_{T_o} represent the inner and outer layer eddy viscosity. The closure coefficient and auxiliary relations can be found in Johnson and King (1985) and Wilcox (2008).

The Johnson and King (1985) model is an algebraic equilibrium model [4] which was formulated to improve the deficiency of the Baldwin and Lomax (1978) and Cebeci and Smith (1974) models in predicting separated flow. In the Stanford Olympics II (1981) it was shown that the Johnson and King (1985) model fared rather poorly for attached boundary layer flows compared to the Baldwin and Lomax (1978) and Cebeci and Smith (1974) models (Wilcox, 2006). However Menter (1992b) shows that the Johnson and King (1985) model is far better suited for separated flows compared to the Baldwin and Lomax (1978) and Cebeci and Smith (1974) models.

3.4.2 One-equation models

One-equation models, also based on the Boussinesq approximation, improve the ability to predict turbulent flows and are a more realistic mathematical description of the turbulent stresses compared to algebraic stress models (Wilcox, 2006). One-equation models were initially conceived by Prandtl (1945). Prandtl postulated a model in which the eddy viscosity depends upon the kinetic energy of the turbulent fluctuations (k) and modeled a partial differential equation approximating the exact equation for k. This improvement was to take into account the fact that turbulent stresses and thus, the eddy viscosity are affected by the flow history (Wilcox, 2006). One-equation turbulence models solve one turbulent transport equation [5] and include a prescription for the eddy viscosity (ν_t) (Wilcox, 2006).

One-equation turbulence models by Spalart and Allmaras (1992) and Baldwin and Barth (1990) have been optimized for boundary layer flows and specifically for flow past a wing (Wilcox, 2006). The Spalart and Allmaras (1992) turbulence model couples, to the RANS equations, a partial differential equation for the kinematic eddy-viscosity parameter ($\tilde{\nu}$) and includes a prescription for the kinematic eddy vis-

[4] The Johnson and King (1985) algebraic equilibrium model is also known as a half-equation model.

[5] Turbulence transport equations are exact or modeled partial differential equations that describe the transport of turbulence quantities (e.g turbulence kinetic energy (k), dissipation (ϵ), rate of dissipation (ω)) to incorporate the effects of turbulent flow history in turbulence modeling.

cosity (ν_t) as shown in equations 3.22 and 3.21. The closure coefficient [6] and auxiliary relations can be found in Spalart and Allmaras (1992); Versteeg and Malalasekera (2007) and Wilcox (2006).

Kinematic eddy viscosity

$$\nu_t = \tilde{\nu} f_{v1}, \quad f_{v1} = \frac{\chi^3}{\chi^3 + C_{v1}^3}, \quad \chi := \frac{\tilde{\nu}}{\nu} \tag{3.21}$$

Eddy viscosity equation

$$\begin{aligned} \frac{\partial \tilde{\nu}}{\partial t} + u_j \frac{\partial \tilde{\nu}}{\partial x_j} =& C_{b1}[1 - f_{t2}]\tilde{S}\tilde{\nu} + \frac{1}{\sigma}\{\nabla \cdot [(\nu + \tilde{\nu})\nabla\tilde{\nu}] + C_{b2}|\nabla\tilde{\nu}|^2\} \\ & - \left[C_{w1} f_w - \frac{C_{b1}}{\kappa^2} f_{t2}\right] \left(\frac{\tilde{\nu}}{d}\right)^2 + f_{t1}\Delta U^2 \end{aligned} \tag{3.22}$$

The Baldwin and Barth (1990) turbulence model couples, to the RANS equations, a partial differential equation for the turbulence Reynolds number ($\nu\tilde{R}_T$) and includes a prescription for the kinematic eddy viscosity (ν_t) as shown in equations 3.24 and 3.23. The closure coefficient and auxiliary relations can be found in Baldwin and Barth (1990) and Wilcox (2006).

Kinematic eddy viscosity

$$\nu_t = C_\mu \nu \tilde{R}_T D_1 D_2 \tag{3.23}$$

Turbulence Reynolds number equation

$$\begin{aligned} \frac{\partial}{\partial t}\left(\nu\tilde{R}_T\right) + U_j \frac{\partial}{\partial x_j}\left(\nu\tilde{R}_T\right) =& \left(C_{\varepsilon 2} f_2 - C_{\varepsilon 1}\right)\sqrt{\nu\tilde{R}_T P} + \left(\nu + \frac{\nu_T}{\sigma_\varepsilon}\right)\frac{\partial^2}{\partial x_k \partial x_k} \\ & - \frac{1}{\sigma_\varepsilon}\frac{\partial \nu_T}{\partial x_k}\frac{\partial\left(\nu\tilde{R}_T\right)}{\partial x_T} \end{aligned} \tag{3.24}$$

[6] According to Spalart and Allmaras (1994) it is safer to use the closure coefficient $C_{t3} = 1.2$ and $C_{t4} = 0.5$

From the Stanford Olympics II (1980) skin friction coefficient results documented in Wilcox (2006), the Baldwin and Barth (1990) model fares well for favorable and mild adverse pressure gradient flow but consistently predicted skin friction values that were lower than experimental values for adverse pressure gradient flow and it predicts flow separation for three cases although all the flows are attached. The fact that the model predicted too large a decrease in skin friction reveals that the model tends to respond too strongly to adverse pressure gradients (Wilcox, 2006). The Baldwin and Barth (1990) models fares poorer than the Baldwin and Lomax (1978) and Cebeci and Smith (1974) algebraic models for attached flows while the Spalart and Allmaras (1992) model's predicted skin friction values are in close agreement with both the experimental values and the Baldwin and Lomax (1978) and Cebeci and Smith (1974) algebraic models in all the cases considered. Menter (1992a) shows that the Spalart and Allmaras (1992) model predicts a separation bubble that is 60% larger than that observed experimentally while the Baldwin and Barth (1990) model's results are poorer than those of the Baldwin and Lomax (1978) algebraic model, with a predicted separation bubble twice the size of the experimentally observed bubble. Poor results from the Baldwin and Barth (1990) model for separated flows [7] are expected since it is sensitive to adverse pressure gradients (Wilcox, 2006). Wilcox (2006) further shows that the Spalart and Allmaras (1992) model has satisfactory flow reattachment prediction capabilities. Sai and Lutfy (1995) compares the Baldwin and Barth (1990) and Spalart and Allmaras (1992) models and all the cases studied showed the superiority of the Spalart and Allmaras (1992) model for adverse pressure gradient and incipient separation flow. On balance, the Spalart and Allmaras (1992) model is preferred over the Baldwin and Barth (1990) model. The Spalart and Allmaras (1992) model was validated with the RAE 2822 airfoil test case and its results proved to be accurate relative to the experimentally observed values.

[7] Flow with a strong enough adverse pressure gradient cause the boundary layer to separate (Wilcox, 2006).

3.4.3 Two-equation models

Two-equation models are a superior concept for modeling turbulent flows than one-equation models, including a second turbulent transport equation, to offer a more realistic description of the turbulent stresses and improve the ability to predict turbulent flows. Two-equation models were initially conceived by Kolmogorov (1942). He realized the need to incorporate turbulence production and dissipation in turbulence modeling and thus proposed the need for two turbulence transport equations, one for kinetic energy (k) and the other for the specific dissipation rate (ω) (Wilcox, 2006; Versteeg and Malalasekera, 2007). Two-equation turbulence models solve two turbulent transport equations and include a prescription for the eddy viscosity (ν_t) (Wilcox, 2006). Virtually all two-equation models include a turbulent transport equation for the kinetic energy while the choice for the second transport quantity has been different for the various two-equation model authors. Chou (1945) proposed modeling the exact equation for dissipation (ϵ) and Rotta J.C (cited by Wilcox, 2006) first (1951) proposed an equation for the turbulent length scale (ℓ) and later (1968) for the product of the kinetic energy (k) and the turbulent length scale (ℓ). Zeierman and Wolfshtein (1986) introduced the equation for the product of the kinetic energy (k) and turbulence dissipation time (τ) while Speziale et al. (1990) have postulated an equation for the turbulence dissipation time.

The standard $k-\epsilon$, $k-\omega$ and SST $k-\omega$ two-equation turbulence models by Launder and Sharma (1974), Wilcox (1988) and Menter (1992c) respectively, were the most noteworthy for boundary layer flows.

The Launder and Sharma (1974) $k-\epsilon$ turbulence model couples, to the RANS equations, partial differential equations for the turbulence kinetic energy (k) and the specific dissipation (ϵ) and includes a prescription for the kinematic eddy viscosity (ν_t) as shown in equations 3.25, 3.26 and 3.27. The closure coefficient and auxiliary relations can be found in Launder and Sharma (1974); Versteeg and Malalasekera (2007) and Wilcox (2006).

Turbulence eddy viscosity

$$\nu_t = C_\mu \frac{k^2}{\epsilon} \tag{3.25}$$

Turbulence kinetic energy

$$\frac{\partial}{\partial t}(k) + \frac{\partial}{\partial x_i}(k u_i) = \frac{\partial}{\partial x_j}\left[\left(\nu + \frac{\nu_t}{\sigma_k}\right)\frac{\partial k}{\partial x_j}\right] + P_k + P_b - \epsilon - Y_M + S_k \tag{3.26}$$

Dissipation rate

$$\frac{\partial}{\partial t}(\epsilon) + \frac{\partial}{\partial x_i}(\epsilon u_i) = \frac{\partial}{\partial x_j}\left[\left(\nu + \frac{\nu_t}{\sigma_\epsilon}\right)\frac{\partial \epsilon}{\partial x_j}\right] + C_{1\epsilon}\frac{\epsilon}{k}\left(P_k + C_{3\epsilon}P_b\right) - C_{2\epsilon}\frac{\epsilon^2}{k} + S_\epsilon \tag{3.27}$$

The standard $k-\epsilon$ by Launder and Sharma (1974) is one of many efforts, since the earliest $k-\epsilon$ models by Chou (1945); Harlow and Nakayama (1968) and Harlow and Nakayama (1968), to improve its predictive accuracy for near-wall flows by introducing viscous modifications. The $k-\epsilon$ model performs very well for turbulent shear flows but very poorly for near-wall flows. It fails to obtain accurate results when integrating through the viscous sublayer of a near-wall turbulent flow velocity profile Wilcox (2006); Versteeg and Malalasekera (2007). Other notable viscous modifications to the $k-\epsilon$ model are by Jones and Launder (1972); Lam and Bremhorst (1981); Chien (1982). Wilcox (2006) documents predicted standard $k-\epsilon$ model's skin friction coefficient results from the Stanford Olympics II (1980). The model's skin friction predictions are accurate for flows with constant pressure and favorable pressure gradients while discrepancies increase with increasingly adverse pressure gradients. For strong adverse pressure gradients, the computed skin friction coeffiecients exceeds the measured values by as much as 47% (Wilcox, 2006). The other modified $k-\epsilon$ models with viscous damping, viz.,Jones and Launder (1972); Lam and Bremhorst (1981); Chien (1982) and Chien (1982) exhibit exactly the same behavior (Wilcox, 2006). In a perturbation analysis of the boundary layer for the

standard $k-\epsilon$ model, Wilcox (2006) shows that the $k-\epsilon$ model's inability to accurately predict low-Reynolds number effects lies in the increasing sensitivity of its defect layer solutions to increasingly adverse pressure gradients. Specifically, the computed wake strength parameter (Π) deviates from the experimentally observed values with increasingly adverse pressure gradients and consequently, results in incorrect skin friction coefficient prediction (Wilcox, 2006). Wilcox (2006) further shows that the viscous modifications in the viscous sublayer can only correct the prediction of the velocity profile approximating the wall[8] but cannot remove the $k-\epsilon$ model's deficiency to adverse pressure gradient flows. Other authors such as such as Speziale et al. (1990) and Menter (1992a) have also pointed out the Launder and Sharma (1974) $k-\epsilon$ model's deficiency to adverse pressure gradient flows.

The Wilcox (1988) $k-\omega$ turbulence model couples, to the RANS equations, partial differential equations for the turbulence kinetic energy (k) and the specific dissipation rate (ω) and includes a prescription for the kinematic eddy viscosity (ν_t) as shown in equations 3.28, 3.29 and 3.30. The closure coefficient and auxiliary relations can be found in Wilcox (1988) and Versteeg and Malalasekera (2007).

Turbulence eddy viscosity

$$\nu_T = \frac{k}{\omega} \tag{3.28}$$

Turbulence kinetic energy

$$\frac{\partial k}{\partial t} + U_j \frac{\partial k}{\partial x_j} = \tau_{ij} \frac{\partial U_i}{\partial x_j} - \beta^* k\omega + \frac{\partial}{\partial x_j}\left[(\nu + \sigma^* \nu_T)\frac{\partial k}{\partial x_j}\right] \tag{3.29}$$

Specific dissipation rate

$$\frac{\partial \omega}{\partial t} + U_j \frac{\partial \omega}{\partial x_j} = \alpha \frac{\omega}{k} \tau_{ij} \frac{\partial U_i}{\partial x_j} - \beta \omega^2 + \frac{\partial}{\partial x_j}\left[(\nu + \sigma \nu_T)\frac{\partial \omega}{\partial x_j}\right] \tag{3.30}$$

[8] The only thing that low-Reynolds number modifications achieve is predicting the additive constant, C, in the law of the wall (Wilcox, 2006).

The Wilcox (1988) $k-\omega$ model and its recent modification,Wilcox (2008), prove to be superior to all the $k-\epsilon$ formulations for turbulent boundary layer flow prediction. In the cases considered at the Stanford Olympics II (1980), the worst predicted case was that of the incipient transition flow with predicted skin friction of 28% higher than the measured value. On balance, for all considered cases, the maximum overall average difference between predicted and measured values is 7% (Wilcox, 2006).

In spite of its success in predicting turbulent boundary layer flows, the Wilcox (1988) $k-\omega$ model is not without flaw. Speziale et al. (1990) and Menter (1992b) showed that the Wilcox (1988) $k-\omega$ model is extremely sensitive to the free stream values for ω and although it performs very well for near-wall flows, its sensitivity to ω can be a stumbling block, thus caution needs to be exercised in this regard and furthermore, for the same reason, the model performs very poorly for shear flows. The Wilcox (2008) version includes a **cross diffusion** term to remedy the sensitivity of the Wilcox (1988) model to free stream values of ω and a built-in **stress limiter** that makes the eddy viscosity a function of k and ω, and effectively, the ratio of turbulence energy production to turbulent energy dissipation (Wilcox, 2006).

The earliest attempts to remedy the Wilcox (1988) $k-\omega$ model to free stream values of ω were by Menter (1992c) who proposed the SST $k-\omega$ model as a remedy. Menter (1992c) applies a change of variables to the standard $k-\epsilon$ model to transform the dissipation (ϵ) to become the dissipation rate (ω),viz., $\epsilon = k\omega$ and in essence creates a hybrid model that behaves like the Launder and Sharma (1974) $k-\epsilon$ in the fully turbulent region far from the wall and like the Wilcox (1988) $k-\omega$ model near the wall. Specifically the SST $k-\omega$ model includes a cross diffusion term ($\frac{\partial k}{\partial x_i}\frac{\partial \omega}{\partial x_i}$) to remedy the Wilcox (1988) $k-\omega$ model's sensitivity to the free stream values for ω. Since the SST $k-\omega$ model is a hybrid model of the $k-\epsilon$ the $k-\omega$ models it requires a blending function, F_1, in order to distinguish the regions where each of the two models will be applied. The blending function causes all the model's closure coefficient to assume values appropriate for the $k-\omega$ model near the solid boundaries and to asymptotically approach values similar to those used with the $k-\epsilon$ model otherwise. Specifically it causes the cross diffusion to be nullified near the wall and

effects it elsewhere in the flow (Menter, 1992c; Wilcox, 2006).

The SST $k-\omega$ turbulence model couples, to the RANS equations, partial differential equations for the turbulence kinetic energy (k) and the specific dissipation rate (ω) and includes a prescription for the kinematic eddy viscosity (ν_t) as shown in equations 3.31, 3.32 and 3.33. The closure coefficient and auxiliary relations can be found in Menter (1992c) and Versteeg and Malalasekera (2007).

Turbulence eddy viscosity

$$\nu_T = \frac{a_1 k}{\max(a_1\omega, SF_2)} \tag{3.31}$$

Turbulence kinetic energy

$$\frac{\partial k}{\partial t} + U_j \frac{\partial k}{\partial x_j} = P_k - \beta^* k\omega + \frac{\partial}{\partial x_j}\left[(\nu + \sigma_k \nu_T)\frac{\partial k}{\partial x_j}\right] \tag{3.32}$$

Specific dissipation rate

$$\frac{\partial \omega}{\partial t} + U_j \frac{\partial \omega}{\partial x_j} = \alpha S^2 - \beta\omega^2 + \frac{\partial}{\partial x_j}\left[(\nu + \sigma_\omega \nu_T)\frac{\partial \omega}{\partial x_j}\right] + 2(1-F_1)\sigma_{\omega 2}\frac{1}{\omega}\frac{\partial k}{\partial x_i}\frac{\partial \omega}{\partial x_i} \tag{3.33}$$

Wilcox (2006) underscores the importance for a turbulence model to be able to predict both free shear and wall-bounded flows since most complex flows include both types of regions. The SST $k-\omega$ turbulence model was tested with several aeronautical cases. In free shear-layer test cases, the model achieved results in accordance with the $k-\epsilon$ model and for cases with wall-bounded flows with adverse pressure gradients the Menter SST $k-\omega$ model proved to be highly accurate relative to experimentally observed results (Menter, 1992c). Menter (2009) summarises a series of modifications to optimize the performance of the SST $k-\omega$ model based on experience with the model in general purpose computation. The main improvements include revised model constants, improved blending functions and eddy viscosity limiters.

According to Versteeg and Malalasekera (2007) and Woelke (2007) the SST $k-\omega$ two-equation turbulence model by Menter (1992c) is most preferred for wall-bounded flows compared to the Launder and Sharma (1974)$k-\epsilon$ and Wilcox (1988) $k-\omega$ models.

3.5 Transition modeling

Transition is a complex phenomenon, defined as the process of change from laminar to turbulent flow as a consequence of instabilities in the laminar boundary layer. Anderson (2010); Bradshaw (1976.); Ferziger and Perić (2002); Tennekes and Lumley (1972); Versteeg and Malalasekera (2007). There are three main mechanisms that lead to turbulence, viz., natural transition, bypass transition and separation induced transition.

Low-speed aerodynamics comprises of a range of Reynolds numbers wherein the flow cannot be assumed to be entirely turbulent thus, the transition from laminar to turbulent flow plays an important role in predicting boundary layer phenomena. The turbulence models considered thus far have assumed the flow to be fully turbulent everywhere in the boundary layer. However, in reality, the flow always starts out at the leading edge as laminar and then at some point downstream, the boundary layer becomes unstable and small bursts of turbulence begin to grow in the flow and finally over a certain region, called the transition region, the boundary layer becomes fully turbulent. The consequence of assuming the flow to be fully turbulent is an incorrect prediction of aerodynamics coefficient, specifically an inaccurate prediction of skin friction and pressure drag and consequently, an overprediction of total drag (Anderson, 2010). The importance of modeling transition for transitional flow is underscored by examples 4.8-4.11 in Anderson (2010). A flat plate laminar boundary layer flow assumption in example 4.8 underpredicts skin friction drag coefficent, c_f, while it is overpredicted when using a fully turbulent boundary layer flow assumption in example 4.9. In examples 4.10-4.11, more realistic results relative to the experimentally observed values that were obtained when boundary layer transition

over the NACA 2412 was considered. Transition prediction is, therefore, of major importance in the pursuit of an accurate and realistic description of turbulent flow phenomena.

3.5.1 Transition models

A good transition model must appreciate that transition occurs through different mechanisms in different applications, viz., natural transition, bypass transition and separation-induced transition and thus have good prediction capabilities in all three cases (Eggenspieler, 2012). Various approaches have been developed in the CFD community to model transition, viz., DNS and LES for transition, stability theory [9], low-Reynolds number turbulence modeling, intermittency transport, etc. Di Pasquale et al. (2009) gives an overview of the eight most widely used approaches to model transition in Computational Fluid Dynamics.

DNS and LES are the most suitable tools to predict transition (see Jacobs and Durbin, 2001). Unfortunately, these methods are far too costly for typical engineering applications.

The most popular method for predicting natural transition is the e^n criterion, based on linear stability theory by Smith and Gamberoni (1956) and van Ingen (1956), see review on van Ingen (2008). The e^n model finds extensive use in the aerospace industry for natural transition prediction and is considered the state of the art when it comes to airfoil analysis[10]. It also gives satisfactory results for simple 3D flows over simple geometries. A draw back of this method is its inability to predict bypass transition and its incompatibility with general purpose CFD methods (RANS operations) as typically applied to complex geometries (Di Pasquale et al., 2009). Since

[9] Stability theory is based on the study of the behavior of small flow disturbances to see whether they grow or not. The single oscillation of the disturbance is assumed to be $\psi(x, y, z) = \phi e^{i(\alpha x - \beta t)}$, if the disturbance amplitude grows the flow is unstable and transition to turbulent flow is expected (Aupoix et al., 2011; Di Pasquale et al., 2009).

[10] The e^n criterion finds its implementation in preliminary aircraft design tools such as XFOIL and XFLR5.

the e^n criterion transition model is based on linear stability theory, it cannot predict the transition due to non-linear effects such as high free stream turbulence or surface roughness (Di Pasquale et al., 2009).

Low- Reynolds number turbulence models are calibrated to predict transition by integrating through the viscous sublayer. The earliest efforts in this direction of transition prediction were from Craft et al. (1997); Westin and Henkes (1997) and Wilcox (1994) while Langtry and Sjolander (2002) and Walters and Leylek (2004) are more recent efforts. These models have been amongst the most successful and widely used transition prediction methods. The Wilcox (1988) $k-\omega$, Wilcox (2008) $k-\omega$ and Menter (1992c) $k-\omega$ have also been recalibrated to offer this transition prediction capability (see Siemens, 2017). According to Di Pasquale et al. (2009), at best, low-Reynolds number models can only be expected to simulate bypass transition and separation induced transition.

According to Di Pasquale et al. (2009), the concept of transition prediction via intermittency transport, which was first introduced by Dhawan and Narasimha, is the blending together the laminar and turbulent flow regimes based on empirical correlations. Many detailed investigations of the process of transition reveal that, over a certain range of Reynolds numbers around the critical value, the flow becomes intermittent and thus alternates in time between being laminar and turbulent (Di Pasquale et al., 2009). The physical nature of the flow is described with the aid of an intermittency factor (γ) which is defined as the fraction of time that the flow is turbulent during the transition phase. The start and evolution of transition is imposed by allowing the intermittency to grow from zero to unity (Di Pasquale et al., 2009). According to Eggenspieler (2012) intermittency is given by $\gamma = \frac{t_{turb}}{t_{lam}+t_{turb}}$ where $\gamma = 0$ for laminar flow, $\gamma = 1$ for turbulent flow and $0 < \gamma < 1$ for transitionl flow.

Menter et al. (2004;b) proposed the $\gamma - Re_\theta$ intermittency transition model. The transition model is based on two transport equations, one for the intermittency factor, γ, and one for the transition onset momentum-thickness Reynolds number,

Re_θ. The intermittency equation (3.34) is responsible for triggering the transition process and the production of turbulent kinetic energy inside the boundary layer, while the momentum thickness Reynolds number equation (3.35) avoids additional non-local operations that appear when experimental correlations are used (Menter, 1992a). The closure coefficient and auxiliary relations can be found in (Menter, 1992a).

Intermittency (γ) equation

$$\frac{\partial(\rho\gamma)}{\partial t} + \frac{\partial(\rho U_j \gamma)}{\partial x_j} = P_\gamma - E_\gamma + \frac{\partial}{\partial x_j}\left[\left(\mu + \frac{\mu_f}{\sigma_f}\right)\frac{\partial \gamma}{\partial x_j}\right] \tag{3.34}$$

Transition Momentum Thickness Reynolds Number(Re_θ) equation

$$\frac{\partial(\rho\overline{Re_{\theta t}})}{\partial t} + \frac{\partial(\rho U_j \overline{Re_{\theta t}})}{\partial x_j} = P_{\theta t} + \frac{\partial}{\partial x_j}\left[\sigma_{\theta t}(\mu + \mu_t)\frac{\partial \overline{Re_{\theta t}}}{\partial x_j}\right] \tag{3.35}$$

The $\gamma - Re_\theta$ transition model is CFD compatible with the Menter SST $k-\omega$ model. The combination has been tested on several aeronautical cases and with good agreement relative to experimental data (Menter et al., 2004b).

3.6 Turbulence modeling of flow near the wall

Extensive research that has been conducted on turbulent boundary layer flow reveals that different physical processes and turbulent scales exist in the turbulent boundary layer. Different physical processes such as turbulence production, diffusion, energy cascade, dissipation, etc. Different turbulent scales such as eddy length, velocity and time scales. Experiments and mathematical analysis have shown that the velocity profile of a turbulent boundary layer can be divided into two-layers known as the inner and the outer layer (Wilcox, 2006; Versteeg and Malalasekera, 2007). The inner layer is near the wall while the outer layer approximates the free stream. The

inner layer is further divided into two-layers, viz., the linear/viscous sublayer and the log-law layer. A typical velocity profile for a turbulent boundary layer with its different regions, layers and sublayers is shown in figure 3.3. U_0 is the free stream velocity and δ is the boundary layer thickness.

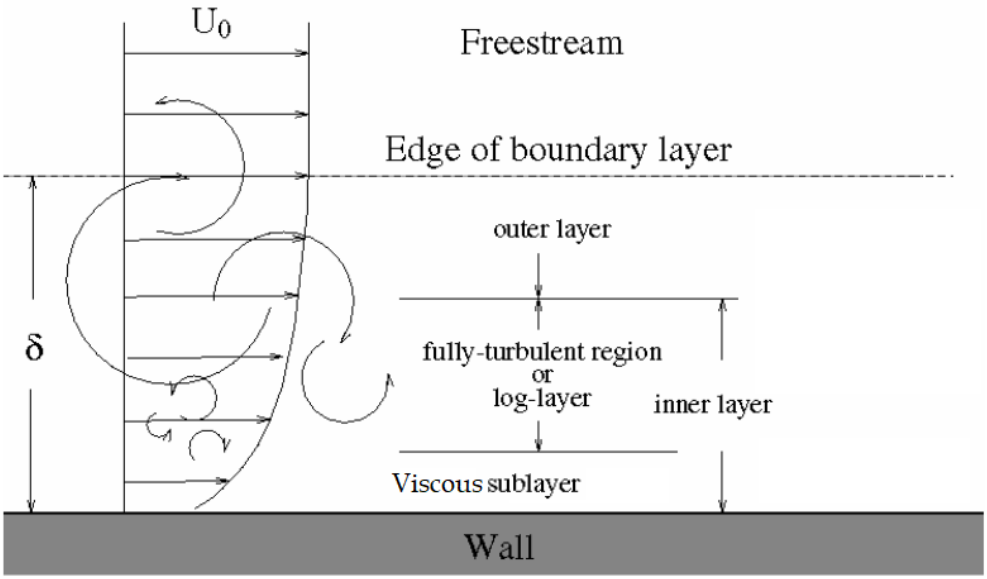

Figure 3.3: Typical velocity profile for a turbulent boundary layer Bakker (2002).

According to Versteeg and Malalasekera (2007), the inner layer occupies a small portion of about 10-20% of the total boundary layer thickness and has a shear stress that is almost constant and equal to the wall shear stress while the outer layer occupies most the boundary layer and is free from direct viscous effects. The viscous sublayer is closest to the wall and thus, the flow in this region is subject to the no-slip wall condition and therefore, viscosity plays a dominant role in momentum and heat transfer. Outside the viscous sublayer, further away from the wall, in the logarithmic layer, the effects of viscosity and inertia are negligible on the flow and thus turbulence plays a dominant role in momentum and heat transfer (Wilcox, 2006). Some authors, such as Versteeg and Malalasekera (2007) have recognized the existence of a third sublayer of the inner layer called the buffer layer. The buffer layer lies between the viscous sublayer and the logarithmic layer and here, the effects of molecular viscosity and turbulence are of equal importance (Versteeg and Malalasekera, 2007). The outer

layer, called the defect law layer or law of the wake, has inertial dominated flow that is free from direct viscous effects.

3.6.1 Wall y^+ and u^+

The velocity profile of a turbulent boundary layer is often described in terms of two non-dimensional parameters namely y^+ and u^+. The concept of wall y^+ and u^+ has been formulated to distinguish the different regions near the wall. The y^+ is a dimensionless quantity and is the distance from the wall measured in terms of viscous lengths. The u^+ is a dimensionless quantity and is the velocity from the wall measured in terms of wall friction velocity. A typical velocity profile of a turbulent boundary layer, with its different layers in terms of dimensionless variables u^+ and y^+ is given in figure 3.4.

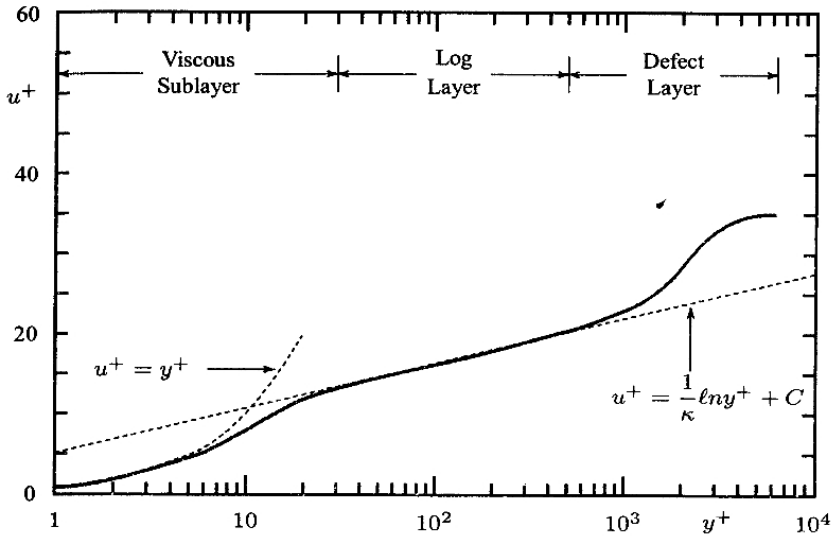

Figure 3.4: Velocity profile in turbulent boundary layer in terms of dimensionless variables u^+ and y^+ (Wilcox, 2006).

Each region of the turbulent boundary layer has different effects on the turbulence and therefore, in the discretization process, particular care must be taken with regards to the y^+ position of the first cell in the boundary layer.

The velocity profile in the region that approximates the wall, the viscous sublayer region is described by a linear relationship between the mean velocity and the distance from the wall as shown in equation 3.36.

$$U = \frac{\tau_w y}{\mu} \tag{3.36}$$

This relationship is often described in terms of dimensionless variables, u^+ and y^+ as shown in figure 3.4 and by equation 3.37. This linear relationship is only valid for y^+ values below five $y^+ < 5$

$$u^+ = y^+, \tag{3.37}$$

where $u^+ = \frac{u}{u_\tau}$,$u_\tau = \sqrt{\frac{\tau_w}{\rho}}$, $U(y, \rho, \mu, \tau_w)$, $y^+ = \frac{y\, u_\tau}{\nu}$.

In the region that approximates the free stream, the velocity defect layer, the velocity defect law accounts for the velocity profile. The velocity defect, initially conceived by Clauser, is an empirically determined relationship in turbulent boundary layer flows far from the wall. Measurements show that the velocity deficit due to the wall shear stress decreases, for both internal and external flows, as the flow approximates the free stream (Wilcox, 2006; Versteeg and Malalasekera, 2007). The velocity defect law is given by equation 3.38 and more explicitly by equation 3.39. Experimental measurements have shown that the log-law is valid in the region $0.02 < \delta < 0.2$ (Versteeg and Malalasekera, 2007).

$$u^+ = \frac{u}{u_\tau} = \frac{U_{max} - U}{u_\tau} = g(\frac{y}{\delta}) \tag{3.38}$$

$$\frac{U_{max} - U}{u_\tau} = -\frac{1}{\kappa} \ln(\frac{y}{\delta}) + A \tag{3.39}$$

where $\kappa \approx 0.41$ and A is a constant (Versteeg and Malalasekera, 2007). In the overlap region between the viscous sublayer and the velocity defect layer, the law of the wall accounts for the velocity profile. The law of the wall, derived by von Karman (1931), is an empirically determined relationship in turbulent flows near the wall. Measurements show that, for both internal and external flows, the streamwise velocity in the flow near the wall varies logarithmically with distance from the surface

(Versteeg and Malalasekera, 2007; Wilcox, 2006). The velocity profile in this region is fully described by a logarithmic relationship between u^+ and y^+ as shown in figure 3.4 and by equation 3.40 which is written more explicitly in equation 3.41.

$$u^+ = \frac{U}{u_\tau} = f(\frac{\rho u_\tau y}{\mu}) = f(y^+), \tag{3.40}$$

$$u^+ = \frac{1}{\kappa}\ln(\frac{y^+}{\delta}) + B = \frac{1}{\kappa}\ln(Cy^+) \tag{3.41}$$

where $\kappa \approx 0.41$, $B \approx 5.5$ and $C \approx 9.8$ for a smooth wall (Versteeg and Malalasekera, 2007). In this layer y^+ takes on the values $30 < y^+ < 500$.

3.6.2 Near-wall treatment

The near-wall modeling significantly impacts the fidelity of numerical solutions. An accurate representation of the flow in the near-wall region determines successful predictions of wall-bounded turbulent flows since the wall is the main source of mean vorticity and turbulence [11] (Salim and Cheah, 2009). In applications where wall effects on flow are significant, i.e., applications that consider the effects of flow transition on skin friction and aerodynamic drag, the flow in the viscous sublayer must be resolved with an appropriate low-Reynolds number turbulence model and the mesh size should be small and dense enough near the wall so that the wall effects on flow are accurately captured (Kalitzin et al., 2005). But in cases where wall effects on flow are less important, i.e., applications that only consider the effects of turbulence on skin friction and aerodynamic drag, the flow in the log-law layer must be resolved with a high Reynolds number turbulence model (assumes full turbulence) and in this case the mesh need not to be dense or small near the wall (Kalitzin et al., 2005).

Most turbulent models are valid for fully turbulent flows (high-Reynolds number flows) and are hence applicable in the log layer region which is some distance from

[11] Depending on the application of a problem under consideration, we may determine in which layer we should resolve the effects of the wall on the flow. The layer that is chosen informs the choice of the turbulence model that will be used and the size of the mesh near the wall.

wall. The $k-\epsilon$ turbulence models are examples of such models (Salim and Cheah, 2009). The wall function, also known as high y^+ wall functions, near-wall treatment is often used for flows with high Reynolds numbers to circumvent the excessive grid requirements (Kalitzin et al., 2005). Wall functions are a set of semi-empirical functions used to satisfy the physics of the flow in the log-law layer of the turbulent boundary layer. In the wall function approach, the assumption is that the near-wall cell lies within the logarithmic region of the boundary layer, and thus, the viscosity affected region does not need to be resolved by the mesh. This substantially saves computational resources since the full resolution of the boundary layer is not necessary (Kalitzin et al., 2005).

The wall function approach is, however, not applicable in flows interested in low-Reynolds number effects, where the flow in the viscous sublayer is of interest. Low-Reynolds number flows require near-wall turbulence models that are valid in the viscosity affected region and accordingly integrable all the way to the wall. Adaptive wall functions, also known as low y^+ wall functions, are applicable in this situation (Kalitzin et al., 2005). The assumption in adaptive wall functions is that the near-wall cell lies within the viscous sublayer region of the boundary layer. Wall integration of turbulence models requires the first computational cell above the wall to be located at about $y^+ < 5$ and thus this wall approach uses a substantial amount of computational resources because it requires a full resolution of the boundary layer since the mesh has to be well resolved all the way to the wall (Kalitzin et al., 2005; Salim and Cheah, 2009). The Spalart-Allmaras and $k-\omega$ turbulence models were designed to be applied throughout the boundary layer(Salim and Cheah, 2009)

The high-y^+ wall treatment which assumes that the near-wall cell lies within the logarithmic region of the boundary layer and is used for core turbulent flows while the low-y^+ wall treatment, which assumes that the viscous sub-layer is properly resolved, is used in transitional flow. The all-y^+ wall treatment is a hybrid treatment of the low-y+ and high-y^+ wall treatments.

3.7 Turbulent wake modeling

The earliest and most significant studies on wake flows that have laid a foundation for wake studies were conducted for symmetrical wakes generated by a flat plate or an airfoil at zero and small incidence angles (see Alber, 1980; Andreopoulos, 1978; Bradshaw, 1970; Hah and Lakshminarayana, 1982; Ramaprian et al., 1982; Ramjee et al., 1988; Ramjee and Neelakandan, 1990). Wake flow research by Alber (1980); Chevray and Kovasznay (1969); Hah and Lakshminarayana (1982); Ramaprian et al. (1982) has assisted to classify the wake into different regions according to the distance from the wake source and to characterize the wake behavior in the various regions. Alber (1980) divided the wake region into three regions, viz., near wake, intermediate wake and far wake as shown in figure 3.5.

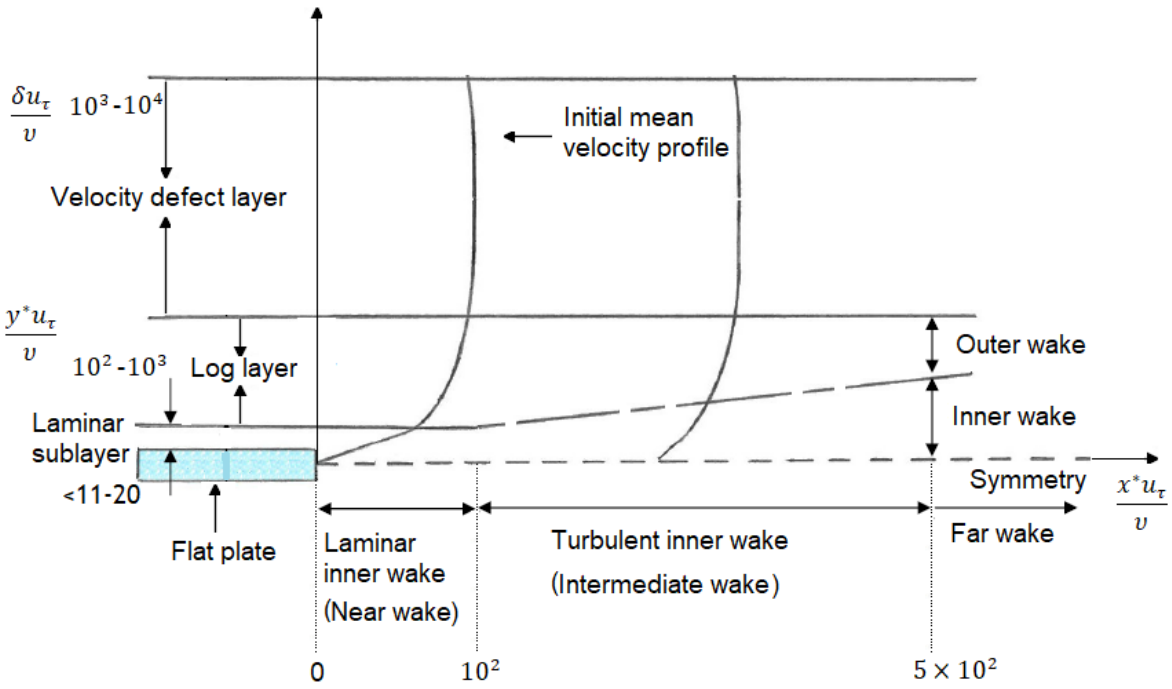

Figure 3.5: Wake regions of a turbulent wake flow (Alber, 1980; Farsimadan, 2008).

To determine whether the wake region is near, intermediate or far, Ramaprian et al. (1982) non-dimensionalised the downstream distance, x, by the initial momentum

thickness, θ. According to Ramaprian et al. (1982) the near wake is defined by $x/\theta \leq 25$, the intermediate wake region by $25 \leq x/\theta \leq 350$ and the far wake region by $x/\theta \geq 350$. Alber (1980) reports that, when measured from the trailing edge, the length of the near wake is approximately equal to ten laminar sublayer thicknesses while the intermediate wake is approximately equal to ten boundary layer thicknesses.

3.7.1 Near, intermediate and far wake modeling

Due to the presence of the linear sublayer velocity profile near the wall at the trailing edge, it is expected that, for a short distance downstream of the trailing edge, a laminar inner wake should develop which behaves like the inner laminar Goldstein solution (Alber, 1980).

$$\frac{u^*}{u_\tau} = (\frac{u_\tau}{\mu})^{1/3} f_o'(\eta) \tag{3.42}$$

with $\eta = \frac{1}{3}(\frac{y^* u_\tau}{\mu})/(\frac{x^* u_\tau}{\mu})^{1/3}$ and $f_o'(\eta) \sim \eta$ as $\eta \to \infty$.

In this region of turbulent wake development laminar diffusion dominates near the axis, i.e., for distances $\frac{x^* u_\tau}{\mu} \leq O(10^2)$, the inner wake layer grows into the laminar sublayer of the initial boundary layer. According to Hah and Lakshminarayana (1982), in this region, the viscous sublayer on the airfoil is not completely mixed with the surrounding inertial sublayer and the molecular viscosity has a substantial effect on the flow evolution in the wake center region and therefore, the velocity defect is large.

Alber (1980) reports that the thickness of the laminar inner wake increases with axial distance to the one-third power and therefore, the inner laminar Goldstein solution will be approximately valid only as long as the thickness of the inner wake layer does not exceed the height of the initial laminar sublayer. , i.e., the laminar wake region will be small and in the range of $0 < \frac{u_\tau}{\mu} < 50 - 400$.

The development of the inner wake beyond the height of the initial laminar sublayer causes it to penetrate into the log law layer of the turbulent boundary layer profile. This takes place in the turbulent inner wake region. The wake in the turbulent inner wake region ($10^2 < \frac{x^* u_\tau}{\mu} < 10^4$) is fully turbulent and therefore, the diffusion

process is assumed to be dominated by turbulent, rather than laminar mixing (Alber, 1980). According to Hah and Lakshminarayana (1982), in this region, the physical characteristics of the airfoil and aerodynamic loading on the airfoil have substantial effects on the evolution of the wake and the effect of molecular viscosity is negligible. The wake defect is of the same order as the mean velocity in this region. Alber (1980) derived an analytic turbulent inner wake solution given by equation 3.43 , which accurately described the behavior of the wake in this region relative to the experimentally observed behavior by Chevray and Kovasznay (1969).

$$\frac{u^*}{u_\tau} = \frac{1}{\kappa}[\ln(\frac{x^* u_\tau}{\nu})\ln(\eta) + E_1(\eta)] + B \tag{3.43}$$

with $\eta = \frac{y}{g(x)}$ and $g(x)[\ln g(x) - 1] = \kappa^2 x$.

The outer wake layer of both the laminar inner wake and turbulent inner wake represents the convected remnant of the upstream boundary layer responding slowly to the changed boundary conditions transmitted to it by the inner wake at a zero pressure gradient (Alber, 1980). This modeling assumption agrees well with the statements by Chevray and Kovasznay (1969) that "Leaving the trailing edge...only the center portion of the flow changes and the outer portion remains the same as the original boundary layer" and that "the constancy of the (wake) momentum thickness in the downstream direction, clearly indicates the absence of any significant pressure gradient."

Experimental observations reveal a self-preserving nature in the mean velocity and turbulent structure of free shear turbulent flows , i.e, a certain distance downstream of the flow, the mean velocity and turbulent structure of free shear turbulent flows becomes independent of the exact nature of the flow source and the local environment appears to control the turbulence in the flow (Hermann and Gersten, 2017.; Pope, 2000; Tennekes and Lumley, 1972; Versteeg and Malalasekera, 2007; Wilcox, 2006). This amounts to stating that two velocity or turbulence stress profiles located at different x stations downstream of wake will have the same shape (Wilcox, 2006). The turbulence structure reaches a self-preserving state after a great distance from

the flow source compared to the mean velocity (Versteeg and Malalasekera, 2007). The self-preserving nature of wake flows is described by equation 3.44 for the mean velocity and equations 3.45 for the turbulence stresses.

$$\frac{U_{max} - U}{U_{ref}} = h(\frac{y}{b}) \tag{3.44}$$

$$\frac{\overline{u_i'^2}}{U_{ref}^2} = f_1(\frac{y}{b}) \qquad \frac{\overline{u_j'^2}}{U_{ref}^2} = f_2(\frac{y}{b}) \qquad \frac{\overline{u_k'^2}}{U_{ref}^2} = f_3(\frac{y}{b}) \qquad \frac{\overline{u_i' u_j'}}{U_{ref}^2} = f_4(\frac{y}{b}) \tag{3.45}$$

$U_{ref} = U_\infty - U_{min}$ and the exact form of functions h, f_1, f_2, f_3 and f_4 are flow dependent. According to Hah and Lakshminarayana (1982), in the far wake, the physical characteristics and aerodynamic loading on an airfoil have almost negligible effects on the development of the wake. The velocity defect is small and history effects such as airfoil shape or loading have vanished.

3.7.2 Turbulent wake models

The following turbulence models were considered for a turbulent wake flow. The algebraic turbulence models by Baldwin and Lomax (1978), Cebeci and Smith (1974), Johnson and King (1985) and a mixing length model that was calibrated by Wilcox (2006)[12], the one-equation turbulence models by Baldwin and Barth (1990) and Spalart and Allmaras (1992) and the standard $k-\epsilon$, $k-\omega$ and SST $k-\omega$ two-equation turbulence models by Launder and Sharma (1974), Wilcox (1988) and Menter (1992c), respectively.

Despite the simplicity of algebraic turbulence models, they have a problem of incompleteness. These turbulence models do not provide a turbulence length scale or its equivalent and therefore, require additional flow information other than the initial and boundary conditions to obtain a solution e.g. a turbulence half wake

[12] Wilcox (2006) calibrated the mixing length model by prescribing a turbulence length scale. He effectively defined a function for the turbulence half wake width ($\delta(x)$) growth and determined the model's closure coefficient by using experimental data by Schlichting and Gersten(cited by Wilcox, 2006).

width ($\delta(x)$) as in the case of the above mentioned mixing length model that was calibrated by Wilcox (2006) for a turbulent wake flow. The turbulence length scale or its equivalent is obtained through an experimental investigation of a specific flow. Algebraic turbulence models are, therefore, flow case specific and lack a wide range of application. They will work well for the flows for which they have been calibrated (Wilcox, 2006). The algebraic turbulence models by Baldwin and Lomax (1978),Cebeci and Smith (1974) and Johnson and King (1985) are calibrated for wall-bounded flows and it would, therefore, be unreasonable to consider them for a wake flow.

Wilcox (2006) compared the computed and measured wake spreading rates for the Baldwin and Barth (1990),Launder and Sharma (1974) $k-\epsilon$, Spalart and Allmaras (1992) and Wilcox (1988) $k-\omega$ models. The Baldwin and Barth (1990) model predicts a spreading rate 2% below the lower bound of measured values while the Spalart and Allmaras (1992) models predicted a wake spreading rate that is within the range of experimentally observed values. The Launder and Sharma (1974) $k-\epsilon$ model underprediced the wake spreading rates by 20% lower than the lower bound of the measured values while the Wilcox (1988) $k-\omega$ overpredicted the spreading rates. The Wilcox (1988) $k-\omega$ model's poor performance is due to its well known sensitivity to the free stream value of the dissipation rate (ω).

Wilcox (2006) also compared the mixing length turbulence model that he calibrated, the Launder and Sharma (1974) $k-\epsilon$ and Spalart and Allmaras (1992) model's computed wake velocity profile for a 2D cylinder with the values that were observed experimentally by Fage and Falkner (1932) and Weygandt and Mehta (1995). The mixing length model produced the best results relative to the experimental data (within the baseline data range), the Spalart and Allmaras (1992) model produced satisfactory results relative the experimental data with only a slight deviation from the baseline data range and the Launder and Sharma (1974) $k-\epsilon$ model performed poorly with a severe deviation from the baseline data range. Menter (1992c) also compared the SST $k-\omega$ computed results with the experimentally observed data by Fage and Falkner (1932). The computed results were in good agreement relative to the experimental data.

In spite the good correlation of the Spalart and Allmaras (1992) and Menter (1992c) SST $k-\omega$ models relative to the experimentally observed data, a number of authors such as Hellsten (2005); Siemens (2017); Versteeg and Malalasekera (2007) and Wallin and Johansson (2000) have pointed out the deficiency of the linear constitutive model (Boussinesq Approximation) which assumes a linear dependency between the turbulent stress and the mean rate tensors. Hellsten (2005); Siemens (2017); Versteeg and Malalasekera (2007) and Wallin and Johansson (2000) have argued that the Boussinesq approximation is a restrictive assumption for highly anisotropic turbulent flows such as boundary layer flows at high angles of attack and turbulent wake flows with sharp fluctuations in turbulence quantities. According to Siemens (2017), turbulence models based on the linear relation between the Reynolds stresses and the mean strain rate tends to strongly underpredict the anisotropy in highly turbulent flows. Siemens (2017) further mentions that the anisotropy of the Reynolds stresses affects the turbulent transport of scalars i.e. velocity and turbulent kinetic energy.

To account for the anisotropy in highly turbulent flows Wallin and Johansson (2000) proposed an Explicit Algebraic Reynolds Stress Model (EARSM) which was later improved by Hellsten (2005). Algebraic stresss models are based on modeling assumptions that reduces the partial differential equations that describe the Reynolds stress transport in a Reynolds Stress Model (RSM) to algebraic equations which are solved along two equation eddy viscosity models with no added computational effort. Algebraic stress models are a non-linear constitutive relation between the Reynolds stresses and the mean strain rate and they effectively offer an extension to the Boussinesq approximation to account for the anisotropy in highly turbulent flows. Regarding the anisotropy of highly turbulent flow, according to Hellsten (2005); Siemens (2017); Versteeg and Malalasekera (2007) and Wallin and Johansson (2000), the EARSM perform much better than eddy viscosity models. A non-linear (EARSM) SST $k-\omega$ model, therefore, offers an advantage compared to the linear SST $k-\omega$ model for boundary layer flows at high angles of attack and turbulent wake flows with sharp fluctuations in turbulence quantities.

3.8 Physical model selection

Based on the limitations of each turbulence and transition model that was discussed in the previous sections, a choice for the most appropriate description for the transitional and turbulent wake flows under consideration was made. The Spalart and Allmaras (1992) and the SST $k-\omega$ Menter (1992c) turbulence models are widely used in the aerospace industry and provide good results for boundary layer and wake turbulent flows (Wilcox, 2006). According to Versteeg and Malalasekera (2007) the Menter (1992c) SST $k-\omega$ is preferred over the Spalart and Allmaras (1992) turbulence model since it is most general, i.e., it gives superior performance for favorable, mild and adverse pressure gradient boundary layers and turbulent flows. The linear Menter (1992c) SST $k-\omega$ model offers satisfactory boundary layer prediction capabilities at low to moderate angles of attack and turbulent wake flows with small to moderate turbulent fluctuations but however fails when it comes to boundary layer flows at high incidence angles and turbulent wake flows with high turbulent fluctuations. The non-linear Menter (1992c) SST $k-\omega$ model is a remedy to the deficiencies of the linear Menter (1992c) SST $k-\omega$ model.

The current project focuses on low-Reynolds number flows with low-turbulence intensity and thus both laminar and turbulent flow is likely to exist on the flow surface; therefore, transition must be modeled. The e^n criterion and the $\gamma - Re_\theta$ transition model are the most widely used in the aerospace industry and both provide satisfactory results in their sphere of application, however, as noted in section 3.5.1, the e^n criterion has a couple of drawbacks, viz., inability to predict bypass transition and incompatibility with general purpose CFD methods. On the other hand the $\gamma - Re_\theta$ transition model presents none of these deficiencies.

Both the Spalart and Allmaras (1992) and SST Menter (1992c) $k-\omega$ models assume fully turbulent flow and are, therefore, not sufficient for a realistic description of a transitional flow. However, the Menter (1992c) has the added advantage, that it is compatible with the $\gamma - Re_\theta$ transition model and consequently, allows for far better

prediction capabilities for low-Reynolds number flows (Menter et al., 2004b). Therefore, the SST $k-\omega$ Menter (1992c) turbulence model with the $\gamma - Re_\theta$ transition model were chosen to model the transitional flow that is considered in this project. Aftab et al. (2016) conducted a numerical study where he showed that the Menter (1992c) turbulence model with the $\gamma - Re_\theta$ transition model are the most suitable descriptions for wall-bounded low-Reynolds number flows, Joao Nuno Dias (2016*a*) came to the same conclusion by conducting a brief literature review on the mathematical modeling for low-Reynolds number flows while Sutalo (2017) conducted a thorough literature review on the mathematical modeling for low-Reynolds number flows and a validation study.

In the transitional and wake 2D validation case in chapter 5, the SST $k-\omega$ turbulence model that uses the Boussinesq approximation with the $\gamma - Re_\theta$ transition model was compared with the and SST $k-\omega$ algebraic turbulence stress model with the $\gamma - Re_\theta$ transition model and the RSM. The object of the comparison was to determine the adequacy of the SST $k-\omega$ turbulence model that uses the Boussinesq approximation with the $\gamma - Re_\theta$ transition model to model a transitional and turbulent wake flow.

The use of the SST $k-\omega$ Menter (1992c) turbulence model (linear and non linear) with the $\gamma - Re_\theta$ transition model comes at a computational cost, four equations are coupled to the RANS equations to make a total of eight equations that must be solved on a finite volume grid.

Summary

This chapter covered the literature on the mathematical modeling of the low-Reynolds number ($Re \approx O(10^6)$) flow phenomena that are encountered in sailplane flight as discussed in chapter 2. The mathematical modeling of phenomena such as turbulent boundary layer flow, transitional boundary layer flow and turbulent wake flow have been discussed in the context of sailplane flight. The most appropriate physical model for describing transitional and turbulent wake flow was chosen based on com-

putational limitations and on the pros and cons of each model that was considered. The Menter (1992c) SST $k-\omega$ turbulence and $\gamma - Re_\theta$ transition model was chosen to model the transitional and turbulent flow considered in this study.

Chapter 4

Methodology

Introduction

This chapter covers the CFD approach that was used in this study. Verification, validation and the major factors that may influence the CFD results in this study are considered. Section 4.1 introduces verification and validation in the context of CFD. Section 4.2 discusses verification and highlights the two forms of error that may be incurred in the current CFD study. The discretization and iterative convergence error are covered in subsections 4.2.1 and 4.2.2, respectively. Section 4.3 presents the verification method that was employed in the present CFD study. Section 4.4 discusses validation and highlights the four forms of uncertainties that may be present in this CFD study. Geometric modeling uncertainty, boundary condition uncertainty, fluid property uncertainty and physical model uncertainty are covered in subsections 4.4.1,4.4.2, 4.4.3 and 4.4.4, respectively. Section 4.5 presents the validation method that was employed in the current CFD study.

4.1 Verification and Validation

Computational Fluid Dynamics analyzes fluid flow systems, heat transfer and associated phenomena by computer-based simulation and thus error and uncertainty are

unavoidable aspects of CFD modeling (Versteeg and Malalasekera, 2007). The use of CFD as a design analysis tool has potential consequences if the simulation results are wrong. According to (Versteeg and Malalasekera, 2007), the consequences of inaccurate CFD results are at best wasted time, money and effort and at worst catastrophic failure of components, structures or machines. Therefore, the use of CFD modeling as an engineering tool can only be justified by ascertaining the level of confidence and accuracy in its results. Extensive research has been carried out to expose the factors which influence CFD results. A systematic process for the quantitative assessment of confidence levels has been developed. This has led to the development of a number of guidelines for best practices in CFD, of which AIAA (1998) is one of the most influential. Verification and validation is mandatory in the use of CFD, it is the primary means to assess accuracy and reliability in computational simulation (Oberkampf and Trucano, 2002). The following, widely accepted terminology from AIAA (1998) and Oberkampf and Trucano (2002) is used to give a description of the verification and validation process. Figure 4.1 shows the basic processes of modeling and simulation.

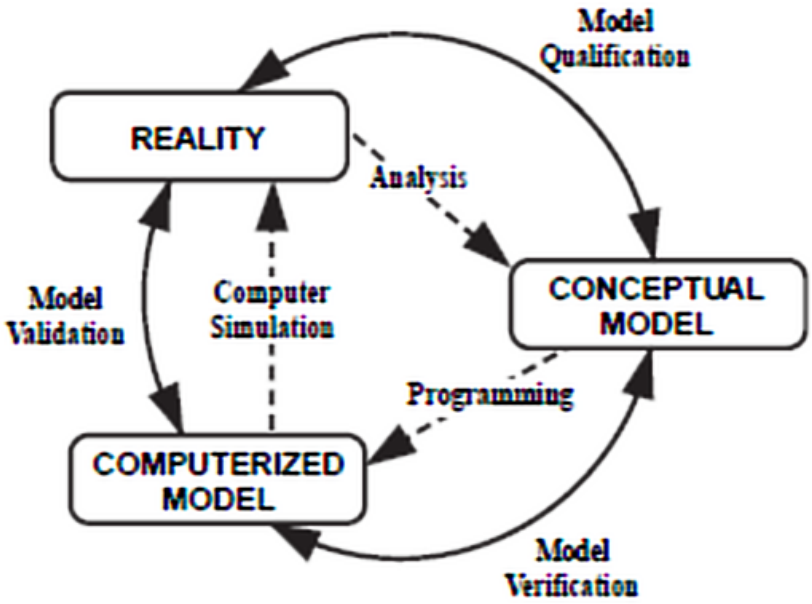

Figure 4.1: Phases of modeling and simulation (AIAA, 1998; Oberkampf and Trucano, 2002).

Two types of models are identified, viz., a conceptual model and a computerized model. The conceptual model is composed of all the modeling information such as the mathematical equations that describe the physical system or process of interest (AIAA, 1998; Oberkampf and Trucano, 2002). The conceptual model is a product of the analysis and observation of a physical system. In CFD, the conceptual model largely comprises of partial differential equations for the conservation of mass, momentum and energy. On the other hand, the computerized model is an operational computer program that implements a conceptual model (AIAA, 1998; Oberkampf and Trucano, 2002).

The meaning of verification and validation and their relationship is also depicted in figure 4.1. Verification is the process of determining that a model implementation accurately represents the developer's conceptual description of the model and the solution to the model (AIAA, 1998; Oberkampf and Trucano, 2002; Versteeg

and Malalasekera, 2007). Thus, the verification processes addresses the question of fidelity of the computerized model to the conceptual model. Verification provides evidence that that the physical model is solved right. It does not address whether the model has any relationship to the real world, therefore, verification activities only evaluate whether the CFD model, the mathematical and the computer code representation of the physical system are solved accurately (AIAA, 1998). On the other hand, validation is a process of determining the degree to which a model is an accurate representation of the real world from the perspective of the intended uses of the model (AIAA, 1998; Oberkampf and Trucano, 2002; Versteeg and Malalasekera, 2007). Therefore, validation addresses the issue of fidelity of the computational model or its results, i.e., simulation, to the real world. Validation ascertains the capability of a physical model to predict a physical phenomenon.

4.2 Verification

Verification is the means by which error is evaluated in a CFD simulation. According to AIAA (1998); Oberkampf and Trucano (2002) and Versteeg and Malalasekera (2007) error is defined as a recognizable deficiency in any phase or activity of the CFD modeling process that is not caused by lack of knowledge. Error in a CFD calculation can be typically defined as

$$E = u_{exact} - u_{discrete}. \tag{4.1}$$

u_{exact} is the mathematically correct solution of the exact equations of the conceptual model PDE for a given set of initial and boundary conditions. $u_{discrete}$ is the numerical solution of a discrete approximation of the same PDE and a set of initial and boundary conditions that is given by the computer code.

The two sources of error that may be incurred in the present CFD study are due to insufficient spatial (i.e. grid) discretization convergence and lack of iterative convergence.

CFD errors due to insufficient spatial discretization convergence and lack of itera-

tive convergence are collectively called numerical errors[1]. Discretisation errors are also classified as acknowledged errors and have procedures for identifying them and possibly removing them (AIAA, 1998; Oberkampf and Trucano, 2002; Versteeg and Malalasekera, 2007).

4.2.1 Discretisation error

CFD errors due to insufficient spatial discretization convergence, also called dicretisation errors, arise from the representation of the equations governing the flow (conceptual model) as algebraic expressions in a discrete domain of space (computerized model). Ideally, discretization should give algebraic expressions that exactly represent or at least gives a satisfactory representation of the continuum description of the flow.

4.2.1.1 Taylor series trunction error

The first discretization error that may be incurred in this CFD study is due to truncating the higher order terms of the spatial derivatives of the flow variables (fluxes, sources and sinks) in the governing equations of the flow (conceptual model). According to Versteeg and Malalasekera (2007), the spatial derivatives of the flow variables are, only, approximated by the chosen discretization scheme and in practice, this corresponds to the truncation of a Taylor series. The result of neglecting the higher order terms of the spatial derivatives of the flow variables in the governing equations of the flow gives rise to a truncation error, which is, in effect, the difference between the continuum description of the flow and the discrete description of the flow. This error may be reduced by increasing the order of accuracy for a discretization scheme. There are a variety of discretization schemes with differing orders of

[1]Round off error is another common yet insignificant numerical error, compared to the other numerical errors, that may be expected with the use of CFD. This error is the result of the computational representation of real numbers by means of significant digits, which is termed Machine accuracy (Versteeg and Malalasekera, 2007)

accuracy (e.g central differencing scheme, upwind differencing scheme etc.) which exist. This CFD study will employ the second order upwind differencing discretization scheme. Fundamentally important factors that inform the use of a particular discretization scheme are conservativeness, boundedness and transportiveness (see Versteeg and Malalasekera, 2007:Chapter 5.4). According to an assessment of the upwind differencing scheme by Versteeg and Malalasekera (2007), conservativeness, boundedness and transportiveness are well accounted for.

4.2.1.2 Interpolation error

The second discretization error that may be incurred in this CFD study is due to interpolation from the approximated boundary values at the grid interface. CFD solves the discretized equations at discrete points and thus, the flow domain is divided into grid points at which the discretized equations are solved by iteration. The fluxes, sources and sinks across the boundaries of the control volume(grid) have a direct influence on the solutions at nodal points. The detail of the flow solution and hence its accuracy depend on the spacing of the grid points. In flow areas where a rapid change of flow variables is anticipated it is necessary that the spacing of the grid points is minimized and consequently, the number of grid points be increased to capture the changes in flow behavior accurately.

In theory, a numerical method that is used should approach a continuum representation of the equation that govern the flow and a zero discretization error as the grid spacing tends to zero (Versteeg and Malalasekera, 2007). In other words, as the mesh is refined, the solution should become less sensitive to the grid spacing and should approach the continuum solution. This is called grid convergence. The grid convergence study is a useful procedure for determining the level of discretization error existing in a CFD solution. A spatial grid convergence study was, therefore, necessary in this project.

4.2.2 Iterative convergence error

Iterative convergence errors are due to truncating the iteration sequence of the solution. That is, iterative convergence errors develop due to the fact that the iterative methods used in the simulation must have a stopping point. In theory the final solution exactly satisfies the discretized flow equations in the interior of the domain and the specified conditions on its boundaries (Versteeg and Malalasekera, 2007). The iteration sequence begins with an initial guess and ideally tends/converges to the final solution and it is said to be convergent when the difference between the final solution and current solution after k iterations is sufficiently small. Factors which strongly dictate truncation of the iteration sequence are solution accuracy, computational resources and time. Therefore, an intelligent decision was necessary when truncating the iteration sequence, to optimize solution accuracy, computational resources and time. Residuals were used as a metric to judge the overall quality of the simulation (convergence) with the best practice demand for convergence of at least the order of 10^{-3}.

4.3 Verification method

The strategy of verification is to identify and quantify the error in a computational model and its solution. Figure 4.2 depicts that the verification process primarily relies in the comparison of the computational solution to the correct answer, which is provided by highly accurate solutions, i.e., the solution of the computational model is compared to the solution of the conceptual model in the form of exact or highly accurate numerical solutions.

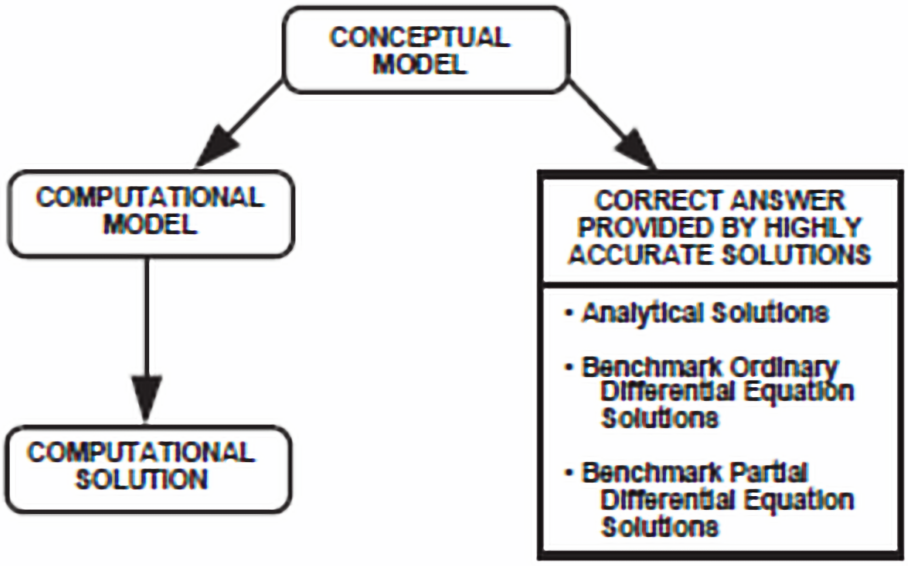

Figure 4.2: Verification test (AIAA, 1998; Oberkampf and Trucano, 2002).

According to AIAA (1998) and Oberkampf and Trucano (2002) highly accurate solutions are only available for simplified model problems. Roache (1997) proposed *a posteriori* verification method and in his paper he motivates his endevour in this direction by stating that a useful *a priori* error estimation is not possible for non-trivial fluid mechanics problems.

The verification method proposed by Roache (1997) is a Grid Convergence Index (GCI) that is based on a generalized Richardson Extrapolation that involves a comparison of discrete solutions at two or more different grid spacings. Therefore, as a requirement for a GCI study, the solution for an engineering quantity of interest should be obtained on two or more grids with different grid spacings. Roache (1997) suggested two or more, successive, levels of mesh refinements[2], where, presumably, the mesh with the least grid spacing (finest mesh) will be employed in the CFD

[2] According to Roache (1997) starting out with a fine mesh and employing two or more, successive, levels of mesh coarsening will also serve the same purpose.

study. The Richardson extrapolation uses the discrete solutions of engineering quantities that are obtained on two or more grids with different grid spacings to calculate for the expected numerically exact value of the engineering quantities. The exact numerical value is an estimate of the continuum solution[3] for the engineering quantities of interest.

4.3.1 Richardson Extrapolation

The Richardson Extrapolation assumes that the discrete solution, f, has a series representation, in the grid spacing h, as shown in equation 4.2.

$$f = f_{h=0} + g_1 h + g_2 h^2 + g_2 h^2 + ... \tag{4.2}$$

$f_{h=0}$ is the estimation of the numerically exact value obtained with a zero grid spacing. The functions g_1, g_2 and so on are defined in the continuum and do not depend on any discretization (Roache, 1997). After some mathematical manipulations, we arrive at an expression that enables the calculation of $f_{h=0}$ as shown in equation 4.3. Equations 4.3 and 4.4 assume that increasing indexes correspond to mesh coarsening, i.e., f_1 is the numerical solution obtained for the fine grid with grid spacing h_1, f_2 is the numerical solution obtained for the intermediate grid with grid spacing h_2 and f_3 is the numerical solution obtained for the coarse grid with grid spacing h_3.

$$f_{h=0} \cong f_1 + \frac{f_1 - f_2}{r^p - 1} \tag{4.3}$$

$r = h_2/h_1$ is the refinement factor between the coarse and the fine grid and p is the formal order of convergence for the numerical algorithm (discretization scheme) that is used. According to Alliance (2018) the numerical algorithm used in CFD provides a theoretical (formal) order of convergence however, the boundary conditions, numerical models and grid are likely to reduce this order so that the observed order of convergence is lower. A more direct evaluation of p is obtained from three discrete solutions using a constant grid refinement ratio, $r = h_2/h_1$, as shown by equation

[3]The CFD solution that would be obtained if an infinitely fine mesh was employed.

4.4.

$$p = \ln(\frac{f_3 - f_2}{f_2 - f_1}) / \ln r \tag{4.4}$$

However, in the case of a GCI study that only uses two discrete solutions, theoretical order of convergence is to be used.

A fine-grid Richardson error estimator approximates the error in a fine-grid solution, f_1, by comparing this solution to that of an infinitely fine grid and is defined by equation 4.5.

$$E = F_s \times \frac{f_{h=0} - f_1}{f_{h=0}} \tag{4.5}$$

F_s is a safety factor. According to Roache (1997) $F_s = 1.25$ is the recommended safety factor for high-quality studies that employ three or more grid solutions while $F_s = 3$ is recommended for studies that employ only two grid solutions.

4.4 Validation

Validation is the process of determining the degree to which a model is an accurate representation of the real world from the perspective of the intended uses of the model (AIAA, 1998; Oberkampf and Trucano, 2002; Versteeg and Malalasekera, 2007). The strategy of validation is the identification and quantification of error and uncertainty in the conceptual and computational models. According to AIAA (1998); Oberkampf and Trucano (2002) and Versteeg and Malalasekera (2007), uncertainty is a potential deficiency in any phase or activity of CFD modeling and simulation that is caused by lack of knowledge. That is, there are always possibilities that inaccuracies can arise in CFD modeling and simulation due to a lack of knowledge about the physical processes that make up a model.

There are four sources of uncertainty that may be present in this CFD study, namely, due to limited information or approximate representation of geometry, boundary conditions, fluid properties and physical model. Uncertainties due to limited information or approximate representation of geometry, boundary conditions and fluid properties are collectively called input uncertainties and they are associated with the discrep-

ancy between the real flow and the problem definition within a CFD model. Uncertainties that involve the physical model are refered to as physical model uncertainties and are associated with the discrepancy between the physical proccess in the real flow and the flow described by a physical model in CFD. Uncertainty is a potential deficiency and hence may or may not exist. In this project, it was, therefore, pivotal that the necessary caution is exercised when defining a flow problem within CFD.

4.4.1 Geometry modeling uncertainty

Modeling of geometry involves the use of CAD tools. According to Versteeg and Malalasekera (2007), when it comes to design work, manufacturing tolerances will always amount to discrepancies between the design intent and manufactured parts, since it is impossible to manufacture parts exactly to the design specifications. Although, often, insignificant, discrepancies may be introduced when the CAD model is converted into a CFD model [4]. On the other hand, significant errors may be introduced in the geometry(CAD model) by a discrepancy between the CFD model (imported) and its discrete representation after meshing. The boundary shape of the CFD model after meshing is a discrete representation (e.g straight lines and curves) of the real boundary shape or the boundary shape of the CFD model that has been imported. Therefore, the geometry within the CFD model may be slightly different from the manufactured part. As a point of caution for this CFD study, this form of uncertainty may be minimized by employing sufficiently low tolerances in the geometric modeling phase and when importing the CAD file into CFD and with sufficient grid refinements near the geometry boundary.

[4] According to Versteeg and Malalasekera (2007), the model in the CFD package may differ slightly from the design intent and the manufactured part. Similar comments apply to the surface roughness.

4.4.2 Boundary condition uncertainty

Apart from the shape and surface state of solid boundaries, it is necessary to specify the conditions for all flow variables on its surface, e.g. inlet velocity, turbulence intensity, pressure etc. According to Versteeg and Malalasekera (2007), it can be difficult to acquire this type of input to a high degree of accuracy. Uncertainty as a result of boundary conditions can arise for the following reasons:

- Boundary conditions are chosen from a limited set of boundary conditions available on the commercial CFD package, therefore, assumed/chosen boundary conditions may only be approximately true.
- The incompatibility between chosen boundary conditions.
- The incompatibility between the chosen open boundary (i.e., inlets and outlets) condition type and available flow information.
- The location of open boundaries. The location of open boundaries must be sufficiently far from the area of interest so that the flow in this region is not affected [5].

As a point of caution for this CFD study, this form of uncertainty may be minimized by the availability of relevant/sufficiently approximate boundary types in a CFD package, the correct use of the relevant/sufficiently approximate boundary types and the adequacy of the available free stream boundary conditions to describe the free stream conditions of the real flow.

4.4.3 Fluid property uncertainty

The uncertainty that arises in this category depends on the extent of the accuracy in the assumptions made on fluid properties (i.e. density). According to Versteeg and

[5] While this is an important consideration, solution economy dictates that the domain should not be excessively large thus a compromise must be found.

Malalasekera (2007), the often used constant fluid property assumption which favors solution economy may compromise solution accuracy. This is because in a real flow, fluid properties are never constant and hence the assumption is only approximately true i.e., it considers the changes in fluid properties to be insignificant. All the flow cases that were considered in this CFD study were at low aerodynamic speeds that are below a Mach number of 0.3. The constant density or incompressible flow assumption was made. According to Anderson (2010), this fluid property assumption is justified for low-speed aerodynamic flow below a Mach number of 0.3, where fluid compressibility effects are insignificant.

4.4.4 Physical model uncertainty

Physical model uncertainties are inaccuracies that arise as a result of the discrepancies between real flows and CFD due to inadequate representation of the physical processes (e.g. transition and turbulence) or due to simplifying assumptions in the modeling process (e.g. incompressible and steady flow).

The CFD modeling of complex flow phenomena such as transition and turbulence makes use of semi-empirical models which encapsulate the best scientific understanding of the complex physical processes. According to Versteeg and Malalasekera (2007); Wilcox (2006), the semi-empirical models contain adjustable constants derived from high-quality measurements on a limited class of flows. Uncertainties may arise in the application of the physical models to flows which do not fall within the range of flows for which it has been calibrated and thus extrapolating beyond the range of the experimental data. The literature review on the physical flow phenomena encountered in sailplane flight and also its modeling in CFD, as presented in chapters 2 and 3, respectively, was intended to minimize this form of uncertainty. The Menter (1992c) SST $k-\omega$ turbulence and $\gamma - Re_\theta$ transition model was justified to model the transitional and turbulent flows considered in this project.

Inaccuracies can also arise in the application of the physical models for which simplifying assumptions have been made to favor solution economy. Simplifying assump-

tions are commonly used in the exercise of CFD modeling and they greatly reduce the complexity of a problem and favor solution economy. A physical model that contains assumptions has limited validity and the use of such models to simulate real-life phenomena must be justified. The steady-state flow assumption was made in all the flow cases in this CFD study. This assumption considers that flow variables, viz., velocity and pressure are not changing with respect to time. Sailplane flight takes place at consant pressure environments with insignificant changes in velocity with respects to time, therefore, the flow steadiness assumption is justified.

4.5 Validation method

The method of measuring the accuracy of the representation of the real world is achieved by systematically comparing CFD simulations with experimental data (AIAA, 1998; Oberkampf and Trucano, 2002; Versteeg and Malalasekera, 2007). Thus, the validation process relies primarily on experimental data as depicted in 4.3. This does not imply that all experimental data has high accuracy. According to AIAA (1998) and Oberkampf and Trucano (2002), experimental data may contain errors, therefore, if available, the estimate of the magnitude of the experimental uncertainty must be included in the comparison with the computer simulations.

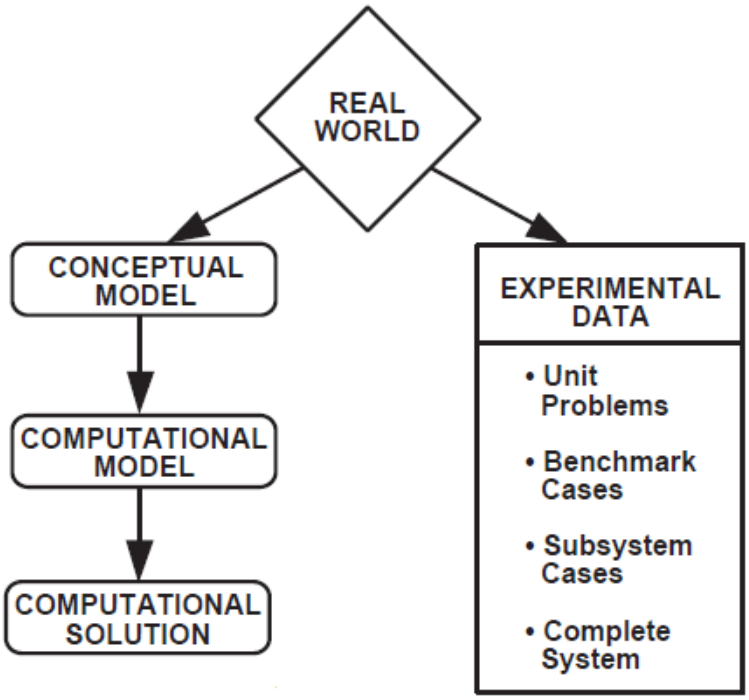

Figure 4.3: Validation test (AIAA, 1998; Oberkampf and Trucano, 2002).

Furthermore, AIAA (1998); Oberkampf and Trucano (2002) and Versteeg and Malalasekera (2007) states that a meaningful validation is only possible in the presence of good quantitative estimates of numerical errors, input uncertainty and uncertainty of the experimental data used in the comparison. If the difference between the computed and the experimental results is sufficiently small the CFD model is considered to be validated.

This study employed a building block validation approach which closely resembles the recommended validation method by AIAA (1998) and Oberkampf and Trucano (2002). The recommended approach by AIAA (1998) and Oberkampf and Trucano (2002) divides the complex engineering system of interest into three progressively simpler phases,, viz., the subsystem phase, the benchmark phase and the unit problems phase as shown in figure 4.4.

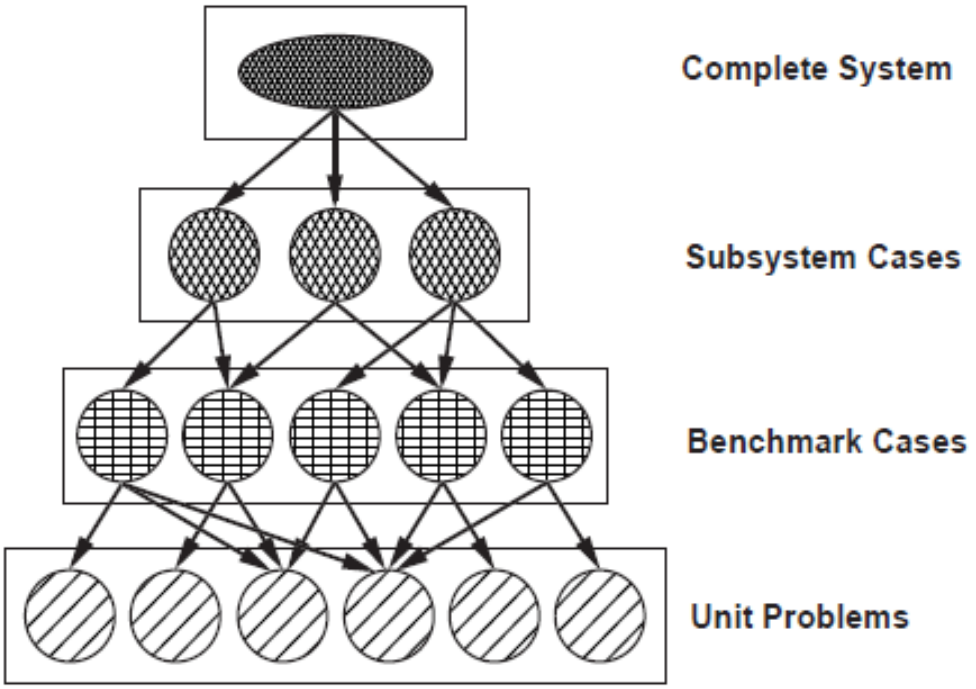

Figure 4.4: Validation phases (AIAA, 1998; Oberkampf and Trucano, 2002)

Each phase of the process represents a different level of flow physics coupling and geometrical complexity while the complete system consists of the actual system for which a validated tool is needed.

In the complete system, the entire geometry with complete flow physics is considered thus all the geometric and flow physics effects occur simultaneously (AIAA, 1998). Subsystem cases represent the first decomposition of the actual system into simplified flow paths and each of the considered cases exhibit restricted geometric or flow features compared to the complete system. AIAA (1998) states that the flow physics of the complete system may be well represented in this phase but the level of coupling between flow phenomena is typically reduced and the quality and the quantity of the data are usually significantly better than the complete system. Benchmark cases represent another level of successive decomposition of the complete system. For these cases, separate hardware is fabricated to represent key features of each subsystem. According to AIAA (1998) the benchmark cases are geometrically simpler and the

flow physics simpler/comparable to those at the subsystem level. Unit problems represent a total decomposition of the complete system and are characterized by very simple geometries and flow physics.

Each phase of the validation process emphasizes the assessment of certain features in the CFD model (AIAA, 1998). The strategy in this approach is the assessment of how accurately the computational results compare with the experimental data (with quantified error estimates) at multiple levels of complexity.

A CFD study was conducted in this project, to investigate the influence of a turbulent wake flow on the fin of the JS-1 sailplane. Based on the literature review in chapters 2 and 3, the implementation of the SST $k-\omega$ turbulence and $\gamma - Re_\theta$ transition model was considered to model the flow physics, i.e., transitional and turbulent wake flow, over the JS-1 sailplane. As a necessary step, the SST $k-\omega$ turbulence and $\gamma - Re_\theta$ transition model had to be validated to justify its use and to certify confidence in its ability to accurately represent the flow physics. The validation process that was employed in this project was aimed at validating the SST $k-\omega$ turbulence and $\gamma - Re_\theta$ transition model for a steady-state, three-dimensional, transitional and turbulent wake flow of an incompressible fluid on the JS-1 sailplane at low-Reynolds number and low-turbulence level. The validation process employed three levels of decomposition of the complete engineering system that was to be validated. The complete system was decomposed into a single subsystem case, three benchmark cases and three unit problems. Figure 4.5 describes the validation process that was employed in the current project.

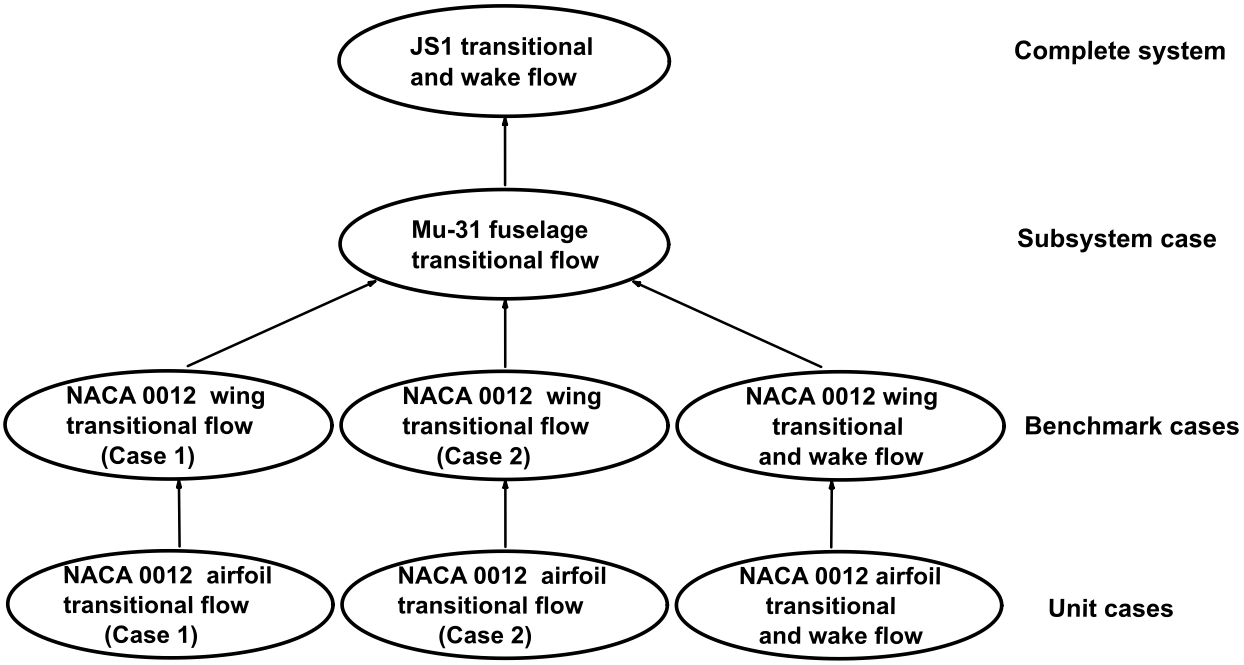

Figure 4.5: Validation phases.

4.5.1 Complete system case

The complete system case was for a steady-state, three-dimensional, transitional and turbulent wake flow of an incompressible fluid on the fin of the JS-1 sailplane at low-Reynolds number and low-turbulence level was considered. The validation focused on streamlines on the JS-1 fin. The oil flow free-flight experimental results that were obtained from the Jonker Sailplane company, was the only source of data that was available for comparison with CFD. The oil flow free-flight experiment is not of scientific value since the experiment was not conducted in a controlled environment, i.e., wind tunnel, and hence the results may be susceptible to error. Although this may be true, it was anticipated that the error may not be so significant as to reveal boundary layer phenomena on the fin that are completely erroneous. While the extent of the observed boundary layer phenomena cannot be quantified, the results convincingly show that it exists to some extent on the JS-1 fin. The comparison was, therefore, a qualitative validation of the computational results. The analysis of the oil flow free-flight experimental results on the JS-1 fin revealed the existence of

a turbulent wake as a result of the boundary layer flow from the fuselage and wing-fuselage junction as mentioned in chapter 1. Therefore, the SST $k-\omega$ turbulence and $\gamma - Re_\theta$ transition model will be sufficiently validated for a transitional and turbulent wake flow on the JS-1 provided that the CFD results correspond in a fundamental manner with the experimentally observed boundary layer phenomena on the JS-1 fin.

4.5.2 Subsystem case

The first level of decomposition considered a steady-state, three-dimensional, transitional flow of an incompressible fluid on the fuselage of the Mu-31 sailplane at low-Reynolds number and low-turbulence level. The engineering quantity of interest was the fuselage and wing drag coefficient (interference drag). Flow streamlines on the fuselage, wing and wing-fuselage junction were also considered. The experimental data by Hulsmann (2006) was consulted for validation. The experimental data was acquired using the low-speed and low turbulence wind tunnel of Delft University of Technology. Measurements were made for a Reynolds number of 1.5 million based on the airfoil chord length of 0.26 m. The wind tunnel turbulence levels were not measured, however, according to Hulsmann (2006), a low degree of turbulence range of 0.002% - 0.1% can be achieved in the wind tunnel test section. Based on previous work from authors such as Bosman (2012), the turbulence level of 0.07% was chosen, which is within the range of turbulence levels of the low-speed and low turbulence wind tunnel of Delft University of Technology.

4.5.3 Benchmark cases

The second level of decomposition considered three cases.

The first case was concerned with a steady-state, three-dimensional, transitional flow of an incompressible fluid on the NACA 0012 wing at low-Reynolds number and low-turbulence level. The engineering quantities of interest were pressure coefficient,

skin friction coefficient and boundary layer transition points for incidence angles, α = 0, 6 , 10 and 14. The experimental data by Gregory and O'Reilly (1973) was consulted for the validation of pressure coefficient for incidence angles, α = 0, 6 , 10 and 14. The experimental data by Gregory and O'Reilly (1973) did not include skin friction coefficient and transition points and therefore, XFOIL data had to be used for the validation of skin friction coefficient and boundary layer transition points for incidence angles, α = 0, 6 , 10 and 14. The Gregory and O'Reilly (1973) data was acquired using the N.P.L. (National Physical Laboratory) low-speed wind tunnel. The measurements were made for a Mach number of 0.16 which corresponds to a free stream velocity of 54.88 m/s and Reynolds number of 2.88 million. The wind tunnel operates at a turbulent intensity range of 0.05% to 0.2% corresponding to a speed range of 8 m/s to 70 m/s (Bradshaw and Ferris., 1963). The turbulence level of the wind tunnel was unknown and therefore, an XFOIL analysis was to be conducted to determine the turbulence levels that best correspond to the Gregory and O'Reilly (1973) data. According to Drela, M & Youngren A.H (2003) and Deperrois (2010) XFOIL data has been thoroughly tested against other software and published experimental results with much success and is, therefore, a trustworthy low-speed aerodynamics preliminary aircraft design tool. The current study, justified by XFOIL, estimates that the turbulence levels corresponding to the Gregory and O'Reilly (1973) data is 0.2%.

The second case was concerned with a steady-state, three-dimensional, transitional flow of an incompressible fluid over the NACA 0012 wing at low-Reynolds number and low-turbulence level. The engineering quantities of interest were lift coefficient and drag coefficient for a range of incidence angles (α) viz., $0 < \alpha < 16$. The experimental data by Shelda R.E. and Klimas, P.C. (1981) and Ladson (1988) was consulted for validation purposes. The experimental data was acquired from low-speed wind tunnels with low-turbulence levels, for free transitional flows. The Shelda R.E. and Klimas, P.C. (1981) data was acquired using the Walter H. Beech Memorial Wind Tunnel at the Wichita State University. The measurements were made for a Mach number of 0.15 which corresponds to a free stream velocity of 51.54 m/s, and a

Reynolds number of 2 million. The wind tunnel operates at a turbulence intensity of 0.11% (Wichita State University, 2008). The Ladson (1988) data was acquired using the NACA Langley Low-Turbulence Pressure Tunnel. The measurements were made for a Mach number of 0.15 ($\approx$ 51.54 m/s) and Reynolds number of 2 million. The turbulence level of the tunnel was unknown at the time that the test program was conducted, however there were indications that it had increased from the original low level measured in the early 1940's as a result of successive damage to the heat exchanger as well as deterioration of the measuring screens (Ladson, 1988:2). According to von Doenhoff, A.E. and Frank T.A. (1947), the original turbulence level measurements were 0.01% - 0.02% . The values of the aerodynamic coeffiecients obtained by Ladson (1988) are close to those obtained by Shelda R.E. and Klimas, P.C. (1981) for the same Reynolds number (see Table A.1 in Appendix A) thus we expect the turbulence level of the Ladson (1988) data to be close to 0.1%. Furthermore, an XFOIL analysis was conducted to determine the turbulence levels that best corresponds to the Ladson (1988) data. The current study, justified by XFOIL, estimates that the turbulence levels for the Ladson (1988) data to be 0.1%. For comparison, the lift coefficient and drag coefficient data by data by Shelda R.E. and Klimas, P.C. (1981),Ladson (1988) and XFOIL are tabulated in Table A.1 in Appendix A and as observed there is a good correlation between the presented data.

The third case was concerned with a steady-state, three-dimensional, transitional and turbulent wake flow of an incompressible fluid on the NACA 0012 wing at low-Reynolds number and low-turbulence level. The engineering quantities of interest were the mean velocity and turbulence stress (**uu**, **vv**, **ww** and **uv**) in the wake. The experimental data by Hah and Lakshminarayana (1982) was consulted for validation purposes. The Hah and Lakshminarayana (1982) data was acquired using the subsonic wind tunnel at the Pennsylvania State University. The measurements were made for a Mach number of 0.088 , which corresponds to free stream velocity of 30 m/s and a Reynolds number of 0.38 million and a turbulence intensity of 0.2%. The wake profiles for the mean velocity and turbulence stresses were measured at $x/c = 0, 0.28, 0.94$ and 1.5 from the trailing edge for incidence angles, α, of 3, 6 and

9 degrees. The present wake validation case deals with the near, intermediate and the far wake. At an α of 3 degrees, x/θ = 0, 111, 372 and 593 which corresponds to x/c = 0, 0.28, 0.94 and 1.5 for θ = 0.506 mm. At an α of 6 degrees, x/θ =0, 82, 276 and 440 which corresponds to x/c = 0, 0.28, 0.94 and 1.5 for θ = 0.682 mm. At an α of 9 degrees, x/θ =0, 60, 203 and 324 which corresponds to x/c = 0, 0.28, 0.94 and 1.5 for θ = 0.926 mm.

4.5.4 Unit cases

The third level of decomposition was composed of three cases. This final level of decomposition was in effect a decomposition of the three benchmark cases that were previously investigated, to consider them on a two-dimensional flow level.

The first case was concerned with a steady-state, two-dimensional, transitional flow of an incompressible fluid on the NACA 0012 airfoil at low-Reynolds number and low-turbulence level. The engineering quantities of interest were lift coefficient and drag coefficient for a range of incidence angles (α) viz., $0 < \alpha < 16$ and the experimental data by Shelda R.E. and Klimas, P.C. (1981) and Ladson (1988) was consulted for validation purposes.

The second case was concerned with a steady-state, two-dimensional, transitional flow of an incompressible fluid on the NACA 0012 airfoil at low-Reynolds number and low-turbulence level. The engineering quantities of interest were pressure coefficient, skin friction coefficient and boundary layer transition points for incidence angles, α = 0, 6 , 10 and 14. The experimental data by Gregory and O'Reilly (1973) was consulted for the validation of pressure coefficient for incidence angles, α = 0, 6 , 10 and 14 and XFOIL data was used for the validation of skin friction coefficient and boundary layer transition points for incidence angles, α = 0, 6 , 10 and 14.

The third case was concerned with a steady-state, two-dimensional, transitional and turbulent wake flow of an incompressible fluid on the NACA 0012 airfoil at low-Reynolds number and low-turbulence level. The engineering quantities of interest were the mean velocity and turbulence stress (**uu**, **vv** and **uv**) at the wake and the

experimental data by Hah and Lakshminarayana (1982) was consulted for validation purposes.

Summary

This chapter covered the approach to the current CFD study. The major factors that may influence the CFD results in this study were highlighted and points of caution were given. The verification and validation method that was employed in the present CFD study was also presented.

Chapter 5

2D airfoil and 3D wing validation

Introduction

This chapter presents the first and second step of the validation process that was employed in this project. A validation of the unit and benchmark cases is presented, viz., a two-dimensional flow validation case for the NACA 0012 airfoil and a three-dimensional flow validation case for the NACA 0012 wing. The SST $k-\omega$ turbulence and $\gamma - Re_\theta$ transition model was validated in the 2D and 3D validation studies. Section 5.1 introduces the requirements for the 2D and 3D validation studies. Section 5.2 presents the geometric modeling. Section 5.3 presents the validation setup for the 2D and 3D studies with the computational domain configuration, computational mesh configurations, flow physics and solver set up and convergence criterion in subsections 5.3.1, 5.3.2, 5.3.3 and 5.3.4, respectively. Section 5.4 presents the results and discussion for the validation. The results for the three validation cases are given in subsections 5.4.1, 5.4.2 and 5.4.3, respectively.

5.1 Validation requirements

The purpose of the 2D validation study was to validate a steady-state, two-dimensional, transitional and turbulent wake flow of an incompressible fluid on the NACA 0012

airfoil at low-Reynolds number and low-turbulence level. The purpose of the 3D validation study was to validate a steady-state, three-dimensional, transitional and turbulent wake flow of an incompressible fluid on the NACA 0012 wing at low-Reynolds number and low-turbulence level. For both the 2D and 3D validation studies, the SST $k-\omega$ turbulence model with the $\gamma - Re_\theta$ transition model was validated against well approved and accepted experimental and XFOIL analysis data. The following reasons motivated the choice of the NACA 0012 airfoil and wing for the 2D and 3D validation studies:

- Availability of airfoil co-ordinates. The airfoil co-ordinates were obtained from Tools (2018)
- The NACA 0012 airfoil/wing has been extensively studied experimentally and has a broad spectrum of low-Reynolds number and low-turbulence level wind tunnel experimental data on boundary layer and turbulent wake flows. Only low-Reynolds number and low-turbulence level wind tunnel data are relevant for comparison in preliminary sailplane design because sailplanes fly under low-Reynolds numbers and turbulence level. Experimental data by Gregory and O'Reilly (1973); Hah and Lakshminarayana (1982); Ladson (1988) and Shelda R.E. and Klimas, P.C. (1981) were consulted.
- The NACA 0012 airfoil/wing is a laminar flow airfoil and thus has sufficiently large regions of laminar flow over its surfaces at low-Reynolds numbers and low-turbulence level. This is important in a study that is interested in flow transition and its consequent influence on the flow evolution and aerodynamic coefficient. The NACA 0012 airfoil/wing is, therefore, relevant to test the $k-\omega$ SST turbulence model along with the $\gamma - Re_\theta$ transition model.

A requirement for the 2D and 3D validation studies was that the calculated aerodynamic coefficient had to be in good agreement in characteristics/behavior and quantity with the baseline data. The engineering quantities of interest for comparison are as follows:

- Lift coefficient (C_l) vs angle of attack (α) for $0 < \alpha < 16$ at a Reynolds number of 2 million.
- Drag coefficient (C_d) vs angle of attack (α) for $0 < \alpha < 16$ at a Reynolds number of 2 million.
- Surface pressure coefficient (C_p) vs chordwise distance (x/c) for α = 0, 6, 10 and 14 at a Reynolds number of 2.88 million.
- Surface skin friction coefficient (C_f) vs chordwise distance (x/c for α = 0, 6, 10 and 14 at a Reynolds number of 2.88 million.
- Onset transition points for α = 0, 6, 10 and 14 at a Reynolds number of 2.88 million.
- Mean velocity and turbulence stresses (viz., **uu**, **vv**, **ww** and **uv**) at the wake for α = 3, 6 and 9 at a Reynolds number of 0.38 million.

5.2 Geometric modeling

The NACA 0012 airfoil and NACA 0012 wing that were employed in the 2D and 3D validation studies are shown in figures 5.1a and 5.2b, respectively.

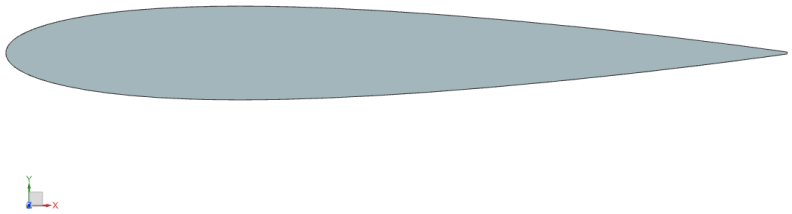

(a) NACA 0012 wing section.

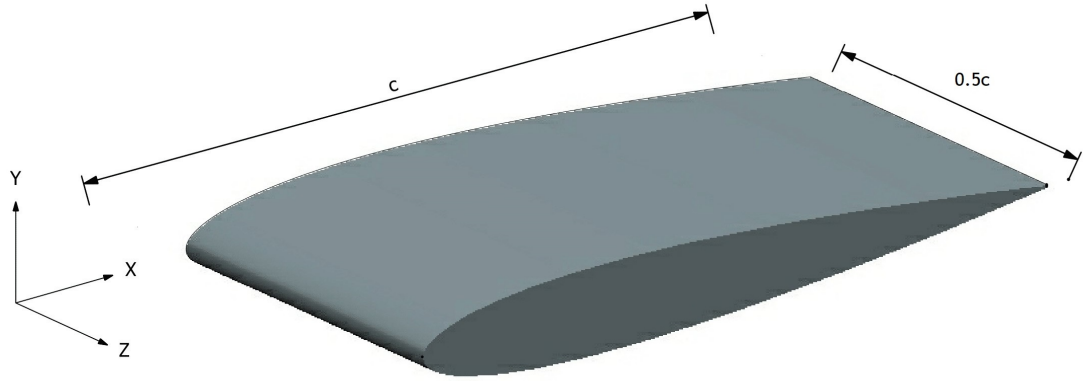

(b) NACA 0012 wing.

Figure 5.1: Geometry under consideration for the 2D and 3D validation studies.

The geometries that were considered in the 2D and 3D validation studies are simple and therefore, only a customized tesselation of the imported surface mesh and automatic surface repair operation was used to prepare the surface for the mesh generation process.

5.3 Validation setup

5.3.1 Computational domain configuration

All CFD problems are defined in terms of initial and boundary conditions [1] and it is, therefore, important that physically realistic and well-posed initial and boundary conditions are supplied. The most common cause of rapid divergence of CFD simulations and incorrect CFD solutions is the inappropriate selection of initial and boundary conditions (Versteeg and Malalasekera, 2007)

A rectangular computational domain was employed in both the 2D and 3D validation studies. A computational domain sensitivity study was conducted to determine the optimal domain size to be employed in all the CFD studies. The domain size was in favor of core mesh cell economy and solution accuracy. The domain sensitivity study is presented in section B.1 in Appendix B. The respective rectangular computational domains with dimensions and boundary conditions are given in figure 5.2.

[1] The flow inside a computational domain is driven by initial and boundary conditions (Versteeg and Malalasekera, 2007).

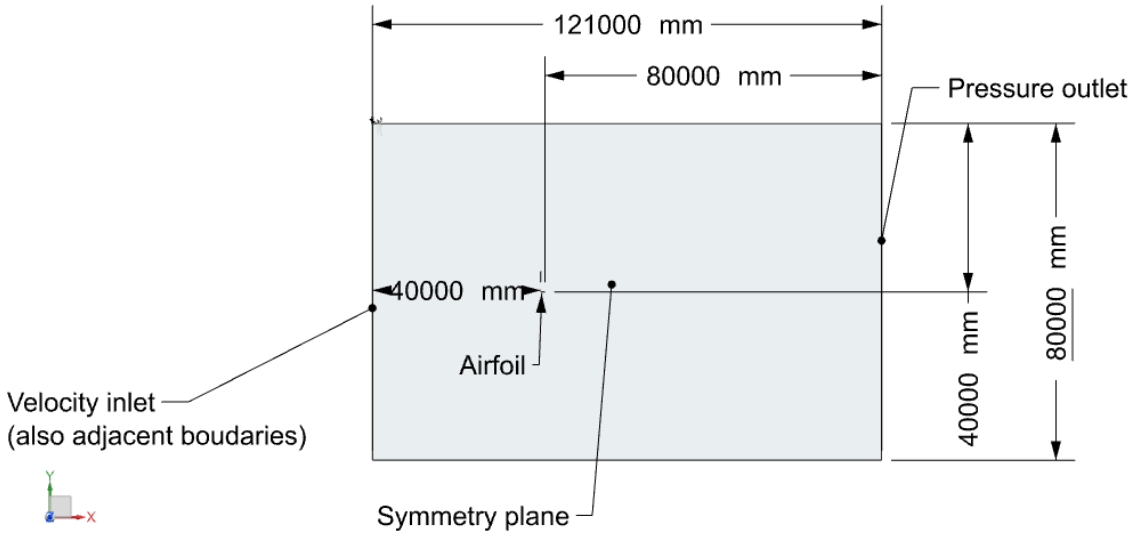

(a) NACA 0012 airfoil computational flow domain configuration.

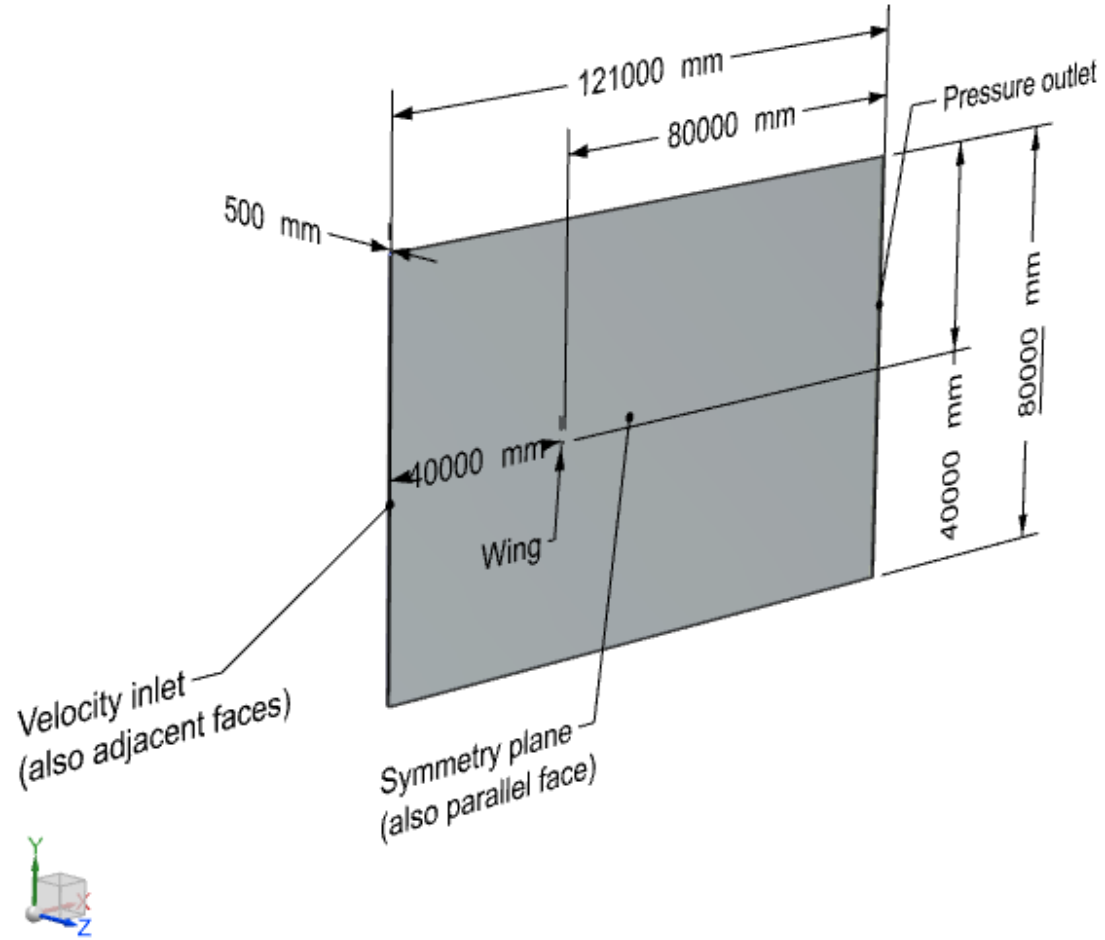

(b) NACA 0012 wing computational flow domain configuration.

Figure 5.2: Computational flow domain configuration with boundary conditions for 1000 mm chord length NACA 0012 airfoil and wing.

The computational flow domain was divided into four boundary types for both the 2D and 3D validation studies. The velocity inlet, pressure outlet, symmetry and wall boundary were used with different conditions imposed on them to accurately model the flow setup by Gregory and O'Reilly (1973); Hah and Lakshminarayana (1982); Ladson (1988) and Shelda R.E. and Klimas, P.C. (1981).

A velocity inlet boundary condition was imposed on the upstream and far field boundaries of the computational domain while the pressure outlet boundary condition was imposed on the downstream boundary of the computational domain[2].

The prescribed inlet boundary conditions were set to approximate the free stream flow conditions that were employed in the wind tunnel tests by Gregory and O'Reilly (1973); Hah and Lakshminarayana (1982); Ladson (1988) and Shelda R.E. and Klimas, P.C. (1981). The magnitude of the initial velocity was set as 51.54 m/s, 54.88 m/s and 30 m/s corresponding to $Mach = 0.15$, 0.16 and 0.088 for the respective validation cases that were considered. The direction of flow was set in the x-direction (1,0,0) for zero angle of attack[3] and was changed by rotating the flow direction about the z-axis.

The symmetry boundary was imposed on the plane of the NACA 0012 airfoil in the 2D validation study and on the sides of the rectangular domain in the 3D validation study, to approximate the infinite nature of the wing.

The no-slip wall boundary condition was imposed on the NACA 0012 airfoil and inifinite wing surfaces to approximate the no fluid slip physical state (i.e., zero velocity) of the flow at the surfaces of the airfoil and wing.

[2]The inlet and outlet boundary conditions are commonly imposed on the upstream, farfield and downstream boundaries for incompressible flows ($Mach < 0.3$) (Ewing, 2015).

[3]The NACA 0012 airfoil and NACA 0012 wing is aligned with the flow direction for zero degrees angle of attack.

5.3.2 Computational mesh configuration

The best practice guidelines provided by Ewing (2015) were closely followed in the mesh procedure for best results. An unstructured 2D and 3D, finite volume, core mesh and prism layer mesh was employed to discretize the computational domain for the respective 2D and 3D validation studies. The core mesh was made up of triangular cells in the 2D validation study while the core mesh was made up of tetrahedral cells in the 3D validation study. The prism layer mesh comprised of prismatic cells. A part-based meshing procedure was executed in STAR-CCM+ for both the 2D and 3D validation studies.

In order to accurately capture important details of the flow, mesh refinements were introduced in specific areas in the computational domain while coarse cells were introduced in areas of less concern to achieve core mesh cell economy.

The core mesh cell density was increased at the leading and trailing edges of the airfoil and wing, around the airfoil and wing surfaces and in the wake region downstream of airfoil and wing to capture the sharp changes in flow variables that are expected in those regions. The core mesh was set to be coarse in areas where sharp changes in flow variables were not expected. These areas include the velocity inlet and pressure outlet boundaries. Prismatic cells were introduced to resolve the boundary layer in close proximity to the airfoil and wing surfaces where viscosity effects are expected to exist.

Figure 5.3 shows the compuational mesh configuration for the 2D and 3D validation studies.

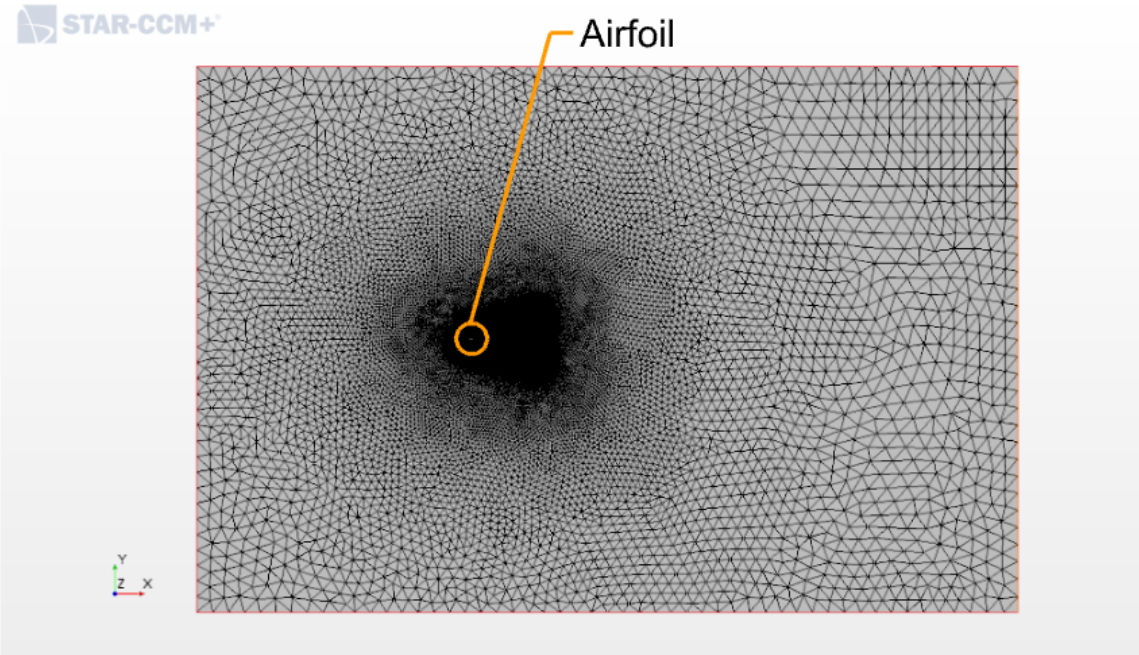

(a) Mesh configuration for the NACA 0012 airfoil flow domain.

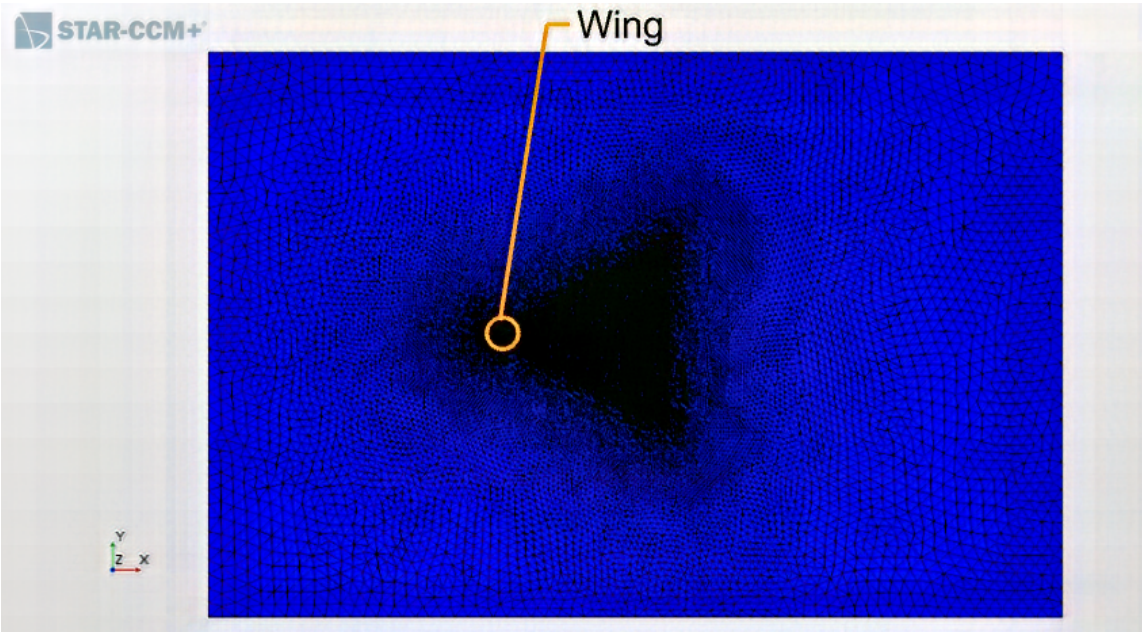

(b) Mesh configuration for the NACA 0012 wing flow domain.

Figure 5.3: Computational mesh configuration for the NACA 0012 airfoil and wing flow domains.

Mesh refinements were introduced in the wake region to capture the sharp changes in flow variables downstream of airfoil and wing viz., mean velocity and turbulence stresses (i.e., **uu**, **vv**, **ww** and **uv**) in the wake. The core mesh, downstream of airfoil and wing, was customized to achieve the mesh refinements in the wake. The cell density was set to decrease gradually with distance, away from the airfoil and wing, towards the velocity inlet and pressure outlet as seen in figure 5.3. Figure 5.4 shows the prism layer and core mesh refinements at the leading edge, trailing edge and around the surface of the NACA 0012 airfoil for a fine mesh.

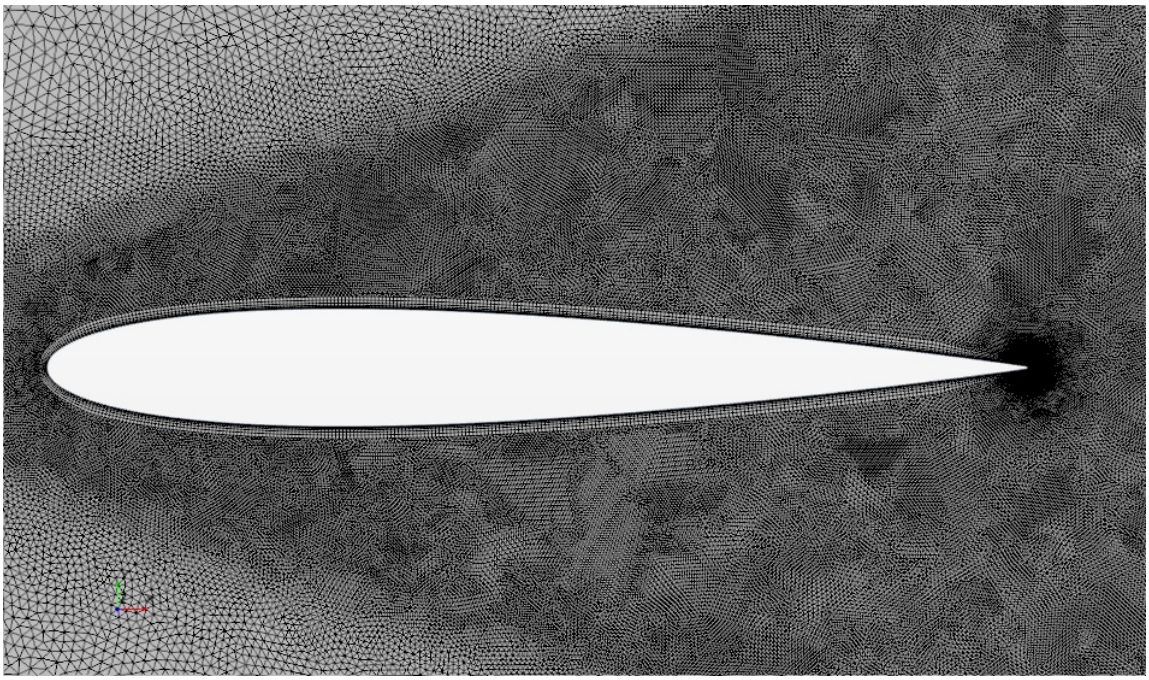

(a) Fine mesh boundary layer.

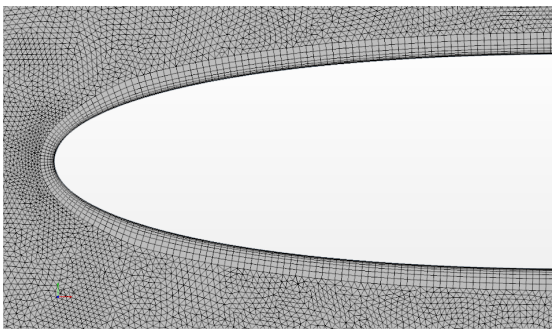

(b) Fine mesh boundary layer at the leading edge.

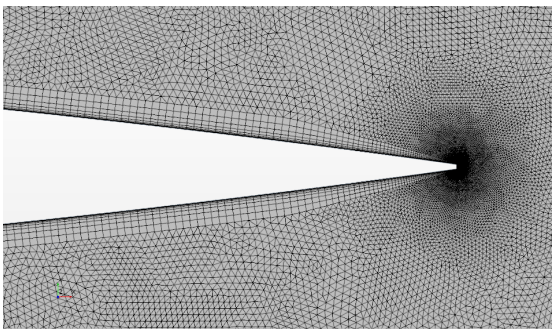

(c) Fine mesh boundary layer at the trailing edge.

Figure 5.4: Fine mesh boundary layers of the NACA 0012 airfoil.

Figures 5.5 and 5.6 show the prism layer and core mesh refinements at the leading edge, trailing edge and around the surface of the NACA 0012 wing for a fine mesh.

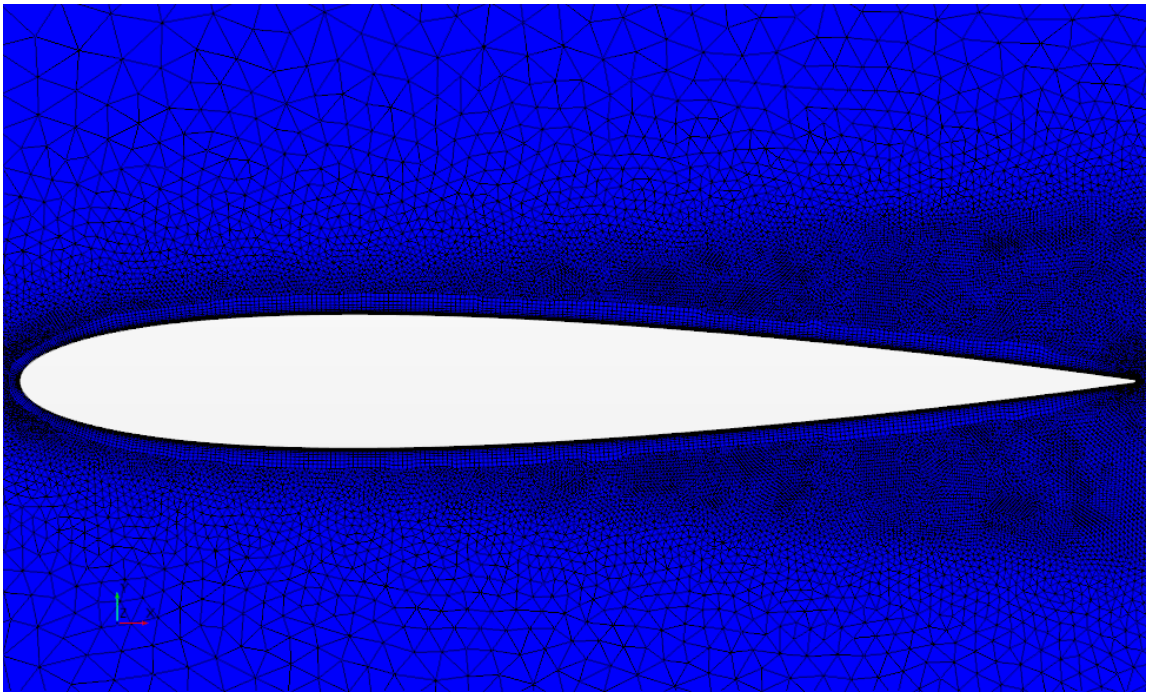

(a) Fine mesh boundary layer.

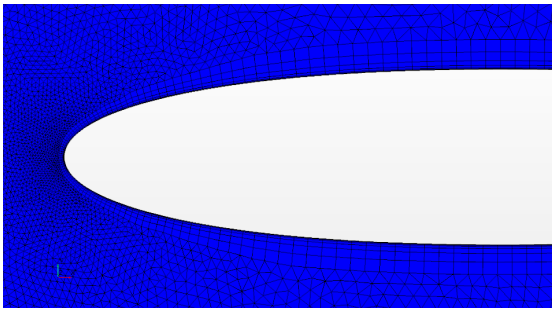

(b) Fine mesh boundary layer at the leading edge.

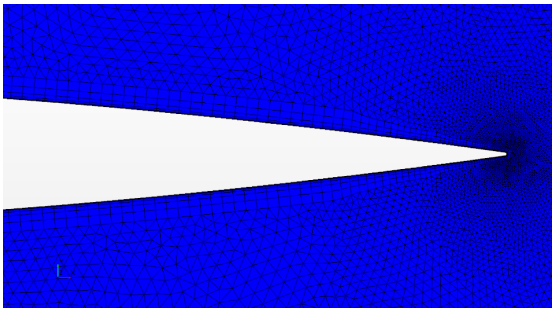

(c) Fine mesh boundary layer at the trailing edge

Figure 5.5: Fine mesh boundary layers of the NACA 0012 wing.

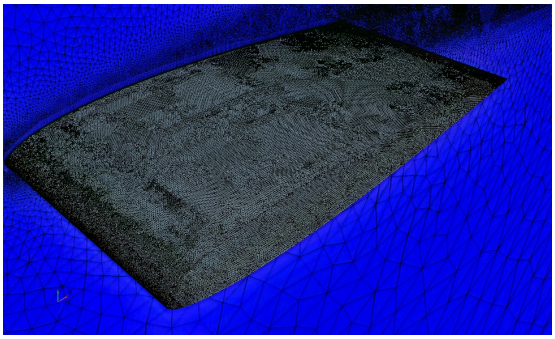

(a) Symmetry plane and wing surface mesh at the leading edge

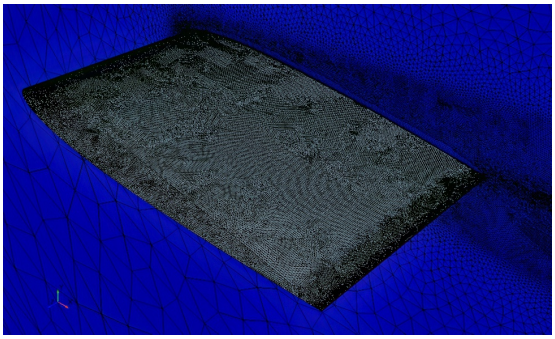

(b) Symmetry plane and wing surface mesh at the trailing edge

Figure 5.6: Symmetry plane and wing surface mesh.

Mesh refinements were introduced at the leading and trailing edges of the airfoil and wing to capture the rapid changes in flow variables expected in those regions. A prism layer mesh model was used to achieve a sufficiently fine mesh around the airfoil and wing boundary layer, i.e., in the viscosity affected region near the airfoil and wing surfaces. Prismatic cells were introduced to resolve the boundary layer. Three important considerations which have implications on the wall y^+ value were made in relation to the boundary layer, viz., the number of prism layers, the boundary layer thickness and the near-wall prism layer cell thickness.

The total thickness of the prism layers, i.e., total boundary layer thickness, was chosen such that all the viscosity effects due to the presence of the airfoil and wing surfaces are captured in the boundary layer. The total thickness of the prism layers was calculated using the flat plate turbulent boundary layer thickness approximation [4] proposed by Schlichting (1978) (also see Anderson (2010); Hermann and Gersten (2017.); Houghton (2012) and Wilcox (2008), viz.,

$$\delta \approx 0.37x/\mathrm{Re}_x{}^{1/5}. \tag{5.1}$$

Re_x is the local Reynolds number at a distance x from a flat plate leading edge.

[4] It is common practice to approximate boundary layer phenomena over an airfoil at zero angle of attack (or small angles of attack) with flat plate boundary layer approximation (Anderson, 2010).

According to Anderson (2010); Hermann and Gersten (2017.); Houghton (2012) and Wilcox (2008) the turbulent boundary layer grows with distance from the leading edge at a rate of $\delta \propto x^{1/5}$, therefore, the furthest distance from the leading edge was used in the calculation. Table 7.1 gives the total boundary layer thickness approximation for each validation case that was considered in the 2D and 3D validation studies.

Table 5.1: Prismatic layer total boundary thickness for the respective validation cases.

Validation cases	**Reynolds number (Re_L)**	**Boundary layer thickness (δ)**
Validation case 1	2.88 $\times 10^6$	0.0189
Validation case 2	2 $\times 10^6$	0.0203
Validation case 3	0.38$\times 10^6$	0.0297

The near-wall prism layer cell thickness was calculated so that a wall y^+ value of less than one ($y^+ < 1$) was achieved in all the simulations that were conducted. In order to capture low-Reynolds number flow effects in the turbulent boundary layer, the viscous/laminar sublayer of the turbulent boundary layer had to be sufficiently resolved and consequently, the wall y^+ value had to be below one. Equation 5.2 was solved iteratively for the desired wall y^+ value (Versteeg and Malalasekera, 2007).

$$y^+ = \frac{y\, u_\tau}{\nu} \tag{5.2}$$

$u_\tau = \sqrt{\frac{\tau_w}{\rho}}$ is the near-wall velocity, $\tau_w = \frac{C_f \rho U_0^2}{2}$ is the wall shear stress, $C_f = 0.058 Re^{-0.2}$ is the skin friction coefficient and y^+ is the target value. All the fluid and flow properties were known.

The number of prism layers, the near-wall prism layer cell thickness and the total boundary layer thickness inform the prism layer cell aspect ratio. The number of

prism layers were chosen to be 24 layers according to best practice guidelines by Ewing (2015). The number of prism layers, boundary layer thickness and near-wall prism layer cell thickness were kept constant in all the simulations.

The refinement and coarsening of the discretized computational domain was achieved by defining a minimum and target cell size at the airfoil and wing surfaces and trailing edge, wake region, velocity inlet, pressure outlet and symmetry plane(s) relative the base size (percentage of base size). The base size for the final computational mesh was set 0.05 and 0.8 of a unit chord length for the 2D and 3D validation studies, respectively. The respective percentages used in the mesh procedure for the 2D and 3D validation studies are presented in Tables 5.2 and 5.3, respectively.

Table 5.2: NACA 0012 airfoil (2D) wind tunnel model mesh configuration percentage values relative to base size.

Refinement	**Minimum size**	**Target size**
Airfoil surfaces	0.1%	1%
Trailing edge	0.01%	0.1%
Wake region	-	1%
Inlet, outlet and symmetry	100%	500%

Table 5.3: NACA 0012 wing (3D) wind tunnel model mesh configuration percentage values relative to base size.

Refinement	Minimum size	Target size
Wing surfaces	0.1%	0.5%
Trailing edge	0.01%	0.08 %
Wake region	-	5 %
Inlet, outlet and symmetry	100	500%

A comparison of the mesh configuration percentage values in Tables 5.2 and 5.3 reveal that a much finer mesh refinement was achieved in the 2D validation study compared to the 3D validation study and therefore, a smaller spatial discretization error was expected in the 2D validation study. Defining the computational mesh values relative to a base size facilitated the grid convergence study which is presented in section B.2 in Appendix B.

5.3.3 Flow physics and solver setup

The Reynolds Averaged Navier-Stokes equations for a two-dimensional, steady-state flow with constant density, coupled with the SST $k-\omega$ turbulence and $\gamma - Re_\theta$ transition model were employed in order to model the air flow over the NACA 0012 airfoil for the 2D validation study. The Reynolds Averaged Navier-Stokes equations for a three-dimensional, steady-state flow with constant density, coupled with the SST $k-\omega$ turbulence and $\gamma - Re_\theta$ transition model were employed in order to model the air flow over the NACA 0012 wing for the 3D validation study.

The SST $k-\omega$ turbulence model requires the specification of the free stream boundary conditions for the turbulent kinetic engergy, k, and specific dissipation rate, ω. The chosen method for specifying the turbulence scales, k and ω, was **turbulent**

intensity + viscosity ratio which calculates k and ω by specifying free stream turbulence intensity (I), turbulence viscosity ratio (μ_t/μ) and turbulence velocity ($\boldsymbol{v}$). Equations 5.3 and 5.4 from Siemens (2017) are used for the calculations.

$$k = \frac{3(I\boldsymbol{v})^2}{2} \tag{5.3}$$

$$\omega = \frac{\rho k}{(\frac{\mu_t}{\mu})\mu} \tag{5.4}$$

The free stream turbulence intensity was set to $I = 0.2\%$, $I = 0.1\%$ and $I = 0.2\%$ respectively for the three validation cases that were considered while the turbulence velocity was set to 54.88 m/s, 51.45 m/s and 30 m/s for the respective validation cases and the turbulence viscosity ratio (TVR) to μ_t/μ=1. According to Verissimo (cited by Joao Nuno Dias, 2016*b*) and Ewing (2015), the ambient turbulence source option should be employed to mitigate the decay of inflow turbulence quantities. According to Siemens (2017) the benefits of using the ambient turbulence source option are easier fine-tuning of turbulence intensity without having to have excessively large turbulent viscosity ratios and the ability to properly simulate an aerodynamic body moving through background turbulence. Siemens (2017) further states that the use of the ambient turbulence source option is particularly advantageous for the transition model. The ambient turbulence source was inferred on the velocity inlet boundary and the initial boundary values that were used for the ambient turbulence source were the same as the initial boundary values for the inlet boundary, viz., $I = 0.2\%, 0.1\%$ and $I = 0.2\%$ for turbulence intensity and 1 for TVR.

The use of the SST $k - \omega$ turbulence and $\gamma - Re_\theta$ transition model requires the definition of a blending function/free-stream edge function. The value that was used for the free-stream edge is the maximum boundary layer thickness calculated with equation 5.1. A low y^+ wall treatment was chosen to resolve the laminar sublayer of the turbulent boundary layer as endorsed by the best practice from Ewing (2015). A maximum wall y^+ of 0.4 was implemented in all the simulations that were conducted in the 2D and 3D validation studies.

The segregated flow solver was chosen to solve the RANS equations. The segregated flow solver has lower memory requirements and is, therefore, faster than the coupled

flow solver. The segregated flow solver is recommended for incompressible flows ($M < 0.3$) while the coupled flow solver is recommended for flow with intermediate and high Mach numbers ($M > 0.3$) (Ewing, 2015). The second order upwind discretization scheme was used for all parameters.

5.3.4 Convergence criterion

Plots for the residuals, lift coefficient and drag coefficient, which typically resemble those shown in figure 5.7, were created to monitor convergence. The convergence of the numerical solution was achieved when the residuals plot and the respective force coefficient plots converged. A minimum residuals plot convergence of the order of 10^{-4} was achieved in all the simulations.

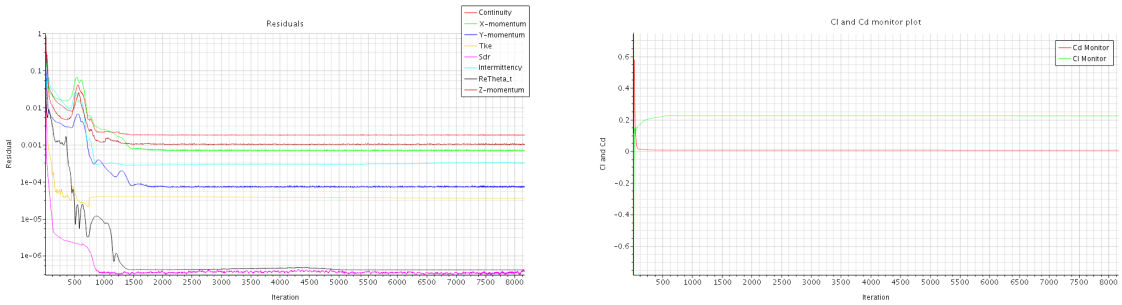

(a) Residuals plot **(b)** Drag and lift coefficient plot

Figure 5.7: Convergence monitor plots

5.4 Results and discussion

This section gives a presentation of the validation results for all the unit and benchmark cases that were considered in this project. The STAR-CCM+ results that were obtained for the 2D and 3D validation cases are compared with the baseline data and in all the validation cases, comparisons are also made between the 2D and 3D STAR-CCM+ results. The data that is presented for the various flow variables and aerodynamic coefficient (see section 5.1) is for a Mach number of 0.16 and a Reynolds numbers of 2.88 million, a Mach number of 0.15 and a Reynolds numbers

of 2 million and a Mach number of 0.088 and a Reynolds numbers of 0.38 million, respectively. As discussed in chapter 4, an integral part of the validation process was the verification of the CFD solutions to quantify the level of numerical inaccuracies that exist due to the discretization. This ensured a fair validation of the SST $k-\omega$ turbulence and $\gamma - Re_\theta$ transition model for the flow cases that were considered in the 2D and 3D validation study. A spatial grid convergence study was conducted for each flow case, however, due to the high volume of data that was handled, only representative engineering quantities for each flow case were considered for the grid convergence index (GCI). The GCI that were obtained for the representative unit and benchmark cases was considered to be sufficiently small to render a fair validation of the SST $k-\omega$ turbulence and $\gamma - Re_\theta$ transition model. The grid convergence study for the unit and benchmark cases is presented in subsections B.3.1 and B.3.2 in Appendix B.

5.4.1 Validation case 1

This subsection gives the comparison for the chordwise pressure coefficient and skin friction coefficient distribution and onset boundary layer transition points for incidence angles of 0, 6, 10 and 14 degrees at a Reynolds number of 2.88 million. The 2D and 3D STAR-CCM+ data are compared with the baseline data by Gregory and O'Reilly (1973) and XFOIL, while comparisons are also made for the 2D and 3D STAR-CCM+ results. Figures 5.8, 5.9, 5.10 and 5.11 give the chordwise pressure coefficient and skin friction coefficient distribution for incidence angles of 0, 6, 10 and 14 degrees, respectively. The onset boundary layer transition points are given in figure 5.12 and tabulated in Table C.1 in Appendix C for comparison.

Figure 5.8 shows the chordwise pressure coefficient and skin friction coefficient distribution for 0 degrees angle of attack.

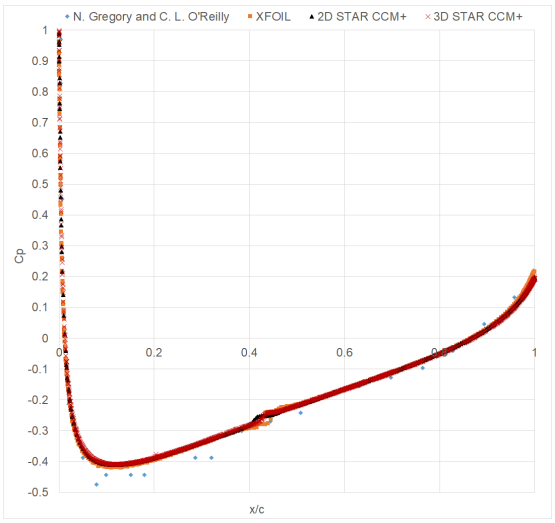

(a) Chordwise pressure coefficient distribution.

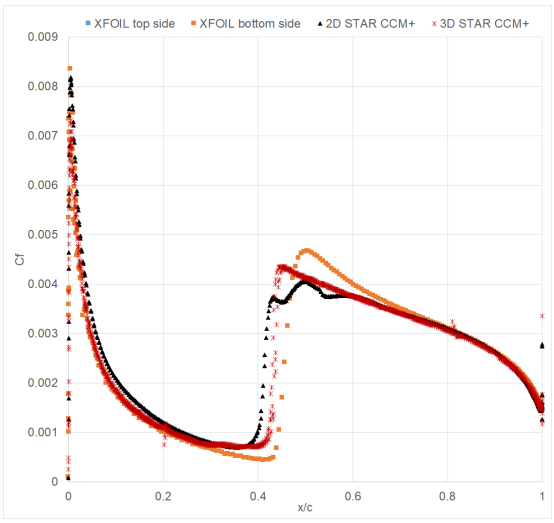

(b) Chordwise skin friction coefficient distribution.

Figure 5.8: Experimental, XFOIL, 2D and 3D STAR-CCM+ data plots for the chordwise pressure distribution and skin friction coefficient distribution on the NACA 0012 airfoil and wing at a 0 degrees angle of attack and Reynolds number of 2.88 million.

Figure 5.8a shows the chordwise pressure coefficient distribution for an angle of attack of 0 degrees. XFOIL, 2D STAR-CCM+ and 3D STAR-CCM+ predict a transitional separation bubble on the top and bottom surfaces of the airfoil and wing. The laminar boundary layer separates from the surfaces and reattaches as a turbulent boundary layer. A discrepancy in the predicted transitional separation bubble is observed. A transitional separation bubble is observed on the top and bottom surfaces of the arfoil and wing at $x/c = 0.437$ in XFOIL, $x/c = 0.39081$ in 2D STAR-CCM+ and $x/c = 0.41722$ in 3D STAR-CCM+. The skin friction and pressure coefficient data plots are in agreement. In figure 5.8b a sudden increase in skin friction drag coefficient values on the top and bottom surfaces of the airfoil and wing, which is characteristic of boundary layer transition, is observed at $x/c = 0.437$ in XFOIL, $x/c = 0.39081$ in 2D STAR-CCM+ and $x/c = 0.41722$ in 3D STAR-CCM+. Weak and mild adverse pressure gradients exist, which do not have sufficient strength to cause boundary layer separation, therefore, the turbulent boundary layer remains

attached to the airfoil and wing surfaces for the remainder of the chordwise flow. In spite the observed discrepancies in boundary layer transition points, the 2D and 3D STAR-CCM+ results compare well with the baseline data by Gregory and O'Reilly (1973) and XFOIL.

Figure 5.9 shows the chordwise pressure coefficient and skin friction distribution for 6 degrees angle of attack.

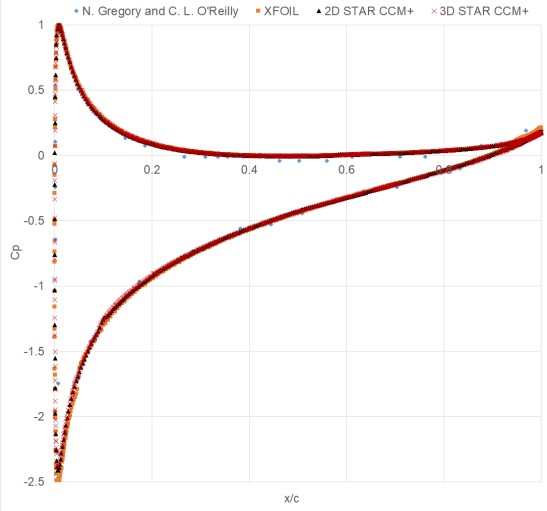

(a) Chordwise pressure coefficient distribution.

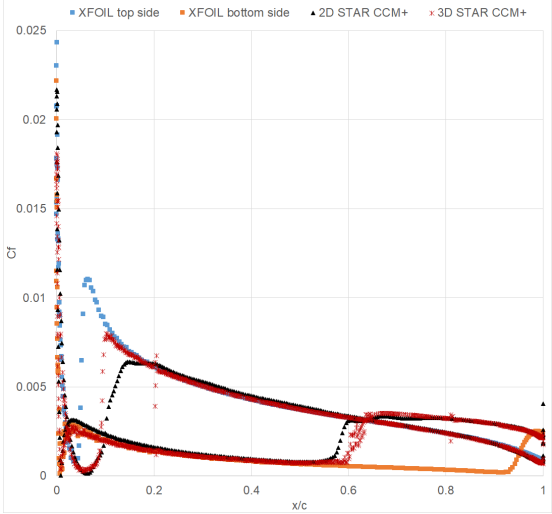

(b) Chordwise skin friction coefficient distribution.

Figure 5.9: Experimental, XFOIL, 2D and 3D STAR-CCM+ data plots for the chordwise pressure distribution and skin friction coefficient distribution on the NACA 0012 airfoil and wing at a 6 degrees angle of attack and Reynolds number of 2.88 million.

Figure 5.9a shows the chordwise pressure coefficient distribution for an angle of attack of 6 degrees. XFOIL, 2D STAR-CCM+ and 3D STAR-CCM+ predict a transitional separation bubble on the top and bottom surfaces of the airfoil and wing [5]. The laminar boundary layer separates from the surfaces, reattaches as a turbulent boundary layer flow and remains attached to the surface for the remainder of the chordwise flow. A difference in the predicted transitional separation bubble is observed. A

[5]The transitional separation bubble is not visible from the pressure coefficient plot shown in figure 5.9a but is shown to exist as observed in the skin friction plot shown in figure 5.9b

transitional separation bubble is observed on the top surface of the airfoil and wing at $x/c = 0.045$ in XFOIL, $x/c = 0.0686$ in 2D STAR-CCM+ and $x/c = 0.0698$ in 3D STAR-CCM+ and on the bottom surface at $x/c = 0.93$ in XFOIL, $x/c = 0.5714$ in 2D STAR-CCM+ and $x/c = 0.059053$ in 3D STAR-CCM+. The skin friction and pressure coefficient data plots are in agreement. In figure 5.9b, 2D STAR-CCM+ shows a rapid increase in skin friction drag coefficient values on the top and bottom surfaces of the airfoil and wing at $x/c = 0.0686$ and $x/c = 0.5714$, respectively, as the laminar boundary layer transitions to a turbulent boundary layer while 3D STAR-CCM+ and XFOIL shows this sudden increase in skin friction coefficient values on the top surface at $x/c = 0.0698$ and $x/c = 0.059053$ and on the bottom surface at $x/c = 0.045$ and $x/c = 0.93$, respectively. The 2D and 3D STAR-CCM+ results are satisfactory relative to the baseline data by Gregory and O'Reilly (1973) and XFOIL.

Figure 5.10 shows the chordwise pressure coefficient and skin friction coefficient distribution for 10 degrees angle of attack.

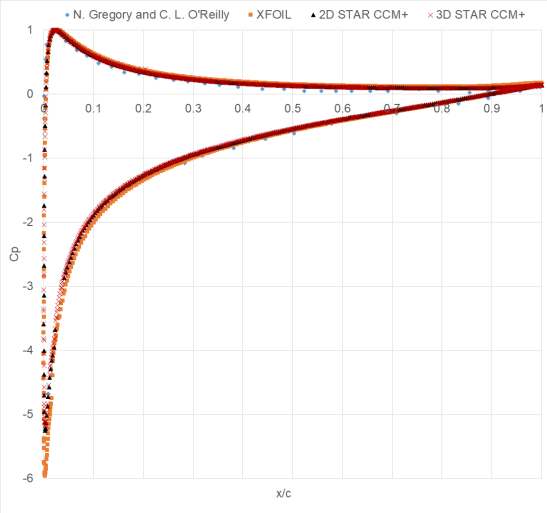

(a) Chordwise pressure coefficient distribution.

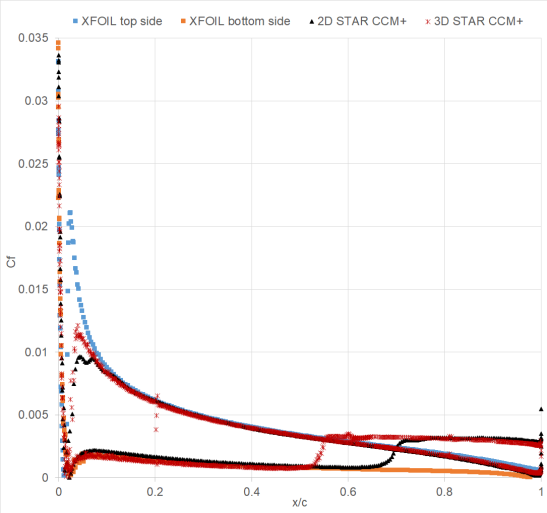

(b) Chordwise skin friction coefficient distribution.

Figure 5.10: Experimental, XFOIL, 2D and 3D STAR-CCM+ data plots for the chordwise pressure distribution and skin friction coefficient distribution on the NACA 0012 airfoil and wing at a 10 degrees angle of attack and Reynolds number of 2.88 million.

Figures 5.10a shows the chordwise pressure coefficient distribution for an angle of attack of 10 degrees. XFOIL, 2D STAR-CCM+ and 3D STAR-CCM+ predict a transitional separation bubble on the top surfaces of the airfoil and wing while 2D STAR-CCM+ and 3D STAR-CCM+ also predict a transitional separation bubble on the bottom surface [6]. The laminar boundary layer separates from the airfoil and wing surfaces and reattaches as a turbulent boundary layer. The turbulent boundary layer remains attached to the airfoil and wing surfaces for the remainder of the chordwise flow. There is a good agreement in the predicted transitional separation bubble on the top surface of the airfoil and wing. A transitional separation bubble is observed on the top surface at $x/c = 0.015$ in XFOIL, $x/c = 0.01594$ in 2D STAR-CCM+ and $x/c = 0.016325$ in 3D STAR-CCM+ and on the bottom surface at $x/c = 0.686$ in 2D STAR-CCM+ and at $x/c = 0.53671$ in 3D STAR-CCM+. XFOIL

[6] The transitional separation bubble is not visible from the pressure coefficient plot shown in figure 5.10a but is shown to exist as observed in the skin friction plot shown in figure 5.10b

predicts the existence of a laminar boundary layer on the bottom surface of the airfoil. The skin friction coefficient and pressure coefficient data plots correspond. In figure 5.10b, the 2D STAR-CCM+ data plot shows a drastic increase in skin friction drag coefficient values on the top surface of the airfoil at $x/c = 0.01594$ and on the bottom surface at $x/c = 0.686$ as the laminar boundary layer transitions to a turbulent boundary layer while 3D STAR-CCM+ shows this rapid increase in skin friction drag coefficient values at $x/c = 0.016325$ and $x/c = 0.53671$ on the top and bottom surfaces of the wing. XFOIL shows the drastic increase in skin friction drag coefficient at $x/c = 0.015$ on the top surface of the airfoil only. The 2D and 3D STAR-CCM+ results are in good agreement with the baseline data by Gregory and O'Reilly (1973) and XFOIL.

Figure 5.11 shows the chordwise pressure coefficient and skin friction coefficient distribution for 14 degrees angle of attack.

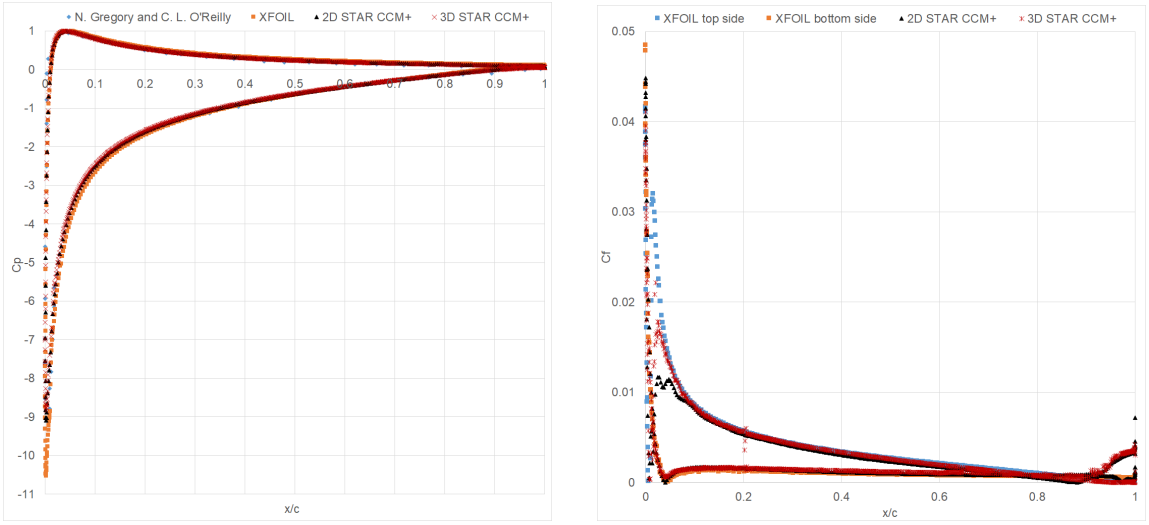

(a) Chordwise pressure coefficient distribution.

(b) Chordwise skin friction coefficient distribution.

Figure 5.11: Experimental, XFOIL, 2D and 3D STAR-CCM+ data plots for the chordwise pressure distribution and skin friction coefficient distribution on the NACA 0012 airfoil and wing at a 14 degrees angle of attack and Reynolds number of 2.88 million.

Figure 5.11a shows the chordwise pressure coefficient distribution for an angle of attack of 14 degrees. XFOIL, 2D STAR-CCM+ and 3D STAR-CCM+ predict a transitional separation bubble on the top surfaces of the airfoil and wing while 2D STAR-CCM+ and 3D STAR-CCM+ also predict a transitional separation bubble on the bottom surface [7]. The laminar boundary layer separates from the airfoil and wing surface, reattaches as a turbulent boundary layer and remains attached to the airfoil and wing surfaces for the remainder of the chordwise flow. There is a good agreement in the predicted transitional separation bubble on the top surface of the airfoil and wing. A transitional separation bubble is observed on the top surface of the airfoil and wing at $x/c = 0.009$ in XFOIL, $x/c = 0.00876$ in 2D STAR-CCM+ and $x/c = 0.0085$ in 3D STAR-CCM+. The predicted transitional separation bubble on the bottom surface of the airfoil and wing agree for the 2D and 3D STAR-CCM+ results, i.e., at $x/c = 0.94$ in 2D STAR-CCM+ and $x/c = 0.924$ in 3D STAR-CCM+. XFOIL predicts the existence of a laminar boundary layer on the bottom surface of the airfoil. The skin friction and pressure coefficient data are in agreement. In figure 5.11b, the 2D STAR-CCM+ data plot shows a drastic increase in skin friction drag coefficient values on the top surface of the airfoil at $x/c = 0.00876$ and the bottom surface of the airfoil at $x/c = 0.94$, as the laminar boundary layer transitions to a turbulent boundary layer while 3D STAR-CCM+ shows a sudden increase in skin friction drag coefficient values at $x/c = 0.0085$ and $x/c = 0.924$ on the top and bottom surfaces of the wing, respectively. XFOIL shows a sudden increase in skin friction drag coefficient values at $x/c = 0.009$ on the top surface of the airfoil only. The 2D and 3D STAR-CCM+ results are sufficiently accurate relative to the baseline data by Gregory and O'Reilly (1973) and XFOIL.

[7] The transitional separation bubble is not visible from the pressure coefficient plot shown in figure 5.11a but is shown to exist as observed in the skin friction plot shown in figure 5.11b.

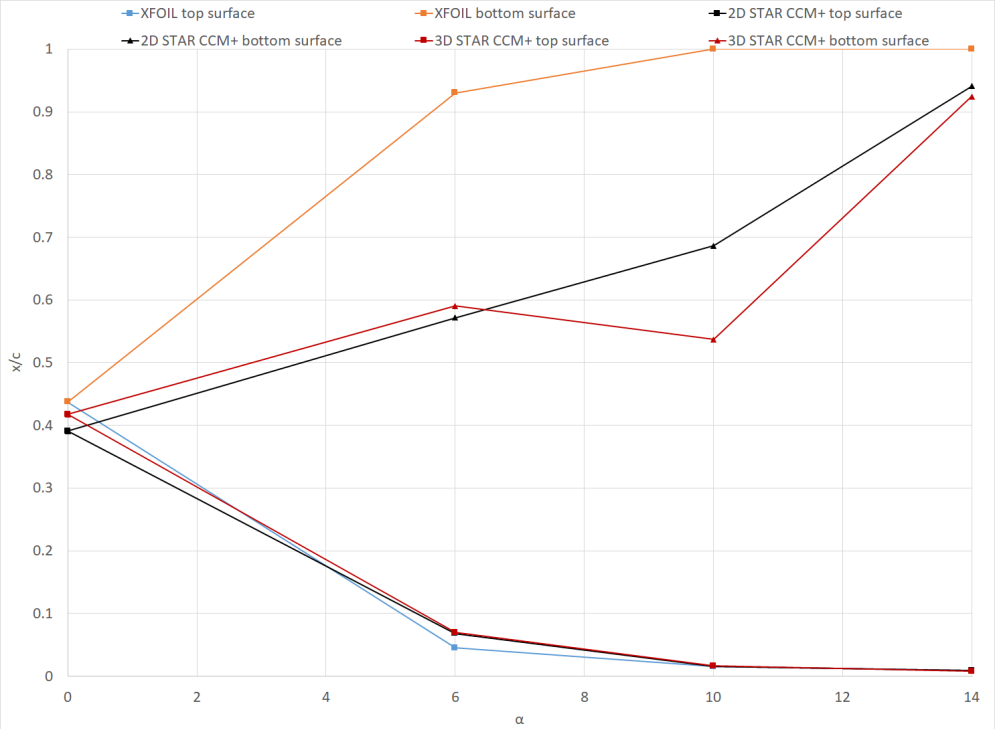

Figure 5.12: XFOIL, 2D and 3D STAR-CCM+ boundary layer transition points for the NACA 0012 airfoil at a Reynolds number of 2.88 million.

There is, overall, a good agreement in the 2D and 3D STAR-CCM+ data and the baseline data. This demonstrates the outstanding capacity of the SST $k-\omega$ turbulence model with the $\gamma - Re_\theta$ transition model to model a 2D transitional flow on an airfoil and 3D transitional flow on a wing. The SST $k-\omega$ turbulence and $\gamma - Re_\theta$ transition model is, therefore, validated for a transitional flow on sailplane airfoil and wing geometries.

5.4.2 Validation case 2

This subsection gives a comparison for the lift coefficient and drag coefficient for the range $0 < \alpha < 16$ degrees of angle of attack at a Reynolds number of 2 million. The 2D and 3D STAR-CCM+ data is compared with the baseline data by Ladson (1988), Shelda R.E. and Klimas, P.C. (1981) and XFOIL. Figures 5.13a and 5.13b give the lift coefficient and drag coefficient respectively. The lift coefficient and drag

coefficient data is tabulated in Tables C.2 and C.3, respectively in Appendix C for comparison.

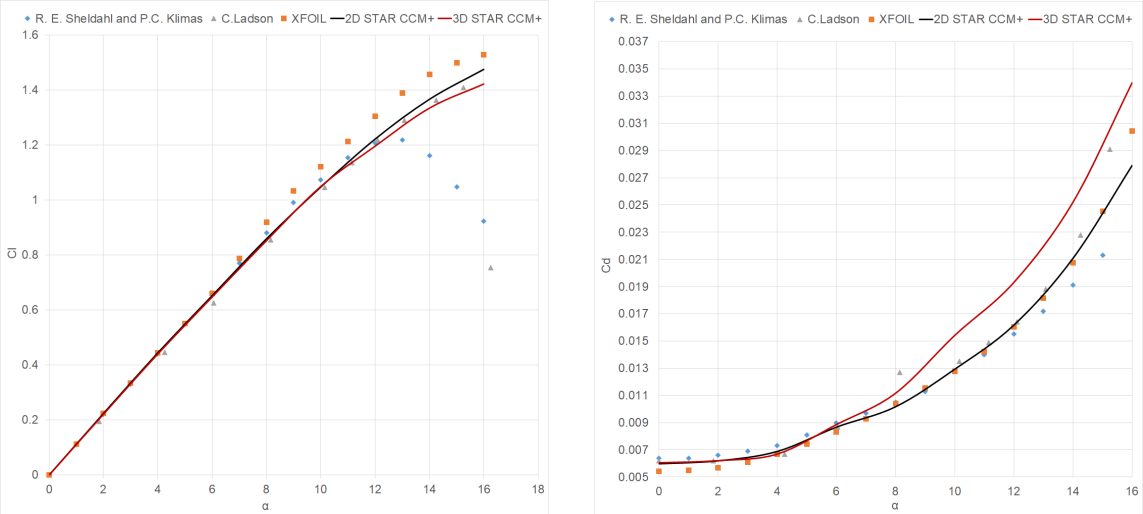

(a) Lift coefficient.

(b) Drag coefficient.

Figure 5.13: Experimental, XFOIL, 2D and 3D STAR-CCM+ validation data plots for the lift coefficient and drag coefficient of the NACA 0012 airfoil and wing at a Reynolds number of 2 million.

Figure 5.13a shows that the lift polar increases linearly until $\alpha \approx 14$ and thereafter increases quadratically as the airfoil and wing approaches stall. An exponential increase in drag polar with angle of attack is observed in figure 5.13b. The predicted behavior in the lift and drag polar agrees with literature such as Anderson (2010) and Houghton (2012). The 2D STAR-CCM+ lift coefficient and drag coefficient results are within the baseline data range for each angle of attack that was investigated. The 3D STAR-CCM+ lift coefficient results are within the baseline data range for each angle of attack that was studied while the drag coefficient results are within the baseline data range, only for small to medium angles of attack ($\alpha < 8$). The drag coefficients are not within the baseline data range for high angles of attack ($\alpha > 8$), however, the deviation is within 19% of the values that were observed experimentally. There is an, overall, good agreement between the 2D and 3D STAR-CCM+ data and the baseline data for all the angles of attack that were studied. The good agreement in the 2D and 3D STAR-CCM+ data and the baseline data demonstrates the capacity

of the SST $k-\omega$ turbulence model with the $\gamma - Re_\theta$ transition model to model a 2D transitional flow on an airfoil and 3D transitional flow on a wing. The SST $k-\omega$ turbulence and $\gamma - Re_\theta$ transition model is, therefore, validated for a transitional flow on sailplane airfoil and wing geometries.

5.4.3 Validation case 3

This subsection gives a comparison for the mean velocity and turbulence stresses (viz., **uu**, **vv**, **ww** and **uv**) at the wake for downstream distances $x/c = 0, 0.28, 0.94$ and 1.5 from the airfoli and wing trailing edge at α = 3, 6 and 9 at a Reynolds number of 0.38 million. The 2D and 3D STAR-CCM+ results are compared with the baseline data by Hah and Lakshminarayana (1982). The 2D STAR-CCM+ data was generated for the SST $k-\omega$ turbulence model that uses a linear stress relation (Boussinesq approximation) and a non-linear stress relation (EARSM) with the $\gamma - Re_\theta$ transition model and the Reynolds stress turbulence model (RSM). The SST $k-\omega$ turbulence model that uses the Boussinesq approximation with the $\gamma - Re_\theta$ transition model was compared with the and SST $k-\omega$ algebraic turbulence stress model with the $\gamma - Re_\theta$ transition model and the RSM to determine its adequacy to model a transitional and turbulent wake flow. Algebraic stress models and Reynolds Stress Models are preferred for their advanced ability to account for the anisotropy in highly turbulent flows. The satisfactory performance of the SST $k-\omega$ turbulence model that uses the Boussinesq approximation in the 2D transitional and turbulent wake flow case study informed its use for in the 3D transitional and turbulent wake flow case study and for the rest of the validation process.

The present wake validation case deals with the near, intermediate and far wake. At an α of 3 degrees, x/θ = 0, 111, 372 and 593 which corresponds to x/c = 0, 0.28, 0.94 and 1.5 for θ = 0.506 mm. At an α of 6 degrees, x/θ =0, 82, 276 and 440 which corresponds to x/c = 0, 0.28, 0.94 and 1.5 for θ = 0.682 mm. At an α of 9 degrees, x/θ =0, 60, 203 and 324 which corresponds to x/c = 0, 0.28, 0.94 and 1.5 for θ = 0.926 mm.

5.4.3.1 Mean velocity profile

This subsubsection gives a comparison for the mean velocity profiles at the wake for downstream distances $x/c = 0, 0.28, 0.94$ and 1.5 from the trailing edge and $\alpha = 3$, 6 and 9. Figures 5.14, 5.15 and 5.16 give a comparison of the mean velocity profile at the wake for $\alpha = 3$, 6 and 9 respectively.

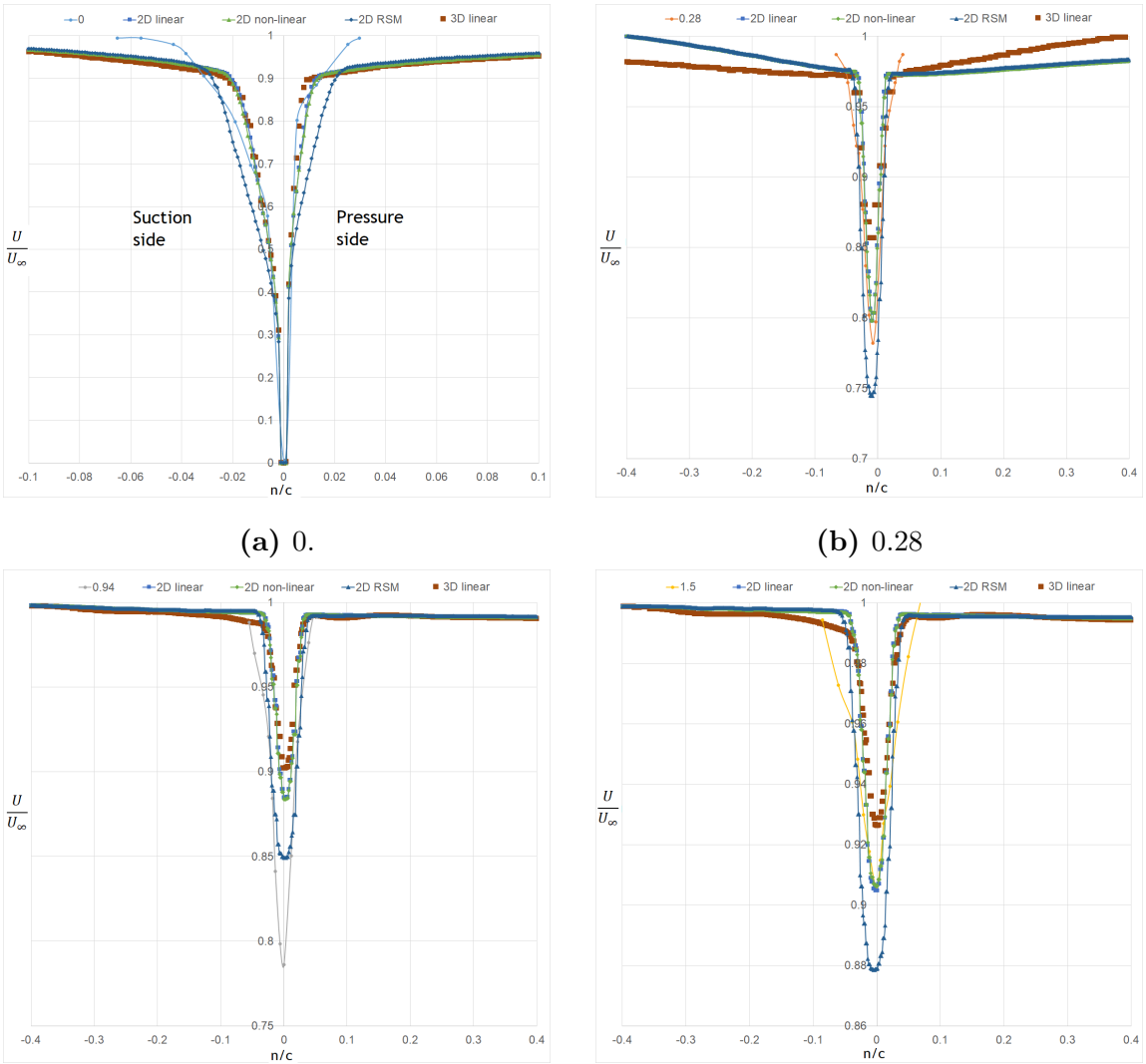

(a) 0.

(b) 0.28

(c) 0.94.

(d) 1.5

Figure 5.14: Experimental, 2D and 3D STAR-CCM+ data plots for the mean velocity in the wake downstream of the NACA 0012 airfoil and wing at a 3 degrees angle of attack and Reynolds number of 0.38 million.

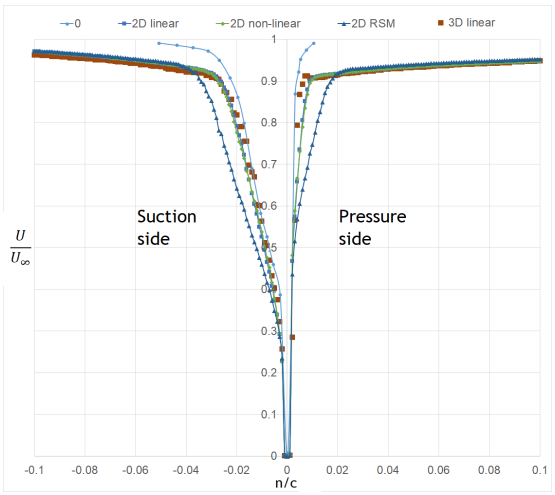

(a) 0.

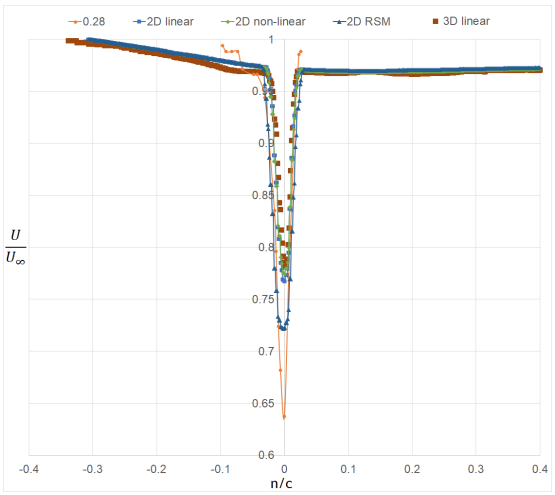

(b) 0.28

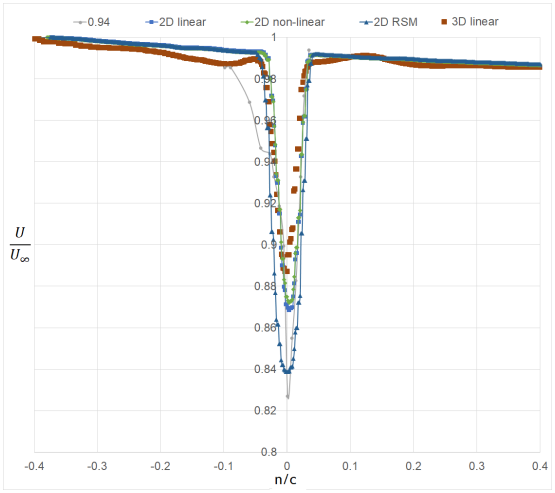

(c) 0.94.

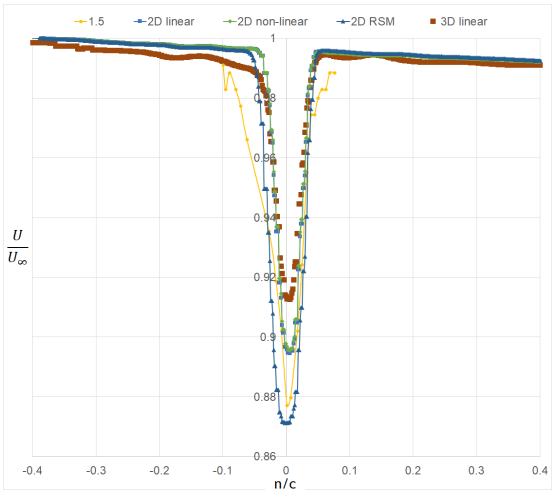

(d) 1.5

Figure 5.15: Experimental, 2D and 3D STAR-CCM+ data plots for the mean velocity in the wake downstream of the NACA 0012 airfoil and wing at 6 degrees angle of attack and Reynolds number of 0.38 million.

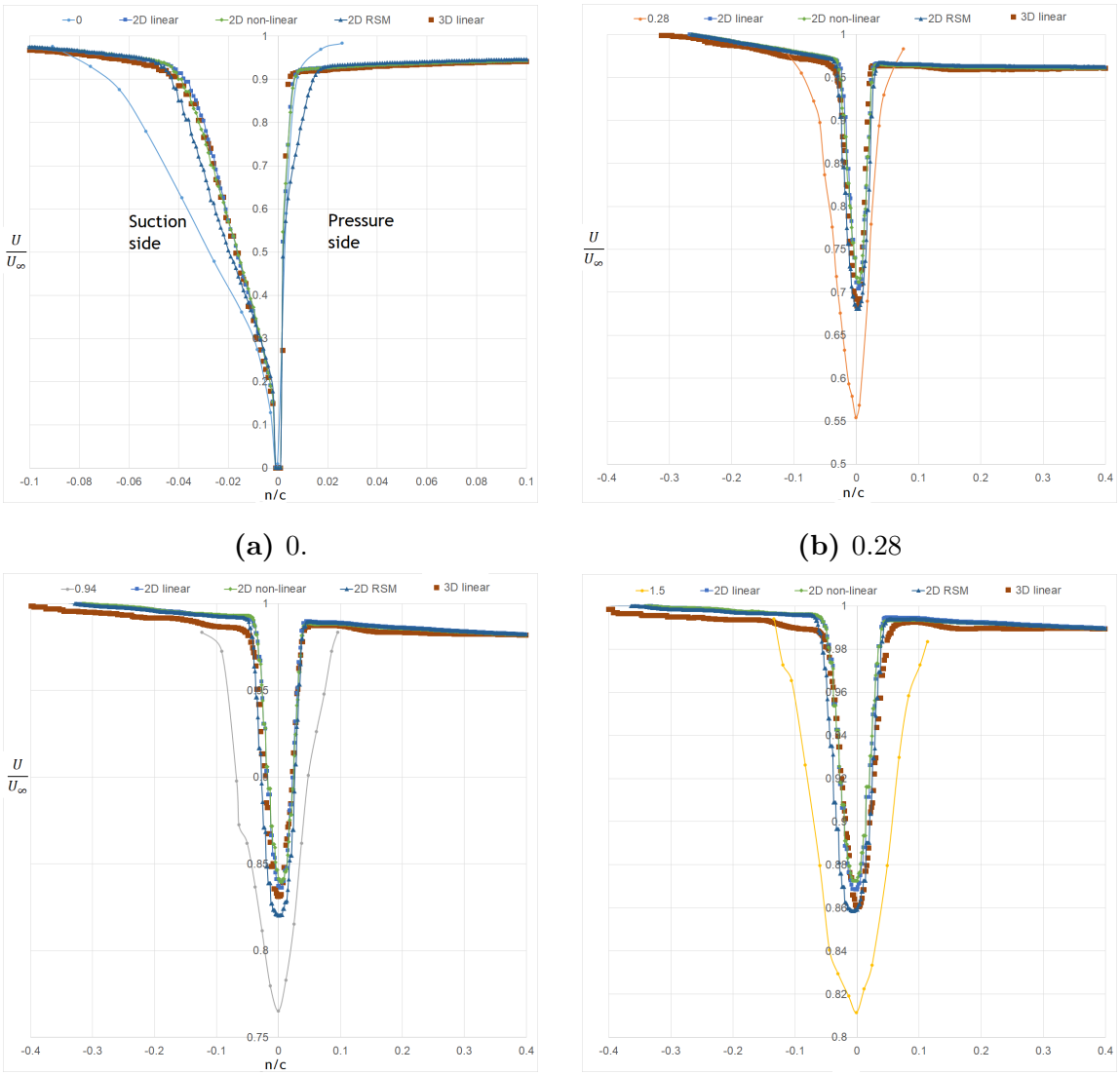

(a) 0.

(b) 0.28

(c) 0.94.

(d) 1.5

Figure 5.16: Experimental, 2D and 3D STAR-CCM+ data plots for the mean velocity in the wake downstream of the NACA 0012 airfoil and wing at 9 degrees angle of attack and Reynolds number of 0.38 million.

The behavior of the computed mean velocity profiles in the wake corresponds to the experimentally observed values by Hah and Lakshminarayana (1982). At the region close to the trailing edge of the airfoil and wing, both the experimental and computed mean velocity profiles show the characteristics of a boundary layer. A substantial velocity defect at the wake center and asymmetry is observed for all three incidence angles. Due to the unfavorable pressure gradient, the boundary layer is thicker in

the suction side than on the suction side near the trailing edge of the airfoil. The velocity gradient is steeper in the suction side compared to the pressure side. This is especially apparent in the near wake region.

The mean velocity profiles becomes almost symmetric after one chord length downstream, the wake spreads with increasing distance downstream and the decay rate slows down with an increase in the incidence as was observed experimentally by Hah and Lakshminarayana (1982)

The computed quantities of the mean velocity are comparable to those observed experimentally by Hah and Lakshminarayana (1982). However, a loss in accuracy is observed with the increase in incidence angle. There was no significant differences in the mean velocity predictions in the wake for the various turbulence models that were employed.

5.4.3.2 Streamwise shear stress

This subsubsection gives a comparison for the streamwise shear stress profiles at the wake for downstream distances $x/c = 0, 0.28, 0.94$ and 1.5 from the airfoil and wing trailing edge and $\alpha = 3$, 6 and 9. Figures 5.17, 5.18 and 5.19 give a comparison of the streamwise shear stress profile at the wake for $\alpha = 3$, 6 and 9 respectively.

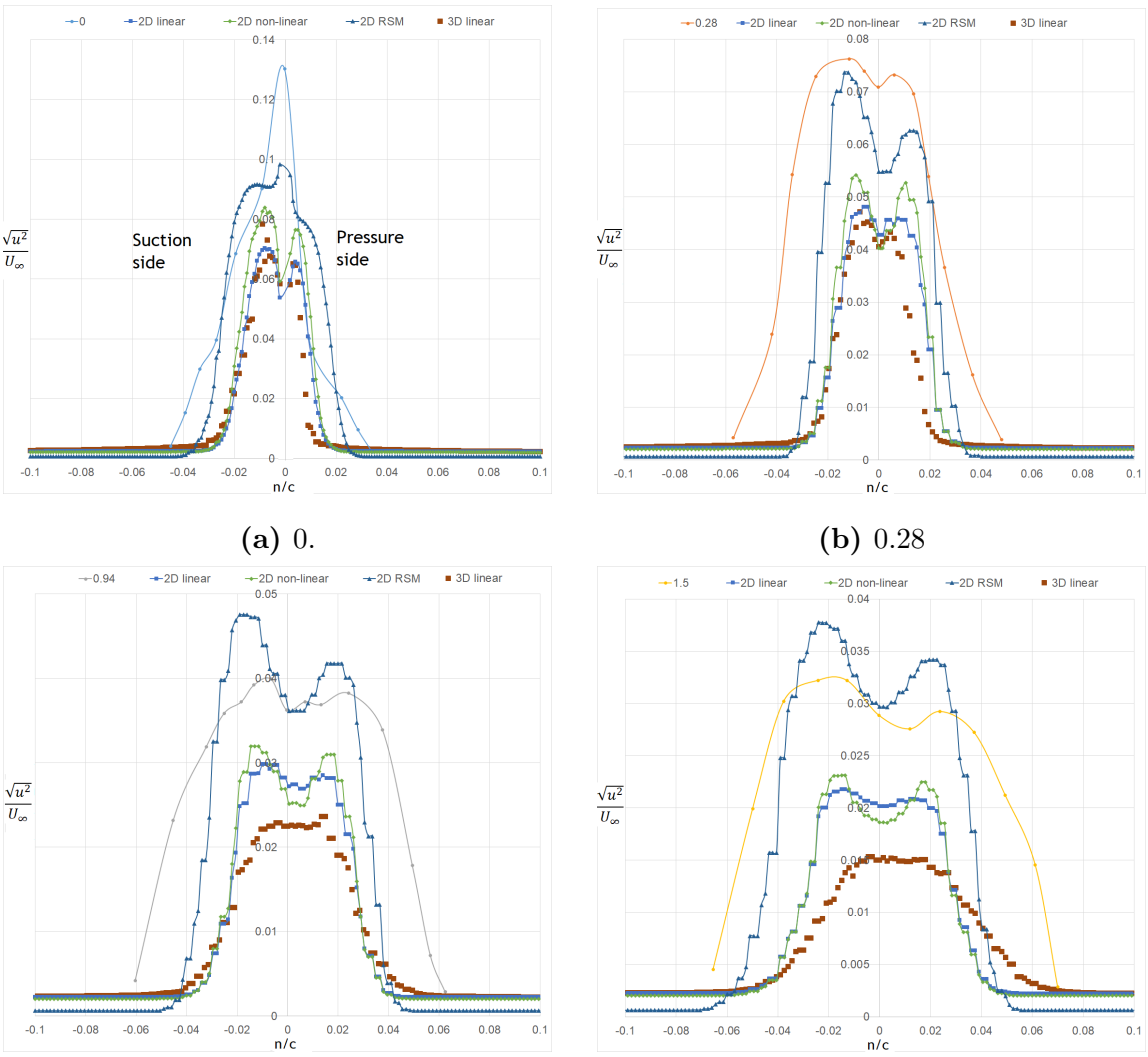

(a) 0.

(b) 0.28

(c) 0.94.

(d) 1.5

Figure 5.17: Experimental, 2D and 3D STAR-CCM+ data plots for the streamwise shear stress in the wake downstream of the NACA 0012 airfoil and wing at 3 degrees angle of attack and Reynolds number of 0.38 million.

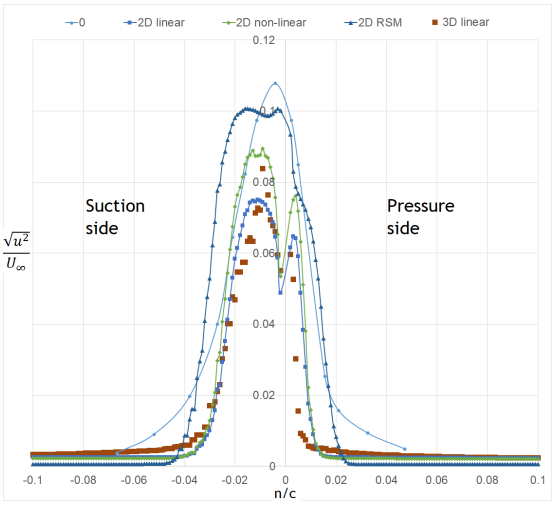

(a) 0.

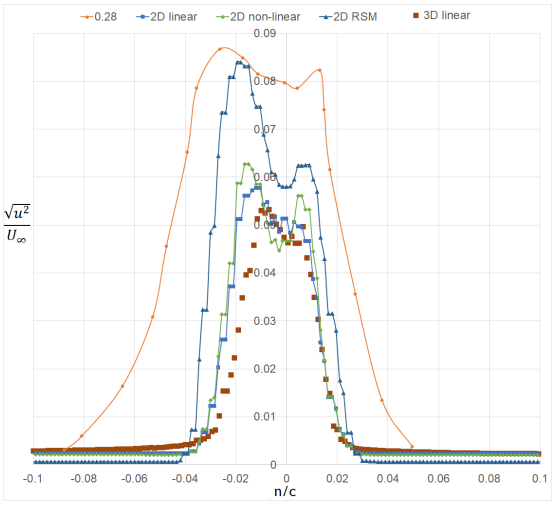

(b) 0.28

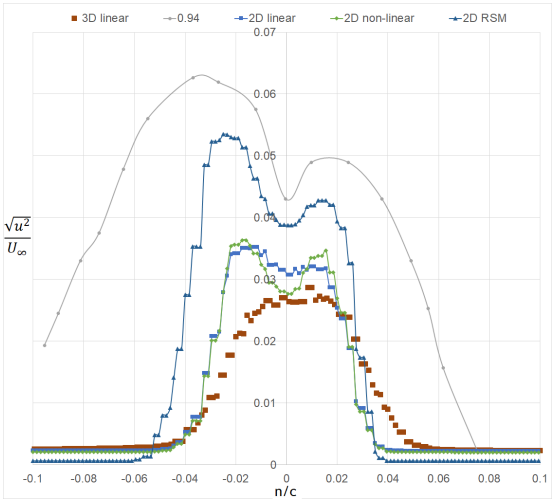

(c) 0.94.

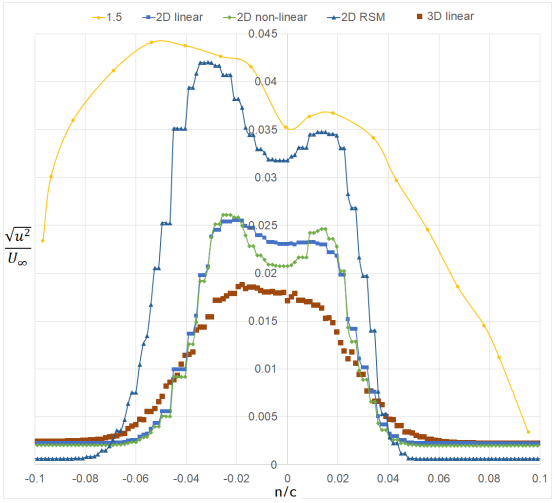

(d) 1.5

Figure 5.18: Experimental, 2D and 3D STAR-CCM+ data plots for the streamwise shear stress in the wake downstream of the NACA 0012 airfoil and wing at 6 degrees angle of attack and Reynolds number of 0.38 million.

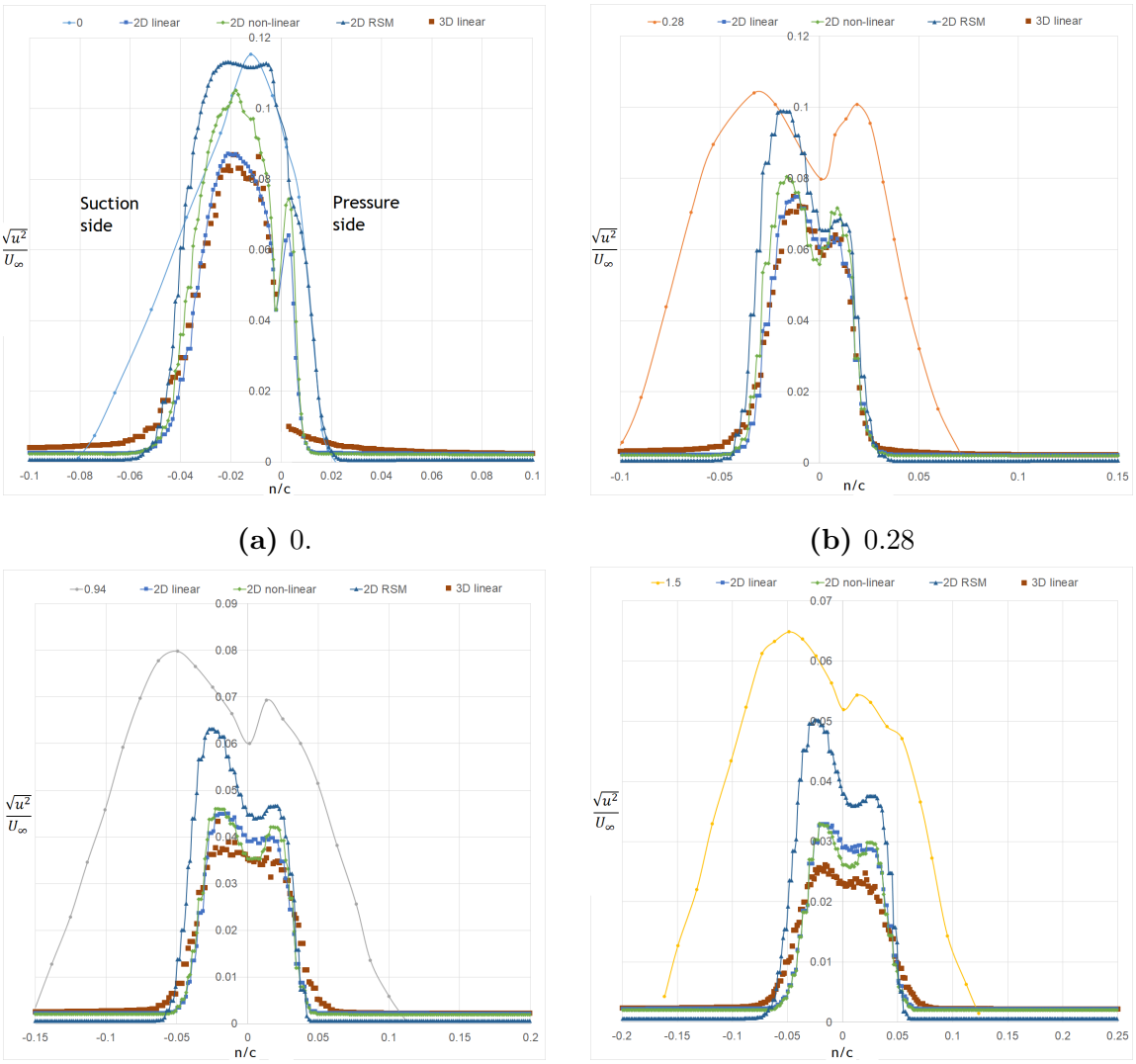

(a) 0. **(b)** 0.28

(c) 0.94. **(d)** 1.5

Figure 5.19: Experimental, 2D and 3D STAR-CCM+ data plots for the streamwise shear stress in the wake downstream of the NACA 0012 airfoil and wing at 9 degrees angle of attack and Reynolds number of 0.38 million.

The behavior of the computed turbulence levels in the streamwise direction agrees with the experimentally observed values by Hah and Lakshminarayana (1982). For all three incidence angles, the turbulence intensity level is lower on the pressure side than in the suction side as was observed experimentally by Hah and Lakshminarayana (1982). The asymmetric distribution of turbulence intensity levels is a consequence of the differences in boundary layer behavior on the pressure and suction side due

the airfoil having some positive incidence angle. This indicates that the suction side experiences more turbulence compared to the pressure side. This observation corresponds to the steeper velocity gradient of the mean velocity profile in the suction side compared to the pressure side as seen in subsubsection 5.4.3.1. According to Versteeg and Malalasekera (2007) the turbulence intensity levels are largest when the velocity gradient is largest, i.e. in regions that experience sharp changes in flow velocity.

A dip near the wake center in the turbulence intensity is observed for all three incidences and the dip reduces with the increase in streamwise distance. The dip in the near wake center exists because of the absence of shear stress production in that region. According to Versteeg and Malalasekera (2007) the value of **uu** only decreases slightly, and is not to zero, as a result of the turbulent flux across the centerline due to the high turbulence production from the surrounding regions. This dip is, however, not observed experimentally in the near wake region. Hah and Lakshminarayana (1982) recognizes this as an experimental flaw due to the fact that in the near wake, the wake width is extremely thin and the measuring stations across the wake were not close enough to detect the dip.

The turbulence levels in the streamwise direction are observed to peak away from the wake center and then decrease to zero towards the free stream. According to Versteeg and Malalasekera (2007) the turbulence intensity levels are highest when the velocity gradient is largest. This observation corresponds to the steep velocity gradients of the mean velocity profile in the suction and pressure side, away from the wake center as seen in subsubsection 5.4.3.1.

The computed quantities of the turbulence levels in the streamwise direction are comparable to those observed experimentally by Hah and Lakshminarayana (1982). However, a loss in accuracy is observed with the increase in incidence angle. The Reynolds stress turbulence model's predictions are closer to the experimentally observed for all the cases that were studied compared to the SST $k-\omega$ turbulence model with the $\gamma - Re_\theta$ transition model that uses the linear and non-linear relations. A

slight loss in accuracy is observed by comparing the 2D and 3D study results for the SST $k-\omega$ turbulence model with the $\gamma - Re_\theta$ transition model that uses the linear relations. This is due to interpolation errors which are more pronounced at the wake region in the 3D wake case. This was expected as mentioned in subsection 5.3.2. On the other hand, the flow behavior is well represented.

5.4.3.3 Transverse shear stress

This subsubsection gives a comparison of the transverse shear stress profiles at the wake for downstream distances $x/c = 0, 0.28, 0.94$ and 1.5 from the airfoil and wake trailing edge and $\alpha = 3$, 6 and 9. Figures 5.20, 5.21 and 5.22 give a comparison of the transverse shear stress profiles at the wake for $\alpha = 3$, 6 and 9 respectively.

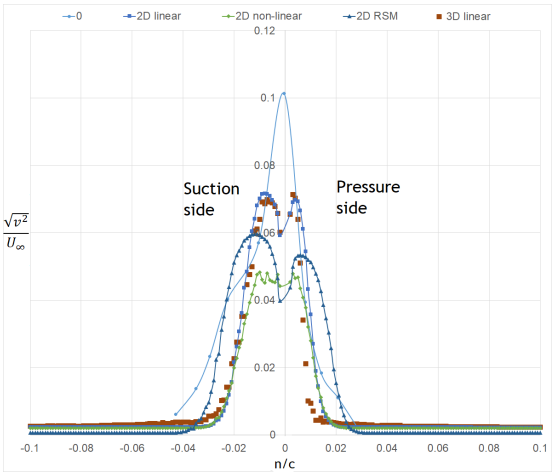

(a) 0.

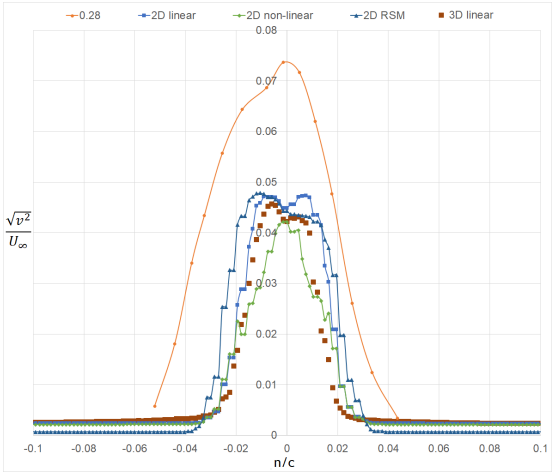

(b) 0.28

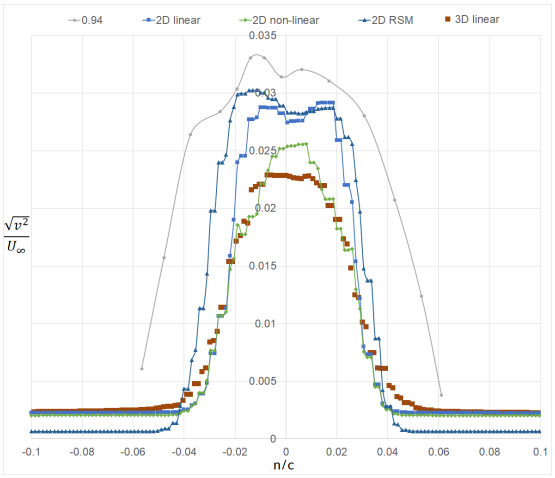

(c) 0.94.

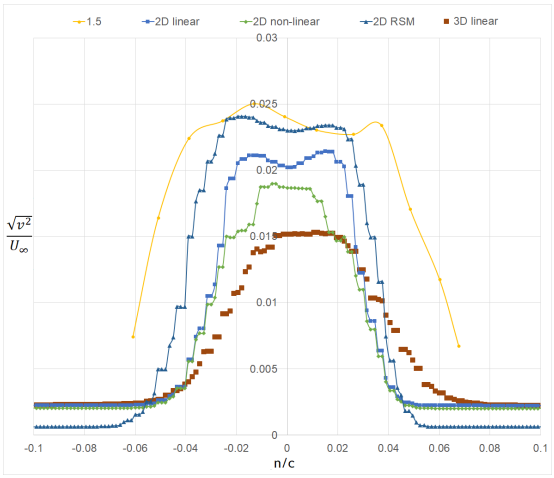

(d) 1.5

Figure 5.20: Experimental, 2D and 3D STAR-CCM+ data plots for the transverse shear stress in the wake downstream of the NACA 0012 airfoil and wing at 3 degrees angle of attack and Reynolds number of 0.38 million.

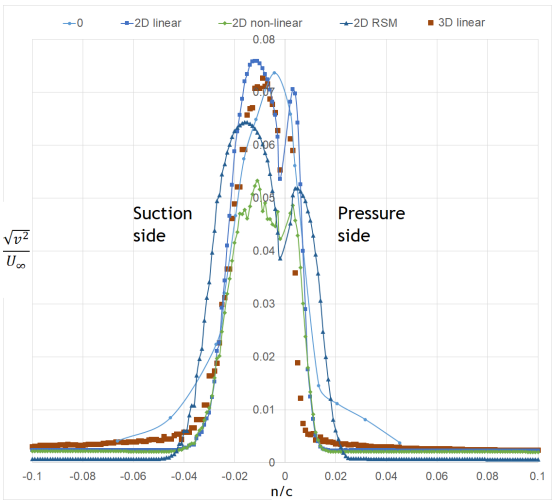

(a) 0.

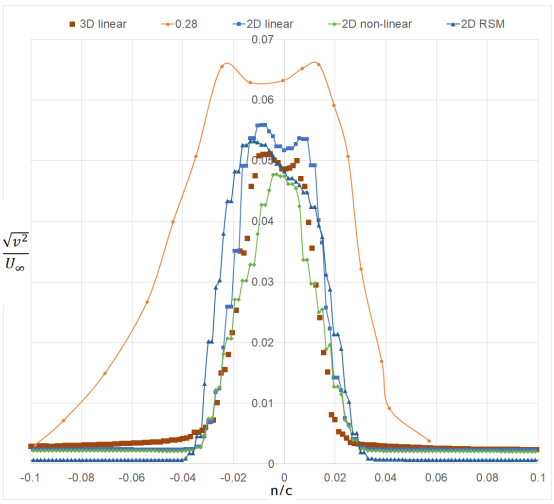

(b) 0.28

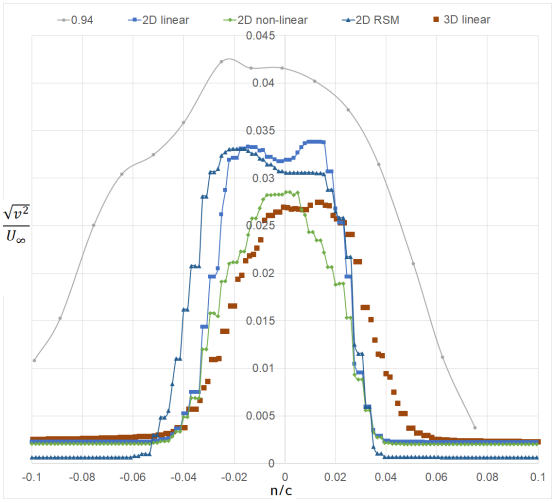

(c) 0.94.

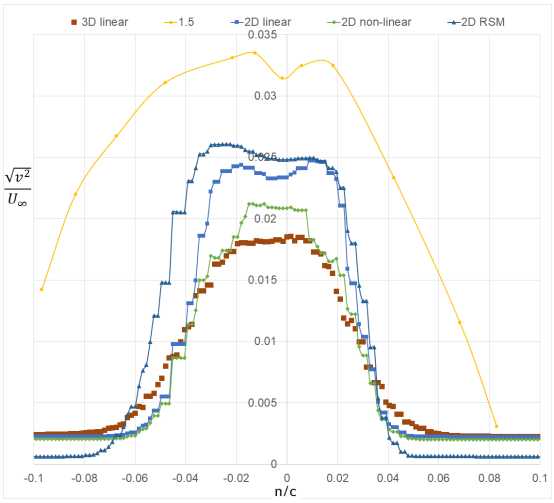

(d) 1.5

Figure 5.21: Experimental, 2D and 3D STAR-CCM+ data plots for the transverse shear stress in the wake downstream of the NACA 0012 airfoil and wing at 6 degrees angle of attack and Reynolds number of 0.38 million.

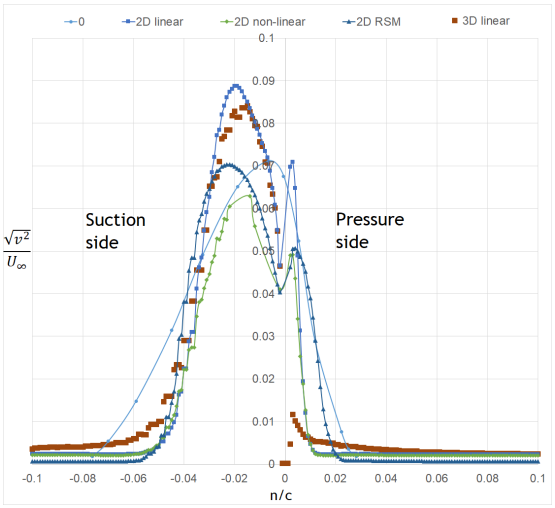

(a) 0.

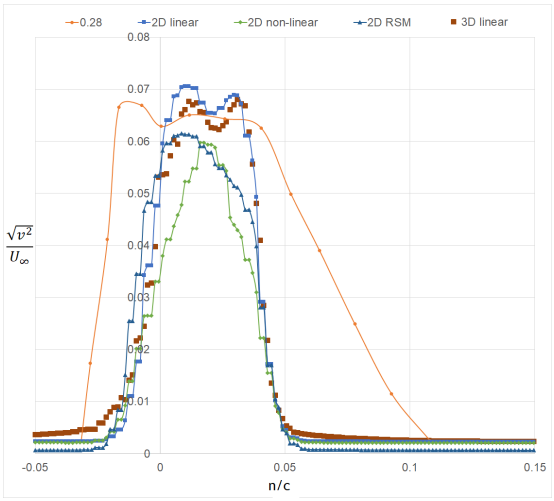

(b) 0.28

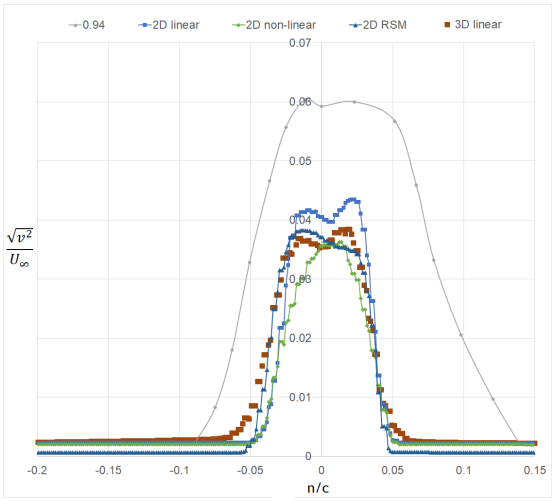

(c) 0.94.

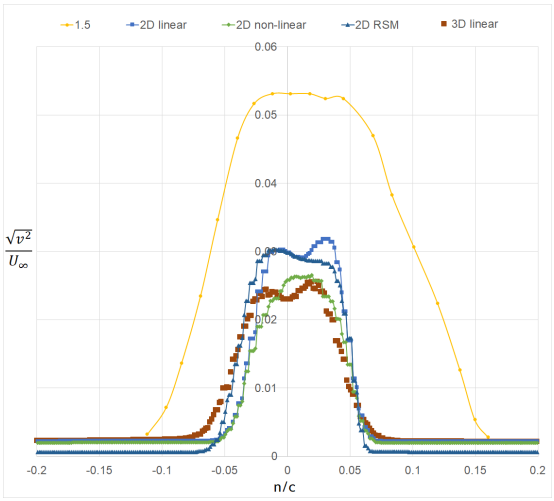

(d) 1.5

Figure 5.22: Experimental, 2D and 3D STAR-CCM+ data plots for the transverse shear stress in the wake downstream of the NACA 0012 airfoil and wing at 9 degrees angle of attack and Reynolds number of 0.38 million.

The behavior of the computed turbulence intensity in the transverse direction corresponds with the experimentally observed values by Hah and Lakshminarayana (1982). For all three incidence angles, the turbulence intensity level in the transverse direction is lower on the pressure side than in the suction side and there exists a dip near the wake center. The dip reduces much faster with the increase in streamwise distance compared to the turbulence intensity level in the streamwise direction as

was observed experimentally by Hah and Lakshminarayana (1982).

The turbulence levels in the transverse direction are observed to peak away from the wake center and then decrease to zero towards the free stream. According to Versteeg and Malalasekera (2007) the turbulence intensity levels are highest when the velocity gradient is largest. This observation corresponds to the steep velocity gradients of the mean velocity profile in the suction and pressure side, away from the wake center as seen in subsubsection 5.4.3.1.

The SST $k-\omega$ turbulence model with the $\gamma - Re_\theta$ transition model that uses a cubic relation (algebraic stress model) and the Reynolds stress turbulence model predict that the turbulence levels in the streamwise direction are much higher compared to those in the transverse direction as was observed experimentally by Hah and Lakshminarayana (1982). However, while the SST $k-\omega$ turbulence model with the $\gamma - Re_\theta$ transition model that uses a linear relation (Boussinesq approximation) has accurately predicted the flow behavior in the wake, it slightly underpredicts the anisotropy in turbulence at the wake.

The computed quantities of the turbulence levels in the transverse direction are comparable to those observed experimentally by Hah and Lakshminarayana (1982). However, a loss in accuracy is observed with the increase in incidence angle. The predictions of the SST $k-\omega$ turbulence model with the $\gamma - Re_\theta$ transition model that uses the linear turbulence approximation are closer to the experimentally observed for all the cases that were studied compared to the SST $k-\omega$ turbulence model with the $\gamma - Re_\theta$ transition model that uses the non-linear turbulence relations and the Reynolds stress turbulence model. A slight loss in accuracy due to interpolation errors is observed in the 3D results.

5.4.3.4 Spanwise shear stress

This subsubsection gives a comparison for the transverse shear stress profiles at the wake for downstream distances $x/c = 0, 0.28, 0.94$ and 1.5 from the airfoil and wing trailing edge and $\alpha = 3$, 6 and 9. Figures 5.23, 5.24 and 5.25 give a comparison of

the transverse shear stress profiles in the wake for $\alpha = 3$, 6 and 9 respectively.

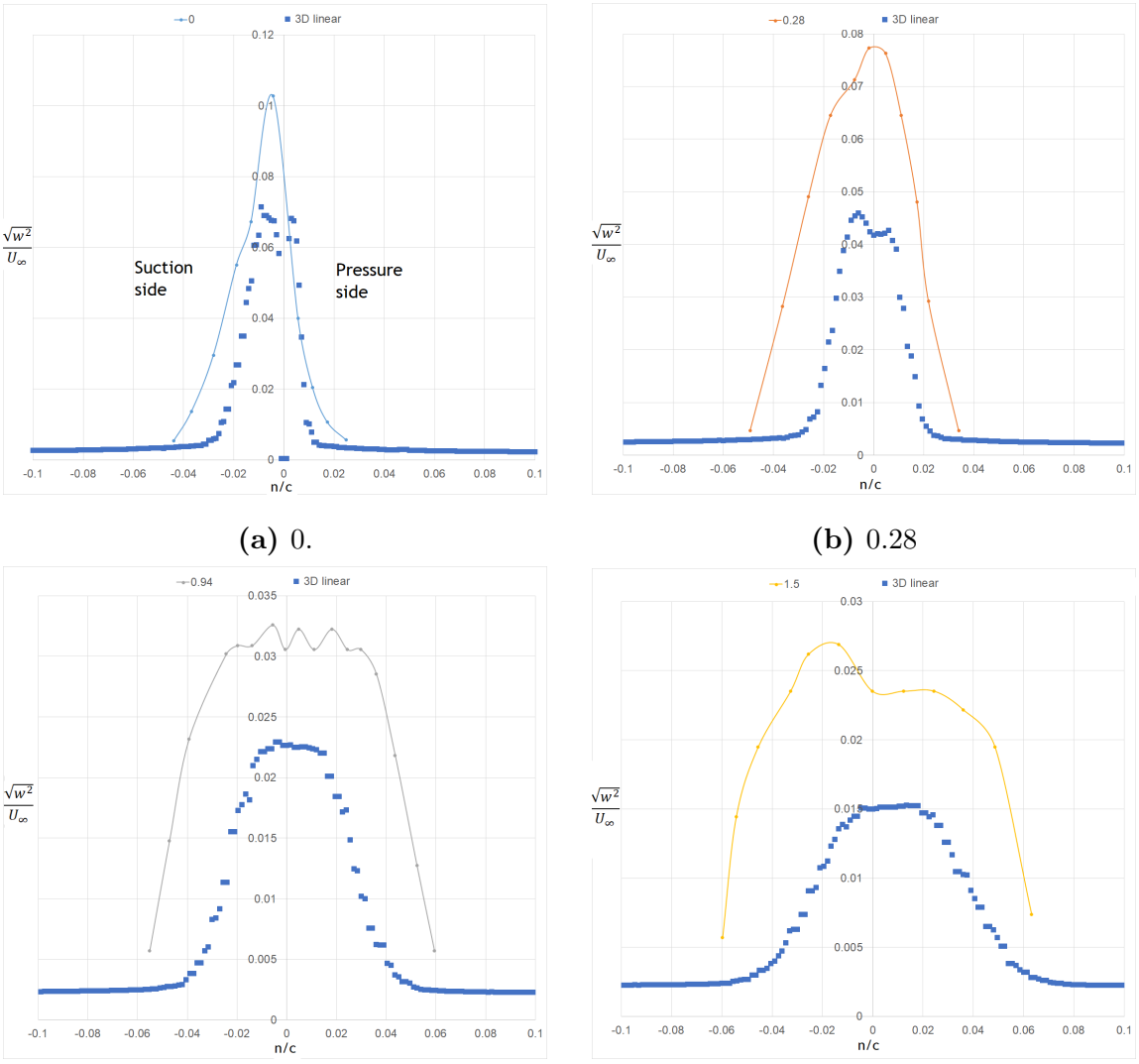

(a) 0.

(b) 0.28

(c) 0.94.

(d) 1.5

Figure 5.23: Experimental, 2D and 3D STAR-CCM+ data plots for the spanwise shear stress in the wake downstream of the NACA 0012 wing at 3 degrees angle of attack and Reynolds number of 0.38 million.

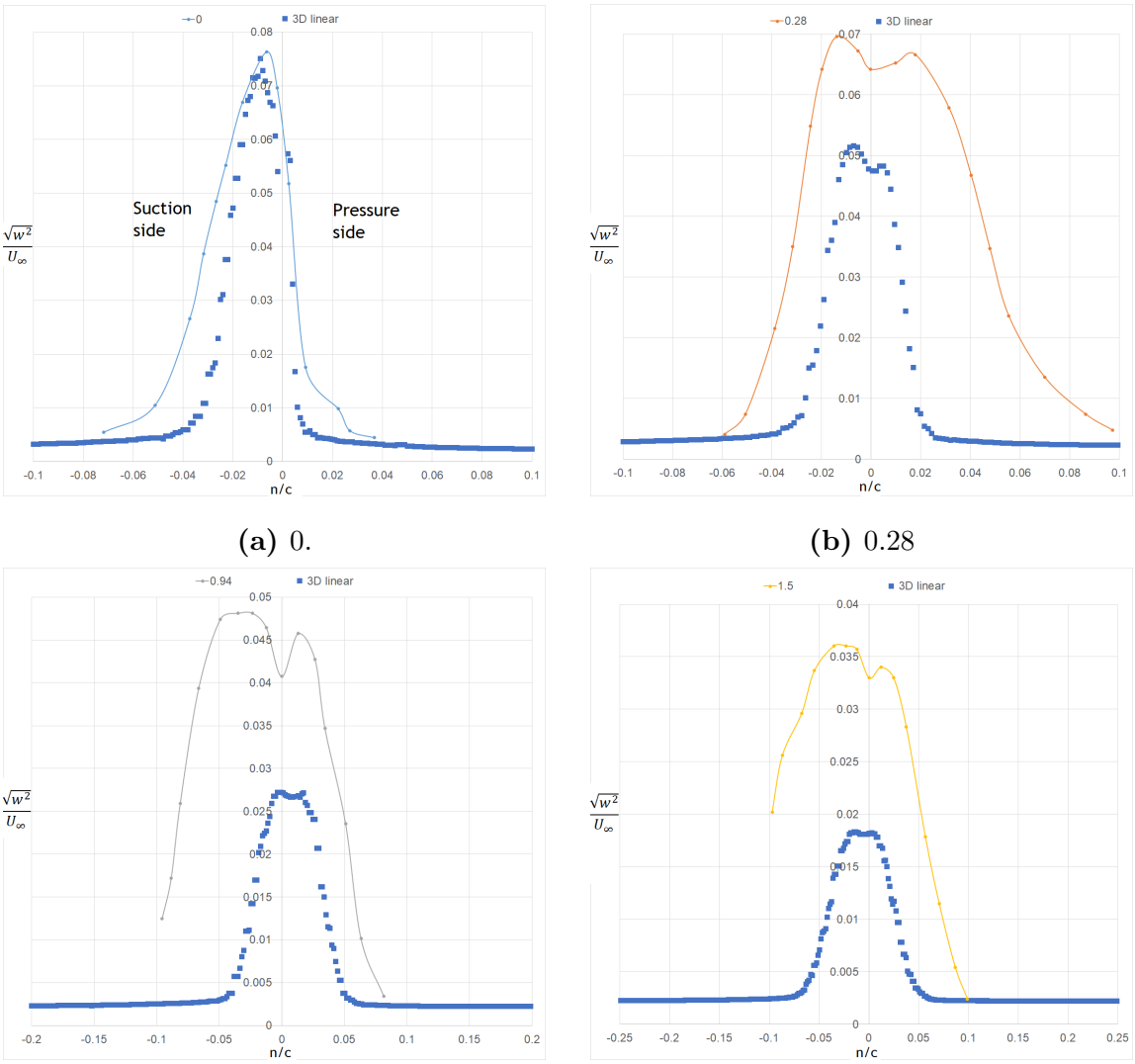

(a) 0.

(b) 0.28

(c) 0.94.

(d) 1.5

Figure 5.24: Experimental, 2D and 3D STAR-CCM+ data plots for the spanwise shear stress in the wake downstream of the NACA 0012 wing at 6 degrees angle of attack and Reynolds number of 0.38 million.

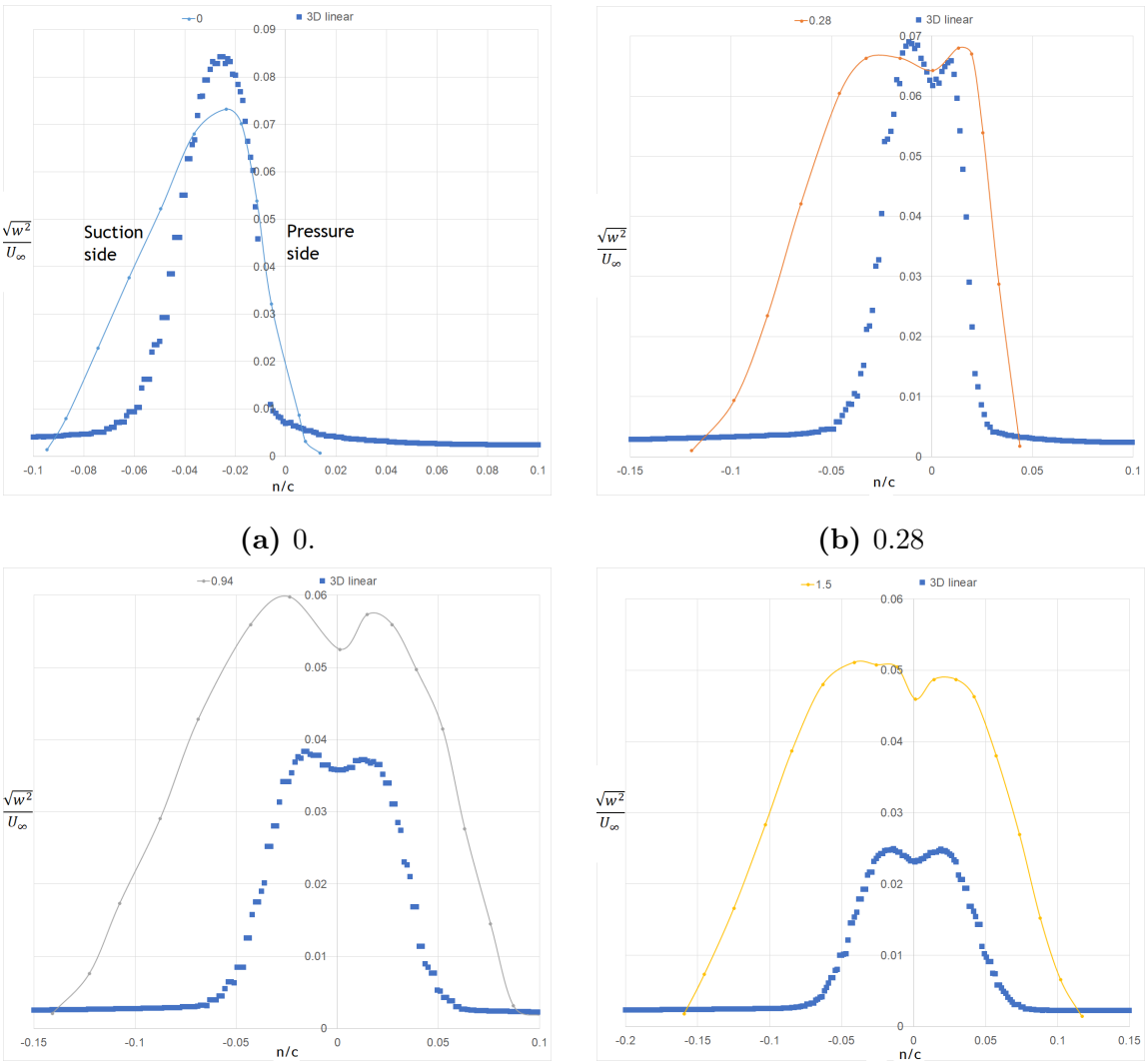

(a) 0. **(b)** 0.28

(c) 0.94. **(d)** 1.5

Figure 5.25: Experimental, 2D and 3D STAR-CCM+ data plots for the spanwise shear stress in the wake downstream of the NACA 0012 wing at 9 degrees angle of attack and Reynolds number of 0.38 million.

The behavior of the computed turbulence intensity in the spanwise direction corresponds with the experimentally observed values by Hah and Lakshminarayana (1982). For all three incidence angles, the turbulence intensity level in the spanwise direction is lower on the pressure side than in the suction side and there exists a dip near the wake center. The dip reduces with the increase in streamwise distance as was experimentally observed by Hah and Lakshminarayana (1982).

The turbulence levels in the spanwise direction are observed to peak away from the wake center and then decrease to zero towards the free stream. This observation corresponds to the steep velocity gradients of the mean velocity profile in the suction and pressure side, away from the wake center as seen in subsubsection 5.4.3.1 and has been observed in subsections 5.4.3.2 and 5.4.3.3.

The computed quantities of the turbulence levels in the spanwise direction are comparable to those observed experimentally by Hah and Lakshminarayana (1982). However, a loss in accuracy is observed with the increase in the stream wise distance, more than an increase in the incidence angle.

5.4.3.5 Shear stress

This subsubsection gives a comparison of the shear stress profiles in the wake for downstream distances $x/c = 0, 0.28, 0.94$ and 1.5 from the airfoil and wing trailing edge and $\alpha = 3$, 6 and 9. Figures 5.26, 5.27 and 5.28 give a comparison of the shear stress profiles at the wake for $\alpha = 3$, 6 and 9 respectively.

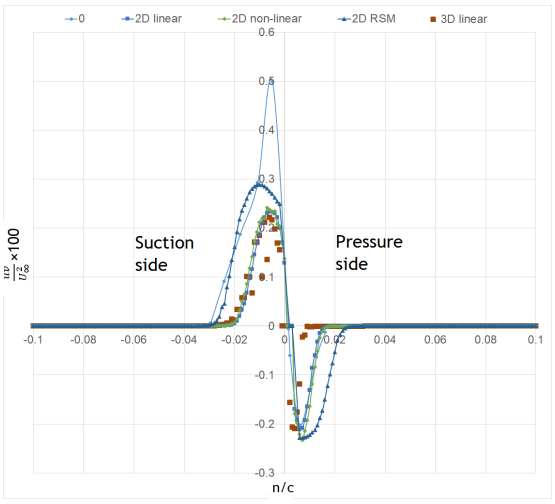

(a) 0.

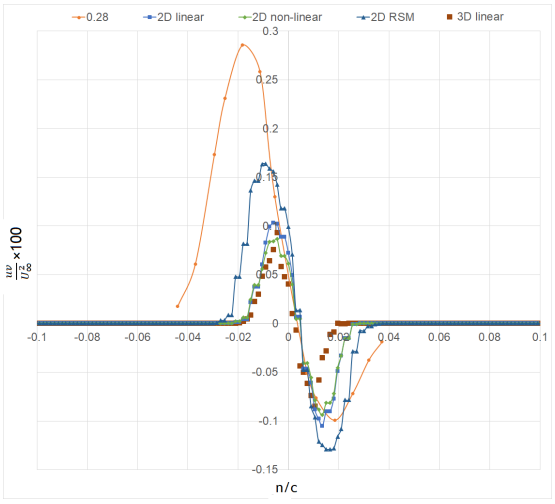

(b) 0.28

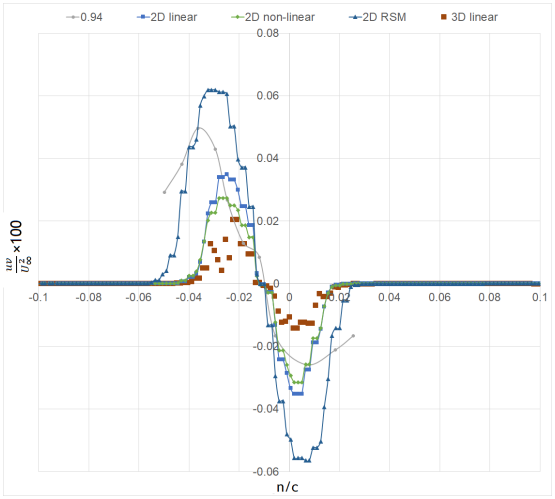

(c) 0.94.

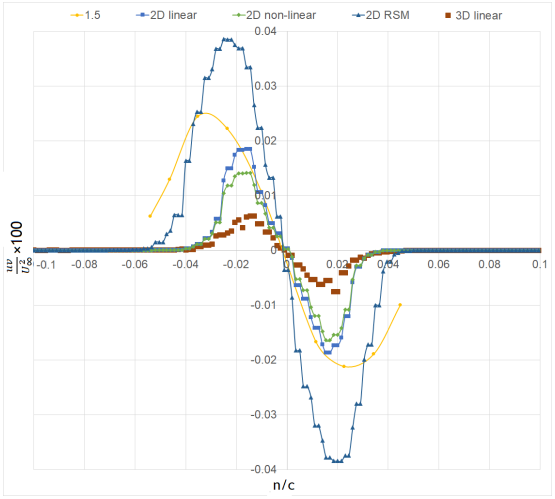

(d) 1.5

Figure 5.26: Experimental, 2D and 3D STAR-CCM+ data plots for the shear stress in the wake downstream of the NACA 0012 airfoil and wing at 3 degrees angle of attack and Reynolds number of 0.38 million.

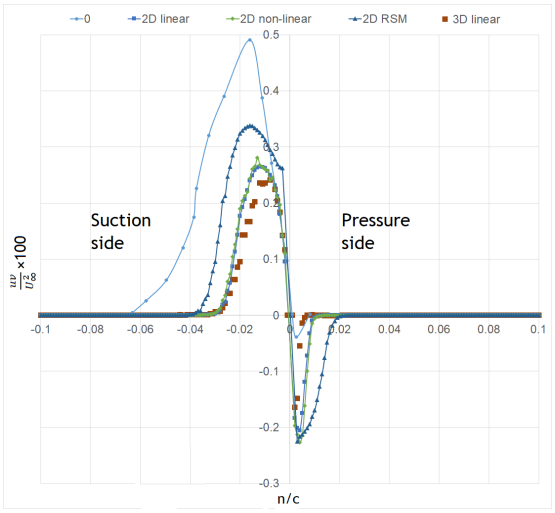

(a) 0.

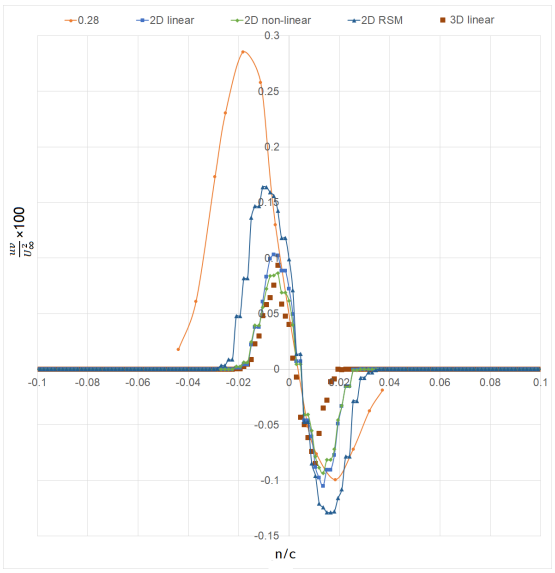

(b) 0.28

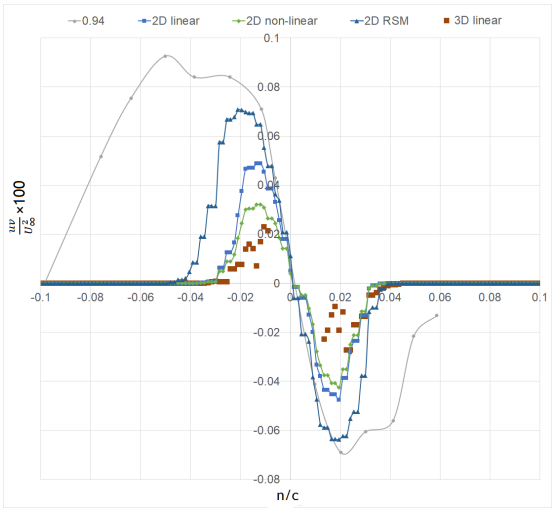

(c) 0.94.

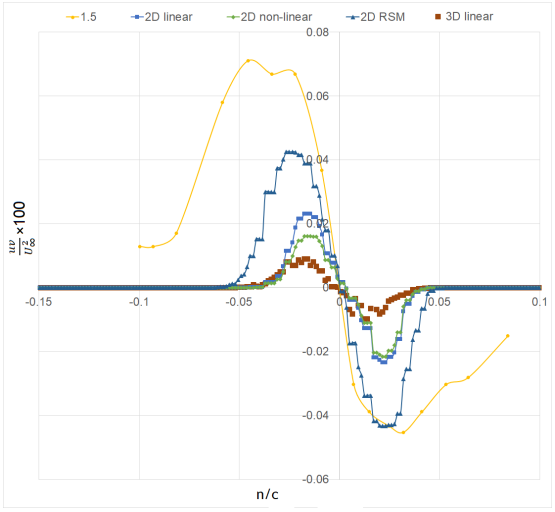

(d) 1.5

Figure 5.27: Experimental, 2D and 3D STAR-CCM+ data plots for the shear stress in the wake downstream of the NACA 0012 airfoil and wing at 6 degrees angle of attack and Reynolds number of 0.38 million.

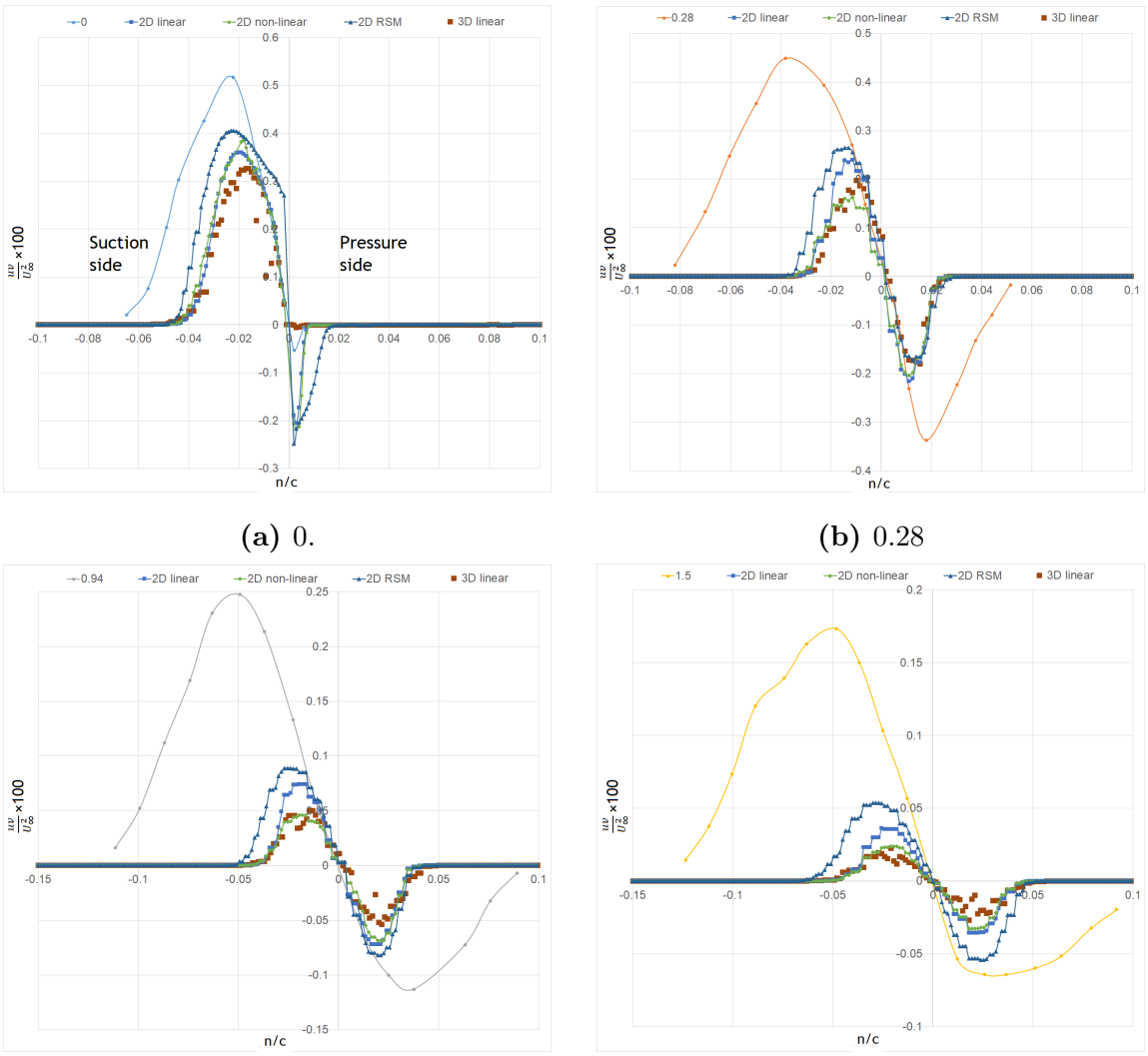

(a) 0. **(b)** 0.28

(c) 0.94. **(d)** 1.5

Figure 5.28: Experimental, 2D and 3D STAR-CCM+ data plots for the shear stress in the wake downstream of the NACA 0012 airfoil and wing at 9 degrees angle of attack and Reynolds number of 0.38 million.

The behavior of the computed shear stress in the wake shows the same trend which was observed experimentally by Hah and Lakshminarayana (1982). The shear stress profiles are asymmetric at the near wake for all studied cases and tend towards being symmetric beyond one chord downstream as was observed experimentally by Hah and Lakshminarayana (1982). At the near wake the magnitude of the shear stress is observed to be smaller in the pressure side compared to the suction side. This

corresponds to the observations made in subsubsections 5.4.3.2, 5.4.3.3 and 5.4.3.4, that the suction side experiences more turbulence compared to the pressure side as a consequence of the airfoil being at a positive incidence angle. The difference in magnitude between the suction and pressure side of the airfoil decreases with streamwise distance as was observed experimentally by Hah and Lakshminarayana (1982).

The shear stress changes sign at the wake center and the magnitude of the shear stress is observed to peak away from the wake center and then decrease to zero towards the free stream. According to Versteeg and Malalasekera (2007) the turbulence intensity levels are highest when the velocity gradient is largest. This observation corresponds to the steep velocity gradients of the mean velocity profile in the suction and pressure side, away from the wake center as seen in subsubsection 5.4.3.1. This peak in shear stress away from the wake center also corresponds to the observed peaks in turbulence levels in subsubsections 5.4.3.2, 5.4.3.3 and 5.4.3.4.

The computed quantities for the shear stress are comparable to those observed experimentally by Hah and Lakshminarayana (1982). However, a loss in accuracy is observed with the increase in incidence angle and streamwise distance. The predictions of the Reynolds stress turbulence model are closer to the experimentally observed values for all the cases that were studied compared to the SST $k-\omega$ turbulence model with the $\gamma - Re_\theta$ transition model that uses the linear and non-linear turbulence relations. A slight loss in accuracy due to interpolation errors is observed for the 3D results and becomes more pronounced with downstream distance.

There is an, overall, satisfactory agreement between the 2D and 3D STAR-CCM+ data and the baseline data for the angles of attack that were studied. The good agreement in the 2D and 3D STAR-CCM+ data and the baseline data demonstrates the satisfactory capacity of the SST $k-\omega$ turbulence model with the $\gamma-Re_\theta$ transition model to model a 2D transitional and turbulent wake flow on an airfoil and a 3D transitional and turbulent wake flow on a wing. The SST $k-\omega$ turbulence and $\gamma - Re_\theta$ transition model is, therefore, validated for a transitional and turbulent

wake flow on sailplane airfoil and wing geometries.

Summary

This chapter covered the first and second steps of the validation process that was employed in the current project. A validation employing the unit and benchmark cases was presented. The SST $k-\omega$ turbulence model with the $\gamma - Re_\theta$ transition model was validated for a steady-state, 2D and 3D transitional and turbulent wake flow of an incompressible fluid on the NACA 0012 airfoil and wing at low-Reynolds numbers and low-turbulence levels. Therefore, the SST $k-\omega$ turbulence and $\gamma - Re_\theta$ transition model was validated for a transitional and turbulent wake flow on sailplane airfoil and wing geometries.

Chapter 6

Mu-31 validation

Introduction

This chapter presents the third step of the validation process that was employed in this project. A validation of the SST $k-\omega$ turbulence model with the $\gamma - Re_\theta$ transition model for the subsystem case is given. Section 6.1 introduces the requirements Mu-31 validation study. Section 6.2 presents the geometric modeling. Section 6.3 presents the validation setup with the computational domain configuration, computational mesh configurations, flow physics and solver set up and convergence criterion in subsections 6.3.1,6.3.2, 6.3.3 and 6.3.4, respectively. Section 6.4 presents the validation results and discussion.

6.1 Validation requirements

A requirement for the validation case on the Mu-31 is a good agreement in the characteristics/behavior and the quantity of the computed engineering quantities with the experimental results. The engineering quantities of interest were the fuselage and wing drag coefficient (interference drag). Flow streamlines on the fuselage, wing and wing-fuselage junction were also considered. The experimental data by Hulsmann (2006) was consulted for validation purposes.

6.2 Geometry modeling

The CAD model of the Mu-31 sailplane fuselage was provided by the Delft University of Technology. Figure 7.1 gives the initial configuration of the Mu-31 wind tunnel model with a zero degrees flap configuration.

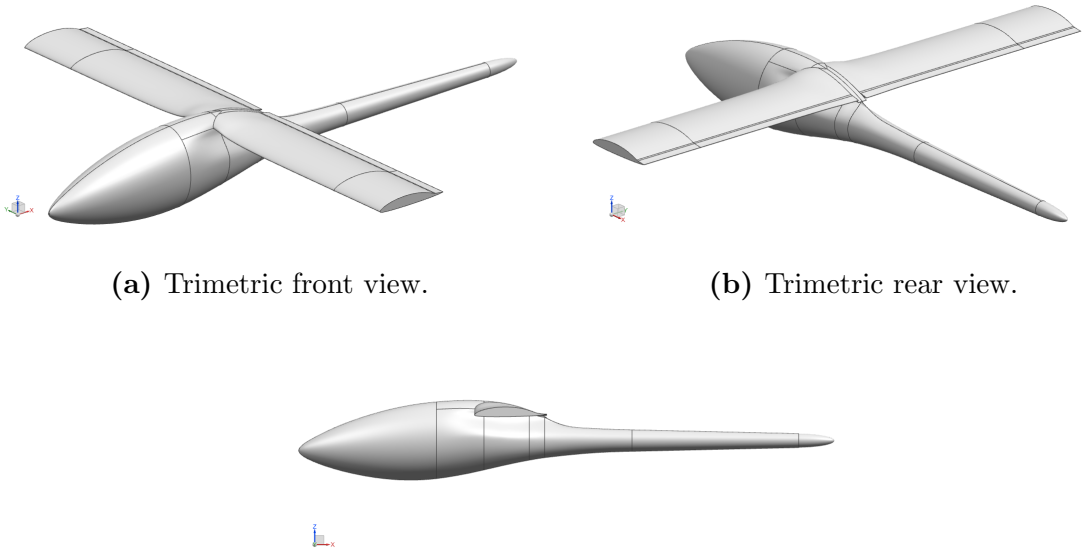

(a) Trimetric front view.

(b) Trimetric rear view.

(c) Side view.

Figure 6.1: Initial configuration of the Mu-31 sailplane fuselage wind tunnel model.

CFD analysis demands a highly detailed geometry with extremely small scales for contact edges and no intersecting faces. The stringent demand for geometric detail has implications on the cell count at the discretization stage, depending on the complexity (detail) of the geometry. In order for the meshing code, incorporated in STAR-CCM+, to discretize the domain, all self-intersecting surfaces that may be present in the geometry must be remedied. It was therefore, necessary to prepare the Mu-31 geometry for the CFD analysis. The CAD model of the Mu-31 was already simplified for the CFD analysis, i.e. all geometric complexities (components) which would have demanded an unnecessary large number of computational cells to capture the exact geometry of the components were already removed and therefore, the geometry clean-up process was not necessary. Due to the symmetric nature of

the Mu-31 geometry, only half of the sailplane was modeled.

6.2.1 Surface preparation

Importing low quality or complex CAD geometries often generates problems with the meshing operations. Self intersecting surfaces, holes, gaps etc., are commonly encountered in low quality or complex CAD geometries and may render the imported geometry not usable for surface and volume meshing, i.e., although surfaces may look joined in a large scale, however, when zoomed in, self-intersecting surfaces, holes or gaps may exist at a microscopic level.

Self intersecting faces and microscopic gaps were found to exist in the Mu-31 CAD model and it was consequently, impossible to discretize the flow domain. A surface wrapper operation was performed on the geometry to remedy the self-intersecting faces and microscopic gaps. The surface wrapper operation wraps the initial surface to provide a closed and manifold surface mesh from a poor or complex geometry. This procedure ensures that the geometry is closed and of sufficient quality for generating surface and volume meshes. The result of a surface wrapping operation is a closed, water-tight, surface that is shown in figure 6.2 (Ewing, 2015; Siemens, 2017; 2018).

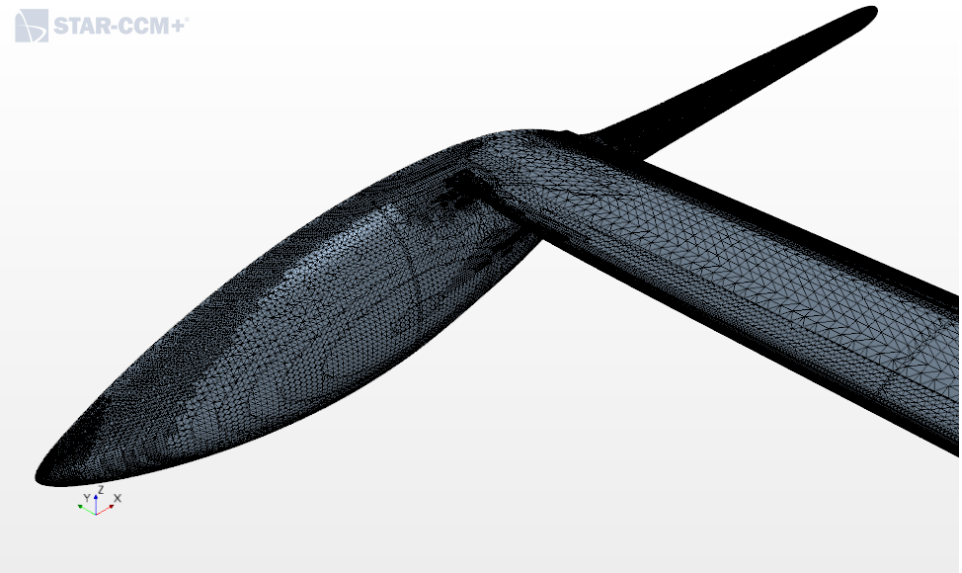

Figure 6.2: Mu-31 geometry after surface wrapper operation.

The surface obtained by the wrapping process became the new reference geometry for the surface and volume mesh. The automatic surface repair operation was used to improve mesh quality.

6.3 Validation setup

6.3.1 Computational domain configuration

A three-dimensional rectangular computational domain, shown in figure 7.5, was employed in the validation study of Mu-31 sailplane geometry.

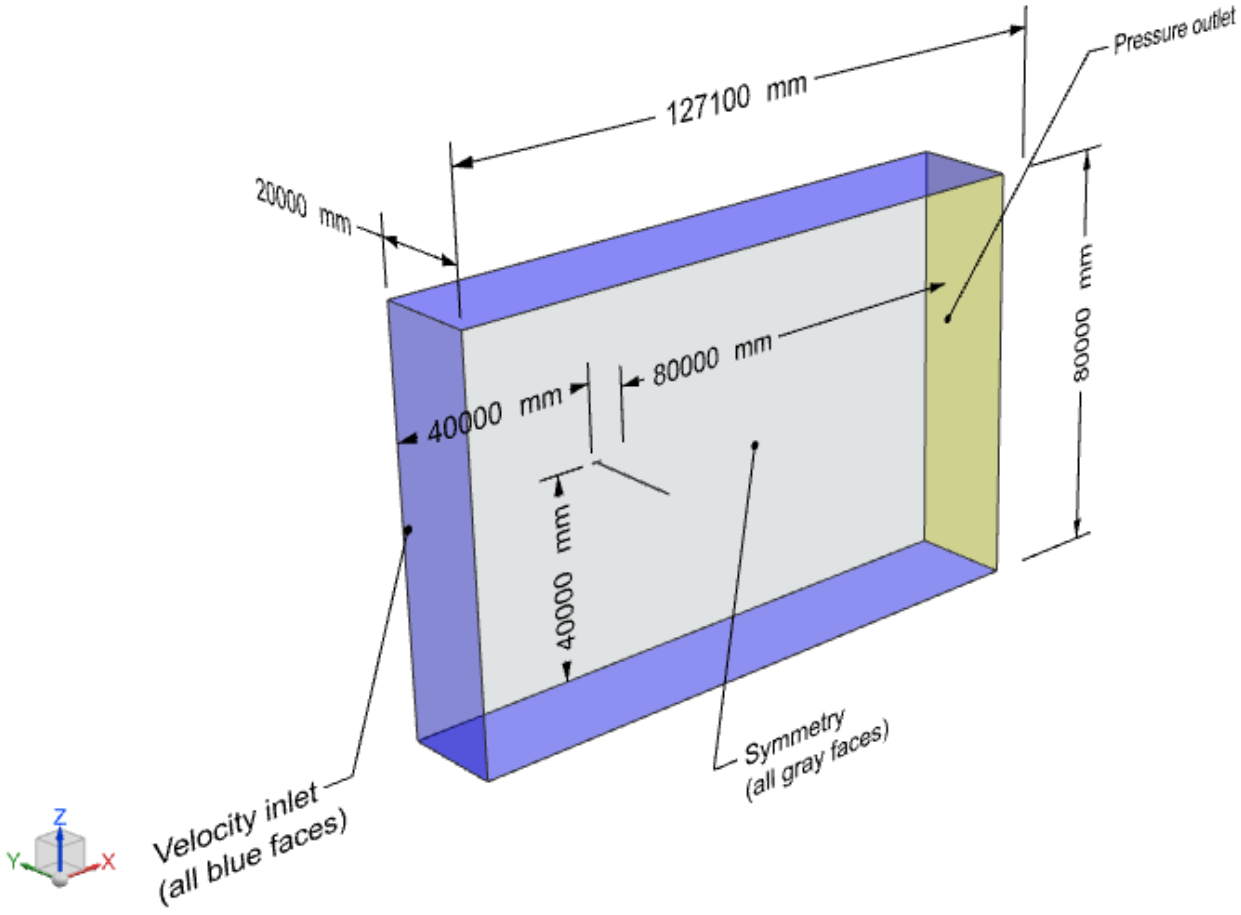

Figure 6.3: JS-1 wind tunnel model.

The computational domain was divided into four boundary types, viz., velocity inlet,

pressure outlet, symmetry and wall boundaries, with different conditions imposed on them to accurately model the Mu-31 fuselage wind tunnel experiment that was conducted by Hulsmann (2006). A velocity inlet boundary condition was imposed on the upstream and far field boundaries of the computational domain while the pressure outlet boundary condition was imposed on the downstream boundary of the computational domain.

The prescribed inlet boundary conditions were set to approximate the free stream flow conditions that were employed in the wind tunnel tests by Hulsmann (2006). Measurements were made for a Reynolds number of 1.5 million based on the airfoil chord length of 0.26 m. At standard density and dynamic viscosity, the magnitude of the initial velocity was calculated to be 84.3 m/s corresponding to $Mach = 0.245$. The direction of flow was set in the x-direction$(1, 0, 0)$ for zero angle of attack and was changed by rotating the flow direction about the y-axis.

The symmetry boundary was imposed on the sides of the rectangular domain to approximate the infinite nature of the Mu-31 wing. The no-slip wall boundary condition was imposed on the Mu-31 surfaces to approximate the no fluid slip physical state (i.e. zero velocity) of the flow at the surfaces of the Mu-31.

6.3.2 Computational mesh configuration

An unstructured 3D , finite volume, core mesh and prism layer mesh was employed to discretize the computational domain. The core mesh was made up of tetrahedral cells while the prism layer mesh comprised of prismatic cells. A part-based mesh procedure was executed in STAR-CCM+.

In order to accurately capture certain, important, details of the flow, mesh refinements were introduced around the Mu-31 surfaces and in the wake region downstream of the fuselage. Figure 6.4 shows the core mesh refinements at the fuselage and the wing-fuselage junction area of the Mu-31 sailplane.

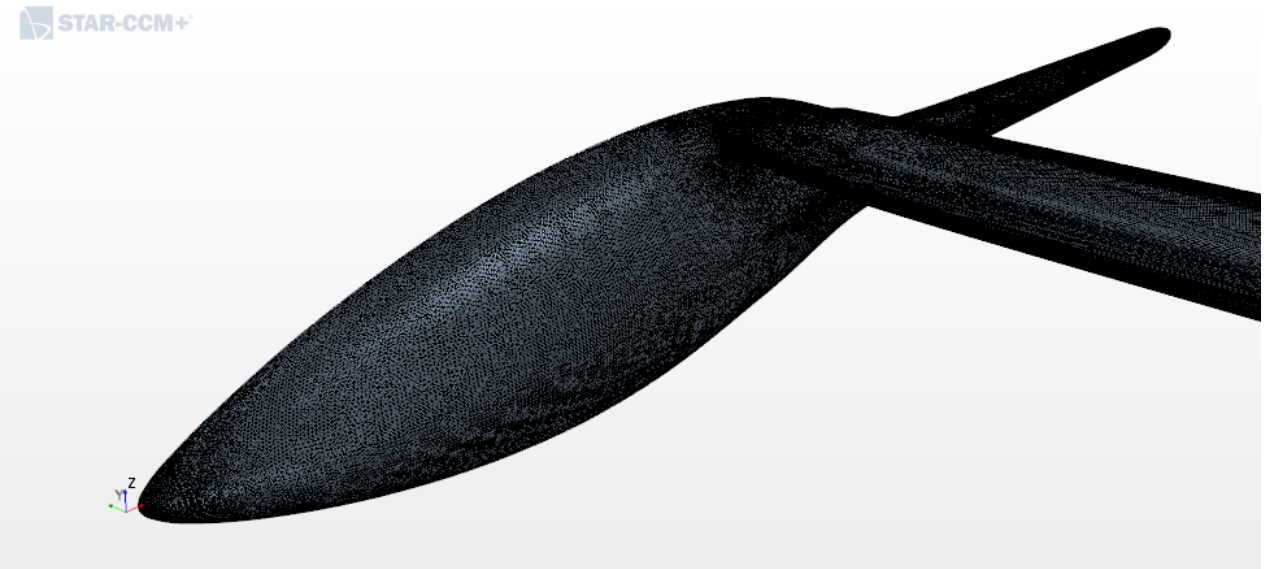

Figure 6.4: Mu-31 fuselage and wing-fuselage junction core mesh refinements.

The core mesh cell density was allowed to decrease gradually with distance, away from the Mu-31 surfaces, towards the velocity inlet and pressure outlet to achieve core mesh cell economy. Prismatic cells were introduced to resolve the boundary layer in close proximity to the Mu-31 surfaces where viscosity effects are expected to exist. A prism layer mesh model was used to model achieve a sufficiently fine mesh in the boundary layer of the fuselage, wing-fuselage junction area of the Mu-31 sailplane. The boundary layer mesh at the fuselage and wing is shown in figures 6.5 and 6.6, respectively.

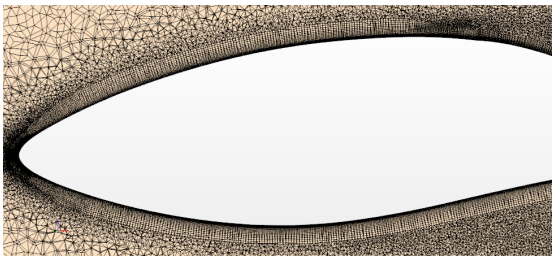

(a) Fuselage leading edge.

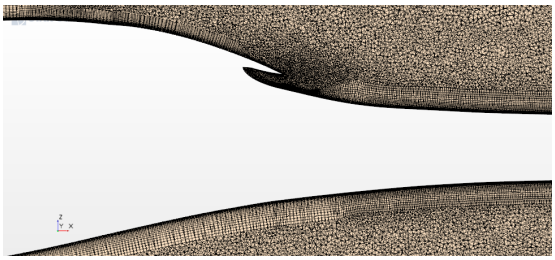

(b) Mid fuselage.

(c) Fuselage trailing edge.

Figure 6.5: Mu-31 fuselage boundary layer.

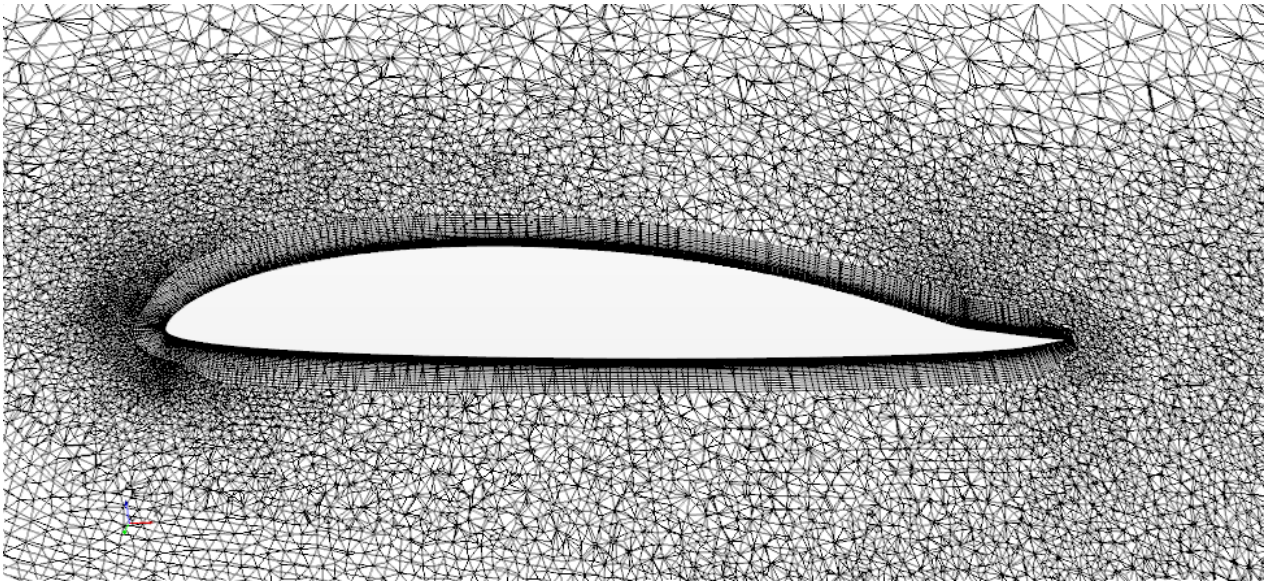

Figure 6.6: Mu-31 wing boundary layer.

The total thickness of the prism layers, i.e., total boundary layer thickness, was chosen such that all the viscosity effects due to the presence of the Mu-31 surfaces are captured in the boundary layer. The total thickness of the prism layers was calculated using the flat plate turbulent boundary layer thickness approximation

proposed by Schlichting (1978) as shown in equation 5.1. Table 6.1 gives the total boundary layer thickness approximation for each part surface of the Mu-31.

Table 6.1: Prismatic layer total boundary thickness for each part surface of the Mu-31.

Mu-31 surfaces	**Reynolds number (Re_L)**	**Boundary layer thickness (δ)**
Fuselage	11.118×10^6	0.0276
Root wing and wing	1.5×10^6	0.005

The near-wall prism layer cell thickness was calculated so that a wall y^+ value of less than one ($y^+ < 1$) was achieved in all the simulations that were conducted. The number of prism layers were chosen to be 20 layers. The number of prism layers, boundary layer thickness and near-wall prism layer cell thickness were kept constant in all the simulations.

The refinements and coarsening of the discretized computational domain was achieved by defining a minimum and target cell size for each part surface of the Mu-31, the wake regions, velocity and pressure outlet and symmetry plane relative to the base size. The base size for the final computational mesh was set to 0.4 of unit chord length. The respective percentages used in the mesh procedure are presented in Table 6.2.

Table 6.2: Mu-31 wind tunnel model mesh configuration percentage values relative to base size

Refinements	Minimum size (% of base)	Target size (% of base)
Velocity inlet, pressure outlet and symmetry boundaries	50%	800%
Fuselage	0.1%	5%
Fuselage wake	1%	1%
Root wing and wing	0.1%	10%
Root wing and wing trailing edge	0.08%	5%

Defining the cells sizes relative to a base size facilitated the grid convergence study which is presented in subsection B.3.3 in Appendix B.

6.3.3 Flow physics and solver setup

The Reynolds Averaged Navier-Stokes equations for a steady-state flow with constant density, coupled with the SST $k-\omega$ turbulence and $\gamma - Re_\theta$ transition model were employed in order to model the air flow over the Mu-31 sailplane. The method that was chosen to specify the turbulence scales, k and ω, was **turbulent intensity + viscosity ratio** which calculates k and ω by specifying free stream turbulence intensity (I), turbulence viscosity ratio (μ_t/μ) and turbulence velocity ($\boldsymbol{v}$). Equations 5.3 and 5.4 from Siemens (2017) were used for the calculations. According to Hulsmann (2006), a low degree of turbulence range of 0.002% - 0.1% can be achieved in by the low-speed and low turbulence wind tunnel of the Delf University of Technology. The free stream turbulence intensity was set to $I = 0.07\%$, based on previous work from authors such as Bosman (2012). The turbulence velocity was set to 84.3 m/s and the turbulence viscosity ratio (TVR) to μ_t/μ=1. The ambient turbulence source option was inferred from the velocity inlet boundary and the initial boundary

values that were used for the ambient turbulence source are the same as the initial boundary values for the inlet boundary, viz., $I = 0.07\%$ for turbulence intensity and 1 for TVR. The SST $k-\omega$ turbulence and $\gamma - Re_\theta$ transition model requires the definition of a blending function/free-stream edge function. The value that was used for the free-stream edge is the Mu-31 fuselage boundary layer thickness calculated with equation 5.1. A low y^+ wall treatment was chosen to resolve the laminar sub-layer of the turbulent boundary layer as endorsed by best practice (Ewing, 2015). A maximum wall y^+ of 1.0 was implemented. The segregated flow solver was chosen to solve the RANS equations and the second order upwind discretization scheme was used for all parameters.

6.3.4 Convergence criterion

Plots for the residuals, lift coefficient and drag coefficient were created to monitor convergence. In all the simulations, the minimum residual that were obtained were of the order of 10^{-4}.

6.4 Results and discussion

This section gives a presentation of the validation results for a transitional flow on the fuselage of the Mu-31 sailplane. A spatial grid convergence study was conducted to quantify the level of discretization error that exists in the CFD solution. The obtained GCI was considered to be sufficiently small to certify the numerical integrity of the CFD solutions that were obtained with the SST $k-\omega$ turbulence and $\gamma - Re_\theta$ transition model. The grid convergence study on the subsystem case is presented in subsection B.3.3 in Appendix B.

6.4.1 Drag coefficient

Table 6.3 gives the total fuselage and wing drag coefficient results for the Mu-31 fuselage at a Reynolds number of 1.5 million and lift coefficient of 0.32.

Table 6.3: Drag coefficient results for the Mu-31 fuselage at a Reynolds number of 1.5 million and lift coefficient of 0.32.

	U. Hulsmann	**STAR-CCM+**
C_L	0.31	0.32
C_D	0.87	0.96

The STAR-CCM+ results were generated for a 2 degrees angle of attack to match the lift coefficient value which was obtained experimentally by Hulsmann (2006). As seen in Table 6.3, the computed lift coefficient value was sufficiently close. The engineering quantity of interest for this validation case was the fuselage and wing drag coefficient. The results in the computed drag coefficient relative to the experimentally observed by Hulsmann (2006) was satisfactory. The estimated error was calculated to be approximately 10%. The satisfactory prediction in drag coefficient indicates that the pressure distribution and skin friction distribution on the Mu-31 fuselage is well captured. Necessarily, the boundary layer phenomena on the Mu-31 fuselage are sufficiently predicted. This shows the ability of the SST $k-\omega$ turbulence and $\gamma-Re_\theta$ transition model to model a complex 3D transitional flow on sailplane geometries.

6.4.2 Flow streamlines

The flow streamlines on the fuselage, wing and wing-fuselage junction of the Mu-31 sailplane were also considered.

Figure 6.7 gives a comparison of the computed results with the experimentally observed values by Hulsmann (2006) for the oil flow streamlines on fuselage for a Reynolds number of 1.5 million and lift coefficient of 0.32.

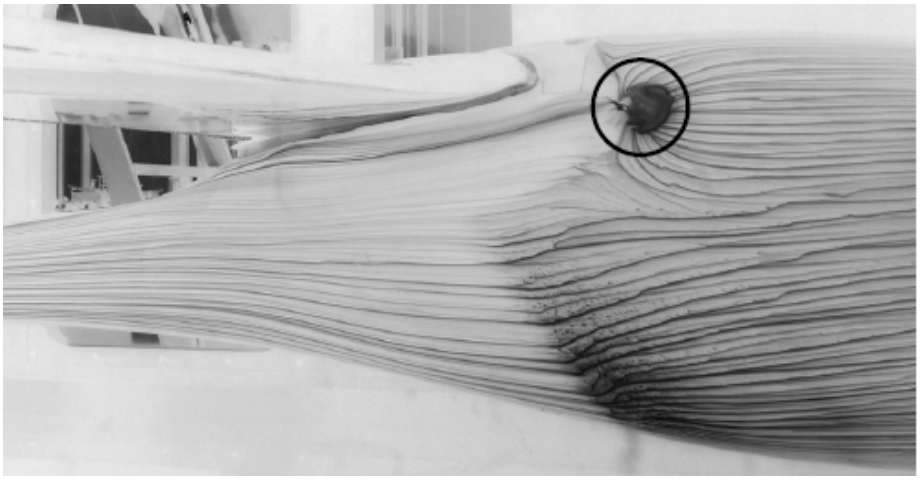

(a) Wind tunnel.

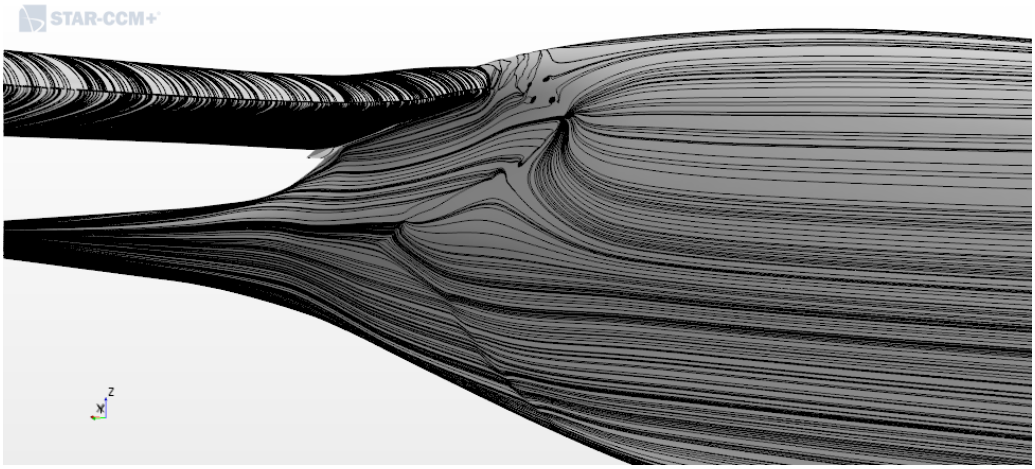

(b) CFD.

Figure 6.7: Oil flow streamlines on the fuselage for a Reynolds number of 1.5 million and lift coefficient of 0.32.

A comparison of figures 6.7a and 6.7b shows that the flow streamlines around the

wing-fuselage junction in the CFD simulation is very similar to the experimentally observed by Hulsmann (2006). As seen, the location of boundary layer transition on the fuselage is sufficiently predicted by CFD. The laminar flow separation bubble which is encircled in figure 6.7a is also accurately predicted in the CFD simulations. According to Bosman (2012), a modification that was made on the Mu-31 fuselage to reduce interference drag necessitated a deformation of the Mu-31 fuselage which starts behind the cockpit. Bosman (2012) further states that as a result of this geometric change, a separation bubble is expected right where the deformation starts due to strong adverse pressure gradients which cause the boundary layer to separate. There is a satisfactory agreement in the computed and experimentally observed results by Hulsmann (2006) for the boundary layer behavior on the fuselage. This shows that the SST $k-\omega$ turbulence and $\gamma - Re_\theta$ transition model is able to satisfactorily model a complex 3D transitional flow on the fuselage of a sailplane.

Figure 6.8 gives a comparison of the computed results with the experimentally observed values by Hulsmann (2006) for the oil flow streamlines on the upper surface for a flap setting zero degrees for a Reynolds number of 1.5 million and lift coefficient of 0.32.

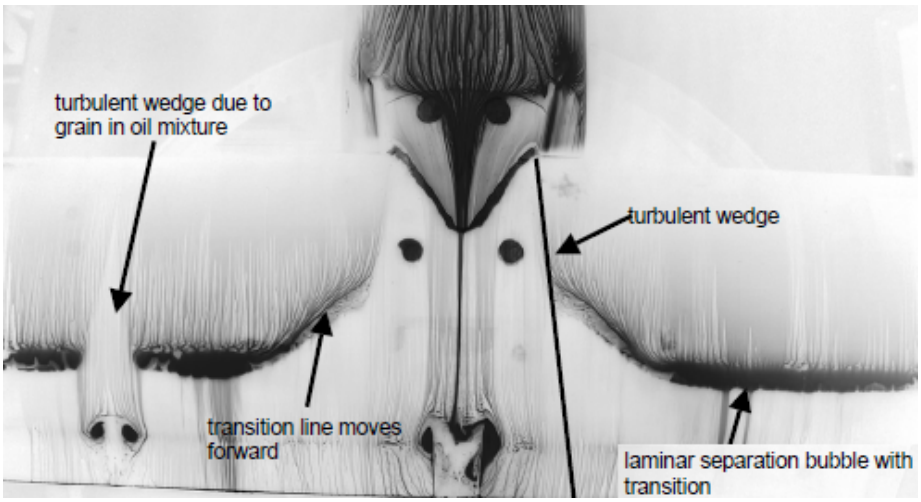

(a) Wind tunnel.

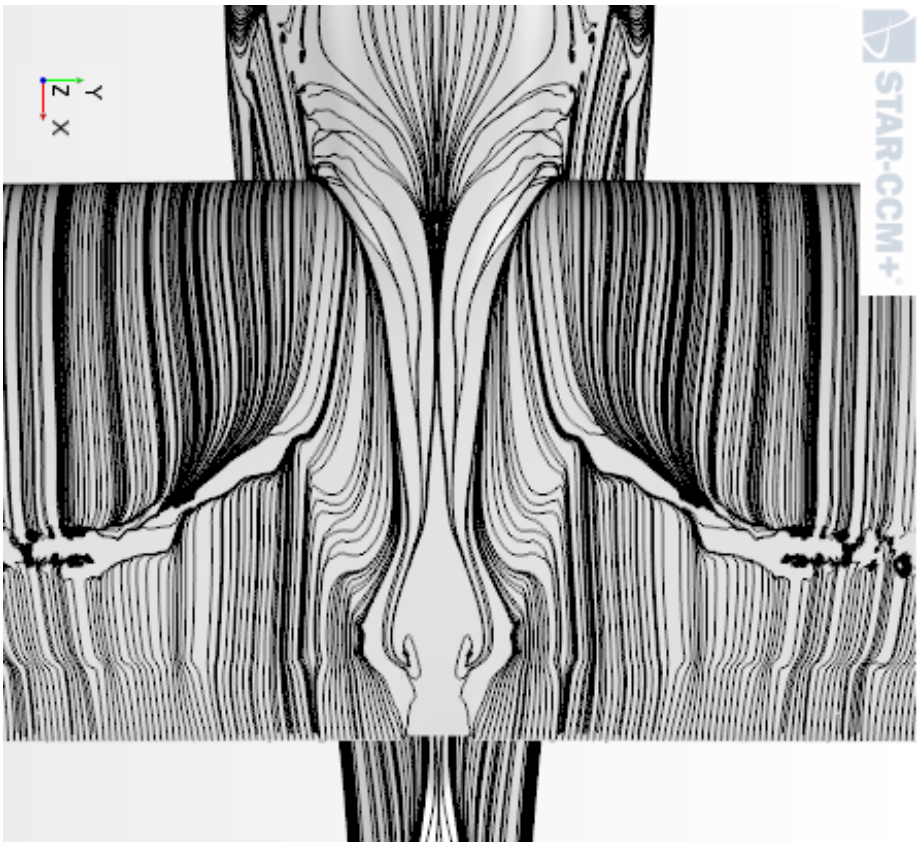

(b) CFD.

Figure 6.8: Oil flow streamlines on the upper surface of the wing and fuselage for a wing flap setting of zero degrees at a Reynolds number of 1.5 million and lift coefficient of 0.32.

A comparison of figures 6.8a and 6.8b shows a good agreement between the CFD streamlines and the experimentally observed streamlines by Hulsmann (2006) for the flow on the upper side of the wing and the wing-fuselage junction area. The laminar separation bubble which was observed experimentally by Hulsmann (2006) is accurately captured in CFD. This separation bubble indicates boundary layer transition. According to Hulsmann (2006), the boundary layer transitions at a position of approximately 60% of wing chord length. The experimentally observed results by Hulsmann (2006) reveal the existence of a turbulent wedge. The transition line moves forward towards the center of the wing-fuselage area. According to Hulsmann (2006), a blending area exists towards the fuselage where laminar and turbulent airfoil meet and thus causing the transition line to move forward. As seen in figure 6.8b, this boundary layer phenomenon is accurately captured in the CFD results. The experimentally observed turbulent wedge is also accurately captured in the CFD simulation. The small recirculating vortex at the flap gaps due to flow separation which were observed experimentally by Hulsmann (2006) are accurately predicted by the CFD simulation. There is a very good agreement between the computed results and the experimentally observed results by Hulsmann (2006) for a complex 3D transitional flow on the upper side of the wing and wing-fuselage junction area of the Mu-31 sailplane. This shows that the SST $k-\omega$ turbulence and $\gamma - Re_\theta$ transition model is able to model a complex 3D transitional flow on the wing and wing-fuselage junction for sailplane geometries.

Figure 6.9 shows a comparison between the computed results and the experimentally observed results by Hulsmann (2006) for the oil flow streamlines on the lower side of the wing for a flap setting of zero degrees for a Reynolds number of 1.5 million and lift coefficient of 0.32.

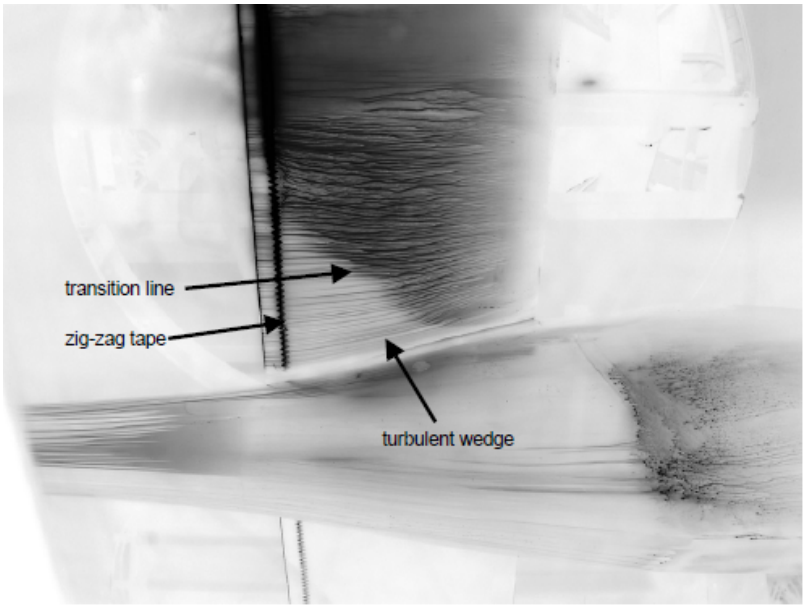

(a) Wind tunnel.

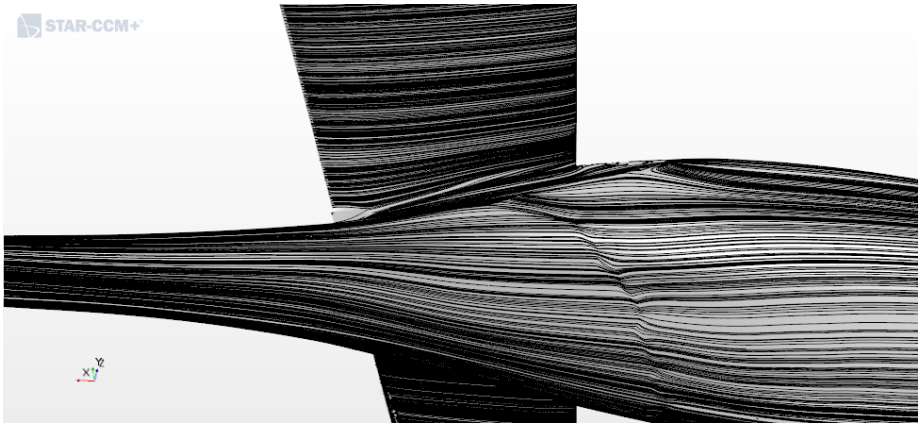

(b) CFD.

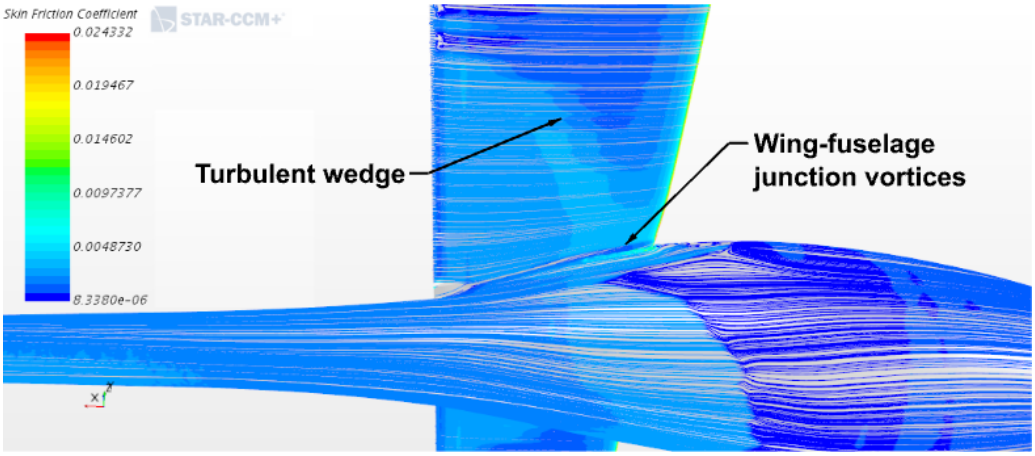

(c) CFD.

Figure 6.9: Oil flow patterns on the lower side of the wing for a flap setting zero degrees for a Reynolds number of 1.5 million and lift coefficient of 0.32.

A comparison of figure 6.9a with figures 6.9b and 6.9c shows a satisfactory agreement between the CFD simulation results and the experimentally observed results by Hulsmann (2006) for the flow lower wing and wing-fuselage junction. The boundary layer transition on the bottom part of the fuselage was seen by Hulsmann (2006) and is captured well by the CFD simulations. A turbulent wedge on the lower surfaces of the Mu-31 fuselage which is due to the wing-fuselage interaction, was observed experimentally by Hulsmann (2006). The transition line moves forward with distance towards the fuselage. This was also observed in the CFD results. The streamlines in figure 6.9b fail to show this phenomena, however a careful consideration of figure 6.9c shows that the turbulent wedge is, to some extent, captured in the CFD simulation. There is a satisfactory agreement between the computed results and the experimentally observed results by Hulsmann (2006) for a complex 3D transitional flw on the underside of the Mu-31 sailplane fuselage. This shows that the SST $k-\omega$ turbulence and $\gamma - Re_\theta$ transition model is able to model a complex 3D transitional flow on the fuselage and wing-fuselage junction of a sailplane.

Overall, the computed results and the experimentally observed results by Hulsmann (2006) are in good agreement. The SST $k-\omega$ turbulence and $\gamma - Re_\theta$ transition model can, therefore, be considered as validated for a complex transitional flow on sailplane fuselage geometries.

Summary

This chapter dealt with the third step of the validation process. The SST $k-\omega$ turbulence model with the $\gamma - Re_\theta$ transition model was validated for a 3D complex transitional boundary layer flow on the Mu-31 fuselage. The accurate prediction of the boundary layer phenomena for the complex three-dimensional flow is was an important achievement in this study and instills confidence in the ability of the SST $k-\omega$ turbulence and $\gamma - Re_\theta$ transition model to model 3D transitional flow on sailplane geometries.

Chapter 7

JS-1 turbulent wake and fin boundary layer analysis

Introduction

This chapter presents a brief validation case for the complete engineering system, i.e., a transitional and turbulent wake flow on the JS-1 sailplane. The validation case serves as the final stage of the validation process to render the SST $k-\omega$ turbulence model with the $\gamma - Re_\theta$ transition model as a validated CFD tool for the modeling of transitional and turbulent wake flow on sailplane geometries. The behavior of the JS-1 turbulent wake and fin boundary layer is also characterized and the implications of the turbulent wake for the aerodynamic performance of the JS-1 are discussed. Section 7.1 presents the geometric modeling. Subsections 7.1.1 and 7.1.2 focus on the geometry clean-up and surface preparation, respectively. Sections 7.2, 7.3, 7.4 and 7.5 discuss the computational domain configuration, computational mesh configuration, flow physics and solver setup and convergence criterion, respectively. Section 7.6 presents the simulation results. Subsections 7.6.1, 7.6.2 and 7.6.3 include a brief JS-1 wake validation, a JS-1 wake analysis and a JS-1 fin boundary layer analysis, respectively. Section 7.7 discusses the turbulent wake influence on the JS-1 sailplane aerodynamic performance. The calculations for the wake-induced

drag and discussion of results are given in subsection 7.7.1 and the possible design improvements to reduce the wake-induced drag are considered in subsection 7.7.2.

7.1 Geometric modeling

The CAD model of the JS-1 sailplane was provided with courtesy of the Jonker Sailplane company. Figure 7.1 gives the initial configuration of the JS-1 model in flight with the landing gear retracted into the fuselage.

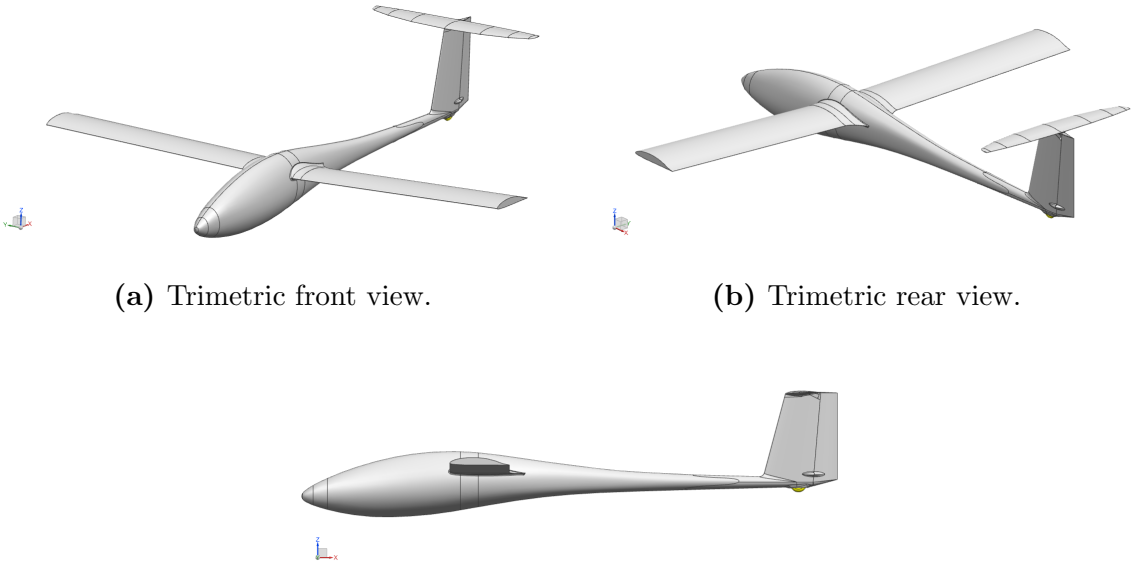

(a) Trimetric front view.

(b) Trimetric rear view.

(c) Side view.

Figure 7.1: Initial configuration of the JS-1 model in flight.

7.1.1 Geometry clean up

The first step in the preparation of the geometry for the CFD analysis was to remove all geometric complexities which will not have a significant bearing on the flow phenomena under consideration. Components in the JS-1 which were outside of the scope of interest were removed. External components such as the tail-fin landing gear, rudder horn fairing and fin-rudder junction have undesired geometrical details that must be resolved in the discretization process. Although STAR-CCM+ has the

ability to perform an analysis on the initial configuration of the JS-1 model, these components contribute very little to the flow that was investigated in the current study and due to the high surface proximities that are involved in the geometry of the components, they demand a large number of cells to capture the exact geometry.

Figure 7.2 shows the geometry clean-up operation that was performed on the JS-1 tail to remove the landing gear and the fin and rudder hinge mechanism while figure 7.3 shows the geometry clean-up operation that was performed to remove the fin and rudder junction. All geometry clean-up operations were performed by using NX 12.

(a) Initial geometry. **(b)** Final geometry.

Figure 7.2: JS-1 tail.

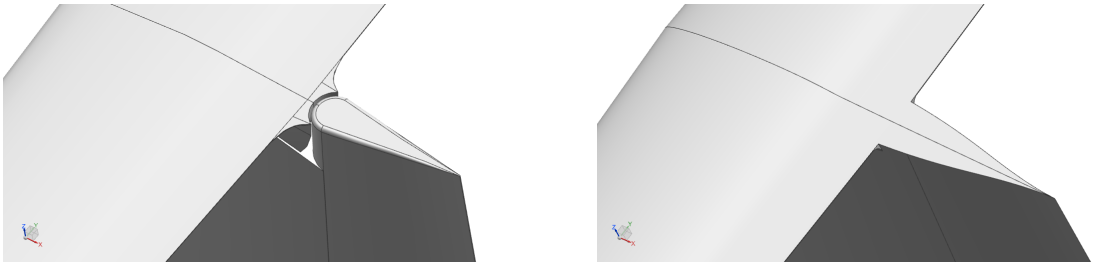

(a) Initial geometry. **(b)** Final geometry.

Figure 7.3: JS-1 fin and rudder junction.

The simplified geometry of the JS-1 sailplane CAD model was intended to reduce the computational effort without making any major changes that may influence the flow behavior on the fuselage wake and fin.

7.1.2 Surface preparation

Self intersecting faces and microscopic gaps were found to exist in the simplified model of the JS-1. A surface wrapper operation was performed on the geometry to remedy the self-intersecting faces and microscopic gaps. The result of the surface wrapping operation was a closed, water-tight surface which is shown in figure 7.4.

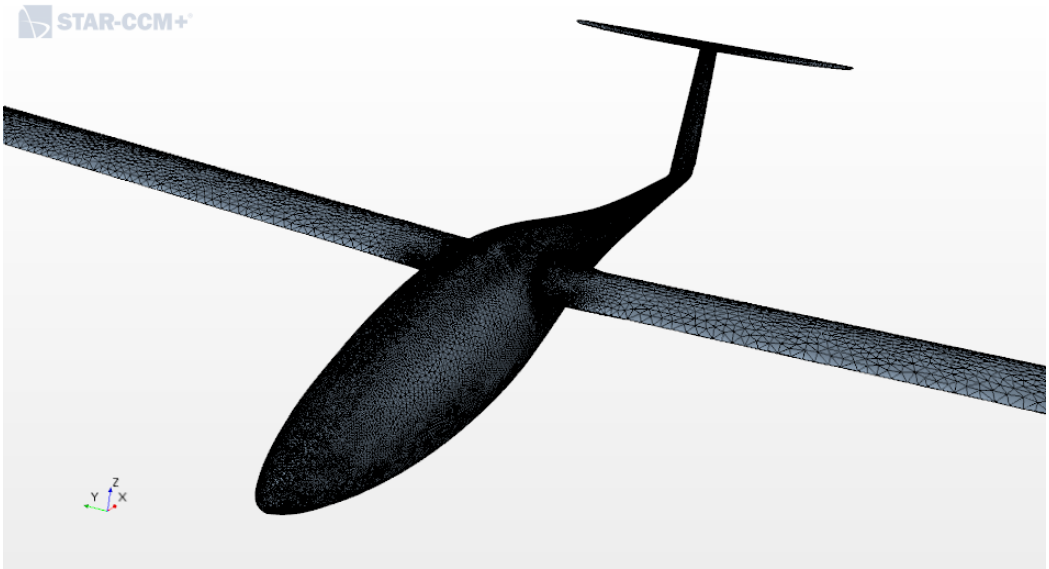

Figure 7.4: JS-1 geometry after surface wrapper operation.

The surface obtained by the wrapping process became the new reference geometry for the surface and volume mesh. The automatic surface repair operation was used to improve mesh quality.

7.2 Computational domain configuration

A three-dimensional rectangular computational domain was employed for the analysis of the transitional and turbulent wake flow on the JS-1. The computational domain with dimensions and boundary conditions is shown in figure 7.5.

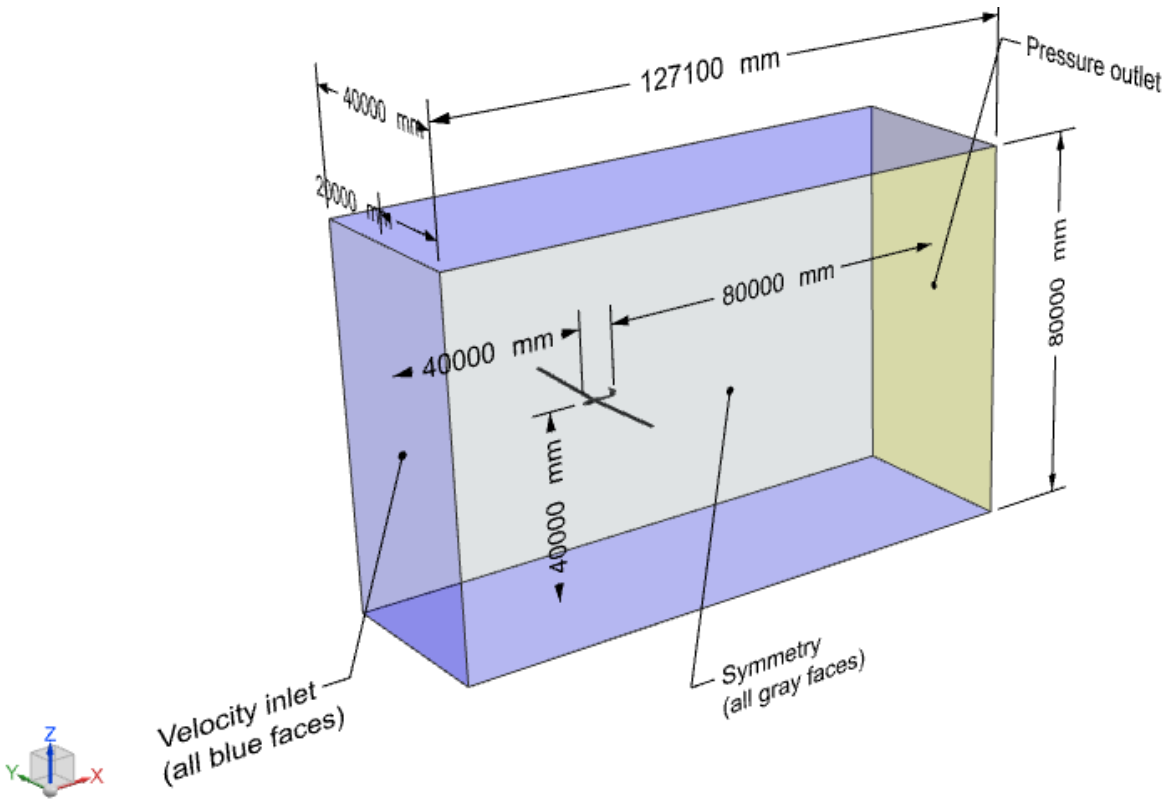

Figure 7.5: JS-1 wind tunnel model.

The computational domain was divided into four boundary types, viz., velocity inlet, pressure outlet, symmetry and wall boundaries with different conditions imposed on them to accurately model the JS-1 sailplane in free-flight. A velocity inlet boundary condition was imposed on the upstream and far field boundaries of the computational domain while the pressure outlet boundary condition was imposed on the downstream boundary of the computational domain.

The prescribed inlet boundary conditions were set to approximate the free stream flow conditions present in the flow on JS-1 sailplane in free-flight. The JS-1 typically soars at an approximate velocity of $120km/h$ and an altitude of $10000ft$ ($\approx 3050m$). The magnitude of the initial velocity was set to 33.33 m/s ($\approx$ $120km/h$) which corresponding to a Mach number of 0.088. The direction of flow was set in the x-direction (1,0,0) for zero angle of attack.

The symmetry boundary was imposed on the sides of the rectangular domain to approximate the infinite nature of the simplified JS-1 wing. The no-slip wall boundary condition was imposed on the JS-1 surfaces to approximate the no fluid slip physical state (i.e. zero velocity) of the flow on the surfaces of the JS-1.

7.3 Computational mesh configuration

An unstructured 3D , finite volume, core mesh and prism layer mesh was employed to discretize the computational domain. The core mesh was made up of tetrahedral cells while the prism layer mesh comprised of prismatic cells. A part-based meshing procedure was executed in STAR-CCM+.

In order to accurately capture particular, important, details of the flow, mesh refinements were introduced around the JS-1 surfaces and in the wake region downstream of the fuselage. Particularly, of all the JS-1 surfaces, the fuselage, wing-fuselage junction and fin and rudder combination received the most refinement because of their importance in the currently investigated flow phenomenon. Figure 7.6 shows the core mesh refinements at the fuselage, the wing-fuselage junction area and the tail of the JS-1.

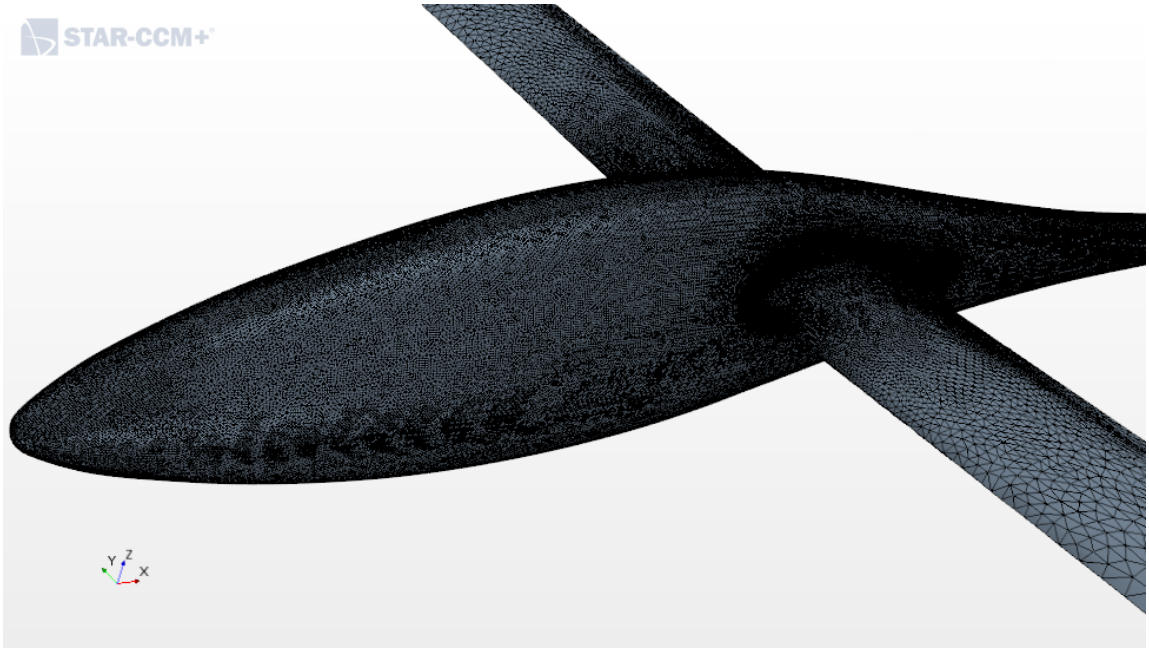

(a) Fuselage and wing-fuselage junction core mesh.

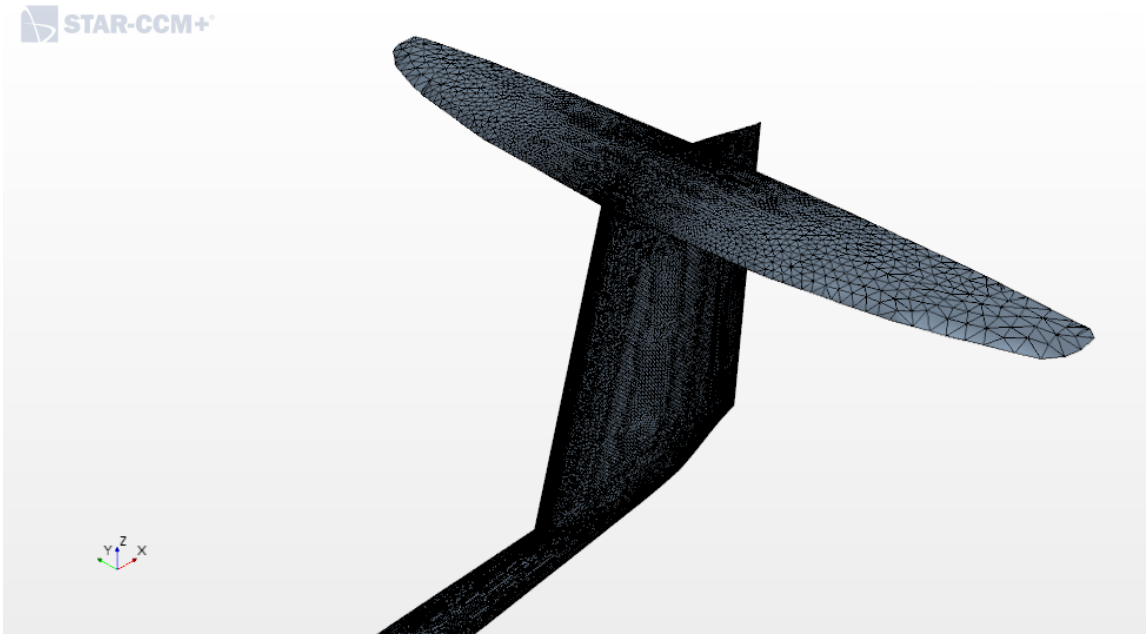

(b) Tail core mesh.

Figure 7.6: JS-1 fuselage, wing-fuselage junction and tail core mesh refinements.

The flow over the wing and stabilizer had no significant influence on the flow phenomena under consideration and therefore, to achieve core mesh cell economy, the core mesh in those areas was allowed to be coarse relative to the core mesh on the

fuselage, wing-fuselage junction area and at the fin and rudder combination as seen in figure 7.6.

Mesh refinements were introduced in wake regions, downstream of the fuselage to capture the sharp changes in mean velocity and turbulence stresses (viz., **uu**, **vv** and **ww**) and downstream of the tail. The core mesh downstream of fuselage and rudder was customized to achieve the mesh refinements in the wake. The cell density was set to decrease gradually with distance away from the JS-1 surfaces towards the velocity inlet and pressure outlet to achieve core mesh cell economy. Prismatic cells were introduced to resolve the boundary layer in close proximity to the JS-1 surfaces where viscosity effects are expected to exist. A prism layer mesh model was used achieve a sufficiently fine mesh in the boundary layer region of the fuselage, wing-fuselage junction area and at the fin and rudder combination. Figure 7.7 shows the boundary layer mesh at the fuselage, root wing and aft root wing while figure 7.8 shows the boundary layer mesh at the tail.

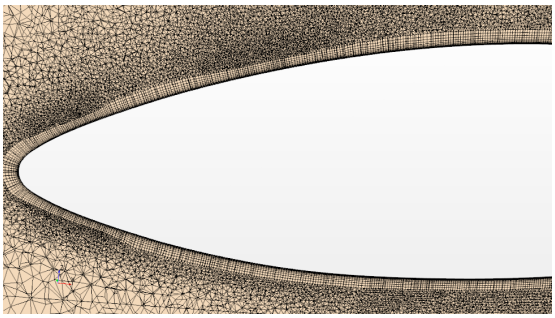

(a) Fuselage leading edge boundary layer mesh.

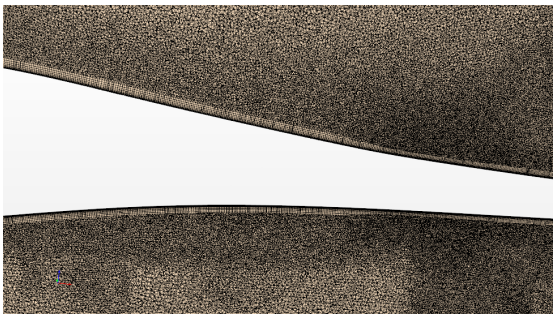

(b) Fuselage trailing edge boundary layer mesh.

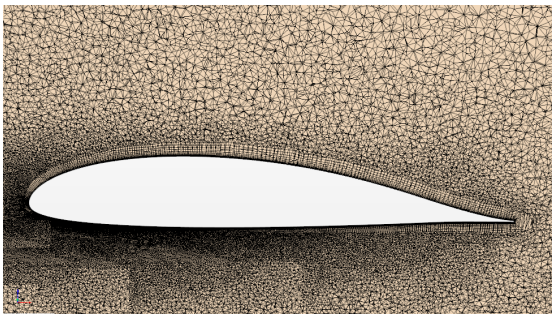

(c) Root wing boundary layer mesh.

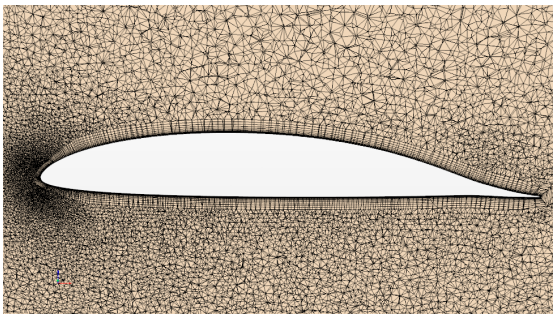

(d) Aft root wing boundary layer mesh.

Figure 7.7: JS-1 fuselage, root wing and aft root wing boundary layer mesh.

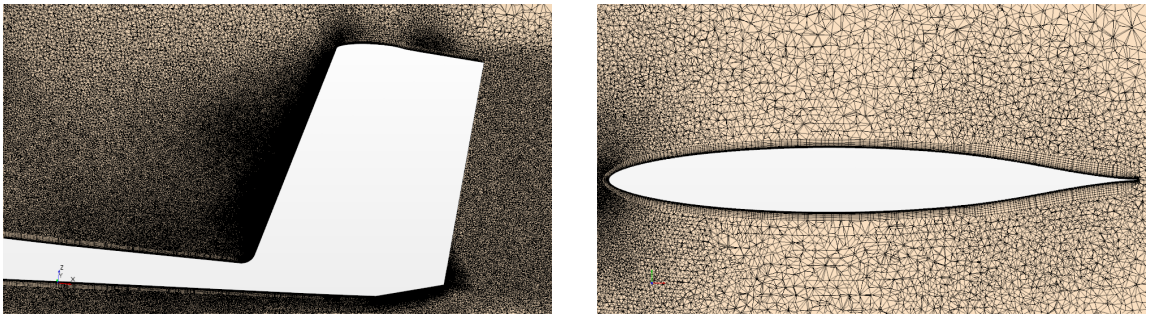

(a) Tail boundary layer and wake mesh. **(b)** Fin and rudder boundary layer mesh.

Figure 7.8: Tail boundary layer mesh.

The total thickness of the prism layers, i.e., total boundary layer thickness, was chosen such that all the viscosity effects due to the presence of the JS-1 surfaces are captured in the boundary layer. The total thickness of the prism layers was calculated using the flat plate turbulent boundary layer thickness approximation proposed by Schlichting (1978) and given in equation 5.1. Table 7.1 gives the total boundary layer thickness approximation for each part surface of the JS-1.

Table 7.1: Prismatic layer total boundary thickness for each part surface of the JS-1.

JS-1 surfaces	**Reynolds number (Re_L)**	**Boundary layer thickness (δ)**
Fuselage	12.192 $\times 10^6$	0.1
Wing root	5.152$\times 10^6$	0.05
Aft wing root and wing	1.717 $\times 10^6$	0.021
Fin	1.116 $\times 10^6$	0.0148
Rudder	1.803$\times 10^6$	0.0218
Stabilizer	1.545 $\times 10^6$	0.0193

The near-wall prism layer cell thickness was calculated so that a wall y^+ value of

less than one ($y^+ < 1$) was achieved in all the simulations that were conducted. The number of prism layers was chosen to be 20 layers. The number of prism layers, boundary layer thickness and near-wall prism layer cell thickness were kept constant in all the simulations.

The refinements and coarsening of the discretized computational domain was achieved by defining a minimum and target cell size for each part surface of the JS-1, the wake regions, velocity and pressure outlet and symmetry plane relative to the base size. The base size for the final computational mesh was set to a unit chord length. The respective percentages used in the mesh procedure are presented in Table 7.2.

Table 7.2: JS-1 wind tunnel model mesh configuration percentage values relative to base size

Refinements	**Minimum size (% of base)**	**Target size (% of base)**
Velocity inlet, pressure outlet and symmetry boundaries	50%	800%
Fuselage	0.5%	5%
Fuselage wake region	1%	1%
Wing	5%	10%
Wing trailing edge	1%	5%
Wing root and aft wing root	0.1%	5%
Wing root trailing edge and aft wing root trailing edge	0.08	1
Fin	0.1%	5%
Rudder	0.1%	1%
Stabilizer	5%	10%
Rudder and stabilizer wake	1%	1%

Defining the cells sizes relative to a base size facilitated the grid convergence study

which is presented in subsection B.3.4 in Appendix B.

7.4 Flow physics and solver setup

The Reynolds Averaged Navier-Stokes equations for a steady-state flow with constant density, coupled with the SST $k-\omega$ turbulence and $\gamma - Re_\theta$ transition model were employed in order to model the air flow over the JS-1 in free-flight. The chosen method for specifying the turbulence scales k and ω was **turbulent intensity + viscosity ratio** which calculates k and ω by specifying free stream turbulence intensity (I), turbulence viscosity ratio (μ_t/μ) and turbulence velocity ($\boldsymbol{v}$). Equations 5.3 and 5.4 from Siemens (2017) were used for the calculations. The free stream turbulence intensity was set to $I = 0.07\%$, based on previous work from authors such as Bosman (2012). The turbulence velocity was set to 84.3 m/s and the turbulence viscosity ratio (TVR) to μ_t/μ=1. The ambient turbulence source option was inferred from the inlet boundary and the initial boundary values that were used for the ambient turbulence source are the same as the initial boundary values for the upstream inlet boundary, viz., $I = 0.07\%$ for turbulence intensity and 1 for TVR. The SST $k-\omega$ turbulence and $\gamma - Re_\theta$ transition model requires the definition of a blending function/free-stream edge function. The value that was used for the free-stream edge is the JS-1 fuselage boundary layer thickness calculated with equation 5.1. A low y^+ wall treatment was chosen to resolve the laminar sublayer of the turbulent boundary layer as endorsed by best practice (Ewing, 2015). A maximum wall y^+ of 1.0 was implemented. The segregated flow solver was chosen to solve the RANS equations and the second order upwind discretization scheme was used for all parameters.

7.5 Convergence criterion

Plots for the residuals, lift coefficient and drag coefficient were created to monitor convergence. The minimum residual that were obtained in all the simulations, were

of the order of 10^{-4}.

7.6 Results and discussion

This section gives a presentation of the results for a transitional and turbulent wake flow on the JS-1. A spatial grid convergence study was conducted to quantify the level of the discretization error that exists in the CFD solution. Due to the high volume of data that was handled, only representative engineering quantities were considered for the grid convergence index (GCI). The obtained GCI was considered to be sufficiently small to comfirm the numerical integrity of the CFD solutions that were obtained with the SST $k-\omega$ turbulence and $\gamma - Re_\theta$ transition model. The grid convergence study on the complete system case is presented in subsection B.3.4 in Appendix B.

7.6.1 Wake validation

This subsection presents a brief validation of the SST $k-\omega$ turbulence and $\gamma - Re_\theta$ transition model for a steady-state, three-dimensional, transitional and turbulent wake flow of an incompressible fluid on the JS-1 sailplane at low-Reynolds number and low-turbulence level. The oil flow free-flight results that were obtained from the Jonker Sailplane company were used for comparison with the CFD results. As mentioned in section 4.5, the oil flow free-flight experiment results are not of scientific value and therefore, the comparisons that were made with the CFD results are qualitative. The analysis of the oil flow free-flight experimental results on the JS-1 fin revealed the existence of a turbulent wake as a consequence of the boundary layer flow from the fuselage and wing-fuselage junction. The SST $k-\omega$ turbulence and $\gamma - Re_\theta$ transition model will be sufficiently validated for a transitional and turbulent wake flow on the JS-1 provided that the CFD results correspond in a fundamental way with the experimentally observed boundary layer phenomena on the JS-1 fin.

A comparison of the oil flow free-flight experimental results and the CFD results on

the JS-1 fin is given in figure 7.9.

(a) Oil flow JS-1 fin boundary layer phenomena.

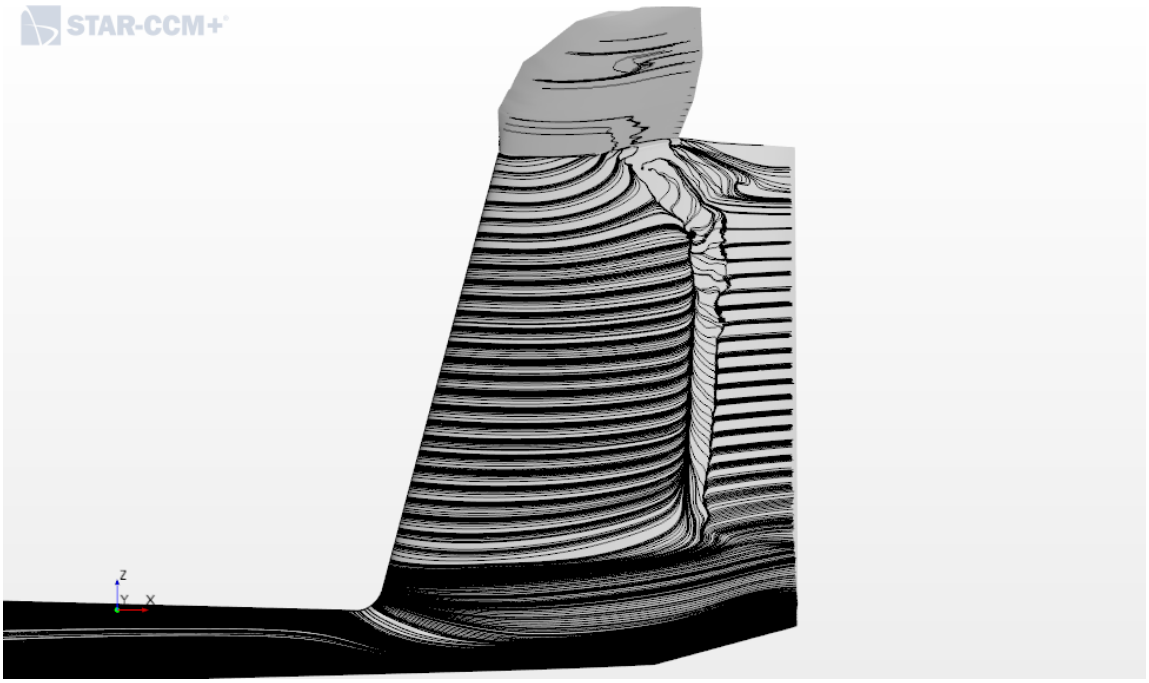

(b) Boundary layer phenomena predicted by CFD for JS-1 fin.

Figure 7.9: Oil flow free-flight experiment and CFD results on the JS-1 fin for the JS-1 turbulent wake validation.

Figures 7.9a and 7.9b shows the JS-1 fin boundary layer phenomena that were obtained in the oil flow experiment and in the CFD simulation, respectively. A boundary layer transition from a laminar to a turbulent boundary layer is observed in the top section of the fin as shown in figure 7.9b and as was observed experimentally. The boundary layer transition is identified by the existence of a transitional flow separation bubble. A transitional flow separation bubble is a visualization of the stagnant air beneath a separated layer of air from the JS-1 fin, which later reattaches downstream of the separation point (Hermann and Gersten, 2017.; Houghton, 2012; U.S. Department of Transportation, 2013). The transitional flow separation bubble indicates that a transition from a laminar to turbulent boundary layer has occured (Hermann and Gersten, 2017.; Houghton, 2012). The transitional flow separation bubble is not observed on the bottom part of the fin and therefore, there is no boundary layer transition as was observed experimentally. This strongly suggests the existence of a turbulent wake as a consequence of separated boundary layer flow from the fuselage and wing-fuselage junction as was observed experimentally. The turbulent wake affects approximately 23.6% of the total fin height. There is a good agreement between the computational and the oil flow experimental results in the observed boundary layer phenomena on the JS-1 fin. This, therefore, serves as a sufficient validation of the SST $k-\omega$ turbulence and $\gamma - Re_\theta$ transition model for a transitional and turbulent wake flow on the JS-1.

The validation process to this point has shown, at different levels, a very agreement of the results of the SST $k-\omega$ turbulence and $\gamma - Re_\theta$ transition model with the experimentally observed results for transitional and turbulent wake flow. Therefore, henceforth, the SST $k-\omega$ turbulence and $\gamma - Re_\theta$ transition model should be considered as validated CFD analysis tool for a transitional and turbulent wake flow on sailplane geometries and it can be confidently used to predict transitional and turbulent wake flow phenomena.

7.6.2 JS-1 wake analysis

This subsection presents the analysis of the wake results that were obtained by the SST $k-\omega$ turbulence and $\gamma - Re_\theta$ transition model for a steady-state, three-dimensional, transitional and turbulent wake flow of an incompressible fluid on the JS-1 sailplane at low-Reynolds number and low-turbulence level. Figure 7.10 shows the complex behavior of the boundary layer on the fuselage and wing-fuselage junction.

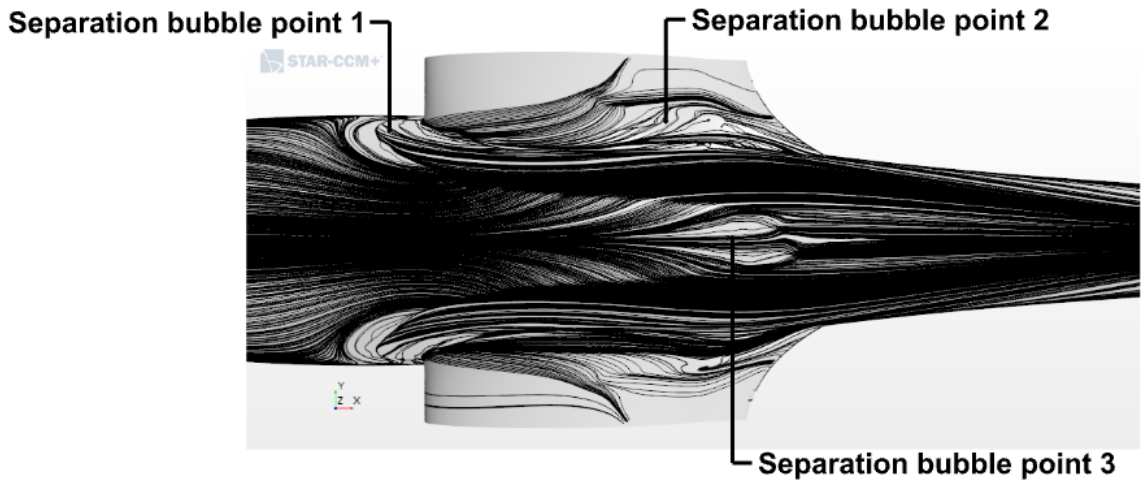

(a) Wing and fuselage junction surface streamlines.

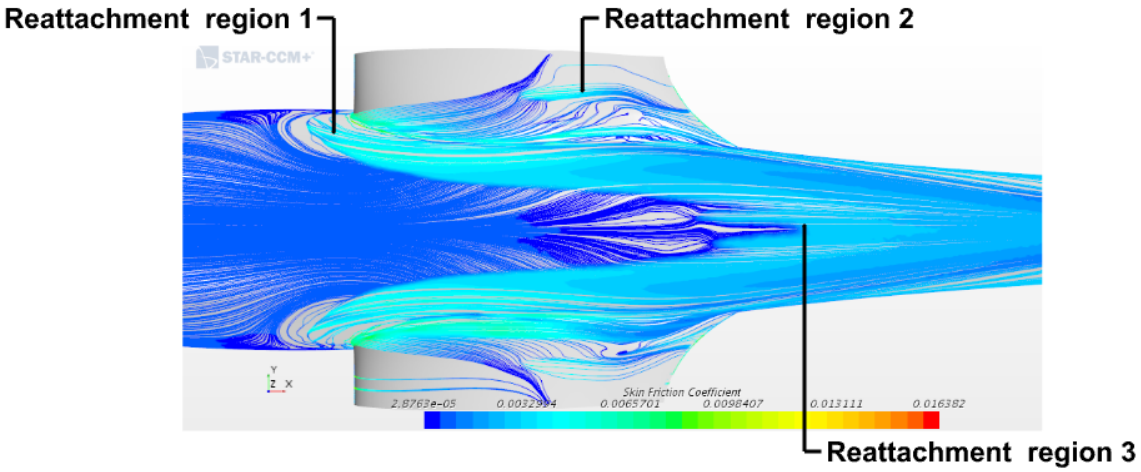

(b) Wing and fuselage junction skin friction coefficient.

Figure 7.10: JS-1 wing-fuselage junction transition points

An inspection of the boundary layer behavior in figures 7.10a and 7.10b reveals that,

overall, the boundary layer transitions at three different points on the surfaces of the fuselage and wing-fuselage junction. A separation bubble is observed at three different points on the surfaces of the fuselage and wing-fuselage junction. The separation bubble is shown by the divergence of the flow streamlines at the low skin friction regions on the fuselage and wing-fuselage surface as shown in figures 7.10a and 7.10b. In all three cases the boundary layer reattaches as a turbulent boundary layer as shown by the surge in skin friction that takes place in a short distance from the separation bubble. Figure 7.11 focuses on the boundary behavior after the second boundary layer and reattachment point, i.e., wing-fuselage junction.

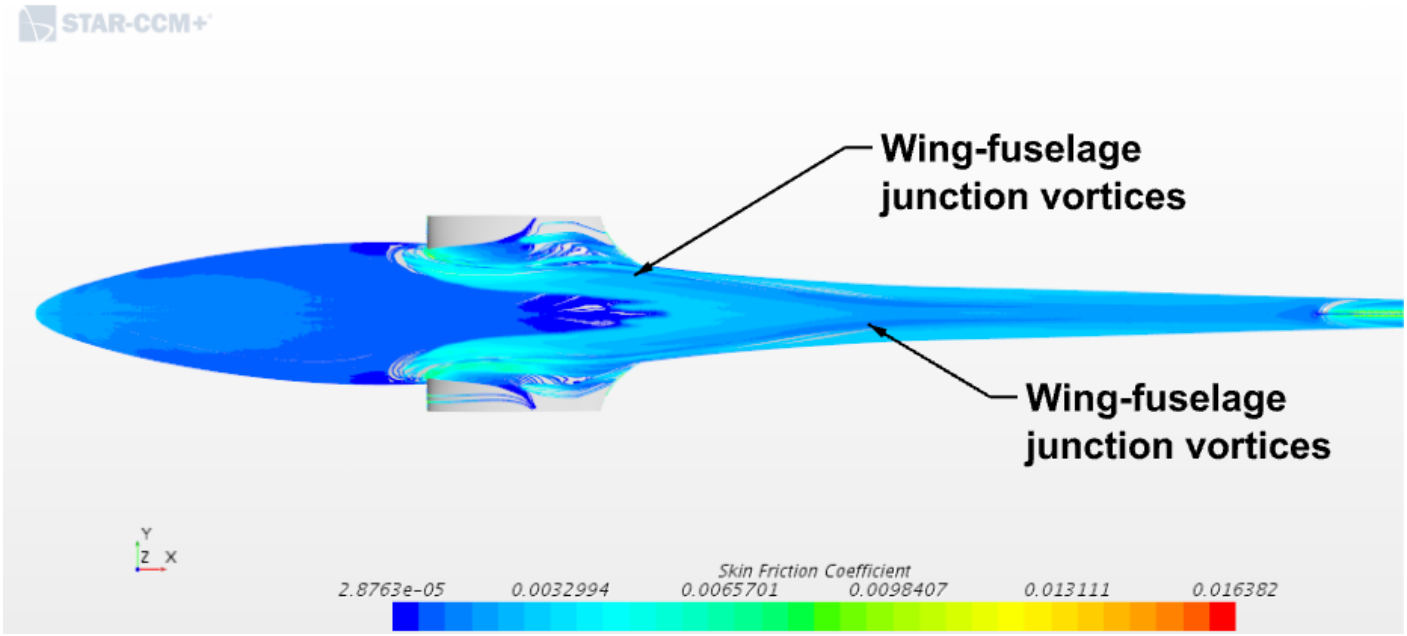

Figure 7.11: JS-1 wing-fuselage junction transition points and wake.

The skin friction coefficient are observed to decrease continuously as seen by the emerging blue contours which trail towards the tail boom of the JS-1. This indicates a low skin friction region and reveals that the turbulent boundary layer has separated to form a turbulent wake. According to Hulsmann (2006), the complex flow interaction on the wing-fuselage junction causes boundary layer separation and consequently, a horseshoe vortex system around the wing root, which disturbs the airflow on the tail boom of the sailplane. Therefore, the source of the turbulent wake on the JS-1 fin is a separated boundary layer from the wing-fuselage junction.

The mean velocity and normal Reynolds stresses were measured at the wake. The wake measurements were made at five different stations, viz., station 1 to 5 at the respective distances of 3.5 m, 4.2 m, 4.8 m, 5.5 m and 6.1 m from JS-1 fuselage leading edge as shown in figure 7.12.

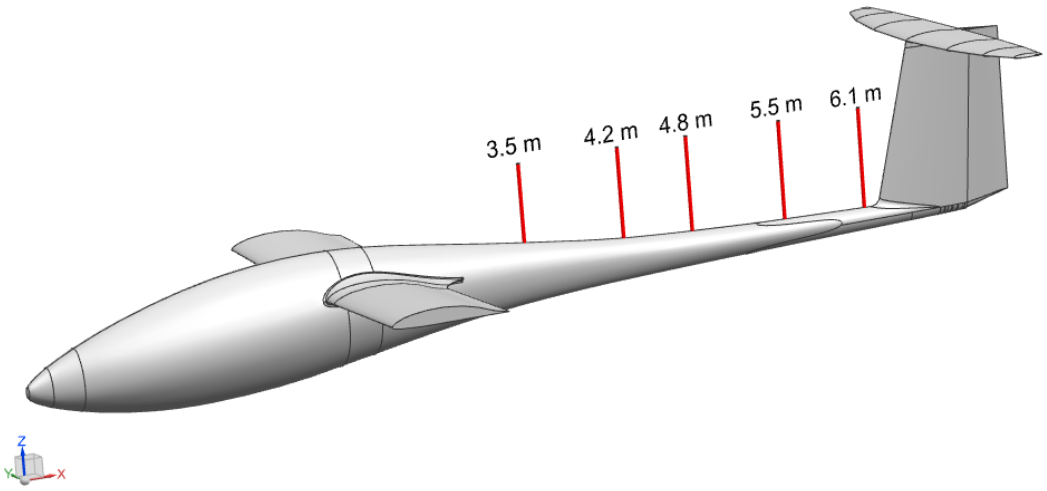

Figure 7.12: Line probes in JS-1 wake region at distances of 3.5 m, 4.2 m, 4.8 m, 5.5 m and 6.1 m from the fuselage leading edge.

The wake results for the mean velocity are given in figure 7.13. The mean velocity that was measured at the different stations in the wake is scaled with the free stream velocity and is plotted in the same co-ordinate system to show the evolution of the mean velocity in the turbulent wake.

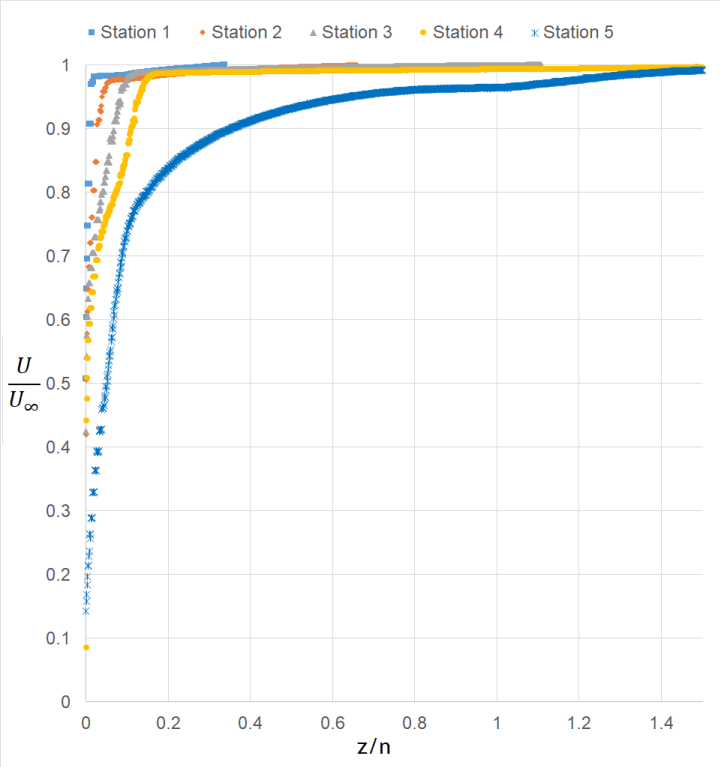

Figure 7.13: JS-1 wake mean velocity profiles at distances of 3.5 m, 4.2 m, 4.8 m, 5.5 m and 6.1 m from the fuselage leading edge.

A slender mean velocity profile is observed at station 1. The mean velocity profiles grow in width with an increase in the distance downstream of the turbulent wake. This indicates that the wake grows and spreads with distance downstream. According to Versteeg and Malalasekera (2007) the turbulence in the wake causes a vigorous mixing of adjacent fluid layers and a rapid expansion of the wake due to a process of entrainment where the fluid from the free stream region is drawn into the turbulent zone.

An extremely steep mean velocity profile is observed at station 1, i.e., a large velocity gradient. The large mean velocity gradient is observed to decrease with distance downstream. According to Versteeg and Malalasekera (2007), turbulence levels are highest when the velocity gradient is largest. Therefore the turbulence levels in the wake are expected to decrease with distance downstream.

For all the velocity profiles, the velocity gradient is observed to decrease at the surface

and towards the free stream. Necessarily, according to Wilcox (2006), turbulence decays at the surface due to the no-slip physical state of the fluid relative to the surface and according to Versteeg and Malalasekera (2007), the turbulence decays towards the free stream due to the laminar flow behavior that exists.

The wake results for the streamwise, spanwise and transverse shear stress are given in figure 7.14a, 7.14b and 7.14c, respectively. The normal turbulent stresses that were measured at different stations in the wake are scaled with the free stream velocity and are plotted in the same co-ordinate system to show the evolution of the normal stresses in the turbulent wake.

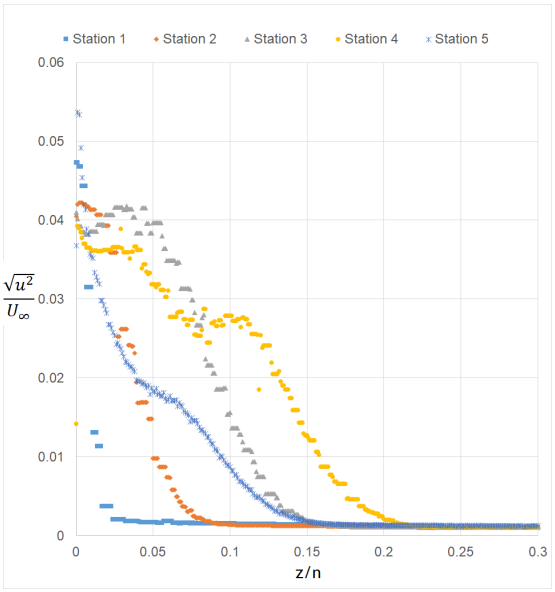

(a) Streamwise shear stress.

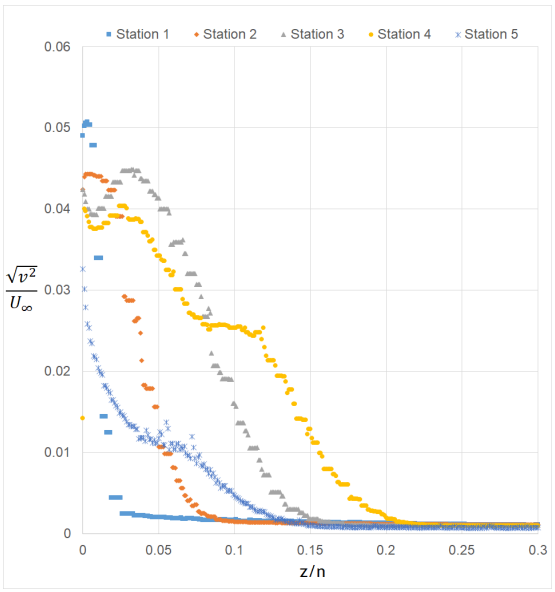

(b) Spanwise shear stress.

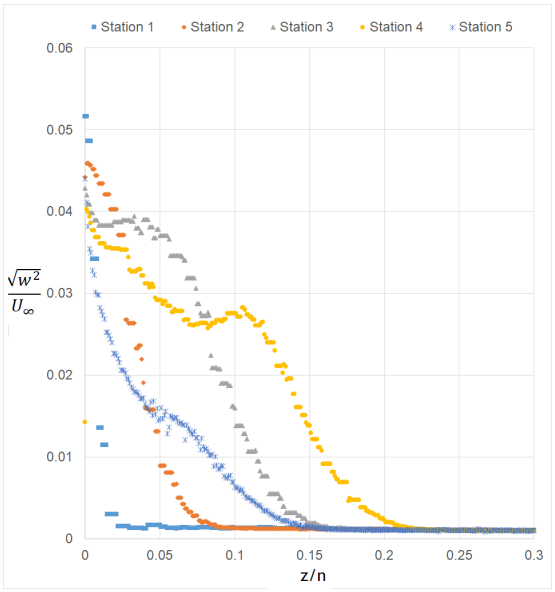

(c) Transverse shear stress.

Figure 7.14: JS-1 turbulent wake stress profiles at distances of 3.5 m, 4.2 m, 4.8 m, 5.5 m and 6.1 m from the fuselage leading edge.

For all the normal directions, the turbulent wake intensity is observed to peak with distance towards the surface. This corresponds to the observation that large velocity gradients exist in the mean velocity profiles, in close proximity to the wall. According to Versteeg and Malalasekera (2007), turbulence levels are highest when the velocity

gradient is largest.

For all the normal directions, the turbulent wake intensity, is observed to decrease at the surface and towards the free stream. According to Wilcox (2006), turbulence decays at the surface due to the no-slip physical state of the fluid relative to the surface and according to Versteeg and Malalasekera (2007), the turbulence decays towards the free stream due to the laminar flow behavior that exists. This corresponds to the decay in the mean velocity profile gradients towards the surface and towards the free stream.

For all the normal directions, the width in the turbulence levels are observed to grow until station 4 and decrease thereafter. This indicates that the turbulence stops developing at some point after station 4 and thereafter starts decaying with distance downstream. According to Alber (1980), the wake is classified into three regions, viz., the near, intermediate and far wake, and Ramaprian et al. (1982) states that significant growth in turbulent stresses is only observed in the near and intermediate wake while, in the far wake, a small development and decay in turbulent stresses is expected.

The turbulence levels in the spanwise and transverse directions near the wall is highest at station 1 and decreases with distance downstream. This corresponds to the observation that the mean velocity profile gradients decrease with distance downstream and according to Versteeg and Malalasekera (2007), turbulence levels are highest when the velocity gradient is largest. A similar behavior is observed for the turbulence levels in the streamwise direction with the exception of the turbulence level at station 5.

7.6.3 JS-1 fin boundary layer analysis

This subsection presents the analysis of the fin boundary layer results that were obtained by the SST $k-\omega$ turbulence and $\gamma-Re_\theta$ transition model for a steady-state, three-dimensional, transitional and turbulent wake flow of an incompressible fluid on the JS-1 sailplane at low-Reynolds number and low-turbulence level. The pressure

coefficient and skin friction coefficient on the fin were measured. The measurements were made at four different stations, viz, stations 1-4 at distances 0.1 m, 0.3 m, 0.7 m and 1 m, respectively, from the bottom of the JS-1 tail as shown in figure 7.15.

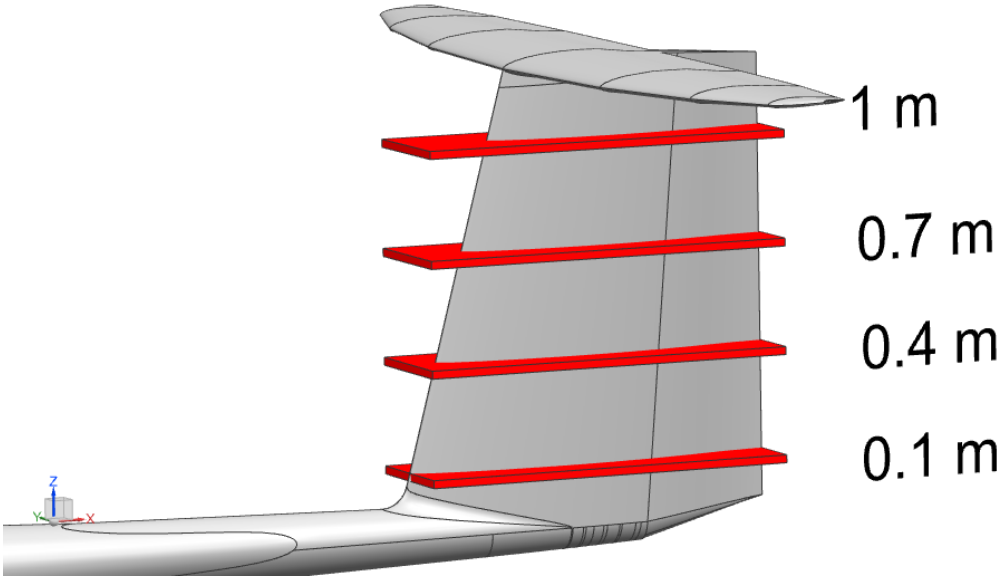

Figure 7.15: Plane sections on JS-1 fin at distances of 0.1 m, 0.3 m, 0.7 m and 1.0 m from the bottom of the JS-1 tail.

The pressure coefficient values on the fin are given in figure 7.16.

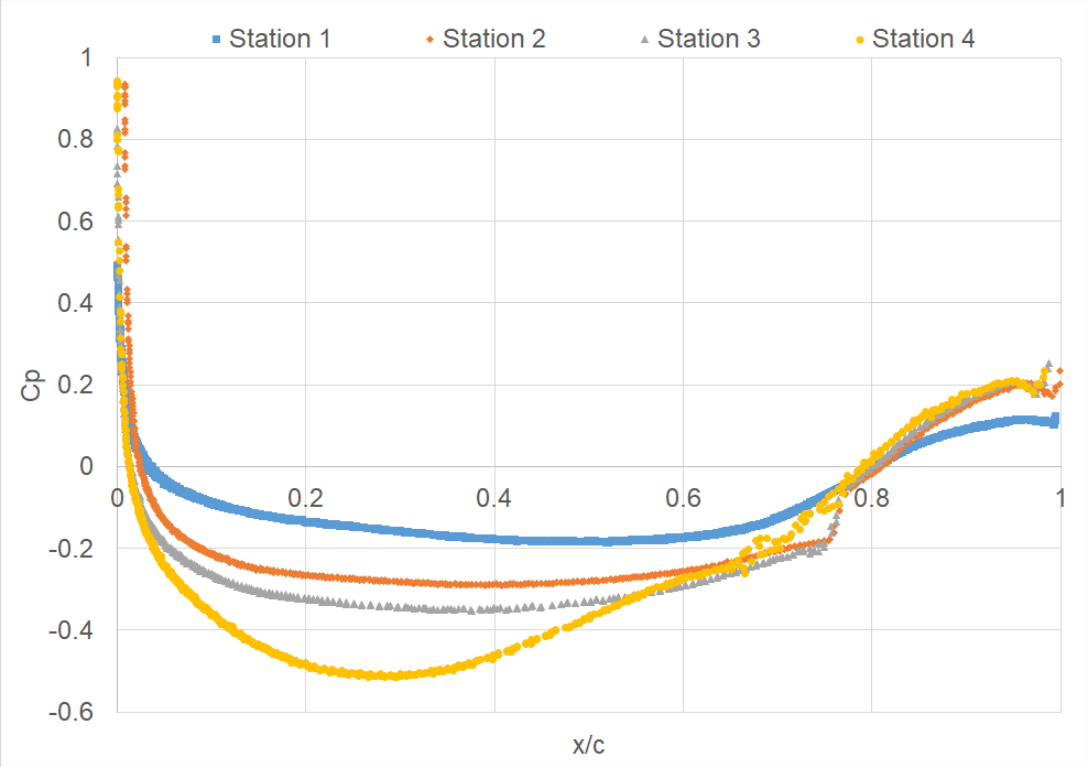

Figure 7.16: Pressure coefficient on the fin at distances of 0.1 m, 0.3 m, 0.7 m and 1.0 m from the bottom of the JS-1 tail.

The pressure coefficient vary from the stagnation point ($x/c = 0$) to the trailing edge ($x/c = 1$). According to Anderson (2010) and Houghton (2012), the magnitude of the pressure coefficient at the stagnation point should be equal to one, i.e., $C_p = 1$, for incompressible flows. This is observed at station 2, station 3 and station 4 but not at station 1. The deficit in pressure at the stagnation point of the fin at station 1 indicates the existence of a turbulent wake, in which, the portion of the fin at station 1 is immersed. According to Anderson (2010), the wake region is a low-pressure region which constitutes recirculation flow. Therefore, a turbulent boundary layer is observed at station 1.

The pressure decreases dramatically to a minimum pressure, $C_{p,min}$, near the leading edge due to the rapid expansion of the flow around the fin leading edge and then gradually increases towards the trailing edge as the flow progresses downstream. According to Anderson (2010) and Houghton (2012), a favorable pressure gradient

is the necessary condition that allows the rapid expansion of the flow whereas the flow is slowed down in an increasing pressure gradient (adverse pressure gradient). A separation bubble is observed at $x/c = 0.74$ at stations 2 and 3 while it is observed at $x/c = 0.68$ at station 2. Strong adverse pressure gradients exist which cause the laminar boundary layer to separate from the fin surfaces. The laminar boundary layer reattaches as a turbulent boundary layer and remains attached for the rest of the chordwise flow. According to Anderson (2010), if the streamwise pressure gradually increases downstream to reach a pressure (p) slightly above the free stream pressure (p_∞) at the trailing edge, i.e., $p > p_\infty$, then the boundary layer has not separated. The turbulent boundary layer at station 1 is also attached and does not separate from the surfaces of the fin.

The skin friction coefficient results on the fin are given in figure 7.17

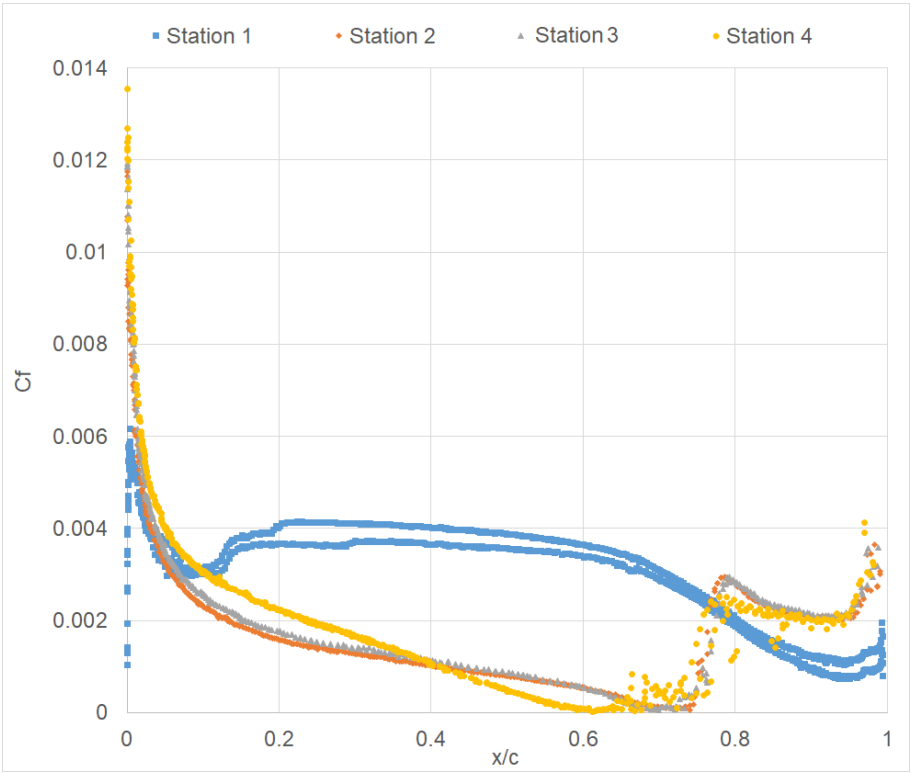

Figure 7.17: Skin friction coefficient on the fin at distances of 0.1 m, 0.3 m, 0.7 m and 1.0 m from the bottom of the JS-1 tail.

The skin friction coefficient vary from the stagnation point to the trailing edge. Ac-

cording to Anderson (2010), the skin friction is a strong function of the Reynolds number where the Reynolds number is based on the chord length of airfoil, $\mathrm{Re}_x = \rho u_0 x/\mu$, and it decreases as the Reynolds number increases. Anderson (2010); Di Pasquale et al. (2009) and Houghton (2012) further states that the value of the skin friction depends on whether the flow is laminar or turbulent with higher skin friction in a turbulent boundary layer compared to that of laminar boundary layer for the same Reynolds number and therefore, in transitional flows, the transition region is characterized by the drastic increase in skin friction. The skin friction coefficient plot corresponds to the pressure coeffcients plot in figure 7.16. A transition from a laminar to a turbulent boundary layer is seen at x/c=0.74 for stations 2 and 3 and at x/c=0.68 for station 4. Transition is not observed in station 1 because the boundary layer is already turbulent. According to Anderson (2010); Hermann and Gersten (2017.) and Houghton (2012), a turbulent boundary layer has a significant contribution of shear stress relative to a laminar boundary layer. U.S. Department of Transportation (2013) and United States Department of Transport (2016) further asserts that the turbulent boundary layer generates five to ten times more skin friction drag than an equivalent laminar boundary layer. Therefore, the turbulent wake influence on the fin has a definite contribution to the total drag force on the JS-1 sailplane.

7.7 Turbulent wake influence on the JS-1 sailplane aerodynamic performance.

Heavier than air flights benefit greatly from producing the least amount of drag force at all incidence angles. This means that for an aerodynamically efficient glider, the drag force must be minimal. The influence of the turbulent wake has been observed to compromise the amount of laminar flow surfaces on the JS-1 fin. A turbulent boundary layer flow exists at the bottom portion of the fin as a consequence of the turbulent wake and contributes to the total drag on the JS-1 sailplane. A

quantitative analysis was conducted to reveal the implications that the existence of the turbulent wake has on the aerodynamic performance and design of the JS-1 sailplane. Drag force calculations were made to determine the amount skin friction drag force that may be generated on the JS-1 fin due to the existence of a turbulent wake. Consequently, the contribution of the skin friction drag force on the JS-1 fin to the total drag force on the JS-1 sailplane was considered and possible improvements to the configuration were suggested.

7.7.1 Calculation of wake-induced drag

The analysis considered the amount of drag force that may exist on the JS-1 fin based on the fin height (also implies fin surface area) that is immersed in the turbulent wake. Five cases were considered. The first case was concerned with calculations for the amount of drag force that may exist on the JS-1 fin for the currently observed turbulent wake influence on the fin. The CFD analysis in subsection 7.6.1 showed that 23.6% of the fin, based on the fin's height, is immersed in the wake. Cases 2-5 considered the amount of drag force that may be generated by the JS-1 fin based on the respective fin heights of 0% (no wake influence), 10%, 30% and 50% that are influenced by the wake as shown in figure 7.18.

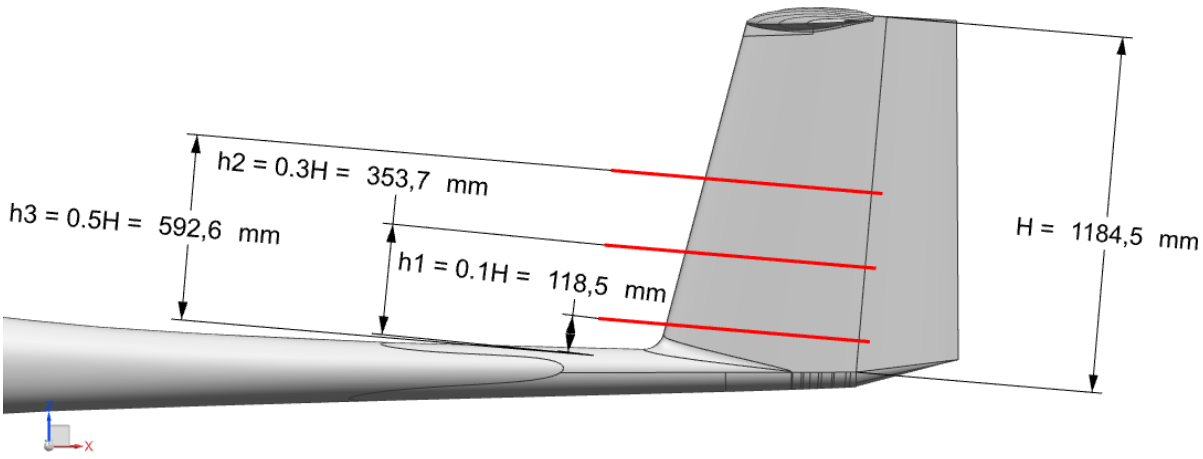

Figure 7.18: 0, 10, 30 and 50 percent of JS-1 total fin heights that is immersed in a turbulent wake.

The fin boundary layer analysis that was considered in subsection 7.6.3 showed that both the separation induced turbulent boundary layer at stations 2-4 and the turbulent boundary layer at station 1 remains attached and do not separate from the fin surface. Thus, only trailing edge separation of the turbulent boundary layer was expected. According to Anderson (2010), for small separation regions, as observed for traling edge separation, the amount of skin friction drag is expected to make a significant contribution to the total drag compared to the form drag. Therefore, only the skin friction drag force on the JS-1 fin and its contribution to the total drag force on the JS-1 sailplane were considered in the analysis.

The drag calculations were made by using equation 7.1.

$$\mathbf{D} = \frac{C_d \rho V_\infty^2 s}{2} \tag{7.1}$$

The CFD analysis for the transitional and turbulent wake flow on the JS-1 yielded a skin friction coefficient value of 0.00364 on the JS-1 fin. An XFOIL analysis was conducted on the JS-1 fin to determine the skin friction coefficient that are expected for a free transitional and a fully turbulent flow. A skin friction coefficient of 0.00307 was obtained for an onset transition point of $x/c = 0.794$ for the free transitional flow on the JS-1 fin. The skin friction coefficient of 0.00828 was obtained for a forced onset transition point of $x/c = 0.01$, which approximates a fully turbulent boundary layer on the JS-1 fin. The free stream density and velocity that was used in the calculations was 0.86341 kg/m^3 and 120km/h ($\approx$ 33.33 m/s) while the wetted surface (s) was calculated. The results for the analysis of the turbulent wake influence on the JS-1 fin total skin friction drag for the five cases that were considered are given by figure 7.19 and table 7.3. The results for the analysis of the turbulent wake influence of the JS-1 total drag is given by figure 7.20 and in Table 7.4.

Figure 7.19 gives a comparison of the total skin friction drag on the JS-1 fin for the cases that were considered.

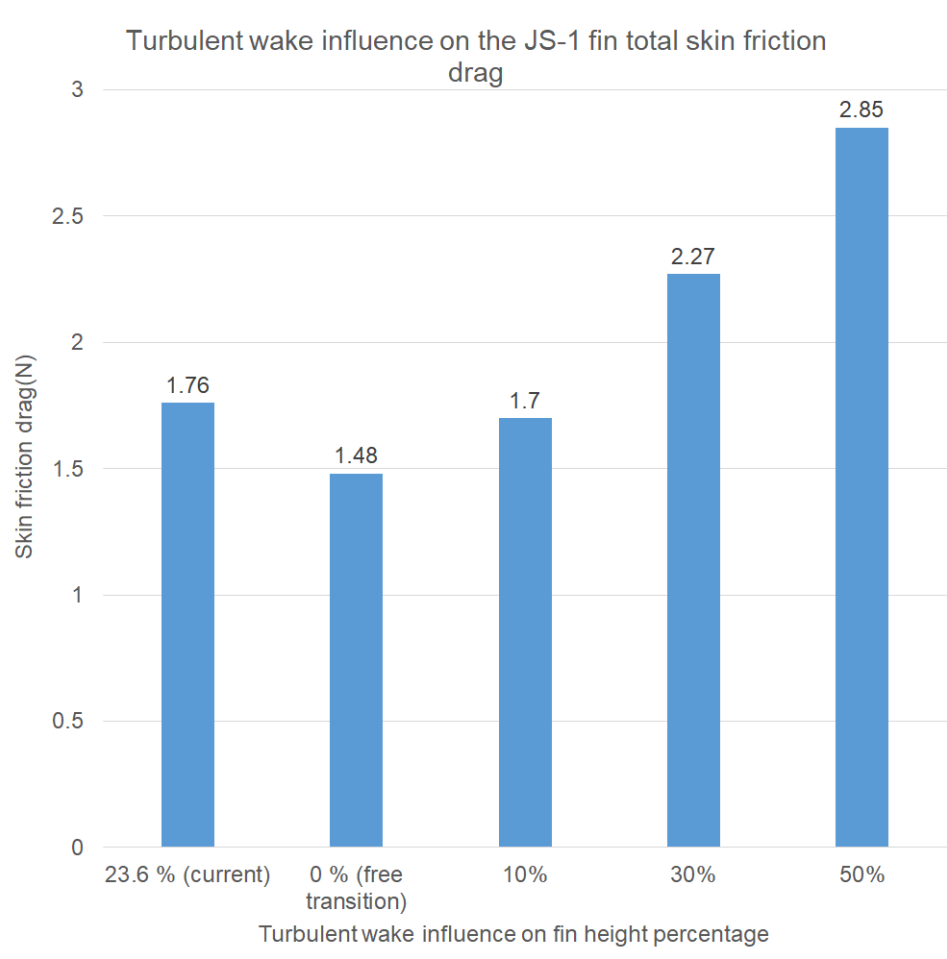

Figure 7.19: Turbulent wake influence on the JS-1 fin total skin friction drag.

A total skin friction drag of 1.76 N was seen on the JS-1 fin for the currently observed turbulent wake influence, with 23.6% of the total fin height immersed in the wake. This represents the total skin friction drag of the JS-1 fin in a fast inter-thermal flight with low angle of attack and high-speed range. For sailplanes, the speed range for fast inter-thermal flight is 120 km/h to 200 km/h, based on the glider's aerodynamic efficiency. A total skin friction drag reduction to 1.48 N and 1.7 N is seen on the JS-1 fin for a design optimization that would yield a 0% and 10% fin height immersion in the turbulent wake for a fast inter-thermal flight. This amounts to the total skin friction drag reduction of 15.61% and 3.33%, respectively (see Table 7.3). The design optimization to yield a 10% fin height immersion in the turbulent wake would produce an insignificant reduction in total skin friction drag on JS-1 fin. On the

other hand, the projected skin friction percentage reduction on the wake for the 0% fin height immersion in the turbulent wake suggests that design optimization in this direction would be worthwhile.

A total skin friction drag of 2.27 N and 2.85 N were observed on the JS-1 fin for a 30% and 50% fin height immersion in the turbulent wake. This represents the total skin friction drag on the JS-1 fin in thermal flight with low-speed and high angle of attack range. Thermalling speed for sailplanes is approximately 110 km/h and also depends on the aerodynamic efficiency of the glider. According to an experimental analysis by Hah and Lakshminarayana (1982), which was also observed in case 3 of the unit and benchmark cases, the turbulent wake intensifies with the increase in incidence angle. According to the analysis by Hah and Lakshminarayana (1982), the turbulent wake spread and turbulence intensity was enhanced. Therefore, the turbulent wake influence can be expected to reach up 50% of the total height of the JS-1 fin. The total skin friction coefficient drag is expected to increase by 29.36% and 62.12% for a 30% and 50% fin height immersion in the turbulent wake, i.e., during thermal flight (see Table 7.3). This is a considerable increase in skin friction drag on the JS-1 fin which strongly suggests a need to improve the design of the JS-1 fuselage and fin to minimize the observed influence of the turbulent wake on the fin at thermal flight.

Table 7.3: Table of results for the total skin friction drag influence on JS-1 fin.

Turbulent wake influence on percentage of fin height	**23.6% (Current)**	**0% (Free transition)**	**10%**	**30%**	**50%**
Total skin friction drag on JS-1 fin	1.76 N	1.48 N	1.7 N	2.7 N%	2.85 N
% Total skin friction drag reduction on JS-1 fin	-	15.61%	3.23%	-	-
% Total skin friction drag increase on JS-1 fin	-	-	-	29.36%	62.18%

Figure 7.20 gives a comparison of the total drag on the JS-1 sailplane as a consequence of the turbulent wake for the five cases that were considered.

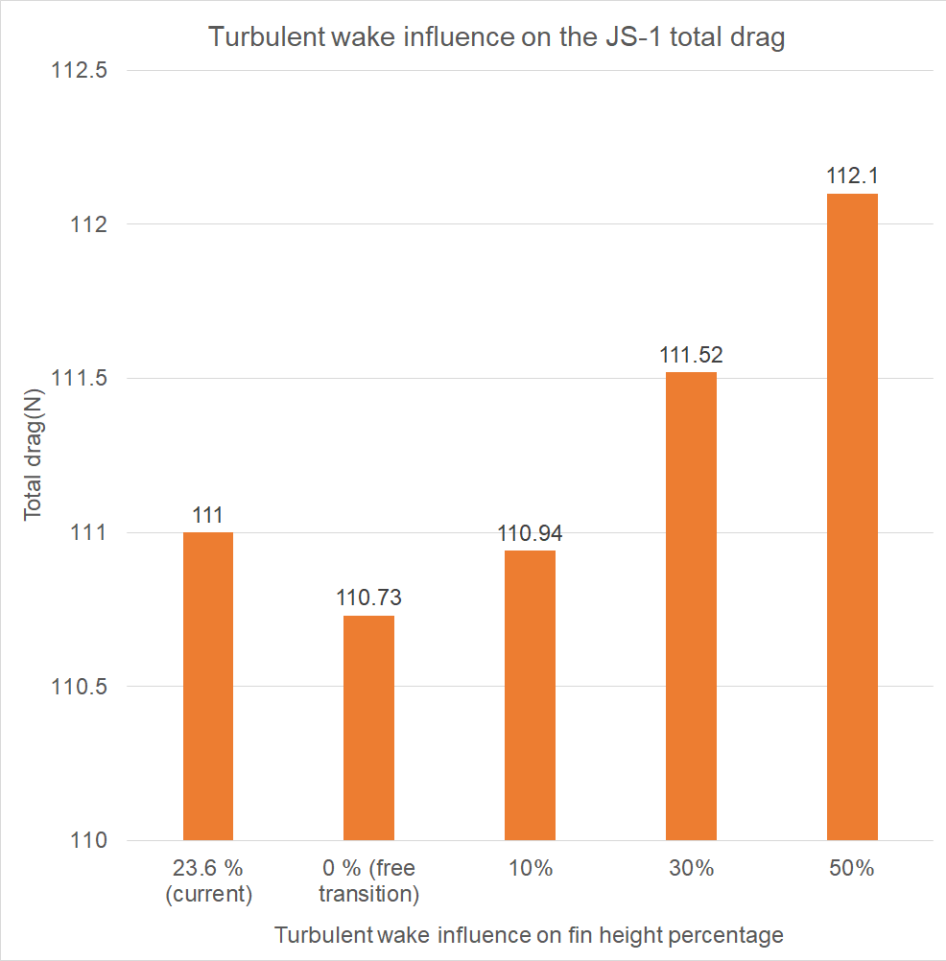

Figure 7.20: Turbulent wake influence on the JS-1 total drag.

According to Bosman (2013), the JS1 is one of the top performing 18 m competition sailplanes with a staggering lift to drag ratio (L/D) of 53:1. Bosman (2013) further calculated that for the 600 kg (approximate) glider, the total drag force amounts to 111 N at fast inter-thermal flights as shown in figure 7.20. This calculated to a 1.58% fin skin friction drag contribution on the total JS-1 sailplane drag (see Table 7.4). A total drag reduction on the JS-1 to 110.73 N and 110.94 N is observed for the design optimization that would yield a 0% and 10% fin height immersion in the turbulent wake. This amounts to 0.25% percent total drag reduction on the JS-1 and an increase in glide ratio to 53.16 for the design optimization that would yield a

0% fin height immersion in the turbulent wake (see Table 7.4). A 0.05% total drag reduction on the JS-1 and a glide ratio increase to 53.15 was observed for the design optimization that would yield a 10% fin height immersion in the turbulent wake (see Table 7.4). The fin skin drag contribution on the total JS-1 drag was observed to reduce to 1.34% and 1.53% for the design optimization that would yield a 0% and 10% fin height immersion in the turbulent wake (see Table 7.4).

An increase in total drag to 111.52 N and 112.09 N on the JS-1 sailplane is observed during thermal flight for a 30% and 50% fin height immersion on the turbulent wake. This equates to a 0.46% total drag increase on the JS-1 sailplane and a glide ratio reduction to 52.78 for a 30% fin height immersion on the turbulent wake (see Table 7.4). For a 50% fin height immersion on the turbulent wake, a total drag increase of 0.98% on the JS-1 and a glide ratio reduction to 52.51 was observed (see Table 7.4). The fin skin friction drag contribution to the total drag on the JS-1 sailplane was seen to increase to 2.04% and 2.54%, respectively, for a 30% and 50% fin height immersion on the turbulent wake (see Table 7.4).

Table 7.4: Table of results for the total drag influence on JS-1 sailplane performance.

Turbulent wake influence on percentage of fin height	**23.6% (Current)**	**0% (Free transition)**	**10%**	**30%**	**50%**
Total drag on JS-1	111 N	110.73 N	110.94 N	111.52 N	112.09 N
% Total drag reduction on JS-1	-	0.25%	0.05%	-	-
% Total drag increase on JS-1	-	-	-	0.46%	0.98%
% Fin skin friction drag contribution on total JS-1 drag	1.58%	1.34%	1.53%	2.04%	2.54%
L/D ratio	53	53.16	53.05	52.78	52.51

On balance, the analysis of the total drag influence on the JS-1 performance as a consequence of a turbulent wake suggests that a design optimization yield a 0% and

10% fin height immersion in the turbulent wake for fast inter-thermal flight would not yield a significant drag reduction. According to Bosman (2013), an improvement of at least 2 glide ratio points is necessary before the effort can be made to introduce a new model. On the other hand, the total drag increase on the JS-1 sailplane is notable during thermal flight due to the existence of a turbulent wake. This suggests a need to improve the design of the JS-1 fuselage and fin to minimize the skin friction contribution to the total drag on the JS-1 sailplane. This qualifies for a discussion on the possible design improvements to enhance the performance of the JS-1 during thermal flights.

7.7.2 Design improvements to reduce wake-induced drag

The objective for the design improvements which are to enhance the performance of the JS-1 sailplane during thermal flights is to remove or to at least minimize the influence of the turbulent wake on the fin. The analysis of the complex boundary layer flow on the fuselage and wing-fuselage junction in subsection 7.6.2, revealed that the turbulent wake is due to the turbulent boundary layer separation on the wing-fuselage junction. The JS-1 sailplane has a mid-wing configuration (Bosman, 2012; 2013). The implementation of a low-wing configuration on the JS-1 fuselage can remove or at least reduce the influence of the turbulent wake on the fin. While this may be true, it can compromise the aerodynamic performance of the JS-1 fuselage design. The work of Bosman (2012; 2013) and Hulsmann (2006) have shown that the higher wing configuration yields superior aerodynamic performance on the fuselage relative to a lower wing configuration. According to Hulsmann (2006) a high wing configuration is best in terms of reduced interference drag because the influence of the fuselage on the upper side of the wing is much lower than it would be on a low-wing configuration. For the current wing configuration of the JS-1, optimization can be implemented by displacing the fin upwards, to remove it from the influence of the turbulent wake. The high tail configuration would reduce the influence of the turbulent wake on the fin, however, it would have significant influence on longitudinal

stability, i.e., pitch, of the JS-1 and the vertical stabilizer configuration on the JS-1 tail would have to be redesigned. Design optimization can be made on both the current wing and tail configurations of the JS-1 to mitigate the draw backs that are associated with them. An optimal low wing and a high tail configuration can be implemented without a compromise in the longitudinal stability and the aerodynamic performance of the JS-1. The JS-1 has a short fin with low aspect ratio and therefore, a large surface area may be affected by the turbulent wake during thermal flight. A high aspect ratio fin, can be implemented to reduce the amount of fin surface area that comes into contact with the turbulent wake.

Summary

This chapter dealt with a brief validation case for the complete engineering system. This final stage of the validation process that was employed in this project, has validated the SST $k-\omega$ turbulence and $\gamma - Re_\theta$ transition model for a transitional and turbulent wake flow at low-Reynolds number and low-turbulence level. The SST $k-\omega$ turbulence model and $\gamma - Re_\theta$ model demonstrated capacity to predict boundary layer phenomena such as flow transition, flow separation and reattachment and turbulent wake flow. The CFD analysis of the transitional and turbulent wake flow on the JS-1 has revealed the existence of a turbulent wake that is caused by the separated boundary layer from the wing-fuselage junction. The turbulent wake was analyzed to revealed its characteristics. The turbulent wake spreads with downstream distance. The turbulence in the wake decreases at the JS-1 fuselage surface, towards the free stream and with downstream distance. The turbulent flow begins to decay at some point after station 5. The fin boundary layer has also been analyzed to reveal its characteristics. The fin boundary layer analysis revealed that 23.6% of the JS-1 fin height is immersed in the turbulent wake on and as a result, this contributes to the total drag force on the JS-1 sailplane. The quantitative drag force analysis that was conducted revealed that the turbulent wake has a significant contribution to the total drag force on the JS-1 during thermal flight. Design optimization recommendations

were made to eliminate or at least reduce the influence of the turbulent wake on the JS-1 aerodynamic performance.

Chapter 8

Conclusion and recommendations

The main goal of the current study was to investigate the turbulent wake influence on the JS-1 sailplane aerodynamic performance. Computational Fluid Dynamics flow analysis was used in order to achieve this goal. From the literature survey that was conducted, the low-speed aerodynamics boundary layer phenomena that are encountered in a typical JS-1 sailplane flight were identified. Identifying the boundary layer phenomena played an important role in determining a mathematical model that was suitable to model the flow on the JS-1. The literature review motivated the use of the SST $k-\omega$ turbulence and $\gamma - Re_\theta$ transition model. The SST $k-\omega$ turbulence model with the $\gamma - Re_\theta$ transition model were validated to determine the confidence level in its predictive capability for the flow phenomena that were relevant in the research. A significant portion of the study focused on validating the SST $k-\omega$ turbulence model with the $\gamma - Re_\theta$ transition model for a transitional and turbulent wake flow on sailplane geometries. The validation process involved four distinct levels, viz, unit cases, benchmark case, subsystem and complete system cases.

Unit and benchmark cases

The unit and benchmark cases were the first and second level of the validation process. The first level in the validation process considered three validation cases which

involved 2D transitional and turbulent wake flow on the NACA 0012 airfoil. The second level in the validation process considered three validation cases which were concerned with 3D transitional and turbulent wake flow on the NACA 0012 wing. In all the cases that were considered, the computational results were satisfactory relative to the experimental data by Gregory and O'Reilly (1973); Hah and Lakshminarayana (1982); Ladson (1988) and Shelda R.E. and Klimas, P.C. (1981). The accuracy of the computed boundary layer and wake phenomena relative to the experimentally observed, established the author's confidence in the SST $k-\omega$ turbulence model with the $\gamma - Re_\theta$ transition model to model a simple 2D and 3D transitional and turbulent wake flow. A satisfactory prediction of turbulent wake flow was a particularly important achievement in this study. The SST $k-\omega$ turbulence model with the $\gamma - Re_\theta$ transition model was, therefore, validated for a 2D and 3D transitional and wake flow on sailplane airfoil and wing geometries.

Subsystem case

The subsystem case was the third level of the validation process. A 3D complex transitional flow on the fuselage of the Mu-31 sailplane was considered. The computational results had a very good agreement with the experimentally observed results by Hulsmann (2006). The accuracy in the computed boundary layer phenomena relative to the experimentally observed was yet another achievement for the author. The SST $k-\omega$ turbulence model with the $\gamma - Re_\theta$ transition model was, therefore, validated for a complex 3D transitional flow on sailplane fuselage geometries.

Complete system case

The final level of the validation process involved a transitional and turbulent wake flow on the JS-1 sailplane. Oil flow free-flight experimental data on the JS-1 fin was used for validation purposes. The computed results were in good agreement with the experimentally observed oil flow streamlines. The computational results that were obtained in the final stage of the validation process comfirmed the ability of the SST

$k-\omega$ turbulence model with the $\gamma - Re_\theta$ transition model to predict a complex 3D transitional and turbulent wake flow. The SST $k-\omega$ turbulence model with the $\gamma - Re_\theta$ transition model was, therefore, validated for a complex 3D transitional and wake flow. The analysis of the turbulent wake influence on the JS-1 fin and its contribution to the JS-1 performance could, therefore, be carried out confidently.

The verification of the CFD solutions formed an integral part of the validation process. The widely used, Richardson extrapolation method that was proposed by Roache (1997) was employed in the verification process.

JS-1 wake influence

The CFD analysis of the fuselage and wing-fuselage boundary layer, revealed that the source of the turbulent wake is a separated turbulent boundary layer from the fuselage and wing-fuselage junction. The wake analysis revealed that the turbulent wake spreads with downstream distance. The turbulence in the wake decreases at the surface of the JS-1 fuselage towards the free stream and with downstream distance. The fin boundary layer analysis revealed that 23.6% of the JS-1 fin is affected by the turbulent wake. The quantitative drag force analysis revealed that the turbulent wake has a significant contribution to the total drag force on the JS-1 during thermal flight. Based on the outcomes of this study, design optimization was seen as necessary to reduce the drag influence of the turbulent wake on the JS-1 performance. To enhance the performance of the JS-1 sailplane during thermal flights, it was clear that the turbulent wake influence on the fin should be eliminated or at least minimized. A number of options were considered which explored design optimization in different areas on the JS-1 sailplane. The two most promising options were the implementation of a low wing configuration on the JS-1 fuselage or the implementation of a high tail configuration on the JS-1 tail boom. Based on the analysis of the advantage and drawbacks of each option, a combination of a low wing configuration fuselage and high tail configuration was considered to be optimal. Additionally, the implementation of a high aspect ratio fin would contribute considerably to optimize the JS-1 sailplane

design for thermal flights.

Recommendations for future work

The brief turbulent wake flow validation study on the JS-1 sailplane was sufficient for the analysis that was considered in the current study. The validation process that was employed, confirmed the ability of SST $k-\omega$ turbulence model with the $\gamma - Re_\theta$ transition model to accurately predict the behavior of the low-speed aerodynamic boundary layer and turbulent wake phenomena. However, the validation process also revealed that slight discrepancies exist in the predicted quantities in general and particularly in the turbulence stresses at the wake. A more thorough validation of the ability of the SST $k-\omega$ turbulence model with the $\gamma - Re_\theta$ model to accurately predict the quantity of the turbulence stresses in the turbulent wake would set them firmly as CFD analysis tools for a transitional and turbulent wake flow for sailplane design. An experimental investigation of the JS-1 turbulent wake is recommended to validate the wake measurements that were obtained in the current study.

The implementation of a combined low wing and high tail configuration and high aspect ratio fin on the JS-1 was considered as an optimal design optimization option to enhance the performance of the JS-1 sailplane during thermal flight. A CFD design analysis study of such a new configuration is recommended to determine the extent to which the JS-1 sailplane performance can be enhanced for thermal flight.

Appendices

Appendix A

Experimental and XFOIL analysis data

A.1 Experimental and XFOIL data of the lift and drag coeffiecients for the NACA 0012 airfoil at a Reynolds number of 2 million.

For XFOIL computations, an n_{crit} parameter of 8.15 which corresponds to free stream turbulence intensity of 0.1% was calculated for comparison with the Ladson (1988) and Shelda R.E. and Klimas, P.C. (1981) data.

Table A.1: Experimental and XFOIL data of the lift and drag coeffiecients for the NACA 0012 airfoil at a Reynolds number of 2 million.

	C Ladson's one-way spline interpolation	Robert E. Sheldahl and Paul C. Klimas	XFOIL	C Ladson's one-way spline interpolation	Robert E. Sheldahl and Paul C. Klimas	XFOIL
α	Lift coefficient			Drag coefficient		
0	0	0	0	0.0062	0.0064	0.00541
1	0.10492	0.11	0.1124	0.0062	0.0064	0.00548
2	0.20973	0.22	0.2241	0.0062	0.0066	0.0057
3	0.31507	0.33	0.3345	0.00631	0.0069	0.00609
4	0.41938	0.44	0.4433	0.0066	0.0073	0.00669
5	0.5197	0.55	0.5503	0.00729	0.0081	0.00744
6	0.61979	0.66	0.6598	0.00863	0.009	0.0083
7	0.72934	0.77	0.786	0.01065	0.0097	0.00929
8	0.83948	0.88	0.9187	0.01255	0.0105	0.01039
9	0.93843	0.99	1.0325	0.01307	0.0113	0.01154
10	1.03125	1.0727	1.1203	0.01339	0.0128	0.01277
11	1.12168	1.1539	1.2123	0.01467	0.014	0.01423
12	1.20982	1.2072	1.3033	0.01621	0.0155	0.01603
13	1.28453	1.2169	1.3881	0.01857	0.0172	0.01816
14	1.34818	1.1614	1.4569	0.02168	0.0191	0.02075
15	1.4033	1.0478	1.4991	0.02728	0.0213	0.02454
16	0.99674	0.9221	1.5287	-	0.0237	0.03043

Appendix B

Domain sensitivity and spatial grid convergence

Introduction

This chapter presents a domain sensitivity and a spatial grid convergence study. These are numerical studies which were pivotal in ensuring the numerical integrity of the CFD solutions that were obtained in this project. Section B.1 provides the domain sensitivity study, with a brief methodology and results in subsections B.1.1 and B.1.2, respectively. Section B.2 presents the spatial grid convergence test results. Subsections B.3.1, B.3.2, B.3.3 and B.3.4 give the spatial grid convergence results for the unit cases, benchmark cases, subsystem case and complete system case.

B.1 Computational domain sensitivity study

A computational domain sensitivity study is important in a CFD study. The goal is to determine the smallest possible domain size to employ in CFD study to secure core mesh core mesh cell economy without compromising solution accuracy. Specifically, this study determines the best position for the upstream, farfield and downstream

boundaries relative to the geometry under consideration in favor of core mesh core mesh cell economy and solution accuracy. According to Versteeg and Malalasekera (2007), in a CFD study, it is important to ensure that the computational domain boundaries are sufficiently far from the geometry of interest, to prevent introducing unnecessary errors to the solution and yet sufficiently close to economise on the number of cells that are used in the computation.

In this study, the upstream boundary, viz., the velocity inlet, must be sufficiently far away from the geometry of interest, i.e., NACA 0012 airfoil and wing, Mu-31 fuselage and JS-1 sailplane, to allow the flow to fully develop before it reaches the geometry of interest. A fully developed flow guarantees that no change of flow variables occurs in the flow direction before contact with the geometry of interest.

The farfield boundaries, which were also velocity inlets in this study, must be sufficiently far away to ensure that the flow around the geometry of interest is not disturbed and thereby introducing errors to the CFD solution.

The downstream boundary, viz., pressure outlet, must be sufficiently far away from any flow disturbances that may be induced by the geometry of interest. According to Versteeg and Malalasekera (2007) the flow must be fully developed before it reaches the downstream boundary. Versteeg and Malalasekera (2007) further states that, if the pressure outlet boundary is placed too close to the geometry of interest it is possible that the flow has not yet reached a fully developed state and this may lead to significant errors in the CFD solution.

B.1.1 Methodology

The computational domain sensitivity study was conducted for a 2D transitional flow on the NACA 0012. This single study was representative for all the other flow cases that were considered in this project and consequently, the resulting computational domain size was used in all the flow cases. The computational domain sensitivity study employed four domains of different sizes. The computational flow domain was divided into four boundary types, viz., velocity inlet, pressure outlet, symme-

try and wall boundary. The velocity inlet boundary condition was imposed on the upstream and far field boundaries of the computational domain while the pressure outlet boundary condition was imposed on the downstream boundary of the computational domain and the symmetry boundary on the plane of the NACA 0012 airfoil. Figure B.1 shows the rectangular computational domain with dimensions and boundary conditions that was employed in the domain sensitivity study.

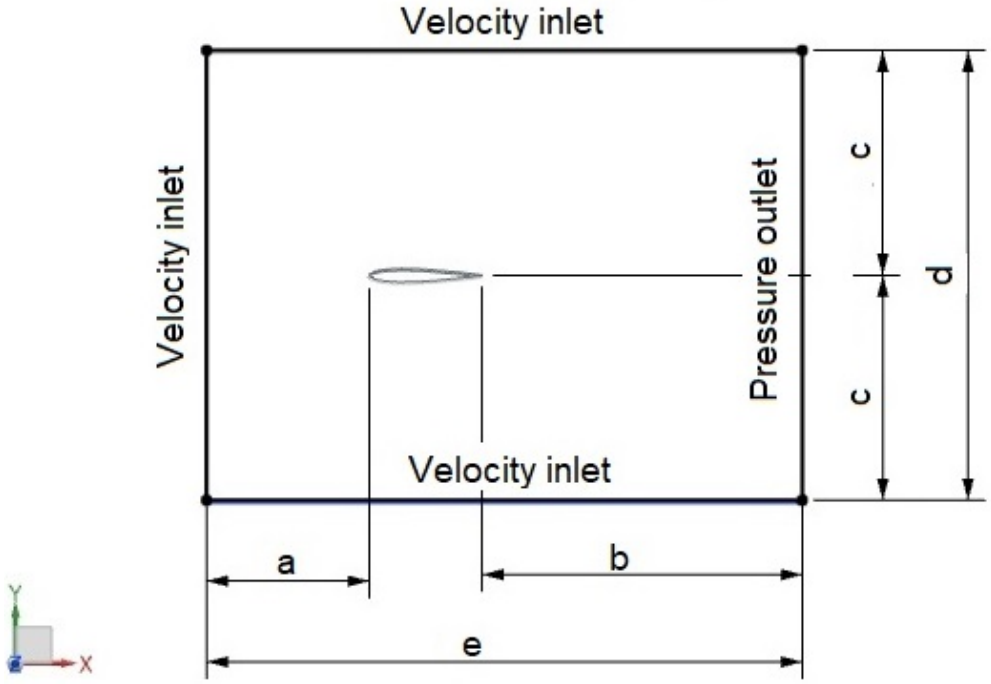

Figure B.1: Computational domain configuration with boundary conditions for the NACA 0012 airfoil.

All four domains made use of an unstructured, finite volume, 2D mesh of triangular cells and prism layer cells. The entire study was conducted on a coarse mesh of base size 1c, which gave satisfactory results relative the experimental data by Shelda R.E. and Klimas, P.C. (1981) and Ladson (1988) and XFOIL for all the domains that were investigated. The domain size and cell count for the various domains that were employed in the domain sensitivity study are tabulated in Table B.1 in order of their size.

Table B.1: Domain size and cell count for domains employed in domain sensitivity study.

Domain variable	Domain 1	Domain 2	Domain 3	Domain 4
a	80c	60c	40c	20c
b	160c	120c	80c	40c
c	80c	60c	40c	20c
d	160c	120c	80c	40c
e	241c	181c	121c	61c
Cells	469101	805586	890611	603368

A series of flow simulations on the NACA 0012 airfoil model were conducted to acquire the lift and drag polar for an initial domain, viz., domain 1. The boundaries for computational domain 1 was set to be far away from the airfoil to ensure that the solution is not affected. The calculated aerodynamic coefficient of interest for the initial domain were in good agreement with the experimental and XFOIL results for all the incidence angles that were investigated, as expected. Succesive reductions to the domain size were made while the influence on solution accuracy was monitored. A domain size that favored core mesh cell economy and solution accuracy was chosen for the CFD studies.

B.1.2 Results

This subsection gives a comparison for the lift coefficient and drag coefficient for the range $0 < \alpha < 16$ of angles of attack at a Reynolds number of 2 million. The STAR-CCM+ data that was generated for the various domain sizes is compared with the baseline data by Ladson (1988) Shelda R.E. and Klimas, P.C. (1981) and XFOIL. Figures B.2a and B.2b compares the STAR-CCM+ lift and drag coefficient

results that was generated for the various domains and the baseline data from Ladson (1988) Shelda R.E. and Klimas, P.C. (1981) and XFOIL. The results for the domain sensitivity study are tabulated in Tables B.2 and B.3 for comparison. The lift and drag coefficients generated in STAR-CCM+ for the various computational domains are all in good agreement with the baseline data.

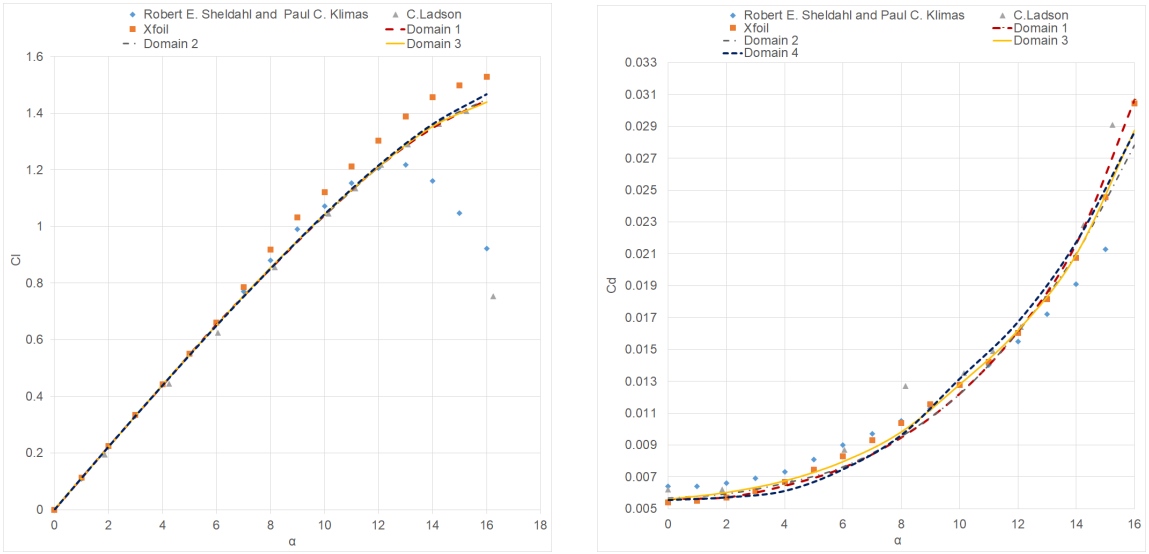

(a) Lift coefficient.

(b) Drag coefficient.

Figure B.2: Experimental, XFOIL and 2D STAR-CCM+ domain sensitivity data plots for the lift coefficient and drag coefficient of the NACA 0012 airfoil at a Reynolds number of 2 million.

The lift coefficient do not change relative to the domain size (see Table B.2). The lift coefficient data suggests that the size of the domains that were investigated have an insignificant ifluence to the lift coefficeint values. There is, however, a notable change in drag coefficient values relative to the domain size. A mild change in overall drag coefficient values is observed for domains 1-3. This change in drag coefficient values is within the baseline data range. A significant change in overall drag coefficient values is observed for domain 4. This change tends to deviate slightly from the baseline data range. The drag coefficient data suggests that the reduction in domain size beyond that of domain 4 begins to introduce errors into the solution. On the other hand, between domains 1-3, domain 3 has the most accurate results relative to the

experimental data (see Table B.3). Domain 3 gave the best results relative to the baseline data and was, therefore, the chosen domain size to be employed in all the CFD studies.

Table B.2: Experimental, XFOIL and 2D STAR-CCM+ domain sensitivity data for the lift coefficient of the NACA 0012 airfoil at a Reynolds number of 2 million.

α	**Domain 1**	**Domain 2**	**Domain 3**	**Domain 4**	**Baseline**
0	0	0	0	0	0
2	0.22256	0.22298	0.22021	0.22219	0.20973-0.2241
4	0.4391	0.43985	0.43985	0.43867	0.41938-0.4433
6	0.6542	0.65301	0.65133	0.64996	0.6200-0.6600
8	0.85108	0.85507	0.85411	0.851	0.83948-0.9187
10	1.03958	1.0391	1.04186	1.04284	1.03125-1.1203
12	1.21104	1.2109	1.21105	1.21529	1.2072-1.3033
14	1.34794	1.35741	1.35339	1.3606	1.34818-1.4569
16	1.44626	1.44957	1.43917	1.46626	0.9221-1.5286

Table B.3: Experimental, XFOIL and 2D STAR-CCM+ domain sensitivity data for the drag coefficient of the NACA 0012 airfoil at a Reynolds number of 2 million.

α	**Domain 1**	**Domain 2**	**Domain 3**	**Domain 4**	**Baseline**
0	0.00560899	0.00567148	0.005604223	0.00553286	0.00541-0.0064
2	0.00570367	0.00593807	0.006027323	0.0057007	0.0057-0.0066
4	0.00642895	0.00660546	0.006755603	0.0061057	0.0067-0.0073
6	0.00755639	0.00763092	0.00796209	0.007465	0.0083-0.0090
8	0.00946502	0.00953702	0.009827635	0.00962161	0.01039-0.01255
10	0.012218154	0.012187	0.012802031	0.013163163	0.01277-0.01339
12	0.0161401	0.016119087	0.016196148	0.016734448	0.0155-0.01621
14	0.0216421	0.021008149	0.020958353	0.021756931	0.0191-0.02168
16	0.0306785	0.027806148	0.028758948	0.028676036	0.0237-0.03043

B.2 Spatial grid convergence study

A spatial grid convergence study is necessary in a CFD study. It is the means by which verification of a CFD solution can be achieved. Numerical errors exist with cell type and cell size. These errors will always exist but can, however, be reduced significantly by a good choice of cell type to employ in a CFD study and grid refinement to obtain a mesh that is fine enough to produce the most accurate solutions which are mesh independent. The goal of a spatial grid convergence study is to reduce and quantify the discretization errors associated with the use of CFD (Versteeg and Malalasekera, 2007). A spatial convergence test was conducted for each flow case that was considered in this project, viz., the unit cases, benchmark cases, subsystem case and complete system. However, due to the high volume of data that was handled in this project, only representative engineering quantities for

each flow case were considered for the spatial grid convergence index.

B.2.1 Methodology

The spatial grid index that was proposed by Roache (1997), as described in section 4.3, was used to verify the CFD solutions. The spatial grid index was based on the Richardson Extrapolation involving a comparison of discrete solutions at two or more different grid spacings to an exact numerical solution. The exact numerical solution was obtained by using equation 4.3 as mentioned in section 4.3.

The spatial grid convergence study for the unit cases employed three unstructured, finite volume, 2D meshes of triangular and prism layer cells with different grid spacings. Coarse, intermediate and fine meshes were generated in STAR-CCM+. A single mesh configuration as described in chapter 5 was used in the spatial grid convergence study for the unit cases. As mentioned in section 4.3, the order of convergence is calculated for a high-quality grid convergence study that employs three or more grids resolutions. The order of convergence (p) was calculated by using equation 4.4 for the unit cases. The GCI was calculated by using equation 4.5 for a safety factor of 1.25 as mentioned in section 4.3.

The spatial grid convergence study for the benchmark cases, subsystem and complete system case employed two unstructured, finite volume, 2D meshes of triangular and prism layer cells with different grid spacings. A coarse and a fine mesh were generated in STAR-CCM+. A single mesh configuration as described in chapters 5, 6 and 7 was used in the spatial grid convergence study for the benchmark cases, subsystem case and complete system, respectively. As mentioned in section 4.3, the formal order of convergence of the discretization scheme is used for grid convergence studies that only employ two grid resolutions. A second order convergence was used for the benchmark cases, subsystem case and complete system case. The GCI was calculated with equation 4.5 for a safety factor of 3 as mentioned in section 4.3.

As suggested by Roache (1997), the study employed successive levels of mesh refinements, i.e. the mesh was refined at each level. In all the cases, the finest mesh was

employed in the CFD study.

The spatial grid convergence mesh values are tabulated in Tables B.4, B.5, B.6 and B.7 for the unit cases, benchmark cases, subsystem and complete system case, respectively.

Table B.4: Spatial grid convergence mesh values for the unit cases.

	Coarse	Intermediate	Fine
Base size	c	0.1c	0.05c
Cells	890611	4739286	17280798

Table B.5: Spatial grid convergence mesh values for the benchmark cases.

	Coarse	Fine
Base size	c	0.6c
Cells	20606940	111835542

Table B.6: Spatial grid convergence mesh values for the subsystem case.

	Coarse	Fine
Base size	0.6c	0.3c
Cells	64349045	91833566

Table B.7: Spatial grid convergence mesh values for the complete system case.

	Coarse	Fine
Base size	2c	c
Cells	77614939	194654291

B.3 Spatial grid convergence results

This section presents the spatial grid convergence results for the unit cases, benchmark cases, subsystem case and complete system. The grid convergence study was conducted for representative engineering quantities for each flow case that was considered in this project.

B.3.1 Unit cases

B.3.1.1 Case 1

The 2D transitional flow on the NACA 0012 airfoil at an incidence angle of 14 degrees and Reynolds number of 2.88 million was chosen to provide a representative GCI of the CFD solutions that were obtained in unit case 1 for the pressure coefficient and skin friction coefficient. The GCI was conducted on the pressure and skin friction coefficient values at a distance of $x/c = 0.9$ on the upper surface of the airfoil. Figure B.3 gives the grid convergence plots for the pressure coefficient and skin friction coefficient at $x/c = 0.9$.

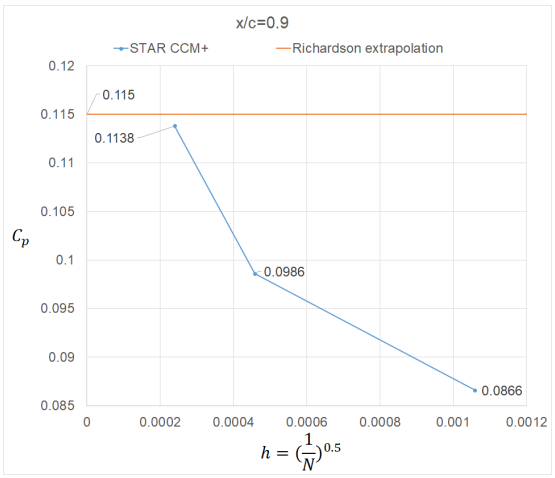

(a) C_p at $x/c = 0.9$

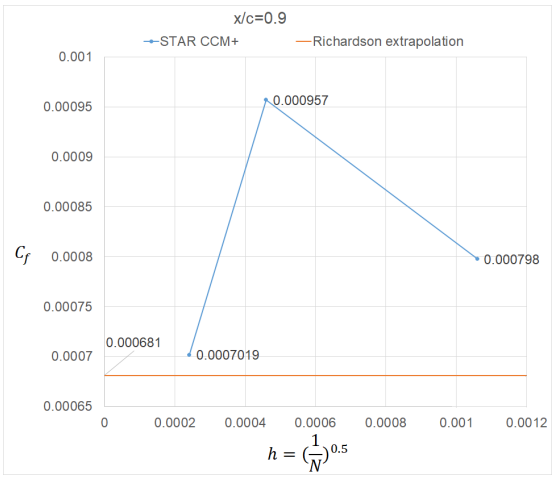

(b) C_f at $x/c = 0.9$

Figure B.3: Grid convergence plots for the pressure coefficient and skin friction coefficient of the 2D transitional flow on the NACA 0012 airfoil at an incidence angle of 14 degrees and Reynolds number of 2.88 million.

The numerical solutions that were obtained for the finest grid were 0.1138 and 0.0007017 for C_p and C_f, respectively, while the numerically exact solutions that were obtained by the Richardson extrapolation procedure were 0.115 and 0.000681. The numerical errors that are associated with discretization on the fine grid were 0.18% and 0.49% for C_p and C_f, respectively. This representative contribution to the inaccuracies in the CFD solutions for the C_p and C_f in unit case 1 was considered to be sufficiently small to render a fair validation of the adequacy of the SST $k-\omega$ turbulence model with the $\gamma - Re_\theta$ transition model to model a 2D transitional flow. The GCI for the finest grid and grid convergence data that was used for the calculation are tabulated in Table B.8.

Table B.8: GCI data for the pressure coefficient and skin friction coefficient of the 2D transitional flow on the NACA 0012 airfoil at an incidence angle of 14 degrees and Reynolds number of 2.88 million.

	C_p	C_f
STAR-CCM+	0.1138	0.0007019
Richardson extrapolation	0.115	0.000681
Fine GCI	0.18%	0.49%

B.3.1.2 Case 2

The 2D transitional flow on the NACA 0012 airfoil at an incidence angle of 6 degrees and Reynolds number of 2 million was chosen to provide a representative GCI of the CFD solutions that were obtained in unit case 2 for the lift coefficient and drag coefficient. Figure B.4 gives the grid convergence plots for the lift coefficient and drag coefficient.

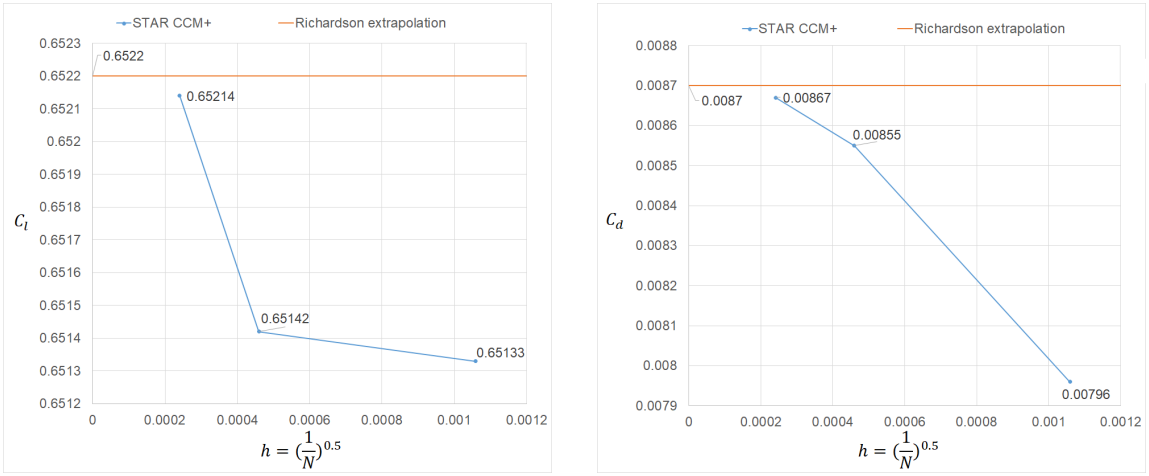

(a) C_l at 6 degrees angle of attack. **(b)** C_d at 6 degrees angle of attack..

Figure B.4: Grid convergence plots for the lift coefficient and drag coefficient of the 2D transitional flow on the NACA 0012 airfoil at an incidence angle of 6 degrees and Reynolds number of 2 million.

The numerical solutions that were obtained for the finest mesh were 0.06521 and 0.00867 for C_l and C_d, respectively. The numerically exact solutions that were obtained with the Richardson extrapolation procedure were 0.06522 and 0.0087 for C_l and C_d, respectively. The numerical errors that are associated with discretization on the fine grid were 0.0015% and 0.0216%, respectively, for C_l and C_d. These representative numerical errors were considered to be sufficiently small and their contributions to the inaccuracies in the CFD solutions for the C_l and C_d in unit case 2 are sufficiently small for a fair validation of the SST $k-\omega$ turbulence model with the $\gamma - Re_\theta$ transition model for 2D transitional flow. The GCI for the finest grid and the grid convergence data that was used for the calculation are tabulated in Table B.9.

Table B.9: GCI data for the lift coefficient and drag coefficient of the 2D transitional flow on the NACA 0012 airfoil at an incidence angle of 6 degrees and Reynolds number of 2 million.

	C_l	C_d
STAR-CCM+	0.06521	0.00867
Richardson extrapolation	0.06522	0.0087
Fine GCI	0.0015%	0.0216%

B.3.1.3 Case 3

The 2D transitional and turbulent wake flow on the NACA 0012 airfoil at an incidence angle of 9 degrees and Reynolds number of 0.38 million was chosen to provide a representative GCI of the CFD solutions that were obtained in unit case 3 for the mean velocity and turbulence stresses. The GCI study was conducted on the maximum values for the streamwise (**uu**), transverse (**vv**) and shear (**uv**) stresses at the respective distances of $x/c = 0.94, 1.5$ and 0 from the airfoil trailing edge and for the minimum value of the mean velocity at $x/c = 0.28$. The grid convergence plots

for the mean velocity and the turbulence stresses are given in figure B.5.

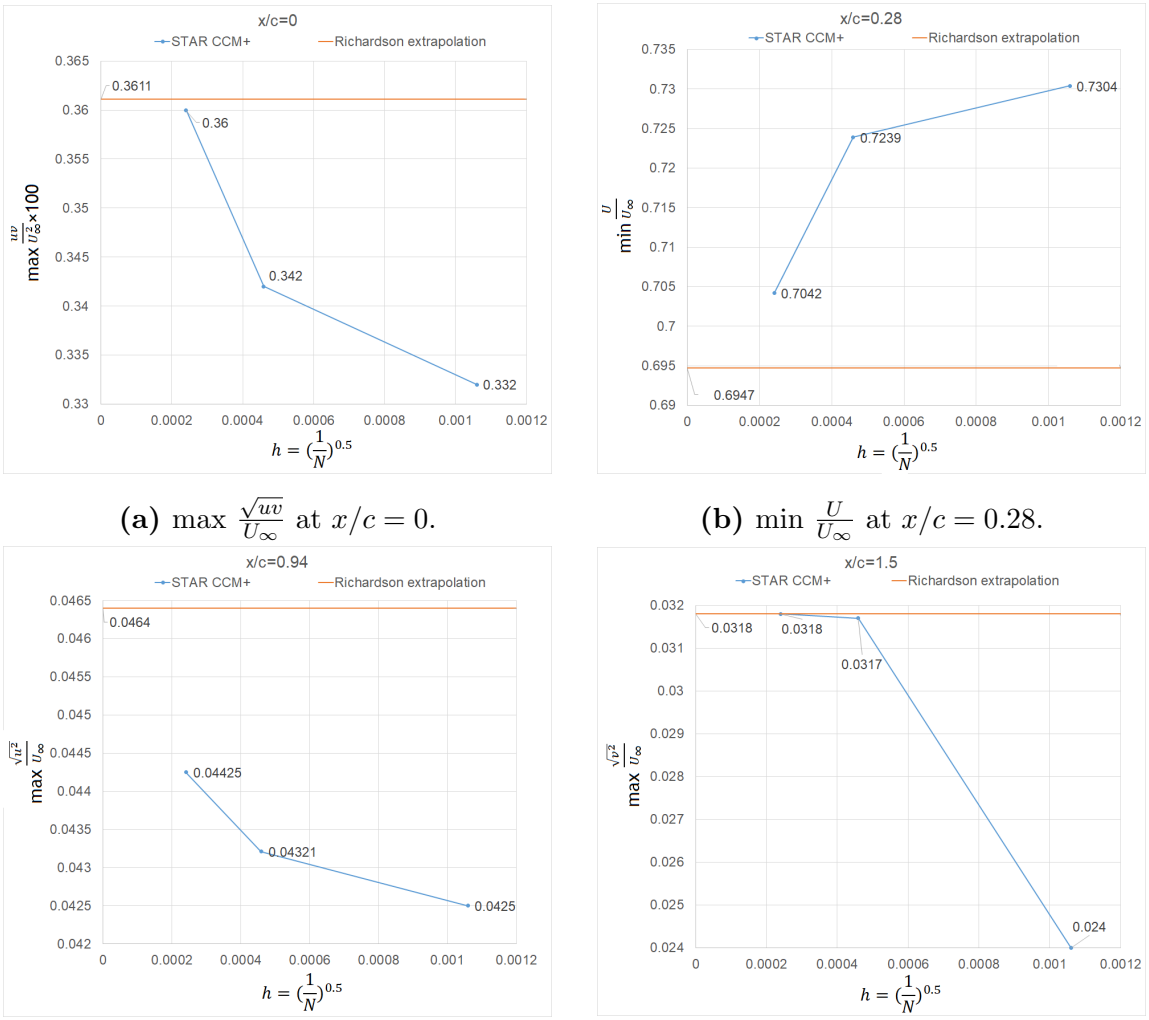

(a) max $\frac{\sqrt{uv}}{U_\infty}$ at $x/c = 0$.

(b) min $\frac{U}{U_\infty}$ at $x/c = 0.28$.

(c) max $\frac{\sqrt{u^2}}{U_\infty}$ at $x/c = 0.94$

(d) max $\frac{\sqrt{V_\infty^2}}{U_\infty}$ at $x/c = 1.5$

Figure B.5: Grid convergence data plots for the mean velocity and turbulence stresses of the 2D transitional and turbulent wake flow on the NACA 0012 airfoil at an incidence angle of 9 degrees and Reynolds number of 0.38 million.

The numerical solutions that were obtained for the finest mesh were 0.7042, 0.04425, 0.0318 and 0.36 for min $\frac{U}{U_\infty}$, max $\frac{\sqrt{u^2}}{U_\infty}$, max $\frac{\sqrt{V_\infty^2}}{U_\infty}$ and max $\frac{\sqrt{uv}}{U_\infty^2} \times 100$, respectively, while the numerically exact solutions that were obtained by the Richardson extrapolation procedure were 0.6947, 0.0464, 0.0318 and 0.3611, respectively. The GCI for the fine mesh was 0.0518%, 0.0901%, 0.0040% and 0.0663% for min $\frac{U}{U_\infty}$, max $\frac{\sqrt{u^2}}{U_\infty}$, max $\frac{\sqrt{V_\infty^2}}{U_\infty}$ and max $\frac{\sqrt{uv}}{U_\infty^2} \times 100$, respectively. The representative numerical errors that

are associated with the discretization on the fine grid was considered to be sufficiently small and their contributions to the inaccuracies in the CFD solutions for the mean velocity and turbulent stresses in unit case 3 are minimal. Therefore, the SST $k-\omega$ turbulence model with the $\gamma - Re_\theta$ transition model was validated fairly for a 2D transitional and turbulent wake flow. The GCI for the finest grid and the grid convergence data that was used for the calculation are tabulated in Table B.10.

Table B.10: GCI data for the mean velocity and turbulence stresses of the 2D transitional and turbulent wake flow on the NACA 0012 airfoil at an incidence angle of 9 degrees and Reynolds number of 0.38 million.

	min $\frac{U}{U_\infty}$	**max** $\frac{\sqrt{u^2}}{U_\infty}$	**max** $\frac{\sqrt{V_\infty^2}}{U_\infty}$	**max** $\frac{\sqrt{uv}}{U_\infty^2} \times 100$
STAR-CCM+	0.7042	0.04425	0.0318	0.36
Richardson extrapolation	0.6947	0.0464	0.0318	0.3611
Fine GCI	0.0518%	0.0901%	0.0040%	0.0663%

B.3.2 Benchmark cases

B.3.2.1 Case 1

The 3D transitional flow on the NACA 0012 wing at an incidence angle of 14 degrees and Reynolds number of 2.88 million was chosen to provide a representative GCI of the CFD solutions that were obtained in benchmark case 1 for the pressure coefficient and skin friction coefficient. The GCI was conducted on the pressure and skin friction coefficient value at a distance of $x/c = 0.9$ on the upper surface of the wing. The grid convergence plots for the pressure coefficient and skin friction coefficient at $x/c = 0.9$ is given in figure B.6.

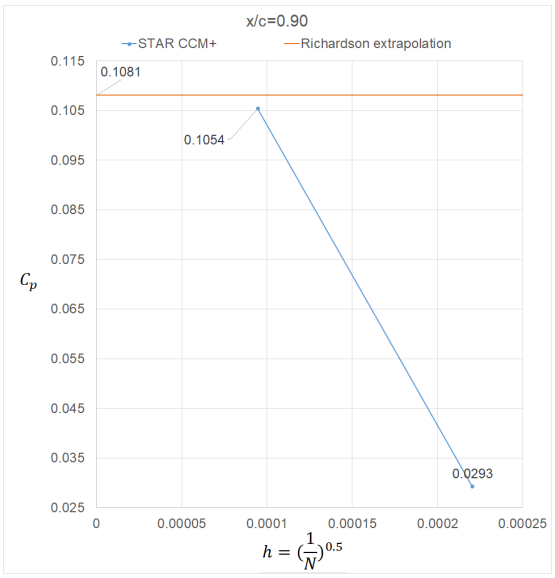

(a) C_p at $x/c = 0.9$

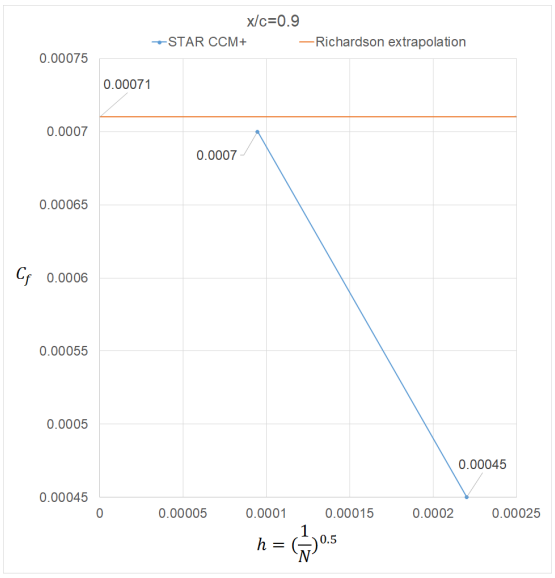

(b) C_f at $x/c = 0.9$

Figure B.6: Grid convergence plots for the pressure coefficient and skin friction coefficient of the 3D transitional flow on the NACA 0012 wing at an incidence angle of 14 degrees and Reynolds number of 2.88 million.

The numerical solutions that were obtained for the finest grid were 0.105 and 0.000709 for C_p and C_f, respectively. The exact numerical solutions that were obtained by the Richardson extrapolation procedure were 0.1081 and 0.000711 for C_p and C_f, respectively. The numerical error that is associated with discretization on the finest mesh were 0.07% and 0.04% for C_p and C_f, respectively. These representative numerical errors were considered to be sufficiently small and their contributions to the inaccuracies in the CFD solutions for C_p and C_f in benchmark case 1 are minimal. The SST $k-\omega$ turbulence model with the $\gamma - Re_\theta$ transition model was fairly validated for a 3D transitional flow. The GCI for the finest grid and the grid convergence data that was used for the calculation are tabulated in Table B.11.

Table B.11: GCI data for the pressure coefficient and skin friction coefficient of the 3D transitional flow on the NACA 0012 wing at an incidence angle of 14 degrees and Reynolds number of 2.88 million.

	C_p	C_f
STAR-CCM+	0.1055	0.0007019
Richardson extrapolation	0.1081	0.000711
Fine GCI	0.07%	0.04%

B.3.2.2 Case 2

The 3D transitional flow on the NACA 0012 wing at an incidence angle of 2 degrees and Reynolds number of 2 million was chosen to provide a representative GCI of the CFD solutions that were obtained in benchmark case 2 for the lift coefficient and drag coefficient. The grid convergence plots for the lift coefficient and drag coefficient are given in figure B.7.

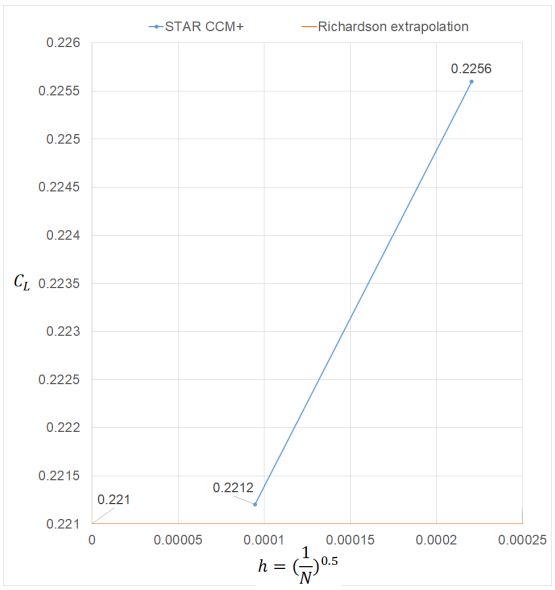

(a) C_L at 2 degrees angle of attack.

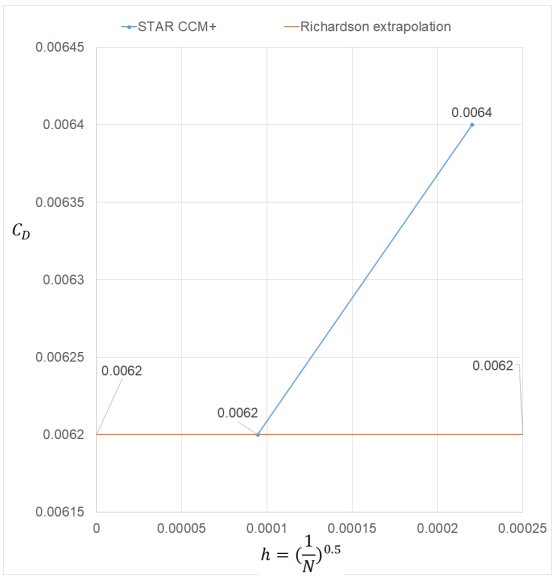

(b) C_D at 2 degrees angle of attack..

Figure B.7: Grid convergence plots for the lift coefficient and drag coefficient of the 3D transitional flow on the NACA 0012 wing at an incidence angle of 2 degrees and Reynolds number of 2 million.

The numerical solutions that were obtained for the fine mesh were 0.221 and 0.00622 for C_L and C_D, respectively while the numerically exact solutions that were obtained by the Richardson extrapolation procedure were 0.2211 and 0.0066221. The numerical discretization errors on the fine grid were 0.0021% and 0.0042%, respectively for C_L and C_D. These representative numerical errors were considered to be sufficiently small and their contributions to the inaccuracies in the CFD solutions for C_L and C_D in benchmark case 2 are minimal. The SST $k-\omega$ turbulence model with the $\gamma - Re_\theta$ transition model was fairly validated for a 3D transitional flow. The GCI for the finest grid and the grid convergence data that was used for the calculation are tabulated in Table B.12.

Table B.12: GCI data for the lift coefficient and drag coefficient of the 3D transitional flow on the NACA 0012 wing at an incidence angle of 6 degrees and Reynolds number of 2 million.

	C_L	C_D
STAR-CCM+	0.221	0.00622
Richardson extrapolation	0.2211	0.006221
Fine GCI	0.0021%	0.0042%

B.3.2.3 Case 3

The 3D transitional and turbulent wake flow on the NACA 0012 wing at an angle of attack of 9 degrees and Reynolds number of 0.38 million was chosen to provide a representative GCI of the CFD solutions that were obtained in benchmark case 3 for the mean velocity and turbulence stresses. The GCI study was conducted on the maximum values for the streamwise (**uu**), transverse (**vv**), spanwise (**ww**) and shear (**uv**) stresses at the respective distances of $x/c = 0.94, 1.5$ and 0 from the wing trailing edge and for the minimum value of the mean velocity at $x/c = 0.28$. Figure B.8 and B.9 gives the grid convergence plots for the mean velocity and the turbulence stresses.

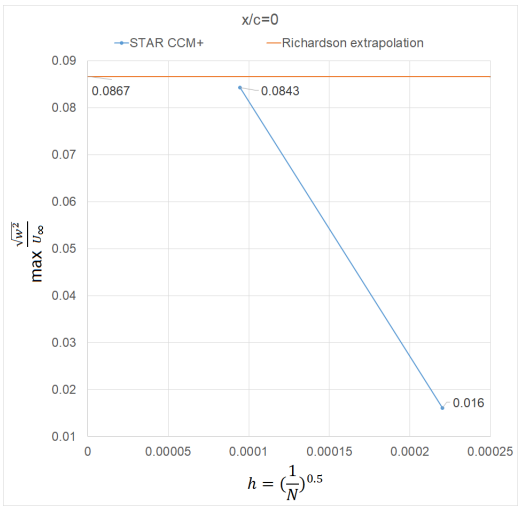

(a) max $\frac{\sqrt{uv}}{U_\infty}$ at $x/c = 0$.

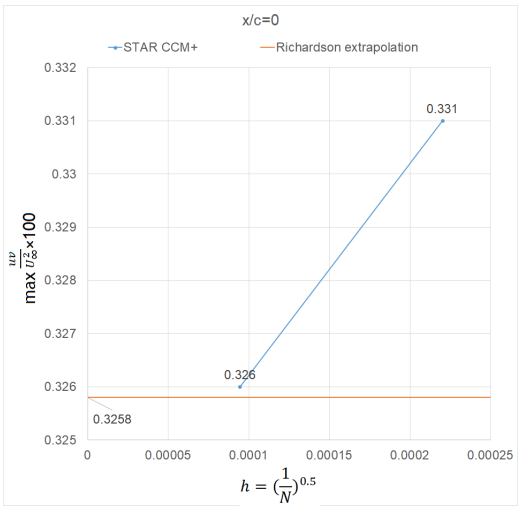

(b) max $\frac{\sqrt{w^2}}{U_\infty}$ at $x/c = 0$.

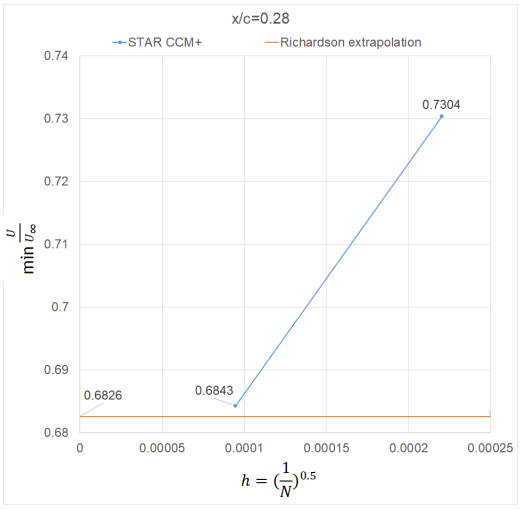

(c) min $\frac{U}{U_\infty}$ at $x/c = 0.28$.

Figure B.8: Grid convergence data plots for the mean velocity and turbulence stresses of the 3D transitional and turbulent wake flow on the NACA 0012 wing at an incidence angle of 9 degrees and Reynolds number of 0.38 million.

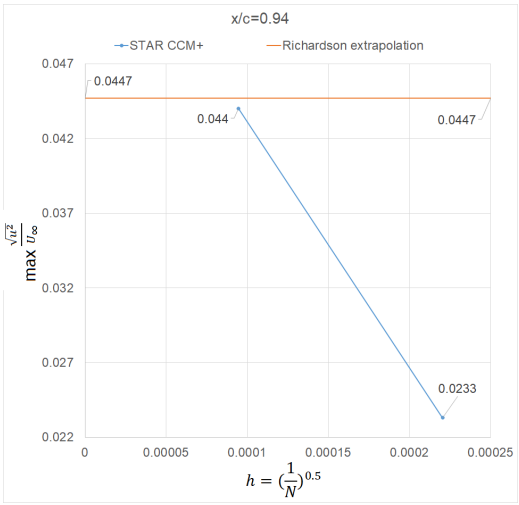

(a) max $\frac{\sqrt{u^2}}{U_\infty}$ at $x/c = 0.94$

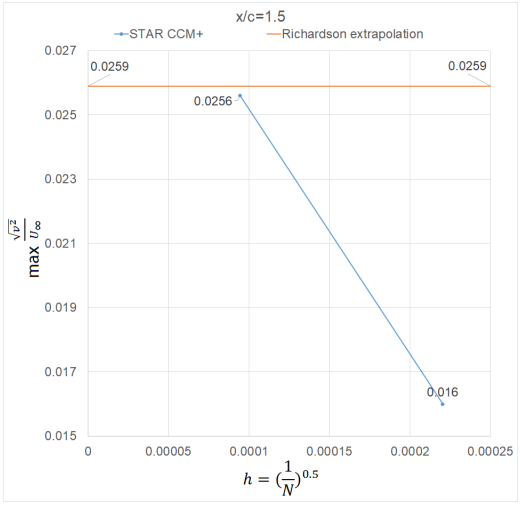

(b) max $\frac{\sqrt{V_\infty^2}}{U_\infty}$ at $x/c = 1.5$

Figure B.9: Grid convergence data plots for the turbulence stresses of the 3D transitional and turbulent wake flow on the NACA 0012 wing at an incidence angle of 9 degrees and Reynolds number of 0.38 million.

The numerical solutions that were obtained for the fine mesh were 0.6843, 0.044, 0.0256, 0.0843 and 0.326 for min $\frac{U}{U_\infty}$, max $\frac{\sqrt{u^2}}{U_\infty}$, max $\frac{\sqrt{V_\infty^2}}{U_\infty}$, max $\frac{\sqrt{w^2}}{U_\infty}$ and max $\frac{\sqrt{uv}}{U_\infty^2} \times 100$, respectively. The numerically exact solutions that were obtained by the Richardson extrapolation procedure were 0.6826, 0.04472, 0.02593, 0.0867 and 0.3258. The GCI for the fine mesh was 0.0071%, 0.0490%, 0.0390%, 0.0830% and 0.0016% for min $\frac{U}{U_\infty}$, max $\frac{\sqrt{u^2}}{U_\infty}$, max $\frac{\sqrt{V_\infty^2}}{U_\infty}$, max $\frac{\sqrt{w^2}}{U_\infty}$ and max $\frac{\sqrt{uv}}{U_\infty^2} \times 100$, respectively. The representative numerical errors that are associated with the discretization on the fine grid were considered to be sufficiently small and their contributions to the inaccuracies in the CFD solutions for the mean velocity and turbulent stresses in benchmark case 3 are minimal. Therefore, the SST $k - \omega$ turbulence model with the $\gamma - Re_\theta$ transition model was fairly validated for a 3D transitional and turbulent wake flow. The GCI for the finest grid and the grid convergence data that was used for the calculation are tabulated in Table B.13.

Table B.13: GCI data for the mean velocity and turbulence stresses of the 3D transitional and turbulent wake flow on the NACA 0012 wing at an incidence angle of 9 degrees and Reynolds number of 0.38 million.

	min $\frac{U}{U_\infty}$	**max** $\frac{\sqrt{u^2}}{U_\infty}$	**max** $\frac{\sqrt{V_\infty^2}}{U_\infty}$	**max** $\frac{\sqrt{w^2}}{U_\infty}$	**max** $\frac{\sqrt{uv}}{U_\infty^2} \times 100$
STAR-CCM+	0.6843	0.044	0.0256	0.0843	0.326
Richardson extrapolation	0.6826	0.04472	0.02593	0.0867	0.3258
Fine GCI	0.0071%	0.0490%	0.0390%	0.0830%	0.0016%

B.3.3 Subsystem case

A GCI was performed for the 3D transitional flow on the fuselage of the Mu-31 sailplane at Reynolds number of 1.5 million based on wing chord. The GCI was based on the drag coefficient. The grid convergence plot for the drag coefficient is given in figure B.10.

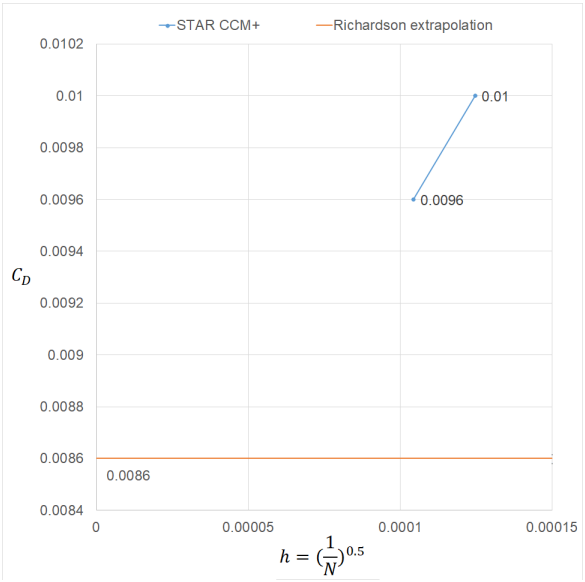

Figure B.10: Grid convergence data plots for the drag coefficient of the 3D transitional and turbulent wake flow on the fuselage of the Mu-31 sailplane.

The numerical solution that was obtained for the fine mesh were 0.0096 while the

numerically exact solutions that were obtained by the Richardson extrapolation procedure were 0.0086. The numerical discretization error on the fine grid was 0.34%. This numerical error was considered to be sufficiently small and its contribution to the inaccuracies in the CFD solutions for the C_D in subsystem case is minimal. The SST $k-\omega$ turbulence model with the $\gamma-Re_\theta$ transition model was fairly validated for a 3D transitional flow on the fuselage of the Mu-31 sailplane. The GCI for the finest grid and the grid convergence data that was used for the calculation are tabulated in Table B.14.

Table B.14: GCI data for the drag coefficient of the 3D transitional flow on the fuselage of the Mu-31.

	C_D
STAR-CCM+	0.0096
Richardson extrapolation	0.0086
Fine GCI	0.34%

B.3.4 Complete system case

The representative GCI study for the complete system was conducted on the pressure and skin friction coefficients values at a distance of $x/c = 0$ on station 1 ($z = 0.1$) of the JS-1 fin. Figure B.11 gives the grid convergence plots for the pressure coefficient and skin friction coefficient at $x/c = 0.9$.

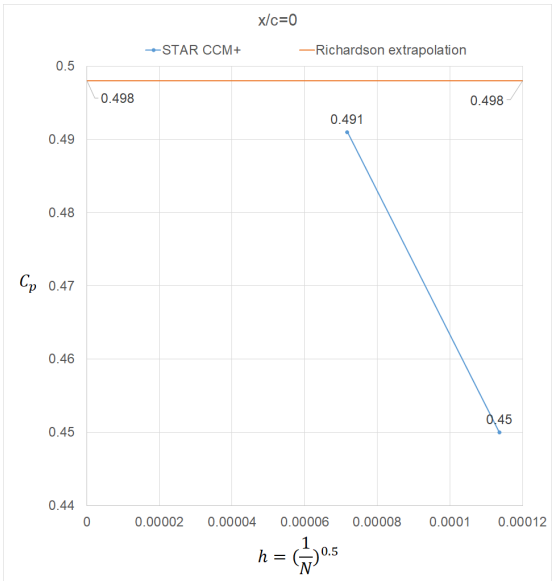

(a) C_p at $x/c = 0$

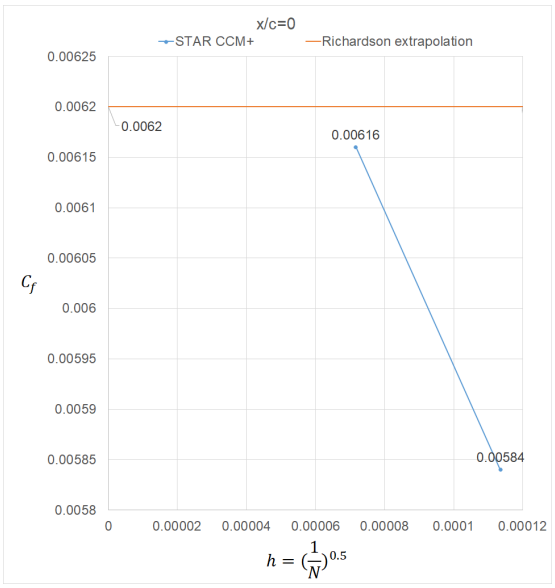

(b) C_f at $x/c = 0$

Figure B.11: Grid convergence plots for the pressure coefficient and skin friction coefficient of the 3D transitional and turbulent wake flow on the JS-1.

The numerical solutions that were obtained for the finest grid were 0.491 and 0.00616 for C_p and C_f, respectively while the numerically exact solutions that were obtained by the Richardson extrapolation procedure were 0.5 and 0.0062. The numerical errors that are associated with discretization on the fine grid were 0.047% and 0.029% for C_p and C_f, respectively. This representative contribution to the inaccuracies in the CFD solutions for the C_p and C_f in the complete system was considered to be sufficiently small to verify the CFD solutions of SST $k-\omega$ turbulence model with the $\gamma - Re_\theta$ transition model for a complex 3D transitional and turbulent wake flow. The GCI for the fine grid and grid convergence data that was used for the calculation are tabulated in Table B.15.

Table B.15: GCI data for the pressure coefficient and skin friction coefficient of the 3D transitional and turbulent wake flow on the JS-1.

	C_p	C_f
STAR-CCM+	0.491	0.00616
Richardson extrapolation	0.5	0.0062
Fine GCI	0.0470%	0.0290%

The representative GCI study for the complete system case was also conducted on the mean velocity and turbulent stresses on the JS-1 wake. The maximum values for the streamwise (**uu**), transverse (**vv**) and spanwise (**ww**) stresses at the respective distances of $x/c = 5.5, 4.8$ and 4.2 from the leading edge of the JS-1 fuselage and for the mean velocity at $z/n = 0.1$ were considered. Figure B.12 gives the grid convergence plots for the mean velocity and the turbulence stresses.

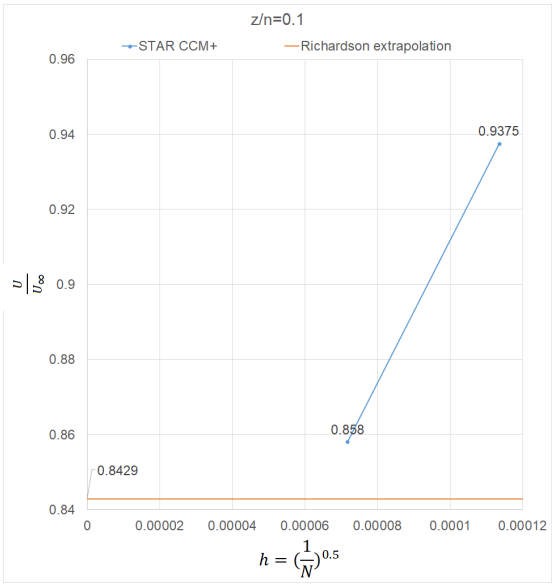

(a) min $\frac{U}{U_\infty}$ at $z/n = 0.1$.

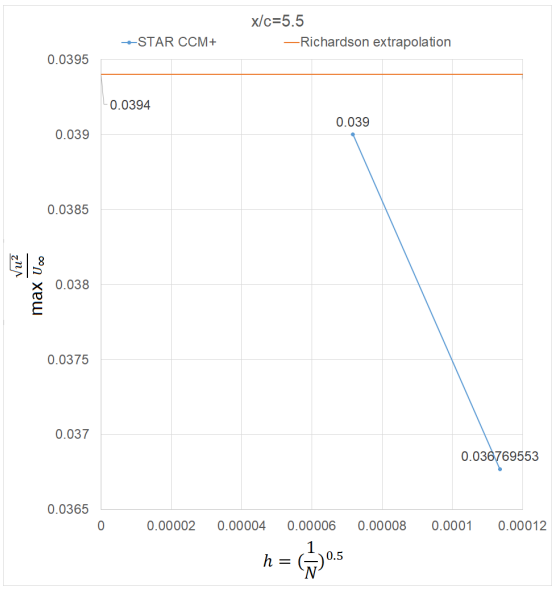

(b) max $\frac{\sqrt{u^2}}{U_\infty}$ at $x/c = 5.5$.

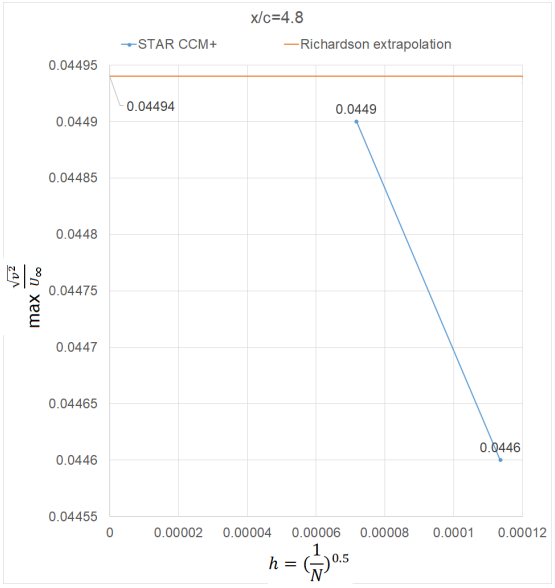

(c) max $\frac{\sqrt{V_\infty^2}}{U_\infty}$ at $x/c = 4.8$

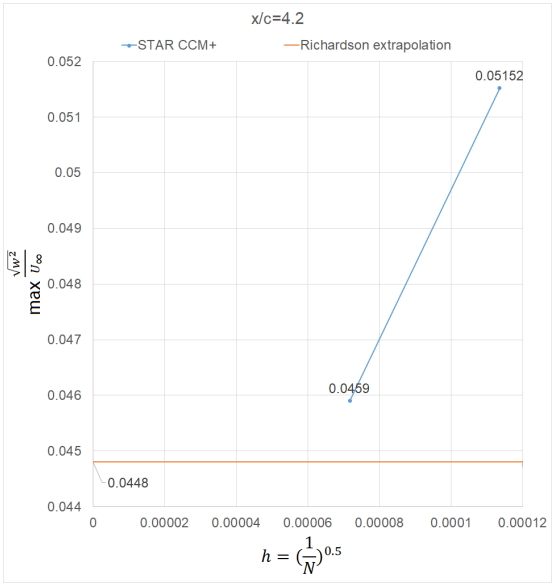

(d) max $\frac{\sqrt{w^2}}{U_\infty}$ at $x/c = 4.2$

Figure B.12: Grid convergence data plots for the mean velocity and turbulence stresses of the 3D transitional and turbulent wake flow on the JS-1 sailplane.

The numerical solutions that were obtained for the fine mesh were 0.858, 0.039, 0.0449, 0.0459 and 0.326 for $\frac{U}{U_\infty}$, max $\frac{\sqrt{u^2}}{U_\infty}$, max $\frac{\sqrt{V_\infty^2}}{U_\infty}$ and max $\frac{\sqrt{w^2}}{U_\infty}$, respectively. The numerically exact solutions that were obtained by the Richardson extrapolation procedure were 0.843, 0.0394, 0.0449 and 0.0448. The GCI for the fine mesh

was 0.052%, 0.0901%, 0.004% and 0.0663% for $\frac{U}{U_\infty}$, max $\frac{\sqrt{u^2}}{U_\infty}$, max $\frac{\sqrt{V_\infty^2}}{U_\infty}$ and max $\frac{\sqrt{w^2}}{U_\infty}$, respectively. The representative numerical errors that are associated with the discretization on the fine grid were considered to be sufficiently small and their contributions to the inaccuracies in the CFD solutions for the mean velocity and turbulent stresses in complete system case are minimal. Therefore, the CFD solutions of the SST $k-\omega$ turbulence model with the $\gamma - Re_\theta$ transition model for a 3D transitional and turbulent wake flow are verified. The GCI for the finest grid and the grid convergence data that was used for the calculation are tabulated in Table B.16.

Table B.16: GCI data for the mean velocity and turbulence stresses of the 3D transitional and turbulent wake flow on the JS-1 sailplane.

	min $\frac{U}{U_\infty}$	**max** $\frac{\sqrt{u^2}}{U_\infty}$	**max** $\frac{\sqrt{V_\infty^2}}{U_\infty}$	**max** $\frac{\sqrt{w^2}}{U_\infty}$
STAR-CCM+	0.858	0.039	0.0449	0.0459
Richardson extrapolation	0.843	0.0394	0.0449	0.0448
Fine GCI	0.0520%	0.0901%	0.0040%	0.0663%

A GCI study was also conducted for the skin friction drag coefficient on the JS-1 fin. The grid convergence data plot is given in figure B.13.

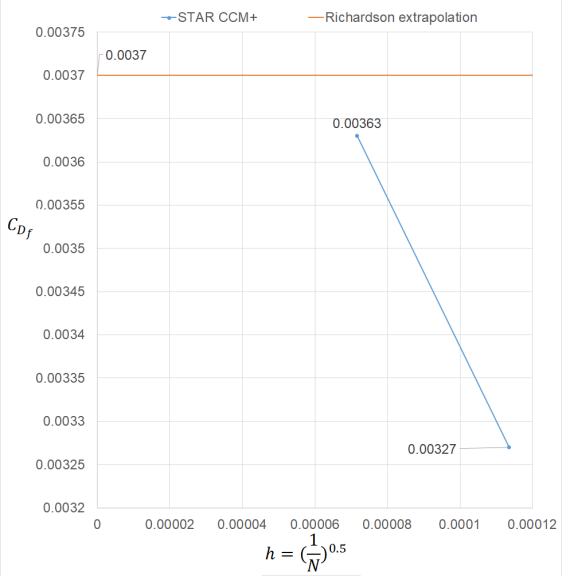

Figure B.13: Grid convergence data plots for the skin friction drag coefficient of the 3D transitional and turbulent wake flow on the fin of the JS-1 sailplane.

The numerical solution that was obtained for the fine mesh was 0.0036 while the numerically exact solution that was obtained by the Richardson extrapolation procedure was 0.0037. The numerical discretization error on the fine grid was 0.05%. This numerical error was considered to be sufficiently small and its contribution to the inaccuracies in the CFD solutions for the C_{Df} in complete system case is minimal. The C_{Df} solution of the SST $k-\omega$ turbulence model with the $\gamma-Re_\theta$ transition model for a 3D transitional and turbulent wake flow on the fin of the JS-1 sailplane was verified. The GCI for the finest grid and the grid convergence data that was used for the calculation are tabulated in Table B.17.

Table B.17: GCI data for the skin friction drag coefficient of the 3D transitional flow on the fin of the JS-1 sailplane.

	C_{Df}
STAR-CCM+	0.0036
Richardson extrapolation	0.0037
Fine GCI	0.05%

Summary

This appendix covered a domain sensitivity and a spatial grid convergence study which were important in ensuring the numerical integrity of the CFD solutions that were obtained in this project. A domain size was chosen which favored solution accuracy and core mesh cell economy while the CFD solutions that were obtained in this study were verified by the Richardson extrapolation procedure.

Appendix C

2D and 3D validation study table of results

C.1 XFOIL, 2D and 3D STAR-CCM+ transition points for the NACA 0012 airfoil and wing at a Reynolds number of 2.88 million.

Table C.1: XFOIL, 2D and 3D STAR-CCM+ data transition points for the NACA 0012 airfoil and wing at a Reynolds number of 2.88 million.

	Transition points (x\c)					
	XFOIL		**2D STAR CCM+**		**3D STAR CCM+**	
α	**Top surface**	**Bottom surface**	**Top surface**	**Bottom surface**	**Top surface**	**Bottom surface**
0	0.437	0.437	0.39081	0.39081	0.41722	0.41722
6	0.045	0.93	0.06806	0.5714	0.069817	0.59053
10	0.015	1	0.01594	0.686397	0.016325	0.53671
14	0.009	1	0.00876	0.940926	0.008507	0.924297

C.2 Experimental, XFOIL, 2D and 3D STAR-CCM+ data for the lift coefficient and drag coefficient for the NACA 0012 airfoil and wing at a Reynolds number of 2 million.

Table C.2: Experimental, XFOIL, 2D and 3D STAR-CCM+ validation data for the lift coefficient of the NACA 0012 airfoil and wing at a Reynolds number of 2 million.

α	**C.Ladson's oneway spline interpolation**	**Robert E. Sheldahl, Paul C. Klimas**	**XFOIL**	**2D STAR-CCM+**	**3D STAR-CCM+**
0	0	0	0	0	0
2	0.20973	0.22	0.2241	0.22418	0.22121
4	0.41938	0.44	0.4433	0.44431	0.44032
6	0.62	0.66	0.6598	0.65214	0.64734
8	0.83948	0.88	0.9187	0.85898	0.85246
10	1.03125	1.0727	1.1203	1.04701	1.04953
12	1.20982	1.2072	1.3033	1.22147	1.19608
14	1.34818	1.1614	1.4569	1.36605	1.33455
16	0.99674	0.9221	1.5286	1.475	1.4222

Table C.3: Experimental, XFOIL, 2D and 3D STAR-CCM+ validation data for the drag coefficient of the NACA 0012 airfoil and wing at a Reynolds number of 2 million.

α	**C.Ladson's oneway Spline interpolation**	**Robert E. Sheldahl, Paul C. Klimas**	**XFOIL**	**2D STAR-CCM+**	**3D STAR-CCM+**
0	0.0062	0.0064	0.00541	0.00597	0.00607
2	0.0062	0.0066	0.0057	0.00619	0.00623
4	0.0066	0.0073	0.00667	0.00688	0.00671
6	0.00863	0.009	0.0083	0.00867	0.00888
8	0.01255	0.0105	0.01039	0.01017	0.01118
10	0.01339	0.0128	0.01277	0.01293	0.01543
12	0.01621	0.0155	0.01603	0.01618	0.01932
14	0.02168	0.0191	0.02075	0.02109	0.02522
16	-	0.0237	0.03043	0.02792	0.034

References

Abbott, I. and von Doenhoff, A. (1959), *Theory of wing sections, including a summary of airfoil data*, New York: Dover.

Aftab, S., Rafie, A., Razak, N. and Ahmad, K. (2016), 'Turbulence model selection for low Reynolds number flows', *PLOS Journals* **11**(4), 1–15.

AIAA (1998), *Guide for the Verification and Validation of Computational Fluid Dynamics simulations.*, Reston: AIAA.

Alber, I. E. (1980), 'Turbulent wake of a thin, flat plate', *AIAA Journal* **18**(9), 1044–1051.

Alliance, N. (2018), 'Examining spatial (grid) convergence'. (Unpublished).
URL: https://www.grc.nasa.gov/www/wind/valid/tutorial/spatconv.html

AlMutairi, J., ElJack, E. and AlQadi, I. (2017), 'Dynamics of laminar separation bubble over NACA-0012 airfoil near stall conditions', *Aerospace Science and Technology* **68**, 193–203.

Anderson, J. (2008), *Introduction to flight*, 6th edn, New York: McGraw-Hill.

Anderson, J. (2010), *Fundamentals of Aerodynamics*, 5th edn, New York: McGraw-Hill.

Andreopoulos, J. (1978), Symmetric and asymmetric near wake of a flat plate, Phd thesis, London: London University.

Aupoix, B., Arnal, D., Bézard, H., Chaouat, B., Chedevergne, F., Deck, G., Grenard, P. and Laroche, E. (2011), 'Transition and turbulence modeling', *Aerospace Lab Journal* **1**(2), 1–13.

Bakker, A. (2002), Applied Computational Fluid Dynamics. (Unpublished).
URL: http://www.bakker.org/dartmouth06/engs150/

Baldwin, B. and Barth, T. (1990), A one-equation turbulence transport model for high reynolds number wall-bounded flows, Report 102847, NACA.

Baldwin, B. and Lomax, H. (1978), Thin-layer approximation and algebraic model for separated turbulent flows, *in* '16th Aerospace Sciences Meeting', Aerospace Sciences Meetings, American Institute of Aeronautics and Astronautics, pp. 1–9.

Boermans, L. and Terleth, D. (1984), 'Wind-tunnel tests of eight sailplane wing-fuselage combinations', *Technical Soaring* **8**(3), 70–85.

Bosman, J. (2013), 'Refinement of glider aerodynamic design using CFD', *Technical Soaring* **37**(2), 20–25.

Bosman, J. J. (2012), Evaluation of new aerodynamic concepts using CFD for the improvement of a glider fuselage, Phd thesis, Potchefstroom: North-West University.

Bradshaw, P. (1970), 'Prediction of the turbulent near-wake of a symmetrical aerofoil', *AIAA Journal* **8**(8), 1507–1508.

Bradshaw, P. (1976.), *Turbulence*, Vol. 12, Berlin: Springer-Verlag, book section 1.

Bradshaw, P. and Ferris., D. H. (1963), Measurements of free stream turbulence in some low speed tunnels at n.p.l., Report 3317, NPL Aerodynamics Division.

Cebeci, T. and Smith, A. (1974), Analysis of turbulent boundary layers, number 15, New York: Academic Press.

Chevray, R. and Kovasznay, L. (1969), 'Turbulence measurements in the wake of a thin flat plate', *AIAA Journal* **7**(8), 1641–1643.

Chien, K. (1982), 'Predictions of channel and boundary-layer flows with a low-reynolds-number turbulence model', *AIAA Journal* **20**(1), 33–38.

Chou, P. (1945), 'On velocity correlations and the solutions of the equations of turbulent fluctuations', *Quarterly of Applied Mathematics* **3**(1), 38–54.

Club, N. U. G. (2018), 'Theory of flight'.
URL: http://www.nugc.net/How20gliders20fly.phps

Craft, T., Launder, B. and Suga, K. (1997), 'Prediction of turbulent transitional phenomena with a nonlinear eddy-viscosity model', *International Journal of Heat and Fluid Flow* **18**(1), 15–28.

Currie, I. (2013), *Fundamental Mechanics of Fluids*, 4th edn, Boca Raton: CRC Press.

Deperrois, A. (2010), 'XFLR5 analysis of foils and wings operating at low Reynolds numbers'.
URL: https://xflr5.com

Di Pasquale, D., Rona, A. and Garrett, S. (2009), A selective review of CFD transition models, *in* '39th AIAA Fluid Dynamics Conference', pp. 1–10.

Drela, M & Youngren A.H (2003), 'XFOIL 6.94 user guide'.
URL: https://web.mit.edu/drela/Public/web/xfoil/

Eggenspieler, G. (2012), Modeling laminar-turbulent transition processes. (unpublished).
URL: https://$support.ansys.com/staticassets/ANSYS/Conference/Confidence/San%20Jose/Downloads/turbulence-transition-modeling-5.pdf$

Ewing, P. (2015), Best practices for aerospace aerodynamics. (unpublished).
URL: https://mdx2.plm.automation.siemens.com/sites/default/files/Presentation/External_AeroSEA-ugm-2015.pdf

Fage, A. and Falkner, V. (1932), 'Notes on experiments on the temperature and velocity in the wake of a heated cylindrical obstacle.', *Proceedings of the Royal Society A: Mathematical, Physical and Engineering Sciences* **135**(828), 702–705.

Farsimadan, E. (2008), A study of the turbulent wake of an airfoil in an airstream with a 90 degrees curvature using hot-wire anemometry and large eddy simulation, PhD thesis, Brunel: Brunel University.

Ferziger, J. and Perić, M. (2002), *Computational methods for fluid dynamics*, 3rd edn, New York: Springer.

Gregory, N. and O'Reilly, C. (1973), Low speed aerodynamic characteristics of naca 0012 aerofoil section, including the effects of upper-surface roughness simulating hoar frost, Report 3726, NPL Aerodynamics Division.

Gur, O., M. W. and Schetz, J. (2010), 'Full configuration drag estimation', *Journal of Aircraft* **47**(4), 1356–1367.

Haggmark, C., Hildings, C. and Henningson, D. (2001), 'A numerical and experimental study of a transitional separation bubble', *Aerospace Science and Technology* **5**(5), 317–328.

Hah, C. and Lakshminarayana, B. (1982), 'Measurement and prediction of mean velocity and turbulence structure in the near wake of an airfoil', *Journal of Fluid Mechanics* **115**, 251–282.

Harlow, F. and Nakayama, P. (1968), Transport of turbulence energy decay rate, Report 3854, Los Alamos Scientific Laboratory of the University of California.

Hellsten, A. (2005), 'New advanced k-w turbulence model for high-lift aerodynamics', *AIAA Journal* **43**(9), 1857–1869.

Hermann, S. and Gersten, K. (2017.), *Boundary layer theory*, 9th edn, Berlin Heidelberg: Springer-Verlag.

Hoerner, S. (1965), *Fluid Dynamic Drag: Theoretical, experimental and statistical information*, New York: Hoerner Fluid Dynamics.

Hosseinverdi, S. and Fasel, H. (2015), 'Laminar-turbulent transition in a laminar separation bubble in the presence of free-stream turbulence', *Procedia IUTAM* **14**, 570–579.

Houghton, E. (2012), *Aerodynamics for engineering students*, 6th edn, Waltham, MA: Butterworth-Heinemann.

Hulsmann, U. (2006), Wind tunnel tests and modification of the wing-fuselage junction of the high-peformance sailplane mu-31, Masters thesis, Delf: Delf University of Technology.

Jacobs, R. and Durbin, P. (2001), 'Simulations of bypass transition', *Journal of Fluid Mechanics* **428**, 185–212.

Joao Nuno Dias, C. (2016*a*), Optimizing UAV Aerodynamics with Computational Fluid Dynamics, Masters thesis, Lisboa: Tecnico Lisboa.

Joao Nuno Dias, C. (2016*b*), Optimizing uav aerodynamics with computational fluid dynamics. (Unpublished).
URL: https://fenix.tecnico.ulisboa.pt/downloadFile/1407770020545515/resumo.pdf

Jobe, C. E. (1984), Prediction of aerodynamic drag, Report 84203, Flight Dynamics Laboratory Air Force Wright Aeronautical Laboratories.

Johnson, D. A. and King, L. S. (1985), 'A mathematically simple turbulence closure model for attached and separated turbulent boundary layers', *AIAA Journal* **23**(11), 1684–1692.

Jones, W. and Launder, B. (1972), 'The prediction of laminarization with a two-equation model of turbulence', *International Journal of Heat and Mass Transfer* **15**(2), 301–314.

Kalitzin, G., Medic, G., Iaccarino, G. and Durbin, P. (2005), 'Near-wall behavior of rans turbulence models and implications for wall functions', *Journal of Computational Physics* **204**(1), 265–291.

Ladson, C. (1988), Effects of independent variation of Mach and Reynolds numbers on the low-speed aerodynamic characteristics of the NACA 0012 airfoil section, Report 4074, NACA.

Lam, K. and Bremhorst, K. (1981), 'A modified form of the k-e model for predicting wall turbulence', *Journal of Fluids Engineering* **103**(1), 456–461.

Langtry, R. and Sjolander, S. (2002), Prediction of transition for attached and separated shear layers in turbomachinery, *in* '38th AIAA/ASME/SAE/ASEE Joint Propulsion Conference and Exhibit'.

Launder, B. and Sharma, B. (1974), 'Application of the energy-dissipation model of turbulence to the calculation of flow near a spinning disc', *Letters in Heat and Mass Transfer* **1**(2), 131–137.

Lyon, C., Broeren, A., Giguere, P., Gopalarathnam, A. and Selig, M. (1997), *Low speed airfoil data*, Virginia: SoarTech.

Menter, F. (1992a), 'Performance of popular turbulence models for attached and separated adverse pressure gradient flows', *AIAA Journal* **30**(8), 2068–2072.

Menter, F. (1992b), 'Influence of freestream values on k-w turbulence model predictions', *AIAA Journal* **30**(6), 1657–1659.

Menter, F. (1992c), 'Two-equation eddy-viscosity turbulence models for engineering applications', *AIAA Journal* **32**(8), 1598–1605.

Menter, F. (2009), 'Review of the shear-stress transport turbulence model experience from an industrial perspective', *International Journal of Computational Fluid Dynamics* **23**(4), 305–316.

Menter, F., Langtry, R., Likki, S., Suzen, Y.B. abd Huang, P. and Völker, S. (2004), A correlation-based transition model using local variables part i - model formulation, *in* 'Proceedings of the ASME Turbo Expo', Vol. 4, pp. 57–67.

Menter, F. R., Langtry, R. B., Likki, S. R., Suzen, Y. B., Huang, P. G. and Völker, S. (2004b), A correlation-based transition model using local variables part II - Test cases and industrial applications, *in* 'Proceedings of the ASME Turbo Expo 2004', Vol. 4, pp. 69–79.

Oberkampf, W. and Trucano, T. (2002), 'Verification and validation in computational fluid dynamics', *Progress in Aerospace Sciences* **38**(3), 209–272.

Piradeepan, N. and Mokhtarzadeh-Dehghan, M. (2005), 'Measurements of mean and turbulence quantities in the curved wake of an airfoil', *Experimental Thermal and Fluid Science* **29**(2), 239–252.

Pope, S. (2000), *Turbulent flows*, Cambridge: Cambridge University Press.

Popelka, L., Kuklova, J., Simurda, D., Souckova, N., Matejka, M. and Uruba, V. (2012), Visualization of boundary layer separation and passive flow control on airfoils and bodies in wind-tunnel and inflight experiments, *in* 'EPJ Web of Conferences', Vol. 25, pp. 1–9.

Ramaprian, B., Patel, V. C. and Sastry, M. (1982), 'The symmetric turbulent wake of a flat plate', *AIAA Journal* **20**(9), 1228–1235.

Ramjee, V. and Neelakandan, D. (1990), 'Curvature effects on the wake of an airfoil and other bodies', *Fluid Dynamics Research* **6**(1), 1–13.

Ramjee, V., Tulapurkara, E. G. and Rajasekar, R. (1988), 'Development of airfoil wake in a longitudinally curved stream', *AIAA Journal* **26**(8), 948–953.

Roache, P. (1997), Quantification of uncertainty in computational fluid dynamics, *in* 'Annual Review of Fluid Mechanics', Vol. 29, pp. 123–160.

Sai, V. and Lutfy, F. (1995), 'Analysis of the Baldwin-Barth and Spalart-Allmaras one-equation turbulence model', *AIAA Journal* **33**(10), 1971–1974.

Salim, S. and Cheah, S. (2009), Wall y+ strategy for dealing with wall-bounded turbulent flows, *in* 'The International MultiConference of Engineers and Computer Scientists', Vol. 2.

Schlichting, H. (1978), *Boundary Layer Theory*, NewYork: McGraw Hill.

Selig, M. (1989), *Airfoils at low speeds*, Virginia: H.A. Stokely.

Selig, M. and Bryan, D. (2004), Wind tunnel aerodynamic tests of six airfoils on small wind turbines, Report 34515, National Renewable Energy Laboratory.

Selig, M., Guglielmo, J., Broeren, A. and Giguere, P. (1995), *Low speed airfoil data*, Virginia: SoarTech.

Selig, M., Lyon, C., Giguere, P., Ninham, C. and Guglielmo, J. (1996), *Low speed airfoil data*, 2nd edn, Virginia: SoarTech.

Shelda R.E. and Klimas, P.C. (1981), Aerodynamic characteristics of seven symmetrical airfoil sections through 180-degree angle of attack for use in aerodynamic analysis of vertical axis wind turbines, Report 4239, SNL.

Siemens (2017), 'STAR-CCM+ user guide'.
URL: file:///C:/Program20Files/CD-adapco/12.02.011/STAR-CCM+12.02.011/doc/en/online/index.htmlpage/connect2Fsplash.html

Siemens (2018), Spotlight on meshing. (Unpublished).
URL: https://salesforce.industrysoftware.automation.siemens.com

Smith, A. and Gamberoni, N. (1956), Transition, pressure gradient anad stability theory, Report 26388, Douglas aircraft company.

Spalart, P. and Allmaras, S. (1994), 'One-equation turbulence model for aerodynamic flows', *Recherche aerospatiale* (1), 5–21.

Spalart, P. R. and Allmaras, S. R. (1992), 'A one-equation turbulence model for aerodynamic flows', *AIAA Paper 92-439* .

Speziale, C., Abid, R. and Anderson, E. (1990), A critical evaluation of two-equation models for near wall turbulence, Conference Proceedings 182068, NACA.

Sutalo, F. (2017), Evaluation of variants of enhanced wall treatment wall function in turbulent flow simulations, Phd thesis, Zagreb: University of Zagreb.

Tennekes, H. and Lumley, J. (1972), *A first course in turbulence*, Cambridge: MIT Press.

Tools, A. (2018), 'Naca 4 digit airfoil generator'.
URL: http://airfoiltools.com

Tulapurkara, E., Vengadesan, S. and Lakshminarasimhan, J. (1993), 'Computation of turbulent asymmetric wake', *International Journal for Numerical Methods in Fluids* **16**(3), 239–248.

United States Department of Transport, F. A. A. (2016), *Pilot's handbook of aeronautical knowledge*, Oklahoma City: United States Department of Transport, Federal Aviation Administration.

U.S. Department of Transportation, F. A. A. (2013), *Glider flying handbook*, Oklahoma City: U.S. Department of Transportation, Federal Aviation Administration.

van Ingen, J. (1956), A suggested semi-empirical method for the calculation of the boundary layer transition region, Report 74, Technische Hogeschool Vliegtuigbuowkunde.

van Ingen, J. (2008), The eN method for transition prediction. Historical review of work at TU Delft, *in* '38th AIAA Fluid Dynamics Conference and Exhibit', pp. 1–49.

Versteeg, H. and Malalasekera, W. (2007), *An introduction to computational fluid dynamics: The finite volume method*, 2nd edn, New York: Pearson Education.

Vlahostergios, Z., Yakinthos, K. and Goulas, A. (2009), 'Separation-induced boundary layer transition: Modeling with a non-linear eddy-viscosity model coupled with the laminar kinetic energy equation', *International Journal of Heat and Fluid Flow* **30**(4), 617–636.

von Doenhoff, A.E. and Frank T.A. (1947), The Langely Two-dimensional Low Turbulence Pressure Tunnel, Report 1283, NACA.

von Karman, T. (1931), Mechanical similitude and turbulence, Report 611, NACA.

Wallin, S. and Johansson, A. V. (2000), 'An Explicit Algebraic Reynolds Stress Model for incompressible and compressible turbulent flows', *Journal of Fluid Mechanics* **403**, 89–132.

Walters, D. and Leylek, J. (2004), 'A new model for boundary layer transition using a single-point RANS approach', *Journal of Turbomachinery* **126**(1), 193–202.

Westin, K. and Henkes, R. (1997), 'Application of turbulence models to bypass transition', *Journal of Fluids Engineering, Transactions of the ASME* **119**(4), 859–866.

Weygandt, J. and Mehta, R. (1995), 'Three-dimensional structure of straight and curved plane wakes', *Journal of Fluid Mechanics* **282**, 279–311.

Wichita State University (2008), Walter H. Beech Memorial 7x10 foot Low Speed Wind Tunnel. (unpublished).

Wilcox, D. (1988), 'Reassessment of the scale-determining equation for advanced turbulence models', *AIAA Journal* **26**(11), 1299–1310.

Wilcox, D. (1994), 'Simulation of transition with a two-equation turbulence model', *AIAA Journal* **32**(2), 247–255.

Wilcox, D. (2006), *Turbulence Modeling for CFD*, 3rd edn, Carlifonia: DCW Industries.

Wilcox, D. (2008), 'Formulation of the k-w turbulence model revisited', *AIAA Journal* **46**(11), 2823–2838.

Williamson, G. (2012), Experimental wind tunnel study of airfoils with large flap deflections at low Reynolds numbers, Phd thesis, Illinois: University of Illinois.

Williamson, G., McGranahan, B., Broughton, B., Deters, R., Brandt, J. and Selig, M. (2012), *Low speed airfoil data*, 5th edn, Virginia: SoarTech.

Woelke, M. (2007), 'Eddy-viscosity turbulence models employed by computational fluid dynamics.', *Prace Instytutu Lotnictwa* **191**(4), 92–113.

Zeierman, S. and Wolfshtein, M. (1986), 'Turbulent time scale for turbulent-flow calculations', *AIAA Journal* **24**(10), 1606–1610.